Characterisation and Structural Health Monitoring of Historic Fibrous Plaster Ceilings

A dissertation submitted towards the degree of

Doctor of Philosophy

Department of Engineering Science

University of Oxford

by

Jiaxu Zuo

Mansfield College, Michaelmas 2025

Abstract

Fibrous plaster (FP) has been widely used in high-profile decorative suspended ceilings across the UK since the late nineteenth century. As a material of significant architectural and cultural value, FP warrants systematic conservation. However, knowledge of its material properties and structural behaviour remains limited, constraining the development of reliable inspection and monitoring practices. Current visual and tactile inspections, which are subjective, invasive, costly, and unsupported by a fundamental understanding of the material and its structural performance, are inadequate. Thorough characterisation of FP, together with objective and accurate inspection methods for historic FP ceilings, is therefore of vital importance and urgently required for FP heritage management. This study addresses these gaps through (i) a comprehensive multi-scale characterisation of FP, spanning constituent, composite, and ceiling-structural (wad) levels, and (ii) the establishment of an automated acoustic emission (AE)-based sensing framework for predictive, non-destructive structural health monitoring. For (i), at the constituent level, plaster of Paris (POP) and jute reinforcement (hessian), extracted from a Grade II listed building, were characterised alongside modern substitutes using physical, chemical, and mechanical testing. Advanced techniques, including digital image correlation (DIC) and X-ray characterisation, revealed new insights into elasticity, tensile strength, and yarn properties. At the composite scale, interfacial bonding was quantified via a novel pullout test with DIC-based slip measurement, analysed using an adapted Naaman model. At the wad level, complementary dogbone specimens representing wad geometry underwent a novel multi-modal in-situ test conducted at the Diamond Light Source (DLS), I12 Joint Engineering, Environmental and Processing (JEEP) beamline laboratory. Direct tensile tests with digital volume correlation (DVC) via synchrotron X-ray computed tomography (sCT), combined with DIC and AE, elucidated failure mechanisms (matrix cracking and fabric–matrix debonding) and also demonstrated that non-uniform debonding and fabric bridging enhance structural ductility and serviceability, thereby informing the reconstruction of durable wads. For (ii), AE

was advanced for source localisation and failure-mechanism classification, using data-driven approaches and machine learning techniques. A one-dimensional convolutional neural network (1D-CNN) achieved high localisation accuracy, validated both in laboratory conditions and in field trials on a Grade II listed ceiling. Parallel unsupervised spherical k-means clustering successfully distinguished matrix cracking from fabric-matrix debonding, validated by in-situ sCT direct tensile tests integrated with AE, DIC, and DVC analyses. This work advances understanding of FP material properties and structural behaviour to provide a strong benchmark for future inspection and maintenance and to inform the manufacture of durable structural components; it also delivers robust, field-deployable AE monitoring tools that enable rapid risk triage, targeted inspection, and continuous condition tracking, offering clear criteria for conservation while minimising intervention within heritage interiors.

Acknowledgements

I am deeply grateful to my supervisors, Professor Sinan Acikgoz, Professor Brian Sheil, and Professor James Marrow, for their invaluable guidance, encouragement, and support throughout this research. I also thank my collaborators, colleagues, and the technical staff in the Civil Engineering Research Group, the Materials Research Group, and the associated laboratories at the University of Oxford for their assistance and insightful discussions.

Special thanks go to the technical team at Diamond Light Source, particularly at Beamline I12, for their support with the experimental work, and to the team at One Great George Street for their help during the fieldwork. I am especially thankful to Sarah Mayfield for introducing this compelling research topic and for her generous support throughout the project.

I gratefully acknowledge the Institution of Civil Engineers for funding this research.

Finally, I am deeply thankful to my family and friends for their unwavering support and encouragement throughout this journey.

Contents

1 Introduction **1**
1.1 Background 1
1.2 Reseasrch objectives 5
1.3 Outline of the thesis 6

2 Literature review **8**
2.1 Materials and construction 8
2.1.1 Constituent materials 8
2.1.2 Ceiling structural support components (wads) 11
2.1.3 Common forms of degradation 14
2.2 Fabric-reinforce composite characterisation 16
2.2.1 Constituent material characterisation 16
2.2.2 Reinforcement-matrix interfacial bonding 20
2.2.3 Tensile behaviour characterisation 27
2.3 Non-destructive techniques for structural health monitoring 29
2.3.1 Overview of non-destructive techniques 29
2.3.2 Acoustic emission 29
2.3.3 Full-field imaging modalities 38
2.4 Summary 44

3 Paper 1: Constituent and composite level characterisation of fibrous plaster in decorative suspended ceilings **46**

4 Paper 2: A three-stage approach based on 1D-CNNs for AE source localisation on historic fibrous plaster ceilings **63**

5 Paper 3:Acoustic emission-based failure detection and event source localisation in a historical fibrous plaster ceiling **82**

6 Paper 4:Acoustic emission and in-situ synchrotron X-ray computed tomography for the investigation of tensile failures in fibrous plaster 97

7 Conclusions and future work 116

7.1 Conclusions 116

7.2 Future work 118

7.2.1 Fracture toughness characterisation of POP (extended to FP) 118

7.2.2 Synchrotron X-ray diffraction strain mapping during in-situ tensile testing 121

7.2.3 Durability characterisation via accelerated ageing 122

7.2.4 Large-scale deployment of integrated AE-based SHM system into heritage practice 123

Bibliography 125

Chapter 1

Introduction

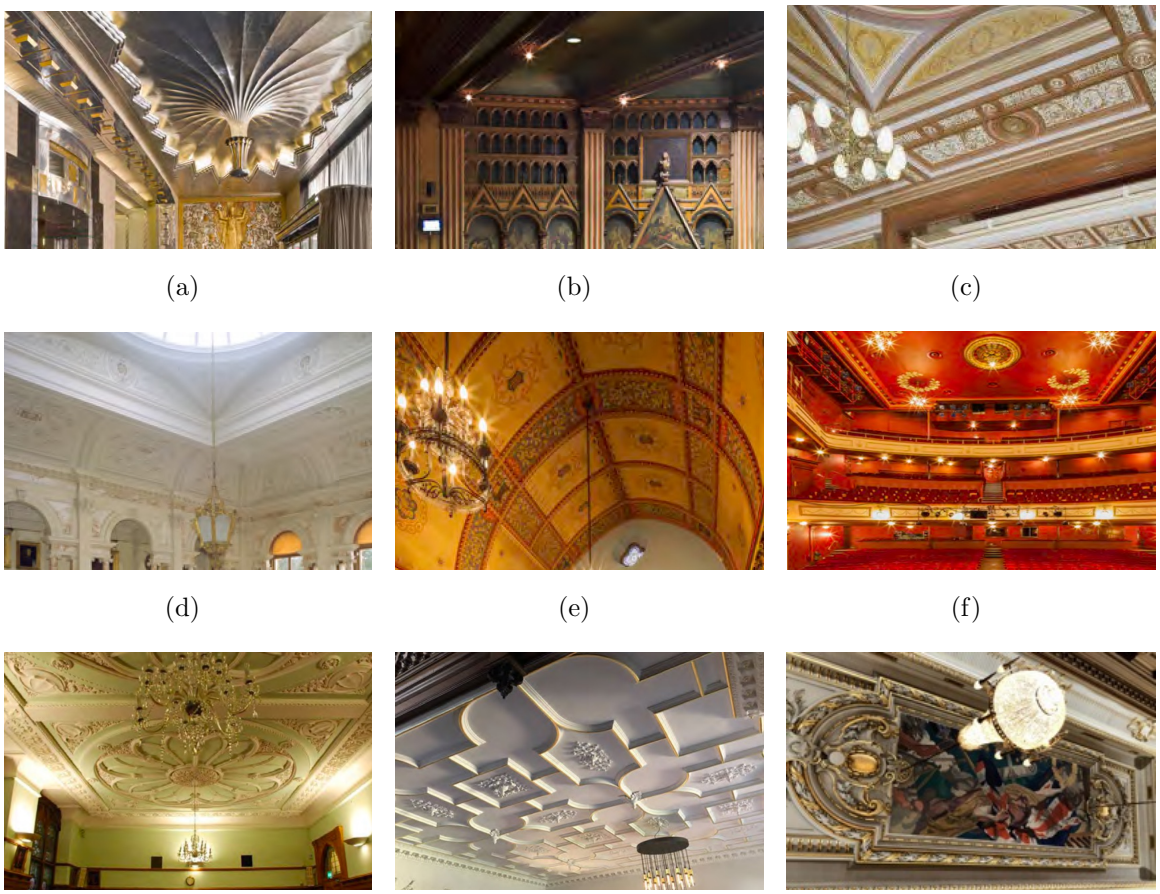
Abbreviations

Abbreviation	Definition
FP	Fibrous Plaster
POP	Plaster of Paris
FRC	Fabric-Reinforced Composite
SHM	Structural Health Monitoring
NDT	Non-destructive Technique
AE	Acoustic Emission
sCT	Synchrotron X-rat Computed Tomography
DIC	Digital Image Correlation
DVC	Digital Volume Correlation

1.1 Background

From the late nineteenth century, fibrous plaster (FP) became extensively employed in the construction of suspended decorative ceilings in buildings across the UK. The material, patented in 1856 by the Frenchman Léonard Alexander Defries, is a fabric-reinforced composite (FRC) comprising plaster of Paris (POP) and woven jute fabrics, the latter commonly referred to as 'hessian' [1]. FP is an important material in the history of decorative architecture, valued for its role in showcasing traditional craftsmanship and sustaining cultural heritage. FP was developed to facilitate the production of lightweight, durable, and intricately detailed architectural features, en-

abling the efficient formation of complicated pre-cast panel shapes such as niches, eccentric vaulting, and serpentine box fronts [1]. It was also widely used for the mass production of smaller architectural enrichments and ornamental elements, including cornices, columns, and ceiling roses [1]. The introduction of FP transformed interior decoration by enabling craftsmen to manufacture mouldings and decorative components off-site, which could then be transported and rapidly assembled on-site [1].



(a) (b) (c)

(d) (e) (f)

(g) (h) (i)

Figure 1.1: Heritage-listed FP ceilings in historic UK buildings: (a) Daily Express Building, London (1932); (b) Former Granada Cinema, Tooting, London (1930-31); (c) Glasgow City Chambers (1888); (d) Marble Hall, Gosford House, Longniddry (1890); (e) Library, Insole Court, Cardiff (1873); (f) New Theatre, Cardiff (1906); (g) Guildhall, Londonderry (1909); (h) Ormiston House, Belfast (1860-79); (i) Great Hall, One Great George Street, London (1910-13).

The use of FP became particularly widespread between the early 1880s and the

1910s, coinciding with a period of significant public building construction during the Victorian and Edwardian eras [1]. It was favoured over traditional lime-based plasters owing to its lower cost, reduced weight, faster setting time, and relative ease of installation [2]. FP was particularly prevalent in places of entertainment, public halls, hotels, and other prominent buildings, where it contributed to ornate interior designs emblematic of the craftsmanship and opulence of the period. By 1921, the UK had around 4,000 cinemas, approaching the 1949 peak of 4,800, many of which featured elaborate interiors decorated with FP [1]. FP became a standard architectural material and remained in use into the 1930s. Following the Second World War, lightweight gypsum plasters and plasterboard largely replaced FP, although it persisted in heritage restoration and for clients favouring traditional designs. The capacity of FP to be cast into complex forms continues to support mass production in decorative architecture, with numerous firms in London specialising in fibrous plasterwork for both domestic and export markets. It is estimated that more than 1,000 buildings in the UK still retain FP ceilings today, many of which are now heritage-listed structures valued for their architectural and cultural significance [3]. Some examples are illustrated in Figure 1.1.



(a) (b)

Figure 1.2: Current inspection of historic FP ceilings. (a) Scaffolding used for visual and tactile inspection. (b) Drilled openings allow access to concealed supporting structural components of FP ceilings.

Despite its cultural importance and widespread use, FP has received limited attention in the scientific literature. Data concerning its material properties remain sparse, and knowledge of the structural behaviour of FP ceilings is similarly lacking. This may be attributed to insufficient awareness of the extent of its historic use, in contrast to other traditional materials such as lime mortar and masonry, and perhaps

also to the perception that it was a less valued material [1]. Consequently, current inspection practices lack a rigorous, standardised technical foundation and rely heavily on the experience and judgement of structural engineers, conservators, and plasterers.

The Association of British Theatre Technicians (ABTT) has issued guidance for the inspection of historic FP ceilings [4], recommending periodic visual and tactile inspections by suitably experienced personnel. However, such inspections are typically costly, with an average cost of approximately £15,000 per theatre [5], and often require the erection of temporary scaffolding (Figure 1.2(a)), which introduces considerable risk to both workers and the building. A particularly significant drawback is the need for destructive access interventions, such as drilling hatches into FP ceiling panels to examine concealed supporting structural components (Figure 1.2(b)). Most importantly, these inspections provide largely subjective assessments and offer only limited assurance of structural safety in the absence of reliable knowledge of material properties and structural behaviour.

The survival of many FP ceilings for more than a century highlights their durability under favourable conditions, particularly in well-maintained buildings. However, their structural integrity has been increasingly compromised by material degradation, defects in structural components, inadequate support, excessive loads, and physical damage. As a composite system, the deterioration of any constituent material, whether the POP matrix or hessian reinforcement, can weaken the entire ceiling. In suspended FP ceilings, localised failures may overstress supporting components, potentially leading to progressive collapse through a domino effect. Recently, several incidents involving the partial or complete collapse of historic FP ceilings have been reported, leading to injuries, operational disruptions, and significant financial losses. Notable examples include the collapse of the Apollo Theatre in London in December 2013 [6], the failure of the Queen's Ballroom ceiling in Blackpool in September 2017 [7], and the collapse of the Savoy Ballroom in London in March 2019 [8]. These events underscore the urgent need for a comprehensive understanding of the material properties and structural behaviour of FP ceilings, particularly given their prevalence in high-profile and densely occupied buildings, where failure poses a serious risk to public safety.

Thorough characterisation of FP is essential to provide a standardised foundation for the inspection of FP ceilings. Equally important is the development of an objective, reliable, and non-destructive structural health monitoring (SHM) system capable of delivering robust and accurate detection of structural deterioration. Although inspection methods have advanced in recent decades, they remain insufficient

to address key challenges, particularly hidden degradation and the early stages of progressive failure. Strengthening detection strategies is therefore both urgent and crucial. There is a pressing need for novel monitoring approaches that combine scientific rigour with practical applicability, ensuring that historic FP ceilings can be safeguarded more effectively. This research directly addresses these needs by consolidating the literature on FP and establishing the basis for monitoring methods with the specific capabilities required to support heritage conservation and risk mitigation.

1.2 Reseasrch objectives

This thesis establishes a systematic framework for understanding and developing monitoring approaches for historic FP ceilings. It provides a robust scientific foundation for future inspection and conservation practice through two core objectives: (i) comprehensive characterisation of FP as a historic material and (ii) development of objective, non-destructive monitoring techniques for early-stage failure detection. Within this framework, two interconnected strands of work are pursued to address the central research problem.

The first strand is directed towards advancing the understanding of the material properties and structural behaviour of historic FP ceilings, thereby supporting more reliable assessment and monitoring. Specifically, this part of the research is concerned with:

- Characterising the physical, chemical, and mechanical properties of historic FP at the constituent level, using modern equivalents to elucidate properties where direct testing of original material is limited;
- Investigating the bonding behaviour between the POP matrix and hessian reinforcement in order to clarify interfacial performance under load;
- Evaluating the tensile properties and internal failure mechanisms of FP composites representative of critical supporting structural components (wads).

The second strand is directed towards the development of a SHM system for historic FP ceilings, designed to enable objective and non-invasive inspection. This is pursued through the application of non-destructive acoustic emission (AE) techniques to detect, localise, and characterise early-stage micro-failures within FP ceiling systems, thereby providing a pathway to evaluate their structural health. Specifically, this part of the research is concerned with:

- Developing and validating an AE-based source localisation model capable of accurately and robustly localising critical micro-failures within FP ceiling systems;

- Developing and validating an AE-based failure characterisation model to distinguish between the mechanisms associated with detected micro-failures and, on this basis, to assess the ongoing overall structural condition of FP ceilings.

Taken together, these strands form an integrated research system that links fundamental material characterisation with advanced monitoring methodologies. This systematic framework provides a technical basis for improved inspection and conservation of historic FP ceilings, contributing directly to their long-term preservation and safety management.

1.3 Outline of the thesis

This thesis begins with an introduction that presents the background and motivation for the study, outlines the research objectives, and defines the scope and structure of the work. A literature review then follows, providing an overview of FP constituents and composites, the structural configuration and supporting components of historic FP ceilings, and the common forms of their degradation. It also reviews relevant mechanical testing approaches and analytical models for material characterisation, and highlights key non-destructive techniques (NDTs) for both characterisation and SHM, including AE and advanced two- and three-dimensional imaging modalities, with particular attention to their theoretical foundations and applications.

The main body of the thesis is structured around four peer-reviewed journal articles, each addressing specific research objectives:

- **Paper 1:** *Constituent and composite level characterisation of fibrous plaster in decorative suspended ceilings.* This paper contributes to the *first objective* by characterising FP at both constituent and composite levels and by examining the behaviour of critical supporting components (wads) in historic FP ceilings.

- **Paper 2:** *A three-stage approach based on 1D-CNNs for AE source localisation on historic fibrous plaster ceilings.* This paper contributes to the *second objective* by developing an AE-based event source localisation model designed to accurately and robustly identify the locations of micro-failures within FP ceiling systems without the need to access concealed internal spaces.

- **Paper 3:** *AE-based failure detection and event source localisation in a historic fibrous plaster ceiling.* This paper advances the *second objective* by validating the AE-based source localisation model developed in **Paper 2** through field trials conducted at the Institution of Civil Engineers (ICE) headquarters, One Great George Street, Westminster, London, a Grade II* listed building of significant heritage value.

- **Paper 4:** *Acoustic emission and in-situ synchrotron X-ray computed tomography for the investigation of tensile failures in fibrous plaster.* This paper contributes to both the *first* and *second objectives*. In relation to the *first objective*, it advances the understanding of internal failure mechanisms governing damage in FP wads through an innovative in-situ experimental campaign at Diamond Light Source (DLS), conducted at the I12 Joint Engineering, Environmental and Processing (JEEP) beamline. The campaign integrated AE, digital image correlation (DIC), and synchrotron X-ray computed tomography (sCT)-based digital volume correlation (DVC) measurements and analyses. In relation to the *second objective*, it develops an AE-based failure characterisation model employing an unsupervised spherical k-means clustering method to classify failure mechanisms associated with detected micro-failures in FP. This model was cross-validated through application to the in-situ experiments and further verified through multi-modal data comparison.

The thesis concludes by summarising the key findings, highlighting the main contributions, and presenting specific recommendations for future research.

Chapter 2

Literature review

2.1 Materials and construction

This section reviews the existing literature on FP and its constituent materials, along with the key structural characteristics of historic FP ceiling systems, and highlights the current knowledge gaps and practical challenges, thereby establishing the context and rationale for the present research.

2.1.1 Constituent materials

FP consists of two principal constituents: POP, which forms the matrix, and woven jute fabric (commonly known as hessian), which provides the reinforcement.

2.1.1.1 Plaster of Paris

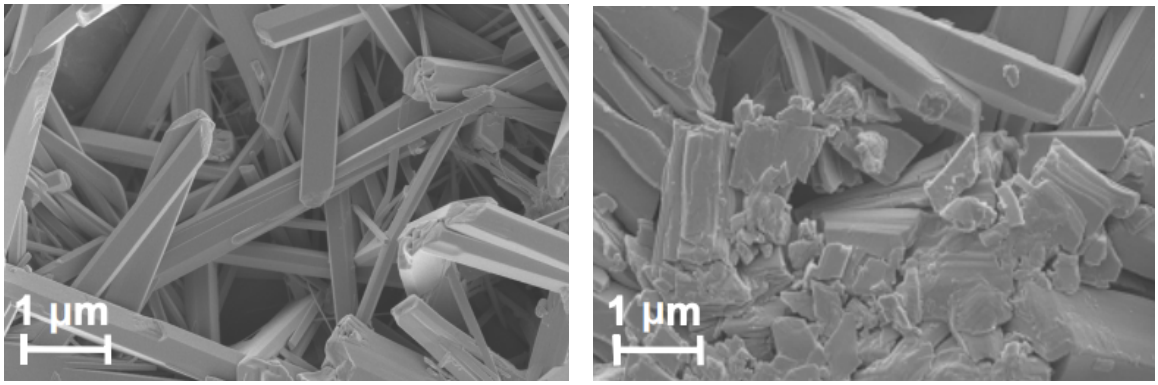
POP is produced through two sequential stages: calcination and hydration. In the calcination stage, calcium sulfate dihydrate (gypsum, $CaSO_4 \cdot 2H_2O$) is subjected to controlled heating at 150-180 °C, during which 1.5 molecules of water of crystallisation are released, yielding calcium sulfate hemihydrate ($CaSO_4 \cdot 0.5H_2O$):

$$CaSO_4 \cdot 2H_2O \xrightarrow{\text{heat}} CaSO_4 \cdot 0.5H_2O + 1.5H_2O \uparrow \tag{2.1}$$

The resulting product is ground into a fine powder, commonly referred to as raw POP. When the hemihydrate powder is subsequently mixed with water, it undergoes an exothermic hydration reaction, re-forming calcium sulfate dihydrate. This process produces POP casts with a rigid, interlocking crystalline structure, which also constitutes the matrix of FP casts [9]:

$$CaSO_4 \cdot 0.5H_2O + 1.5H_2O \rightarrow CaSO_4 \cdot 2H_2O \tag{2.2}$$

POP is characterised by a relatively rapid setting time, with the initial set typically achieved within 10-15 minutes [10]. The material undergoes only minimal shrinkage during hardening [11]. However, its durability is significantly reduced in damp environments, where calcium sulfate dihydrate is susceptible to softening and dissolution [12, 13].



(a) (b)

Figure 2.1: Crystal morphology of hydrated POP observed under SEM: (a) α-form, showing well-structured and entangled crystals, and (b) β-form, showing shorter, stacked crystals [14].

Two principal forms of raw POP (calcium sulfate hemihydrate), α and β, differ in production method, crystal morphology, and mechanical performance. The β-form is produced via dry calcination at low water vapour partial pressure (45-200 °C), yielding irregular and porous crystals that require higher water content for mixing [15]. In contrast, the α-form is obtained through wet calcination under high water vapour partial pressure, with the heating temperature dependent on autoclave conditions. This process produces denser, prismatic crystals that require less water and result in stronger casts [15]. Figure 2.1 shows hydrated POP (calcium sulfate dihydrate) derived from the two forms of raw POP, as observed using a scanning electron microscope (SEM), highlighting their distinct morphological features. The α-form hydrated POP exhibits well-structured crystals with a high degree of entanglement, corresponding to higher strength, whereas the β-form hydrated POP consists of shorter crystals that are stacked rather than entangled, leading to lower strength [14]. Historic FP primarily incorporated the β-form POP due to its lower cost and widespread availability [1]. From the 1930s onwards, α-form POP began to be manufactured and was increasingly adopted for casting FP components. However, during the same period, the overall use of FP declined as demand grew for stronger and more

durable casting materials [1].

Another factor influencing the mechanical performance of POP is the water-to-plaster (W/P) ratio, defined as the amount of water employed during mixing of raw POP with water in the hydration stage. The W/P ratio plays a critical role in governing the microstructural characteristics of the resulting hydrated POP. Previous studies [2, 12, 13, 16, 17] have shown that lower W/P ratios typically yield a denser and more cohesive microstructure, which is associated with enhanced mechanical properties. Conversely, higher W/P ratios lead to increased porosity within the set material, thereby reducing mechanical performance due to the formation of a fragile and discontinuous matrix.

Compressive strengths for β-form POP with W/P ratios between 0.5 and 0.625 have been reported [18–21], generally falling within a range considered low to moderate compared with other construction materials. However, a comprehensive characterisation of β-form POP, the principal constituent of the historic FP matrix, remains lacking in the literature.

2.1.1.2 Woven jute fabric (hessian)

Jute fibre is a natural bast fibre extracted from the inner bark of the *Corchorus* species. It is primarily cultivated in the Ganges River delta, where environmental conditions favour its growth [1]. Jute fibres are composed predominantly of cellulose (60-70%), hemicellulose (13-20%), and lignin (12-13%) [22]. Studies have reported that jute fibres are capable of bearing significant loads and resisting stretch [22–24]. However, the relatively low lignin content of jute renders it susceptible to microbial degradation. Moreover, exposure to moisture promotes the oxidation and degradation of cellulose, resulting in reduced strength [25]. Research on similar bast fibres, such as sisal, shows that prolonged environmental exposure reduces tensile strength through microbial attack, moisture uptake, and UV radiation [26], suggesting that jute fibres are likely to degrade in a similar manner.

Woven jute fabric, commonly known as hessian and traditionally referred to as scrim in the trade, is a coarse fabric made from jute yarns (bundles of jute fibres). The morphology of jute yarns, observed under SEM, is shown in Figure 2.2(a). In historic FP ceilings, these yarns were typically arranged in orthogonal meshes with approximate spacings of 5 mm by 10 mm, as illustrated in Figure 2.2(b). The open weave facilitates the penetration of wet POP, enabling encapsulation of the fabric and the formation of a mechanical interlock upon setting [1].

The primary role of hessian in FP is to reinforce the brittle POP matrix, enhancing



(a) (b)

Figure 2.2: Hessian reinforcement in FP. (a) Crystal morphology of jute yarns from historic FP, showing bundles composed of jute fibres [1]. (b) Hessian used in historic FP, , showing a loosely spaced weave of jute yarns.

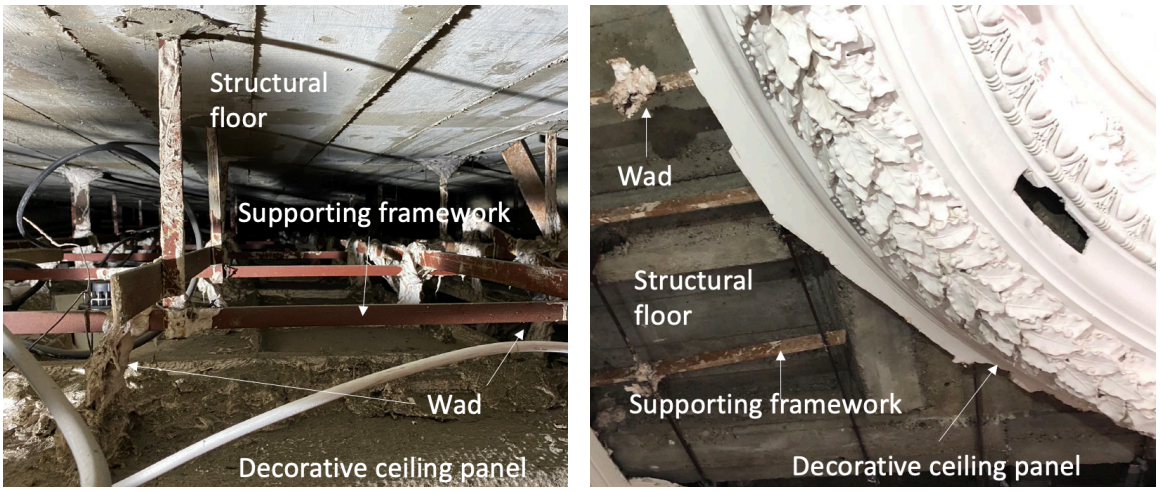
toughness and post-cracking load capacity. The fabric bridges cracks, limits their propagation, and improves resistance to brittle failure [3]. Experimental studies on modern FP replicas have demonstrated the beneficial effect of hessian in improving flexural performance and energy absorption capacity [6].

Although the mechanical behaviour of jute fibres has been studied, detailed characterisation of the principal constituent of hessian, the jute yarns, remains limited in the literature. In particular, quantified investigations of composite behaviour with respect to interfacial interactions and crack-bridging mechanisms are still lacking.

2.1.2 Ceiling structural support components (wads)

Historic FP ceilings possess a distinctive supporting system that integrates decorative elements with load-bearing components. Figure 2.3 illustrates a typical historic FP ceiling in both front and underside views, with annotations. In this system, the decorative ceiling panel is suspended from a timber or metal framework positioned beneath the structural floor above. This framework is securely fixed to the primary structure of the building and supports the FP ceiling panel through numerous tensile connectors known as 'wads'. These wads act as critical components, transferring the load of the suspended ceiling panel to the building framework.

Figure 2.4 shows a schematic of a typical wad supporting system. The wad is secured to the overhead framework beam either by adhesion, using a spread print of wet POP paste, or by wrapping around the framework to form a looped connection. Similar connection options are used at the interface with the ceiling panel below. In historic FP systems, both the ceiling panels and the wads were fabricated from



(a) (b)

Figure 2.3: Typical historic FP ceiling system: (a) front view and (b) underside view, illustrating decorative ceiling panels suspended from the building framework by structural support components known as wads.

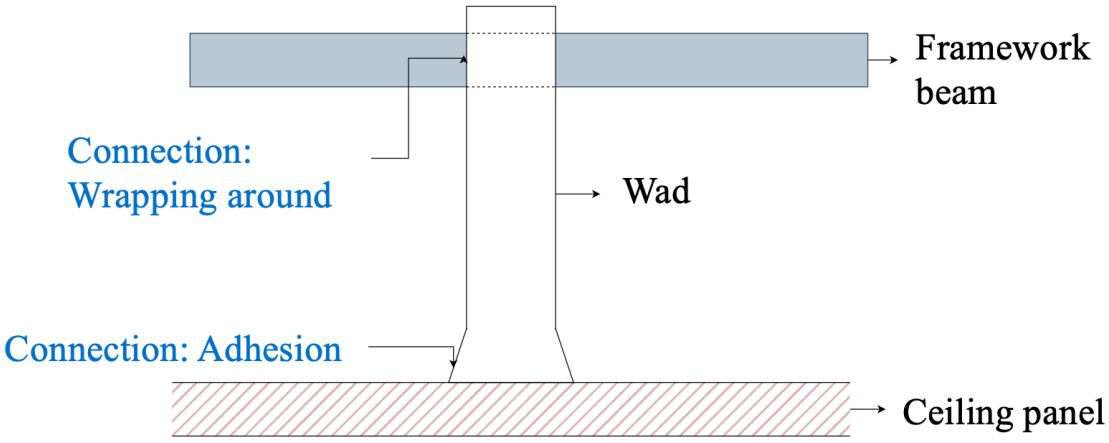


Figure 2.4: Schematic of a typical wad supporting system, showing the wad-framework interface connected by wrapping and the wad-ceiling panel interface connected by adhesion.

POP, but their manufacturing processes differed considerably, resulting in distinct structural configurations and mechanical behaviours.

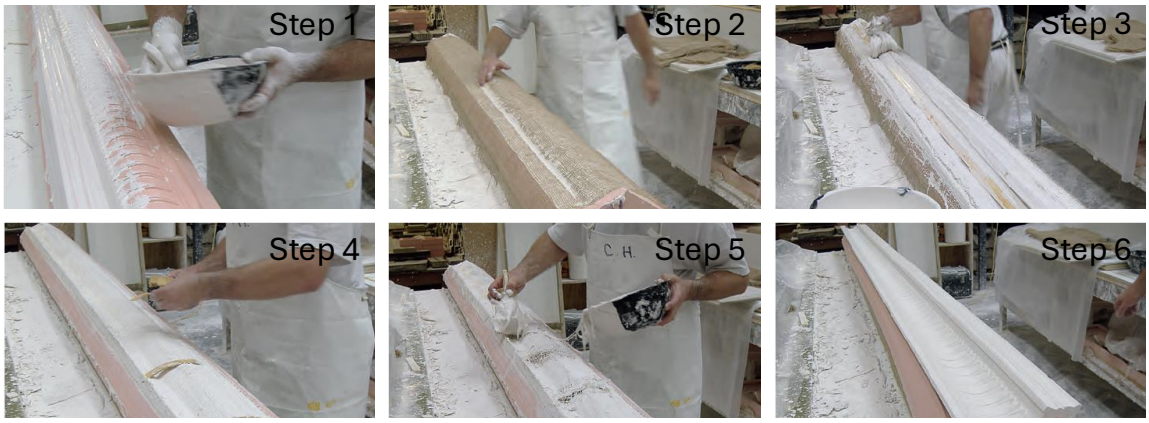
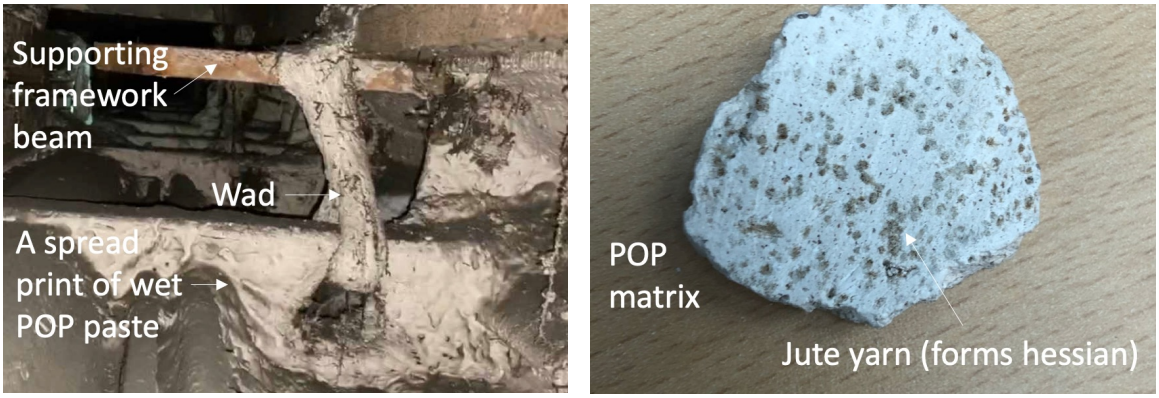


Figure 2.5: Manufacturing process for a typical FP ceiling panel, illustrating the sequential application of POP, the embedding of hessian, and the integration of timber laths [1].

The ceiling panel is cast through a controlled process that ensures uniformity and strength [1]. The manufacturing process for a typical FP ceiling panel is illustrated in Figure 2.5. Panels are fabricated as laminated FP composites incorporating embedded timber laths. Initially, POP is brushed over a mould to form the first coat (firstings), followed by a second coat (seconds) gauged with animal glue to enhance cohesion and bond strength. A layer of hessian is then pressed into the POP to provide primary reinforcement, after which a second layer of hessian is applied with an additional coat of seconds. Timber laths are embedded within the composite to further strengthen the structure, and the assembly is sealed with successive layers of hessian and POP. Ceiling panels are typically limited to dimensions of about 2 m $\times$ 2 m to allow safe handling and ease of installation.

The critical supporting components, wads, are fabricated through a unique manual process that is poorly standardised and often carried out in situ. Hessian is twisted and thoroughly soaked in wet POP paste to ensure complete penetration and encapsulation of the jute fibres. The impregnated hessian is then shaped and left to harden, forming an irregular, non-uniform cylindrical FP element. The final wad consists of a POP matrix reinforced by a central twisted and non-uniformly distributed hessian core, creating a connector that is simple to produce, robust, and slightly flexible, capable of accommodating variable spacing and minor movements within the ceiling system. Figure 2.6 shows a real wad connecting a ceiling panel to the framework, with



(a) (b)

Figure 2.6: Example of a real wad: (a) connection between the framework and ceiling panel; (b) cross-section showing twisted hessian encapsulated within the POP matrix.

its cross-section revealing the alignment of the twisted hessian encapsulated within the POP matrix.

2.1.3 Common forms of degradation

The deterioration of historic FP ceilings arises from multiple factors. A key contributor is exposure to adverse hygrothermal conditions, including extreme or fluctuating temperature and humidity levels [1]. POP, which forms the FP matrix, is slightly soluble in moisture, whether from direct wetting, high humidity, or condensation [1, 12, 13]. Moisture ingress may result from external weathering, air-conditioning systems, or building service failures such as plumbing leaks. A ceiling panel affected by dampness is shown in Figure 2.7(a). Moisture softens the POP matrix, exposing the embedded hessian reinforcement (Figure 2.7(b)), which then becomes vulnerable to biodegradation through fungal activity [25]. Conversely, persistent dryness can also reduce FP integrity. Localised heat sources may elevate ambient temperatures, accelerating the ageing and embrittlement of POP and intensifying the loss of cohesion within the composite [1]. Collectively, these hygrothermal effects progressively weaken FP structural components, leaving them increasingly susceptible to failure under service loads or accidental disturbance.

In addition to progressive environmental deterioration, uneven service load distribution from inadequate (Figure 2.8(a)) or poorly arranged supporting structures (Figure 2.8(b)) can also cause localised failure of FP components. Such deficiencies often reflect inconsistencies in construction practice at the time of installation,



(a) (b)

Figure 2.7: FP affected by adverse hygrothermal conditions: (a) ceiling panel showing dampness, and (b) exposed hessian undergoing biodegradation.

where workers did not consistently follow established standards, thereby introducing inherent vulnerabilities into the ceiling system. Another factor contributing to FP degradation is the imposition of external loads exceeding the ceiling's inherent bearing capacity. These may result from uncontrolled access, the installation of new services, or improper waste disposal (Figure 2.8(c)).



(a) (b) (c)

Figure 2.8: Factors leading to failures in historic FP ceilings: (a) Insufficient wad connections; (b) poorly aligned wads; (c) improper waste disposal in the ceiling void, adding unnecessary load.

Different forms of failure can result from environmental deterioration and physical interventions, including delamination at the wad–ceiling panel interface (Figure 2.9(a)), ceiling panel cracking (Figure 2.9(b)), and, most critically, wad snapping (Figure 2.9(c)). Wad snapping is the most common early-stage failure in historic FP ceilings and often serves as the precursor to complete ceiling collapse. It was the principal cause of the well-known Apollo Theatre ceiling failure [27].



(a) (b) (c)

Figure 2.9: Common forms of mechanical failure in historic FP ceilings: (a) delamination at the wad–ceiling panel interface; (b) ceiling panel cracking; (c) wad snapping.

2.2 Fabric-reinforce composite characterisation

2.2.1 Constituent material characterisation

To understand the behaviour of an FRC material system, it is first essential to characterise its constituent materials.

2.2.1.1 Plaster of Paris

POP is defined by its brittleness and poor impact resistance [28]. Among its key mechanical properties, elastic modulus, compression strength, and tensile strength are of primary importance.

Dynamic elastic modulus ASTM E1876-22 [29] specifies the determination of dynamic elastic modulus, shear modulus, and Poisson's ratio using the impulse excitation of vibration (IEV) method. In IEV, the specimen is placed on a specially designed support system, lightly struck at the impulse point, and its fundamental resonant frequencies are measured at the detecting transducer point using non-contact sensors such as microphones, accelerometers, or laser vibrometers. Two principal modes of vibration are employed: the flexural mode, from which the fundamental flexural frequency is measured and used to calculate the dynamic elastic modulus; and the torsional mode, from which the fundamental torsional frequency is measured and used to determine the shear modulus. Together, these values allow calculation of Poisson's ratio. A typical test setup for both flexural and torsional vibration modes applied to a rectangular specimen is shown in Figure 2.10, where L = length, b = width, t = thickness.

The dynamic elastic modulus is calculated as:

$$E = 0.9465 \frac{m f_f^2 L^3}{b t^3} T \tag{2.3}$$

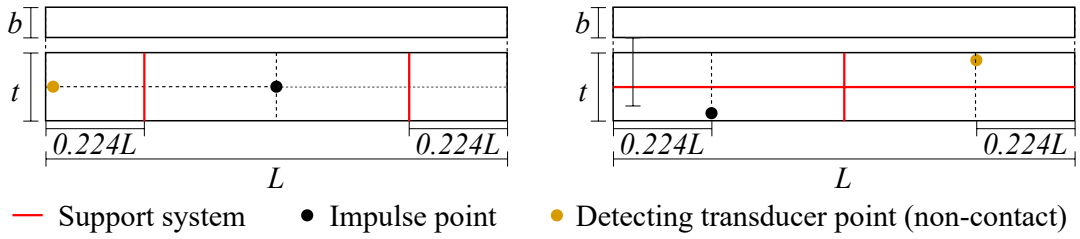


Figure 2.10: Typical impulse excitation of vibration (IEV) setup for a rectangular specimen: flexural mode (left) and torsional mode (right).

where

m = mass of the specimen, f_f = fundamental flexural resonant frequency,

T = correction factor.

The dynamic shear modulus is calculated as:

$$G = \frac{4Lmf_t^2}{bt}R \tag{2.4}$$

where

m = mass of the specimen, f_t = fundamental torsional resonant frequency,

R = correction factor.

The Poisson's ratio is calculated as:

$$\nu = \frac{E}{2G} - 1 \tag{2.5}$$

where

E = dynamic elastic modulus, G = dynamic shear modulus.

Dynamic methods are versatile and well suited to the characterisation of brittle materials [30]. They provide high accuracy without imposing strict requirements on specimen geometry, making them particularly appropriate for historic FP, as original specimens can be more readily extracted and prepared.

Static elastic modulus Determination of the static elastic modulus of POP remains challenging for several reasons: (i) the difficulty of extracting regular specimens such as cubes or prisms from historic FP; (ii) the absence of a dedicated standard testing method; and (iii) the inherent complexities of the testing process itself. With respect to (i), a representative substitute for POP is required. Since the β-form is

the raw POP used in production, the W/P ratio can be adjusted to approximate the properties of historic POP, guided by values obtained from dynamic modulus measurements. Regarding (ii), existing standards for plaster testing, such as BS EN 13279-2 [31] and ASTM C472 [32], provide procedures for compression and flexural strength testing, but do not specify techniques for the precise strain measurement required for static elastic modulus evaluation. In addition, concerning (iii), attempts to determine the static elastic modulus using these frameworks are often compromised by load eccentricity, imperfect specimen preparation, and stress concentrations at contact surfaces, all of which can induce premature microcracking and distort the load-displacement response. As a result, no widely accepted or standardised method currently exists for the accurate measurement of static elastic modulus in brittle materials such as POP, despite its importance for FP characterisation. This highlights the need for a test setup capable of eliminating the above issues through accurate displacement measurement, conducted on reliable POP substitute specimens with regular geometries.

Compression strength According to BS EN 13279-2 [31], compression tests on gypsum plaster are performed using cube specimens with an edge length of 40 mm, as illustrated in Figure 2.11(a). The failure load under axial compression is recorded, and the compression strength is calculated as:

$$\sigma = \frac{F}{A} \tag{2.6}$$

where

F = applied load at failure, A = loaded cross-sectional area of the specimen.

Tensile strength Tensile strength is particularly critical in the context of historic FP ceilings, where wads act as essential structural components supporting ceiling panels under tensile loads. Reliable characterisation of tensile properties in brittle materials such as POP presents considerable challenges. Direct tensile testing is often impractical due to sensitivity to load eccentricity and difficulties in gripping, both of which may cause premature failure and yield unreliable results [33]. Consequently, indirect methods such as flexural tests and Brazilian splitting tests are commonly employed.

Flexural tests, typically performed in three- or four-point bending, provide an indirect measure of tensile strength by loading prismatic specimens in bending until failure. In three-point bending, maximum tensile stress develops at mid-span on the tension side. For POP, BS EN 13279-2 [31] specifies a three-point bending test

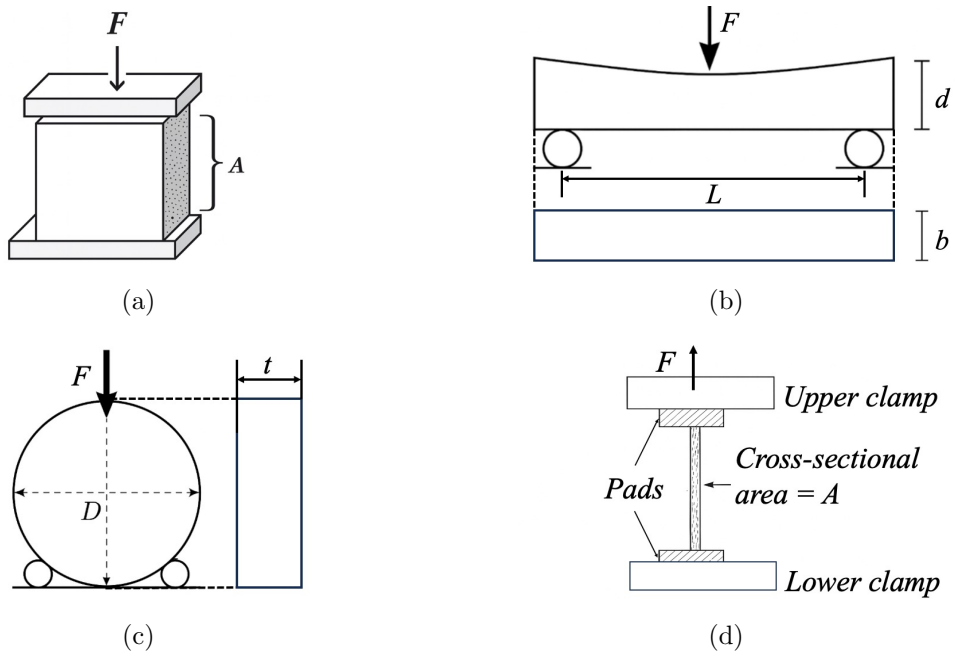


Figure 2.11: Schematic diagrams of test setups: (a) compression test; (b) flexural test (three-point bending); (c) Brazilian splitting test; (d) single-yarn tensile test.

(Figure 2.11(b)), with flexural strength calculated as:

$$\sigma = \frac{3FL}{2bd^2} \tag{2.7}$$

where

$$F = \text{failure load}, \quad L = \text{span length}, \quad b = \text{width}, \quad d = \text{depth}.$$

In theory, flexural strength equals true tensile strength in a perfectly homogeneous material. In practice, the porous, defect-rich microstructure of POP can concentrate stresses and causes premature failure, limiting its reliability. Nevertheless, flexural testing is useful where bending reflects service conditions. Tests on customised flat specimens simulating FP panels have shown that embedded hessian markedly improves the ductility of the POP matrix [6].

The Brazilian splitting test applies compression loading along the diameter of a cylindrical disc, inducing tensile stresses perpendicular to the applied load. Failure occurs when the disc splits along its diameter under these tensile stresses, despite the specimen being compressed, as specified in the ISRM Suggested Method [34]. A schematic of the test setup is shown in Figure 2.11(c). The indirect tensile strength is calculated as:

$$\sigma = \frac{2F}{\pi Dt} \tag{2.8}$$

where

$$F = \text{failure load}, \quad D = \text{diameter}, \quad t = \text{thickness}.$$

The Brazilian test estimates tensile strength assuming uniform stress along the loaded diameter, but it often overestimates true strength [35], and small contact angles can create localised stresses that cause premature cracking [36]. Despite these limitations, it is widely regarded as a reliable method for brittle materials such as rock, concrete, and ceramics [37–39], offering a more uniform tensile stress distribution than flexural tests and reducing the influence of defects. For POP, reported flexural and Brazilian strengths are comparable, reflecting its brittle, low-ductility behaviour [40].

2.2.1.2 Jute

Direct tensile tests of jute yarns are recommended by standards ASTM D3822/D3822M [41] and ASTM D1577 [42]. The failure load is recorded for calculating tensile strength. However, ASTM D1577-07 advises using linear density (mass per unit length, tex) to report mechanical properties as breaking tenacity (N/tex or cN/tex), since accurate cross-sectional area measurement is difficult. However, for composite studies conventional stress units (MPa) are preferred, making area-based values necessary. Optical microscopy can be used to measure fibre diameters at the micrometre scale [43]. To prevent slippage and clamping damage, ASTM D3822/D3822M specifies a tabbing method, in which epoxy-bonded pads are attached to both specimen ends. A typical test setup is shown in Figure 2.11(d), and the tensile strength is calculated as:

$$\sigma = \frac{F}{A} \tag{2.9}$$

where

$$F = \text{failure load}, \quad A = \text{average cross-sectional area}.$$

2.2.2 Reinforcement-matrix interfacial bonding

2.2.2.1 Fibre pullout testing

Reinforcement-matrix interfacial bonding is critical to the mechanical performance of FRCs. Fibre pullout testing is a practical and widely used method for quantifying bond strength between fibres and the surrounding matrix. The stress transfer mechanism during pullout [44] is theoretically analogous to fibre debonding from the matrix in the fracture of FRC materials such as FP.

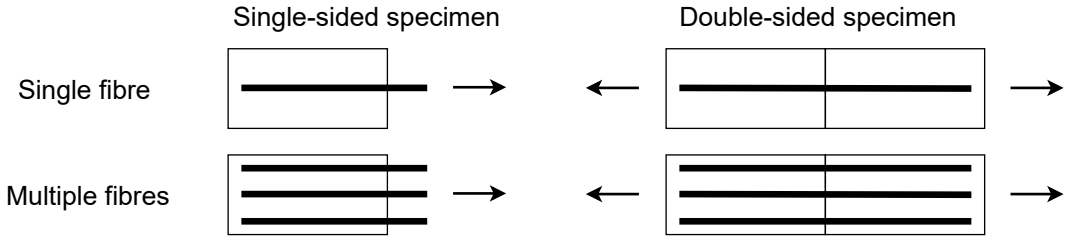


Figure 2.12: Fibre pullout test configurations classified by fibre count and specimen configuration.

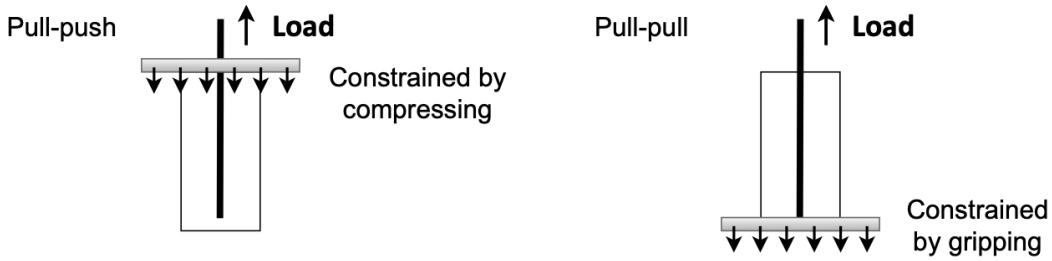


Figure 2.13: Schematic representation of the two principal loading configurations used in single-sided pullout tests: pull-push and pull-pull methods.

Fibre pullout tests are classified by the number of fibres (in this context, the term 'fibre' refers to a single reinforcement unit, which may also correspond to a yarn rather than the individual jute fibres that compose the yarn) and by specimen configuration. The four main types are: (i) a single fibre in a single-sided specimen; (ii) a single fibre in a double-sided specimen; (iii) multiple fibres in a single-sided specimen; and (iv) multiple fibres in a double-sided specimen [45], as shown in Figure 2.12. In single-sided tests, load is applied directly to the fibre(s) while the matrix is fixed, whereas in double-sided tests load is applied to the matrix from both ends while the fibres remain embedded. Both generate relative displacement and interfacial stress along the embedded length. The single-sided configuration is most widely used for its simplicity, reliability, and ease of preparation, with single-fibre pullout tests offering straightforward execution [46]. However, single-fibre tests show high variability and overlook fibre spacing effects important in fabric-reinforced systems, while multiple-fibre tests yield more consistent results [44]. Challenges remain particularly in gripping the brittle matrix and maintaining multiple fibre alignment within the matrix [47].

Two setups are commonly used to secure the matrix in single-sided pullout tests: pull-push and pull-pull (Figure 2.13). In the pull-push setup, the matrix is restrained

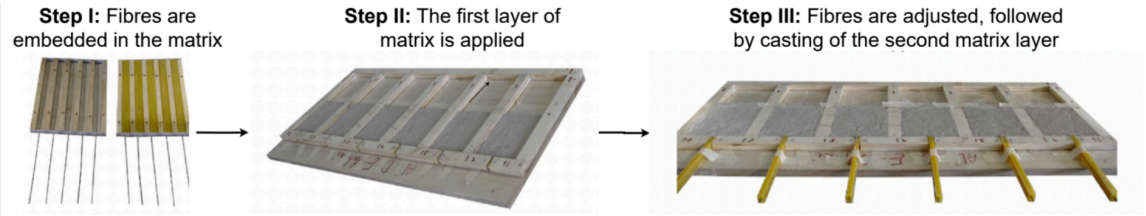


Figure 2.14: Production of a disc-shaped matrix specimen using a mould designed for two-layer casting aligned with the fibre embedment direction [47].

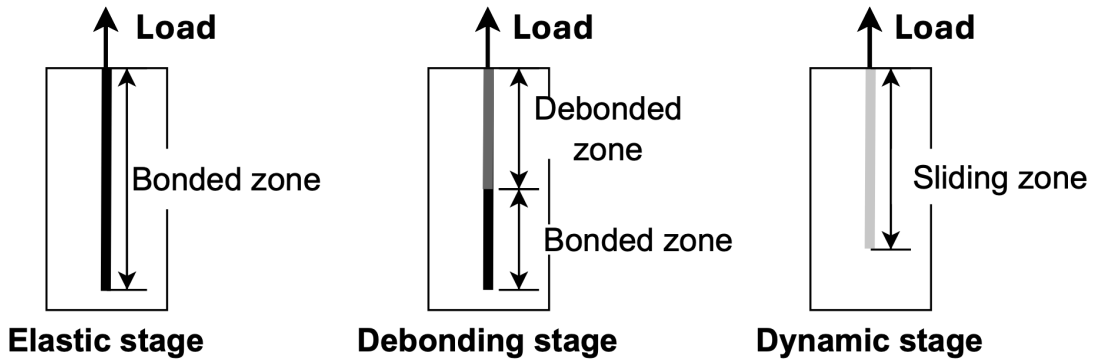


Figure 2.15: Representative interfacial conditions corresponding to the elastic, debonding, and dynamic stages of the pullout process.

by a compressive load from above, while in the pull-pull configuration it is supported from below [47]. Pull-push mitigates gripping issues but reduces slip measurement accuracy and requires a more complex setup. Pull-pull allows more accurate slip measurement, but gripping support may affect debonding, and poor fixation can cause cracking, crushing, or slippage at the matrix-grip interface, compromising test reliability [47].

Beyond gripping and slip measurement, specimen preparation poses challenges with soft natural fibres such as jute yarns. Accurate fibre alignment inside the matrix is essential for reliable debonding results. To improve this, Dalalbashi et al. [47] proposed a disc-shaped matrix with two casting layers aligned to the fibre embedment direction, enhancing alignment and repeatability. The preparation process is shown in Figure 2.14.

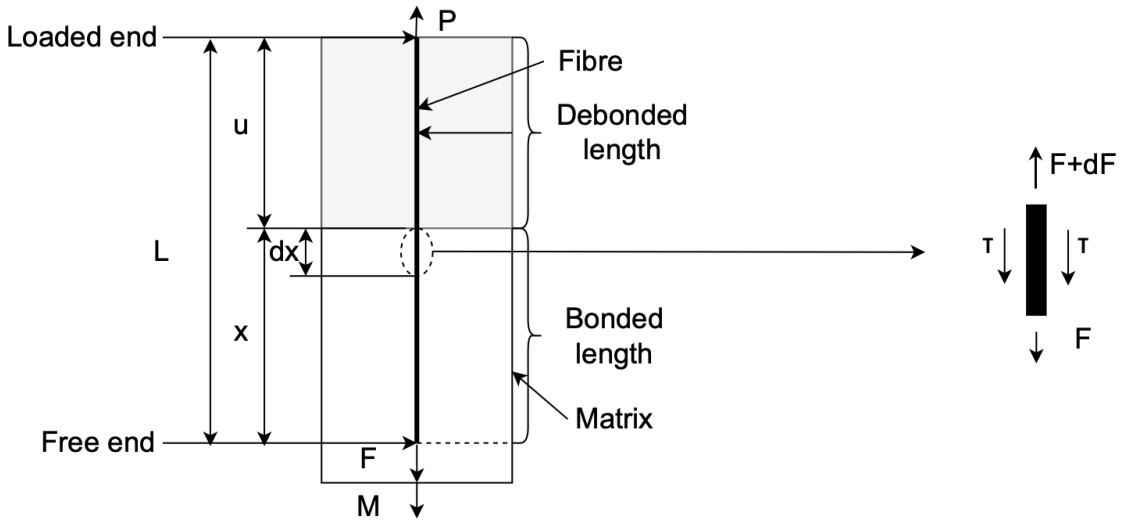


Figure 2.16: Global equilibrium of the fibre pullout system and local equilibrium of a differential fibre element (free-body diagram).

2.2.2.2 Debonding mechanism

Naaman's model [48, 49], developed for a single fibre in a single-sided specimen, is widely used to simulate the debonding process, capture fibre-matrix interactions, and quantify interfacial shear strength. The model assumes that the interface may consist of bonded, debonded, and sliding zones, which can occur either consecutively or simultaneously along the embedded length during pullout. These interfacial conditions are illustrated in Figure 2.15, corresponding to three stages of the pullout process: elastic, debonding, and dynamic [46–51].

In the elastic stage, the fibre-matrix interface remains intact. During debonding, the interface is progressively damaged as the fibre debonds from the matrix. Once full debonding occurs, the dynamic stage begins, where the fibre slides out of the matrix. Figure 2.16 illustrates the global equilibrium framework during the debonding stage, regarded as the most important phase since interfacial separation occurs between the fibre and matrix. L is the total embedded fibre length at the beginning of the pullout process, u the debonded length, x the bonded length, P the total applied force at the loaded end, F the force carried by the fibre, and M the force carried by the matrix. Both loaded and free ends are annotated. Figure 2.16 also shows a free-body diagram of a differential fibre element of length dx located at a distance x from the free end, where F is the force in the fibre and τ the shear stress at the fibre-matrix interface.

From the global and local equilibrium conditions, analytical expressions for the

Table 2.1: Key variables in Naaman's fibre pullout system.

Variables	**Description**
L	Fibre embedded length.
u	Debonded length.
x	Bonded length.
v	Slipped length.
P	Applied load at the fibre loaded end.
F	Force carried by the fibre.
M	Force carried by the matrix.
τ	Fibre-matrix interfacial shear stress.
S	Fibre-matrix slip displacement.
P_{crit}	P at the end of the elastic stage.
S_{crit}	S at the end of the elastic stage.
P_{p}	Maximum P recorded during the pullout process.
S_0	S at the end of the debonding stage.
τ_{max}	Bond shear strength; maximum τ at the loaded end during the elastic stage or at the bonded-debonded interface.
τ_{f}	Frictional shear strength; constant frictional τ along the debonded length $(L-u)$ during the debonding stage, or along the entire embedded length L at the onset of the dynamic stage.
τ_{dyn}	Decreasing residual frictional τ, constant along the remaining embedded fibre length $(L-v)$ during the dynamic stage.

applied force P, interfacial shear stress τ, and fibre-matrix slip S can be derived for all stages of pullout. The debonding mechanism described by Naaman's fibre pullout model [48, 49], with key variables summarised in Table 2.1, is outlined below based on the force-slip relationship and the interfacial shear stress behaviour observed during fibre pullout tests.

The force-slip response, shown in Figure 2.17, describes the relationship between applied load and measured fibre-matrix slip at the loaded end, capturing the three stages and their transitions during pullout: (i) In the elastic (linear) stage, indicated by the bold black line, the fibre and matrix remain fully bonded, with the interface undamaged along the entire embedded length L. The force-slip relationship is linear, terminating at the critical load P_{crit} and corresponding slip S_{crit}; (ii) In the debonding (nonlinear) stage, represented by the dashed black line, interfacial debonding initiates at the loaded end and the force-slip response becomes nonlinear as the debonded

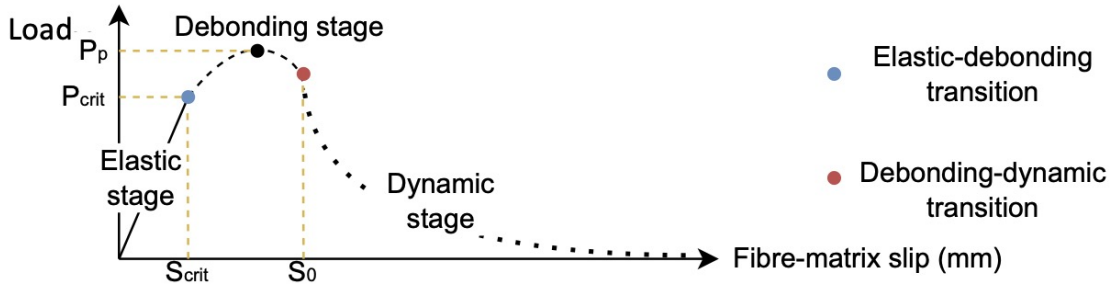


Figure 2.17: Force-slip relationship between the applied load at the fibre's loaded end and the measured fibre–matrix slip, showing three stages and their transitions.

length u progressively grows from the loaded end toward the free end, while the applied load increases to a peak P_{p}. When u reaches the full embedded length L, with corresponding slip S_0, the system transitions to the dynamic stage; (iii) The dynamic stage, indicated by the dotted black line, begins once full debonding occurs. The fibre then slides out of the matrix under the applied load, with slipped length v. Resistance arises solely from interfacial friction along the remaining embedded length $L - v$, as the adhesive bond no longer contributes.

Interfacial shear stress is assumed to be nonlinear during the pullout process, as illustrated in Figure 2.18. Representative shear stress conditions at the fibre-matrix interface for the three stages and their transitions are shown in Figure 2.19. (i) In the elastic stage, bond shear stress decreases along the embedded fibre length L from the loaded end to the free end. At the loaded end, it remains linear until reaching the bond strength $\tau_{\max}$; (ii) In the debonding stage, debonding begins at the loaded end and propagates toward the free end. Along the debonded length u, shear stress is governed by a constant frictional strength τ_f. In the bonded region $L - u$, the fibre remains attached to the matrix, with shear stress reaching $\tau_{\max}$ at the bonded-debonded transition and then decreasing toward the free end. The frictional shear strength τ_f is lower than the bond strength $\tau_{\max}$; (iii) In the dynamic stage, shear resistance is governed entirely by frictional strength τ_f. The fibre undergoes rigid body motion, with a constant value τ_{dyn} along the remaining embedded length $L - v$. This frictional strength value decreases during the stage. Both linear and exponential models describe this decay, though the exponential form is more widely used for its accuracy in representing pullout behaviour [47].

A key limitation of Naaman's model is that it applies only to single-fibre pullout tests. While this assumption aids conceptual understanding and analytical formula-

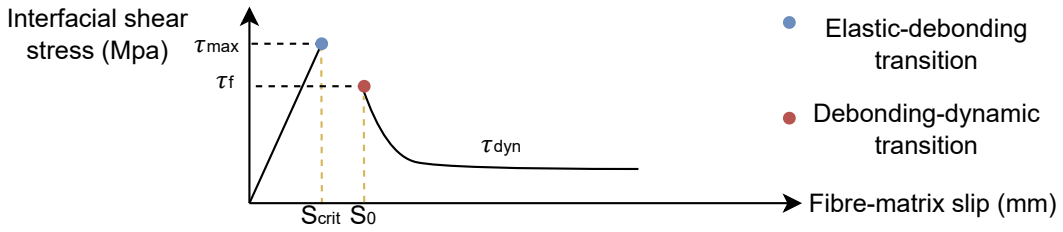


Figure 2.18: Fibre-matrix interfacial shear stress-slip relationship assumed in Naaman's fibre pullout model.

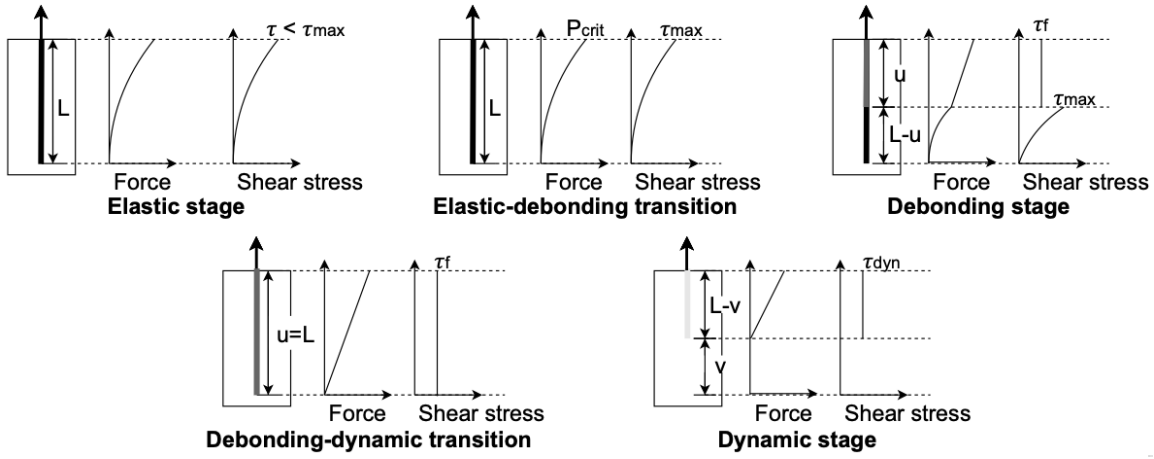


Figure 2.19: Representative interfacial shear stress conditions at the fibre-matrix interface corresponding to the three stages and stage-transitions.

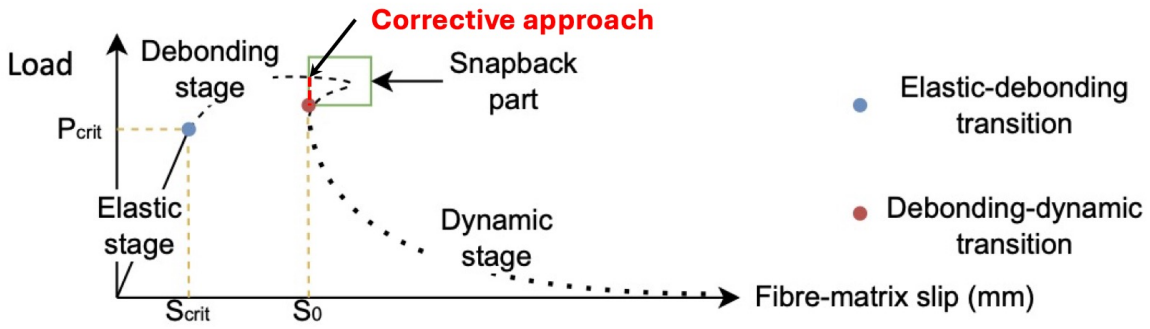


Figure 2.20: Snapback in the analytical force–slip relationship during the debonding stage using Naaman's model.

tion, it does not adequately represent the behaviour of multi-fibre reinforced systems such as FP. For fabric-reinforced composites like FP, modelling approaches that adapt multiple-fibre models are needed to improve physical relevance and the accuracy of interfacial bond–slip characterisation. Another limitation of Naaman's model is its poor fitting accuracy of the analytical force-slip relationship against experimental data, particularly during the debonding stage [46, 47, 52, 53]. A common issue is the appearance of snapback behaviour, where the slip value exceeds and then returns to S_0 [47], as shown in Figure 2.20. This non-physical response is not observed in experiments, and its cause remains unknown. To address it, some previous studies truncated the analytical curve at the point where slip first exceeds S_0 and then artificially linked it to the onset of the dynamic stage [47]. However, this can introduce a discontinuity at the debonding–dynamic transition, undermining the physical validity of the model. These shortcomings highlight the need for improved formulations that better fit experimental data and more accurately capture realistic interfacial bond–slip behaviour.

2.2.3 Tensile behaviour characterisation

The wad is the principal tensile load-bearing component in FP, transferring the weight of ceiling panels to the supporting framework. Wad failures have been identified as early-stage precursors to several ceiling collapses [1]. Despite this critical role, their tensile behaviour remains poorly understood. Comprehensive characterisation of wad tensile response is essential for assessing the residual capacity of existing FP systems and for informing conservation, retrofitting, and replication strategies in heritage practice.

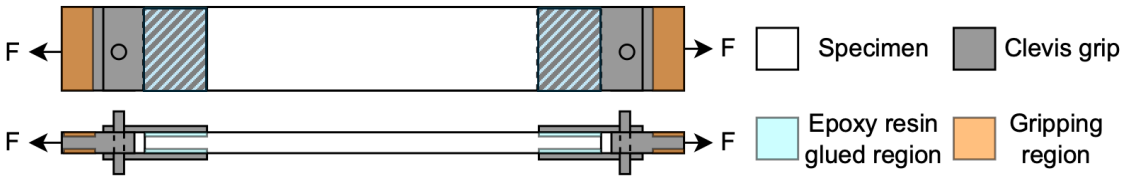


Figure 2.21: Schematic of a typical clevis-gripping setup.

Theoretically, FP is expected to exhibit a tensile response typical of FRCs. The Aveston-Cooper-Kelly (ACK) theory [54] describes three stages: (a) pre-cracking, where the composite behaves elastically until the first macro-crack forms; (b) crack development, with multiple cracks influenced by bond strength; and (c) post-cracking, where cracks widen and load is carried mainly by the reinforcement until failure.

Direct tensile testing is widely used to characterise FRCs. While FP itself has not been studied directly, related composites show the role of fibre reinforcement. Plaster with flax, hemp, or abaca exhibits improved ductility and flexural strength through fibre bridging [55, 56]. Jute fabrics have also been applied: jute fabric-reinforced polymers (JFRPs) display more ductile behaviour than carbon- and glass-fibre composites [57, 58], while in lime-based composites reinforced with hemp, flax, or jute, the jute systems show weaker interfacial bonding [59].

Various gripping configurations have been developed for direct tensile testing of FRCs. Two common approaches are the flexible and stiff gripping methods, which differ in specimen geometries and load transfer mechanisms [60]. In the flexible method, load is transferred from the grip to the fabric extending beyond the matrix and then into the matrix [46]. The stiff method, also known as the clevis-gripping method, secures the specimen in a metal fixture with epoxy resin (clevis grip) [61–63]. A schematic is shown in Figure 2.21. This setup transfers load directly to the matrix and then to the embedded reinforcement, more closely simulating the actual load path in FP.

Although the clevis-gripping method is widely used to evaluate the tensile behaviour of FRCs with brittle matrices, it often causes uneven stress distribution at the specimen ends, leading to premature failure near the grips [61, 63]. To address this, alternative geometries such as waisted [64], bone-shaped [65, 66], and dumbbell-shaped [67] profiles have been proposed to promote controlled cracking. These designs improve stress distribution but are difficult to fabricate, do not always ensure failure within the intended gauge region, and are not representative of wad geometry. A tailored specimen configuration is therefore required to characterise the tensile prop-

erties of FP wads, accounting for both the brittle POP matrix and their handcrafted construction from twisted hessian soaked in POP [1]. These unique features, largely overlooked in the literature, are critical to understanding the true tensile behaviour of historic FP ceilings.

2.3 Non-destructive techniques for structural health monitoring

2.3.1 Overview of non-destructive techniques

A wide range of NDTs are available for material characterisation and structural health monitoring, including vibration-based methods, ultrasonic and impact-echo testing, infrared thermography, DIC, and X-ray imaging [68–70]. Each approach offers distinct advantages but also faces limitations in terms of accessibility, cost, or suitability for historic FP ceilings. While these methods remain valuable and worthy of further investigation, their current applicability to FP systems is restricted. Against this background, AE and advanced imaging modalities such as DIC and sCT have emerged as particularly promising techniques for this study, and are introduced below.

2.3.2 Acoustic emission

2.3.2.1 Fundamentals

AE techniques detect elastic waves generated by the initiation and growth of failures within a material. Unlike active methods such as ultrasonic testing, AE is a passive technique in which signals originate from the failure process itself rather than from an external stimulus. Being inherently non-destructive and highly sensitive to fracture activity, AE can detect damage at an early stage, often well before catastrophic failure occurs [70]. Owing to its responsiveness to non-elastic deformation, AE is particularly effective in capturing new fracture events. Typical sources include crack initiation and propagation, and interfacial activities such as debonding and sliding [70]. Importantly, AE signals provide both temporal and spatial information, with their characteristics varying according to material properties, structural configuration, and specific failure mechanisms. These variations yield valuable insights into both the location and the nature of damage, making AE particularly well-suited for SHM purposes of historic FP ceiling systems.

A typical AE monitoring setup consists of piezoelectric sensors, preamplifiers, and a data acquisition unit. Sensors mounted on the specimen surface act as transducers, converting mechanical vibrations into electrical signals for analysis. This configuration enables continuous, real-time monitoring without interrupting service or loading, which is an essential advantage for heritage structures assessed in situ. Despite these strengths, AE has two notable limitations. First, AE signals are not fully reproducible: specimens of similar geometry under comparable loading can generate variable responses, complicating interpretation and necessitating robust data-processing approaches. Second, as a passive technique, AE often records signals of low amplitude. Even with amplification, weaker events may remain below the detection threshold, resulting in potential data loss [70].

Nevertheless, AE offers significant advantages. It enables early fracture detection, provides detailed temporal and spatial insight into damage evolution, and allows long-term in situ monitoring without service interruption. These capabilities establish AE as a valuable tool for assessing and safeguarding heritage structures, particularly for locating and characterising damage in historic FP ceilings. A generic AE-based framework is widely adopted for architectural SHM applications, as illustrated in Figure 2.22. In this framework, AE signals generated by micro-failures are acquired in situ through a typical monitoring setup and first subjected to localisation analysis. Each recorded signal is then processed to extract characteristic features, which are used to locate the failure, characterise underlying failure mechanisms, and to evaluate the severity, extent, and evolution of damage. The resulting insights can inform maintenance strategies and guide future preservation efforts.

2.3.2.2 AE waveform and parameters

AE waveforms are high-frequency transient voltage signals generated by the rapid release of strain energy as elastic waves during material deformation [71]. In principle, each failure event produces a distinct waveform, which can be characterised in both the time and frequency domains. The associated descriptors are collectively referred to as AE parameters. A schematic representation of a typical AE waveform in both domains, with key parameters annotated, is shown in Figure 2.23, and a detailed description is provided in Table 2.2.

AE waveforms contain temporal and spatial information that is essential for event source localisation. Moreover, AE parameters provide valuable insight into the underlying failure mechanisms [72–75]. For this reason, they are widely used to characterise failures and to evaluate the nature and severity of defects within a material.

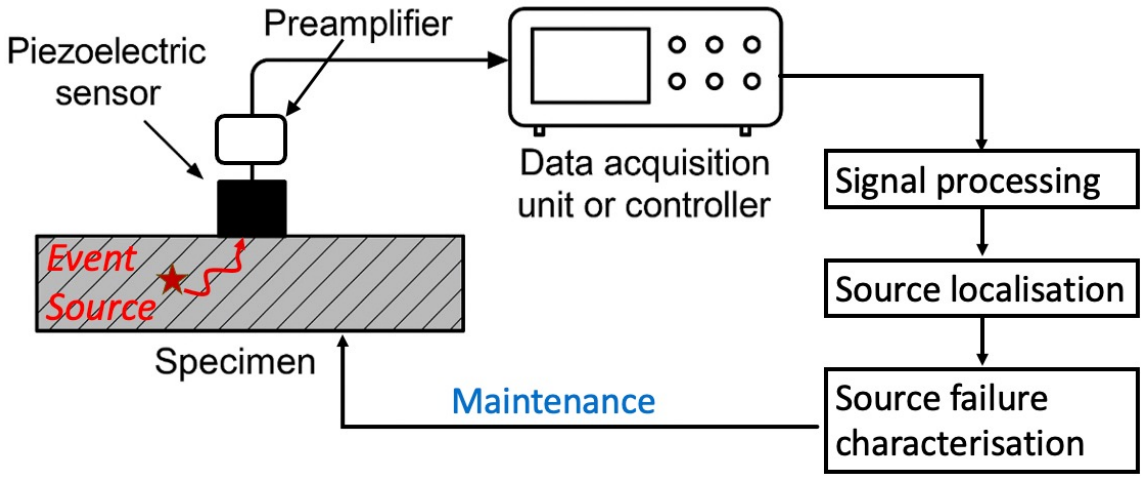


Figure 2.22: Schematic illustration of a typical AE monitoring setup, consisting of piezoelectric sensors, preamplifiers, and a data acquisition unit. Such a configuration enables continuous, real-time monitoring in architectural SHM applications.

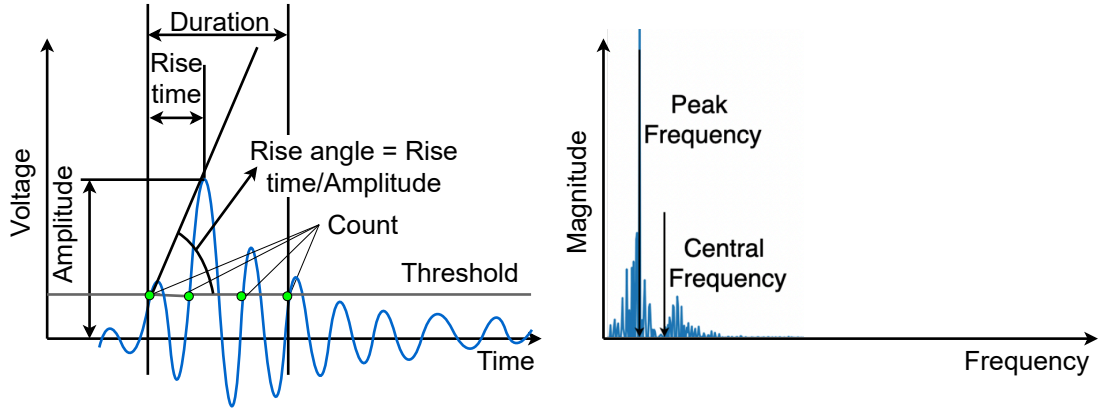


Figure 2.23: Schematic of a typical AE waveform represented in both the time and frequency domains, with key parameters annotated.

Table 2.2: Descriptions of key AE waveform parameters.

Parameter	**Unit**	**Description**
Threshold	dB, V	Voltage level defining the onset and end of an AE event.
Duration (DUR)	µs	Time interval between the first and last threshold crossings.
Counts	–	Number of ascending threshold crossings recorded during the waveform.
Rise Time (RT)	µs	Time from the first threshold crossing to the peak amplitude.
Amplitude (AMP)	dB, V	Maximum signal amplitude; indicates the relative event strength.
MARSE	V·s	Area under the rectified AE waveform, $\int \lvert V(t) \rvert \, dt$; represents the signal energy.
Average Frequency (AF)	kHz	Mean signal frequency, calculated as Counts divided by Duration.
Rise Angle (RA)	–	Ratio of Amplitude to Rise Time, often expressed as an arctangent.
Peak Frequency (PF)	kHz	Frequency corresponding to the maximum in the FFT spectrum.
Central Frequency (CF)	kHz	Frequency centroid derived from the FFT spectrum.

2.3.2.3 Failure localisation

AE techniques can be employed to determine the source location of detected micro-failures. Three general types of localisation are commonly used: linear, planar, and volumetric. Planar localisation is particularly suited to plate-like structures such as ceilings and enables non-destructive damage identification. Its effectiveness has been widely demonstrated in such applications [72, 76].

Conventional localisation methods rely on measuring the time-of-arrival (TOA) of AE waveforms. Assuming constant wave propagation velocity, TOA differences can be directly converted into distances between the damage source and the sensors [77]. These methods typically involve two steps. First, the TOA of each waveform is determined. Accurate detection is critical, as small errors can cause significant localisation inaccuracies. Common approaches include simple threshold crossing and more ad-

vanced methods such as Akaike Information Criterion (AIC) pickers [78]. Second, event association and triangulation are performed, whereby TOAs of waveforms from the same source are grouped across multiple sensors and used to compute the source location based on sensor positions and wave velocity. Multiple sensors are mounted on the flat surface of a panel-shaped structure, with a minimum of three required [70]. Let the AE source be at unknown coordinates (x_s, y_s), and sensors S_i $(i = 1, 2, 3)$ be positioned at (x_1, y_1), (x_2, y_2), and (x_3, y_3). Assuming straight-line propagation at constant velocity v, the time of arrival (TOA) at each sensor is given by

$$t_i = t_0 + \frac{1}{v}\sqrt{(x_s - x_i)^2 + (y_s - y_i)^2}, \quad i = 1, 2, 3 \tag{2.10}$$

where t_0 is the unknown event origin time. Eliminating t_0 by subtracting t_1 from the other TOAs yields

$$t_2 - t_1 = \frac{1}{v}\left[\sqrt{(x_s - x_2)^2 + (y_s - y_2)^2} - \sqrt{(x_s - x_1)^2 + (y_s - y_1)^2}\right], \tag{2.11}$$

$$t_3 - t_1 = \frac{1}{v}\left[\sqrt{(x_s - x_3)^2 + (y_s - y_3)^2} - \sqrt{(x_s - x_1)^2 + (y_s - y_1)^2}\right]. \tag{2.12}$$

This nonlinear system can be solved to estimate the source location (x_s, y_s). Localisation accuracy depends on factors such as sensor placement, wave velocity measurement, signal attenuation, and TOA precision [70]. In general, a uniformly distributed sensor configuration improves accuracy. The wave propagation velocity and attenuation profile of the material are commonly characterised using pencil-lead breakage (PLB), also known as the Hsu–Nielsen source [79], a standard method for generating reproducible artificial AE signals. PLB involves pressing a mechanical pencil against the surface until the lead breaks, releasing stored stress and inducing a microscopic displacement that generates an acoustic wave. Owing to its simplicity and repeatability, PLB is widely used in both laboratory and field AE testing.

Conventional TOA-based methods typically assume a uniform wave velocity and straight-line propagation from source to sensors, assumptions that are generally valid for homogeneous media. In inhomogeneous or anisotropic materials such as FRC, however, both wave velocity and propagation paths vary due to material anisotropy [80], making accurate localisation across complex geometries challenging [81]. Wave attenuation caused by these heterogeneities further reduces localisation accuracy [70]. Consequently, conventional localisation methods must be adapted and further developed for application to FRC materials.

Sensor cluster methods Many methods have been proposed to improve source localisation in anisotropic structures by mitigating wave propagation biases, as summarised in a recent review [77]. One widely used technique for plate-like structures

is the sensor cluster method, commonly implemented through the beamforming approach introduced by Kundu et al. [82]. In this method, a cluster of sensors with small inter-sensor spacing relative to the test object dimensions is employed. A comparison between traditional sensor placement and the clustering technique is shown in Figure 2.24. Because wave velocities and propagation paths from the source to each sensor in the cluster are effectively identical, the method reduces dependence on detailed knowledge of anisotropic propagation properties and minimises the influence of direction-dependent velocities and complex paths. This assumption results in AE signals with similar waveforms and minor time offsets between sensors, improving localisation accuracy and computational efficiency. Sensor clustering has been successfully applied in numerous studies to estimate AE source locations in anisotropic plate-like structures using beamforming theory [83–88].

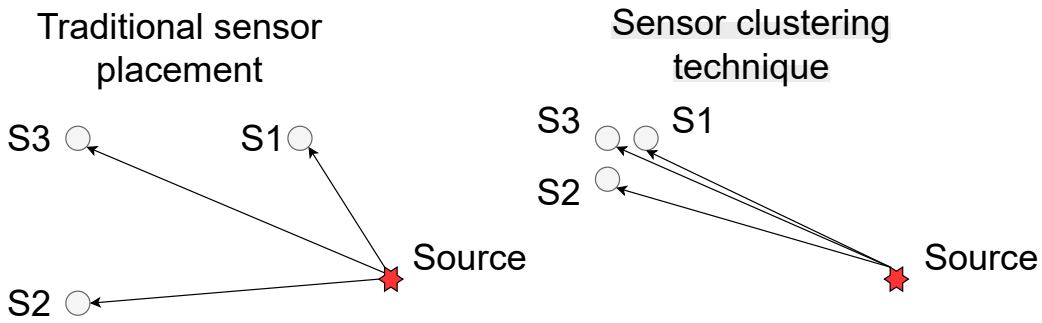


Figure 2.24: Traditional sensor placement versus the clustering method, where closely spaced sensors reduce anisotropy effects on localisation accuracy.

However, the method also has limitations. First, as with conventional localisation approaches, its accuracy depends strongly on the precision of TOA measurements from clustered AE signals [89]. Deviations between estimated and actual TOA values can lead to significant localisation errors. Several methods have been developed to improve TOA accuracy, including wavefront shape-based approaches that detect specific wavefront geometries [84, 87, 90]. While effective, these methods are computationally intensive and demand greater processing resources, making them unsuitable for in-situ real-time monitoring and inspection. Second, although clustering mitigates some propagation biases, variations in wave paths and direction-dependent velocities remain. To address this, Fu et al. [91] proposed a neural network model trained on TOA measurements and known source coordinates, achieving high localisation accuracy. The model estimates TOA based on group velocity distributions experimentally obtained from composites, but this reliance limits its practicality. Such velocities can

be measured for specific specimens, yet they are not transferable to structures with different geometries or material properties. Consequently, methods requiring prior knowledge of anisotropic wave propagation may have restricted applicability in practice.

Deep learning techniques In recent years, neural network methods have been increasingly applied to improve AE event source localisation, particularly with the aid of sensor clusters [92–94]. One-dimensional convolutional neural networks (1D-CNNs) have been shown to automatically extract features such as TOA from raw AE waveform data, allowing training directly on one-dimensional time-series signals [95]. CNNs are a class of deep learning models designed to capture local patterns in data using convolutional filters, making them well suited for structured inputs.

CNNs apply convolutional filters to input data to extract hierarchical features. A typical CNN architecture is composed of several structured layers, including convolutional layers, pooling layers, and fully connected layers. Each convolutional layer contains learnable kernels that slide across the input, detecting local patterns such as edges, textures, or temporal fluctuations, depending on the data type (e.g., two-dimensional images or one-dimensional sequential signals). These local features are progressively combined in deeper layers, enabling the network to capture increasingly abstract and complex representations. Pooling layers are typically inserted after convolutional layers to downsample feature maps, reducing dimensionality while retaining essential information. The extracted features are ultimately passed to fully connected layers, usually located at the end of the network, where they are integrated to perform tasks such as classification, regression, or feature extraction.

The CNN architecture is typically trained on a large labelled dataset, where each input corresponds to a ground-truth label. Training involves minimising a loss function through back propagation and optimisation algorithms, iteratively adjusting the filter weights to improve predictive accuracy. This hierarchical learning mechanism allows CNNs to automatically identify relevant features from raw or pre-processed data, making them highly effective for structured inputs.

The input to a CNN typically consists of raw or pre-processed data (e.g., images or time-series signals), while the output, commonly referred to as the label, depends on the task and may range from classification categories to extracted feature representations. 1D-CNNs are particularly effective for analysing AE waveforms. A CNN is designed with a defined architecture and trained on a large labelled dataset, enabling it to predict outputs for previously unseen inputs. In the case of AE analysis, a trained CNN can extract meaningful temporal features from waveforms, facilitating

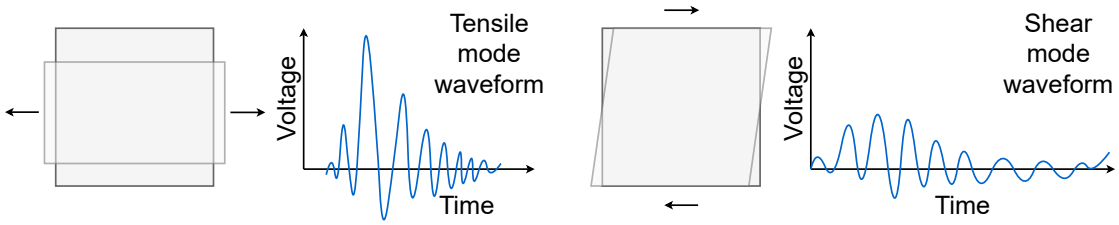


Figure 2.25: Schematic representation of material failure modes: volumetric change induced by tensile force (left) and shape distortion caused by shear force (right), along with their corresponding typical AE waveforms.

accurate TOA estimation and potentially achieving more precise and robust localisation by implicitly accounting for velocity and attenuation variations. When integrated with sensor clustering techniques, this approach offers strong potential for developing generalisable, data-driven AE localisation models that avoid reliance on conventional TOA picking and wave velocity estimation.

2.3.2.4 Failure mechanism characterisation

AE parameters are widely used to characterise failure mechanisms and form the basis of parameter-based analysis. In FRC materials, AE-based classification has gained attention for its ability to provide real-time, non-invasive insight into internal damage evolution [70].

In solid materials, failure-induced AE waveforms are generally classified into two fundamental modes: tensile and shear [96–98]. As illustrated in Figure 2.25, tensile failures involve volumetric change and primarily emit longitudinal (P-) waves, whereas shear failures involve shape distortion and predominantly generate transverse (S-) waves. These modes exhibit distinct waveform characteristics: tensile events typically produce higher frequencies and shorter durations, while shear events are associated with lower frequencies and longer durations. In FRC materials, matrix cracking is usually linked to tensile failure, whereas fibre-matrix interfacial activity corresponds to shear mechanisms [70]. The differentiation of AE parameters for these modes, as outlined in JCMS-III B5706 [99], provides a basis for classifying dominant failure mechanisms in FRC systems.

Rise angle (RA) and average frequency (AF) are among the most widely used AE parameters for distinguishing between tensile and shear failures. Tensile failures are generally characterised by high AF and low RA values, whereas shear failures tend to exhibit low AF and high RA values. Traditional classification methods based on

empirical RA-AF relationships have proven useful but remain limited by material-specific variability and the lack of standardised thresholds [100]. To overcome these limitations, recent studies have adopted machine learning approaches to automate AE signal classification. Clustering, an unsupervised technique, groups data by inherent similarity without requiring labelled datasets. Unlike supervised methods such as CNNs, clustering is particularly suited to AE failure mechanism characterisation, where direct labelling according to the ground truth (the actual failure mechanism corresponding to each waveform) is infeasible. By identifying patterns in the data structure [101], clustering enables classification of AE waveforms according to their underlying failure mechanisms.

The process typically involves feature extraction from raw AE data, followed by normalisation to reduce scale-related bias. Each waveform, represented by its processed features, is then assigned to a cluster based on similarity metrics [101]. Various clustering algorithms can be applied, but all aim to partition the data in a way that reflects its intrinsic structure and facilitates interpretation of damage mechanisms. A variety of clustering algorithms have been applied to AE analysis, including partition-based approaches such as K-means, probabilistic models such as Gaussian Mixture Models (GMM), fuzzy logic-based methods such as Fuzzy C-means (FCM), and density-based approaches such as DBSCAN. These methods differ in how they define similarity and partition the data: for example, K-means minimises intra-cluster variance using Euclidean distance, GMM assigns probabilistic memberships through Gaussian distributions, FCM allows partial membership across clusters to handle overlap, and DBSCAN identifies clusters from local point density. In practice, K-means and GMM are most often used to explore RA–AF patterns in AE datasets [73, 102, 103]. These clustering approaches are frequently combined with supervised classifiers such as Support Vector Machines (SVM) or k-Nearest Neighbours (k-NN) to establish consistent classification thresholds [73, 102].

Despite these advances, challenges remain. Many conventional clustering methods rely on assumptions of Gaussian or spherical data distributions, which may not fully capture the nature of AE features [73, 104]. To overcome these limitations, alternative approaches that offer more robust classification are needed. In summary, integrating AE with advanced data analytics has improved the characterisation of complex failure processes in FRCs. Ongoing advances in machine learning offer further potential to enhance the objectivity, accuracy, and generalisability of AE-based classification. By tracking the evolution of failure mechanisms, the health of FP structures can be assessed more reliably.

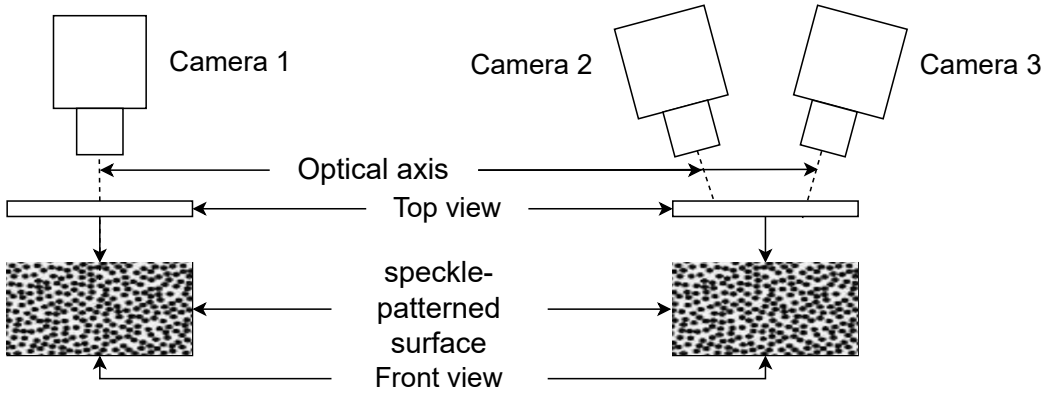


Figure 2.26: Schematic of DIC configurations: 2D (left) and 3D (right), with a speckle pattern applied to the specimen surface.

2.3.3 Full-field imaging modalities

For both material characterisation and SHM, advanced imaging modalities that capture full-field deformation on specimen surfaces and within internal volumes are essential for providing insight into damage evolution. Surface deformation is commonly measured using DIC with sequential high-resolution imaging, while volumetric deformation is assessed via local or global DVC on in-situ sCT data.

2.3.3.1 Digital image correlation (DIC)

DIC is a non-contact optical technique for measuring full-field surface displacement by tracking surface features between reference and deformed images [105, 106]. It can be applied in both 2D and 3D (stereo) configurations to capture surface deformation in real time. Figure 2.26 schematically illustrates typical experimental setups for 2D and 3D DIC. A random speckle pattern or natural surface texture is required to enable accurate tracking, and the analysis assumes that these surface marks passively follow the solid deformation.

In 2D DIC, to minimise perspective distortion from camera position or specimen orientation, the surface is typically flat and aligned normal to the optical axis. Two images acquired before and after deformation are registered by computing the displacement field that best matches corresponding regions. Non-rigid image registration is performed to capture deformation with high accuracy [107]. In 3D DIC (stereo DIC), two synchronised cameras are used to monitor the specimen surface from different angles to reconstruct both out-of-plane and in-plane displacements.

This configuration enables full-field 3D displacement by matching features in stereo image pairs before and after deformation. Accurate reconstruction requires prior camera calibration to determine intrinsic and extrinsic parameters, such as focal length and camera angles, in accordance with stereo photogrammetry principles.

In general, DIC provides full-field surface displacement and strain maps, enabling the observation of temporal deformation evolution and the analysis of complex dynamic mechanical processes, particularly in anisotropic materials [108].

Correlation procedure The DIC correlation procedure aims to determine the full-field displacement field $u(x)$ by comparing a reference image with its deformed counterpart. Let $f(x)$ and $g(x)$ denote the grey-level intensities at position x in the reference and deformed images, respectively, where x represents a spatial 2D or 3D coordinate. Assuming grey-level conservation:

$$f(x) = g(x + u(x)) \tag{2.13}$$

where $u(x)$ is the unknown displacement vector at position x.

In practice, due to noise and illumination variation, this ideal relation rarely holds exactly. Therefore, a correlation criterion is introduced to quantify the similarity between $f(x)$ and $g(x + u(x))$. A commonly used criterion is the sum of squared differences (SSD), defined as:

$$T = \int_{\Omega} [f(x) - g(x + u(x))]^2 \, dx \tag{2.14}$$

where T is the total correlation error to be minimised, and Ω represents the zone of interest (ZOI) in local DIC or the region of interest (ROI) in global DIC [107].

SSD is widely used for its simplicity and effectiveness [109]. Other common correlation criteria include:

- Normalised SSD (NSSD or ZNSSD): A version of SSD that subtracts the mean and divides by the standard deviation within each subset; robust to noise and lighting changes [109].
- Normalised Cross-Correlation (NCC or ZNCC): Measures similarity between patterns; commonly used in rigid-body or low-deformation scenarios [106].

Since $u(x)$ is unknown at every point, it is approximated using a weighted sum of basis functions:

$$u(x) = \sum_{n} u_n \psi_n(x) \tag{2.15}$$

In local DIC, the displacement within each subset is approximated independently using an affine basis:

$$\psi_0 = 1,\ \psi_1 = x,\ \psi_2 = y, \quad u_n = \begin{bmatrix} a_n \\ b_n \end{bmatrix}, \quad n = 0, 1, 2$$

$$u(x) = \sum_{n=0}^{2} u_n \psi_n(x) \tag{2.16}$$

Where:

- $u(x) = \begin{bmatrix} u_x(x,y) \\ u_y(x,y) \end{bmatrix}$: displacement at position (x, y),
- $\psi_n(x, y)$: local affine basis functions.
- x: spatial position in the ZOI.

This captures local translation, strain, and rotation, but does not enforce continuity between subsets.

In global DIC, the displacement field is defined over the entire domain using mesh-based shape functions:

$$u(x) = \sum_{n} u_n \psi_n(x) \tag{2.17}$$

Where:

- $u_n = \begin{bmatrix} u_{x,n} \\ u_{y,n} \end{bmatrix}$: nodal displacement at mesh node n,
- $\psi_n(x)$: shape function associated with node n,
- x: spatial position in the ROI.

This enforces continuity and enables smooth, consistent strain computation across the field.

The displacement field $u(x)$ is updated iteratively to minimise the nonlinear cost function T. At each iteration i, the displacement is updated as:

$$u^{i+1}(x) = u^i(x) + \delta u(x) \tag{2.18}$$

Applying a first-order Taylor expansion to linearise the deformed image:

$$g(x + u^i(x) + \delta u(x)) \approx g(x + u^i(x)) + \nabla g(x + u^i(x)) \cdot \delta u(x) \tag{2.19}$$

Defining the residual $r^i(x) = f(x) - g(x + u^i(x))$, the linearised cost function becomes:

$$T^i[\delta u] \approx \int_\Omega \left[r^i(x) - \nabla g(x + u^i(x)) \cdot \delta u(x)\right]^2 dx \tag{2.20}$$

Assuming the displacement increment is approximated by a linear combination of basis functions, $\delta u(x) = \sum_n \delta u_n \psi_n(x)$, substitution into the cost function followed by enforcing stationarity $\delta T^i / \delta u_n = 0$ yields the linear system:

$$[\mathbf{M}^i]\{\delta u\} = \{\mathbf{b}^i\}, \tag{2.21}$$

with:

$$M^i_{mn} = \int_\Omega \left[\nabla g(x + u^i(x)) \cdot \psi_m(x)\right] \left[\nabla g(x + u^i(x)) \cdot \psi_n(x)\right] dx,$$

$$b^i_m = \int_\Omega r^i(x) \left[\nabla g(x + u^i(x)) \cdot \psi_m(x)\right] dx$$

Here, m and n index the basis functions. Solving for $\{\delta u\}$ yields the incremental displacement, enabling iterative updates of $u(x)$ until convergence.

2.3.3.2 Synchrotron X-ray computed tomography

FP wads exhibit an irregular and highly complex internal microstructure, arising from the random distribution of reinforcements introduced during manual fabrication. This structural heterogeneity plays a critical role in governing the material's mechanical behaviour and failure mechanisms, making accurate microstructural characterisation essential for understanding structural response. DIC techniques are limited to surface observations. However, surface stress states can differ substantially from those within the bulk material, meaning that surface features may not accurately reflect internal damage processes. Consequently, reliance on surface observations alone can obscure the true mechanisms of damage evolution [110, 111]. X-ray computed tomography (XCT), a high-resolution three-dimensional non-destructive imaging technique, provides a complementary approach for evaluating the internal mechanical integrity and failure behaviour of complex FRCs such as FP.

Principles of X-ray computed tomography XCT reconstructs the internal structure of a specimen by combining multiple radiographs acquired as the specimen is incrementally rotated. Each radiograph records the transmitted X-ray intensity as the beam passes through the specimen and reaches the detector, typically a film- or CCD-based system [110]. According to the Beer–Lambert law, the ratio of transmitted to incident photon intensity is governed by the material's absorption coefficient μ, which depends on density, atomic number, and, for monochromatic beams, photon

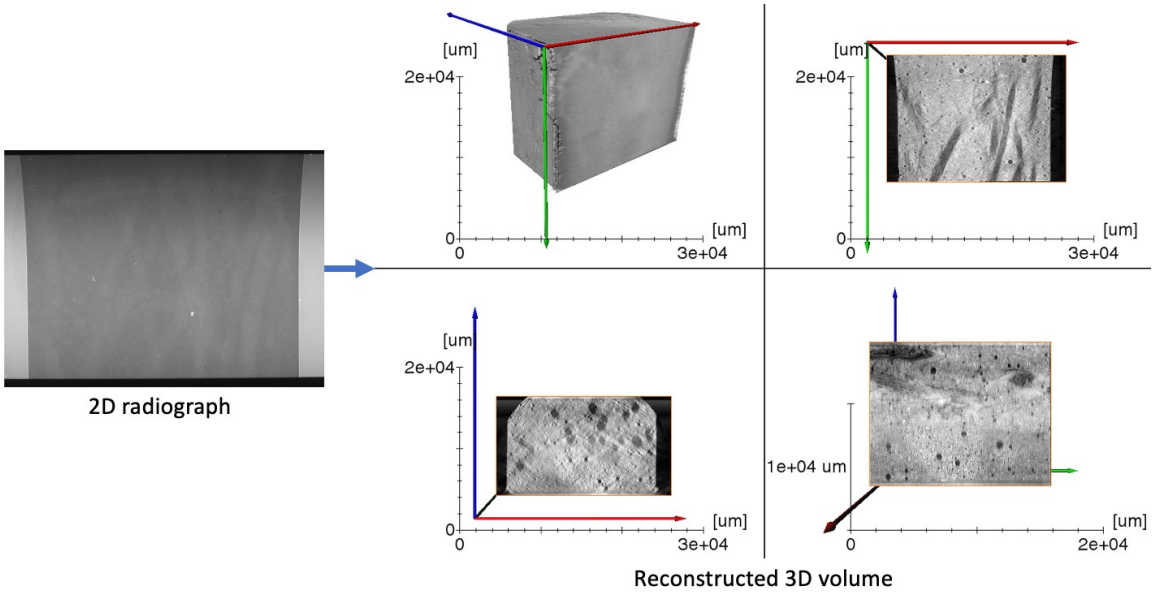


Figure 2.27: Illustration of XCT imaging: from 2D radiographs to reconstructed 3D volumes.

energy [110]. This relationship provides a direct link between X-ray attenuation and material properties, based on empirical laws. Consequently, effective application to FRCs requires sufficient internal phase contrast and adequate X-ray absorption differences [112–114]. Effective contrast requires a suitable balance of X-ray transmission: if transmission is too low, photon statistics deteriorate and image noise increases, whereas if transmission is too high, material contrast is reduced. A typical compromise is to maintain transmission at about 10%, which provides sufficient contrast while preserving image quality [115, 116].

Each radiograph is a 2D projection of the specimen's 3D structure. The complete volume is reconstructed by applying specialised algorithms to the full set of projections [117]. Figure 2.27 illustrates this process, showing both a 2D projection and the corresponding reconstructed 3D volume.

Micro-focus X-ray tube (laboratory system) versus synchrotron radiation XCT can be performed using laboratory systems or synchrotron radiation. Laboratory systems typically employ micro-focus X-ray tubes that emit a polychromatic, divergent beam, from which a conical solid angle is selected [110]. Spatial resolution, generally between 10 and 500 µm, is governed by the system geometry and the characteristics of both source and detector. To fit the specimen within the detector's field of view, a compromise is usually required between resolution and specimen size. Scan durations are relatively long and depend on resolution, detector

dimensions, and source power [110].

In contrast, synchrotron sources produce a highly collimated, parallel beam, which can be polychromatic (white) or monochromatic depending on the experimental configuration. This geometry minimises artefacts such as geometric distortion and beam hardening, enabling accurate quantitative reconstructions [110]. sCT is therefore particularly suited to high-resolution imaging. At facilities such as the DLS, beamline I12 JEEP delivers high-energy X-rays in the range 53–150 keV and provides a versatile suite of detectors, including scintillator-coupled systems with magnifying optics capable of resolutions down to about 1.3 µm. Beamline I12 accommodates a wide range of specimen sizes and supports imaging configurations for both dense materials and fine-scale structures [118]. In-situ experiments are facilitated through the integration of mechanical rigs and furnaces, and rapid acquisition enables complete scans within seconds under optimised conditions [118], making the beamline particularly suitable for time-resolved studies of material behaviour.

Recently, sCT has become a powerful tool for examining the internal features of FRCs [119]. It enables accurate characterisation of composite architectures by generating representative computational models based on high-resolution scans. These models provide a more realistic basis for numerical analysis than idealised structural representations [112, 120–122]. Moreover, sCT is highly effective for tracking structural evolution and damage development in FRCs, including matrix cracking, fibre fracture, and delamination, through repeated scans acquired before, after, or during in situ mechanical testing [112, 123–126]. The resulting volumetric datasets are information-rich and require robust quantitative approaches to extract meaningful insight into internal damage processes and deformation behaviour. To this end, Digital Volume Correlation (DVC) is introduced as a complementary analysis technique.

Digital volume correlation (DVC) DVC measures internal deformation fields from sCT data. As the three-dimensional extension of DIC, it tracks subvolumes of voxels to compute full-field displacement and strain distributions [127]. Its potential has been demonstrated across a wide range of FRCs, as reviewed in [128]. With its volumetric full-field capability, DVC enables investigation of correlations between through-thickness behaviour and surface-level deformation captured by DIC. As in DIC, DVC methods are broadly categorised into local and global approaches. Local DVC tracks small subvolumes (subsets) independently, yielding discrete results with lower computational demand. Global DVC, by contrast, applies a finite element mesh across the volume to compute a continuous and more robust displacement field, though at substantially higher computational cost. Furthermore, DVC provides

valuable insight into failure mechanisms in FRCs by enabling extraction of strain directionality to distinguish tensile from shear modes [129], thereby complementing failure mechanism characterisation.

2.4 Summary

Although FP has been widely used in historic buildings and continues to see use today, it remains significantly under-researched. The lack of systematic data on its material properties and structural behaviour has resulted in reliance on subjective assessment methods, based primarily on visual and tactile inspection. These approaches are inadequate for detecting hidden deterioration and for establishing reliable conservation guidelines, thereby posing risks to public safety.

The literature review highlights several major research gaps:

1. **Constituent- and composite-level properties of FP.** There is no comprehensive characterisation of FP across multiple scales, from the properties of its constituent materials (POP, hessian) through to reinforcement–matrix interfaces and the overall composite response. This includes insufficient knowledge of interfacial debonding mechanisms, failure propagation and evolution, and their influence on global tensile performance. A systematic multi-level experimental programme is required to establish a robust constitutive description. The first paper in Chapter 3, *"Constituent and composite level characterisation of fibrous plaster in decorative suspended ceilings"*, addresses this gap.

2. **Failure localisation in irregular FP ceiling geometries and validation in heritage contexts.** Existing monitoring techniques are poorly suited to FP ceilings because of their irregular geometry and layered construction. Conventional TOA-based AE localisation methods assume homogeneous isotropic media and are unreliable under the anisotropy and attenuation effects present in FP. There is therefore a need for an adaptive localisation framework capable of robustly handling complex ceiling architectures. This challenge is the focus of the paper in Chapter 4, *"A three-stage approach based on 1D-CNNs for AE source localisation on historic fibrous plaster ceilings"*. Even when AE localisation models are developed, their reliability under realistic ceiling-scale conditions has not been demonstrated. Existing approaches remain limited to laboratory specimens, leaving uncertainty over applicability to full-scale heritage structures. The paper in Chapter 5, *"Acoustic emission-based failure*

detection and event source localisation in a historical fibrous plaster ceiling", addresses this through ceiling-scale validation via field trials.

3. **Failure mechanism classification in FP wads and validation via direct volumetric observation using sCT techniques.** Cracking and debonding are the two most common failure mechanisms in the tensile element of FP wads. Accurate characterisation of these mechanisms is essential for assessing the structural health of the wad and for enabling early detection of ceiling failure. No objective and non-destructive method currently exists for identifying whether AE signals correspond to tensile cracking or fibre–matrix debonding in FP. Prior studies have relied on empirical RA–AF thresholds that lack generalisability and robustness across materials. An AE-based, data-driven model with validation via direct observation performed using in situ sCT is required to characterise failure mechanisms rigorously. This challenge is tackled in Chapter 6, *"Acoustic emission and in situ synchrotron X-ray computed tomography for failure classification in fibrous plaster"*.

Together, these gaps define the need for a rigorous experimental and analytical framework for FP, linking multi-scale material characterisation to the development of an AE-based SHM system. The four papers presented in this thesis directly address these gaps, advancing both the scientific understanding of FP and the practical tools required for its inspection and conservation.

Chapter 3

Paper 1: Constituent and composite level characterisation of fibrous plaster in decorative suspended ceilings

Construction and Building Materials 493 (2025) 143035

Contents lists available at ScienceDirect

Construction and Building Materials

journal homepage: www.elsevier.com/locate/conbuildmat

Constituent and composite level characterisation of fibrous plaster in decorative suspended ceilings

Jiaxu Zuo [a,*], Sarah Mayfield [b], Kutsi Akcicek [a], Brian Sheil [c], James Marrow [a], Sinan Acikgoz [a]

[a] Department of Engineering Science, University of Oxford, Parks Road, Oxford, OX1 3PJ, United Kingdom
[b] National Trust, United Kingdom
[c] Department of Engineering, University of Cambridge, Cambridge, CB2 1PZ, United Kingdom

ARTICLE INFO

Keywords:
Fibrous plaster
Plaster of paris
Jute yarn
Optical microscopy
Micro-X-ray computed tomography (μ-XCT)
X-ray diffraction (XRD)
Digital image correlation (DIC)
Virtual field method (VFM)
Dynamic elastic modulus
Static elastic modulus
Direct tensile test
Flexural test
Brazilian splitting test
Fabric pullout test

ABSTRACT

Fibrous plaster (FP) is a fabric-reinforced composite of plaster of Paris (POP) and woven jute fabrics, widely used in historic UK ceilings since the late 19th century. Despite its importance, FP remains under-researched, hindering structural assessments and maintenance. Recent collapses due to tensile failures of the supporting component 'wad' highlight the need for comprehensive characterisation. This study investigates physical, chemical, and mechanical properties of historic FP's constituent materials and their modern proxies using optical microscopy, micro-X-ray computed tomography (μ-XCT), and X-ray diffraction (XRD). The analysis reveals key properties, including density, jute fibre/yarn diameters, yarn's fibre volume ratio, chemical composition, yarn's tensile strength, and POP's dynamic elastic modulus. Modern POP, representative of historic POP, was further assessed for static elastic modulus using the virtual fields method (VFM) applied to digital image correlation (DIC) data, tensile strength measured by direct tensile, flexural, and Brazilian splitting tests, and compressive strength. Fabric-matrix bonding properties were accurately characterised by a innovative fabric pullout test setup, analysed with an adapted Naaman model, and a novel force-fitting method. Direct tensile tests on dogbone FP specimens investigated the composite's tensile behaviour at the wad-scale, providing a detailed demonstration on how hessian enhances FP ductility.

1. Introduction

Fibrous plaster (FP), widely used in the UK for suspended decorative ceilings since the late 19th century (Fig. 1), is a composite of plaster of Paris (POP) and woven jute fabrics ('Hessians'), as a lighter alternative to solid gypsum [1]. POP is favoured for its faster hardening and lower shrinkage compared to lime plaster [2].

Fig. 2 illustrates typical structure of historic FP ceilings, consisting of a thin POP cast reinforced with hessian layers, forming a laminated panel, suspended by manually fabricated 'wads', which are column-shaped FP components. A recent study [3] found these wads prone to tensile failures, which can lead to ceiling collapse and pose structural risks. Such concerns were highlighted by recent FP ceiling failures in London [4]. Despite its widespread use, FP remains understudied, complicating structural assessments and maintenance. Existing inspection guidelines, relying on subjective visual and tactile assessments [4], are often costly, risky, and insufficient. A comprehensive characterisation is necessary to address this knowledge gap.

A previous study investigated two types of POP used in FP: α- and β-type [5], with historic FP predominantly using β-type [4]. Prior to casting, POP appears as a fine powder of calcium sulfate hemihydrate ($CaSO_4 \cdot \frac{1}{2}H_2O$), which, when mixed with water in a process called hydration, forms calcium sulfate dihydrate ($CaSO_4 \cdot 2H_2O$), the primary phase in POP casts [6]. POP strength depends on the water-to-plaster ratio (W/P), with lower ratios yielding denser, stronger structures [1,7]. Studies show compressive strength increases as W/P decreases [8–10]. Historic POP used in FP remains under-researched due to difficulties sourcing intact samples. However, a study [11] identified a W/P of 0.7 as representative of historic FP, based on analysis of samples from One Great George Street, a Grade II listed building in London, housing the Institution of Civil Engineers (ICE). In this study, this W/P serves as the basis for modern POP recipes aimed at replicating the historic material, for addressing POP properties in historic FP.

Hessian, primarily composed of cellulose, is loosely woven from jute yarns. A previous study reported that jute fibre diameter is approximately 80 μm, while jute yarn diameter is about 1.17 mm [12]. However, exact dimensions vary. In historic FP, typical yarn spacing is around 5 by 10 mm [4], allowing POP to penetrate. Hessian enhances FP's mechanical properties by reducing POP's brittleness [13]. Flexural

* Corresponding author.
E-mail address: jiaxu.zuo@eng.ox.ac.uk (J. Zuo).

https://doi.org/10.1016/j.conbuildmat.2025.143035
Received 1 March 2025; Received in revised form 16 July 2025; Accepted 4 August 2025
Available online 19 August 2025
0950-0618/© 2025 The Authors. Published by Elsevier Ltd. This is an open access article under the CC BY license (http://creativecommons.org/licenses/by/4.0/).



Fig. 1. Historic FP ceilings in the UK (from left to right): Marble hall, Gosford house, Longniddry; Library, Insole court, Llandaff, Cardiff; New theatre, Cardiff.

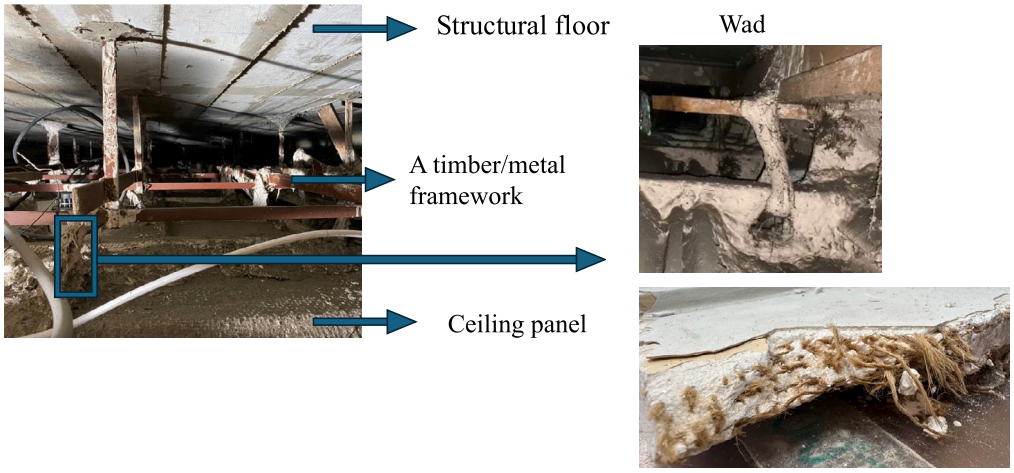


Fig. 2. A typical historic FP ceiling with the supporting wad structure.

tests show hessian can bridge cracks in POP [5]. However, as an organic material, jute is prone to fungal attack [4], which reduces the fibre content in the yarns and their strength, degrading FP over time. There is a lack of data on material properties of historic and modern hessian, for both fibre and yarn.

Previous research has characterised some mechanical properties of POP and jute yarns, which can be referred to for comparison. A study determined the static elastic modulus of POP (W/P = 0.625) to be approximately 4.5 GPa [14]. POP (W/P of 0.5–0.625) yields compressive strengths between 6.68 and 14.6 MPa [14–17]. Tensile strength is critical for understanding POP in historic FP, as FP wads carry ceiling panels under tensile loads. For brittle materials like POP, tensile properties are typically assessed using direct tensile, flexural, and Brazilian splitting tests. Direct tensile testing is challenging due to load eccentricity and stress concentrations [18]. Flexural and Brazilian splitting tests provide tensile strength indirectly, often yielding higher results than direct tensile tests [19]. Previous research [20] shows that the flexural test is susceptible to size effects, where the flexural strength of brittle materials decreases with increasing specimen size. A study on POP (W/P = 0.5) reported comparable flexural and Brazilian splitting strengths using 40 × 40 × 140 prisms (120 mm span) and 46 mm diameter discs, respectively [21], consistent with the brittle behaviour discussed above. Separately, previous research found the tensile strength of jute yarns to be 112.45 MPa (26.16%), and the elastic modulus 610–730 MPa [12,22].

Fabric-matrix bond properties are crucial for understanding fabric-reinforced composites (FRC), especially for FP, where the wad's crack-bridging mechanism involves extensive fabric-matrix interaction. These properties remain under-researched. Fabric pullout tests generate force-slip data, which can be analysed by Naaman's model to assess fabric-matrix shear stress [23,24]. The analytical force-slip relationship by this model involves three stages (Fig. 3): (a) Elastic Stage: matrix and fabric remain fully bonded, with elastic strain. This stage ends when the maximum bond shear stress (i.e. bond shear strength), τ_{max}, is reached, initiating debonding at the loaded end. At this point, the load and slip at the loaded end are denoted as P_{crit} and S_{crit}, respectively. (b) Debonding Stage: fabric debonds from the loaded to the free end. A constant frictional shear stress (i.e. frictional shear strength), τ_f, is maintained over the debonded length, while the bonded length experiences a progressively increasing shear stress, reaching a maximum value τ_{max} at the debonding front. The peak load and slip are denoted as P_p and S_p, respectively. (c) Dynamic Stage: complete debonding occurs, characterised by the fully debonded slip, S_0. In this stage, the fabric-matrix shear stress, the dynamic shear stress τ_{dyn}, gradually decreases from τ_f as the fabric slips out of the matrix. Although this model simulates the fabric pullout process, previous research has shown significant discrepancies between experimental and analytical data [25–28]. A snapback issue in the analytical force-slip response during debonding, where slip exceeds and returns to S_0, was identified [27], which does not occur in experiments. Previous studies addressed this by truncating the analytical curve at S_0, but this does not accurately reflect the process. To resolve this, Naaman's model equation must be carefully derived for the slip expression during debonding, based on the test setup in this study.

Various pullout test configurations, classified as pull–push [29–31] and pull–pull [32,33] (Fig. 4), are used. In the pull–push setup, the matrix is constrained by a compressive load at its top, while in the pull–pull setup, the matrix is supported at its bottom. Ghiassi et al. [26] used a pull–push setup with fibres embedded in cylindrical mortar specimens, but slip measurements were hindered by geometrical constraints and LVDT positioning. Dalalbashi et al. [27] developed a pull–pull configuration to improve slip measurement accuracy; however, the applied

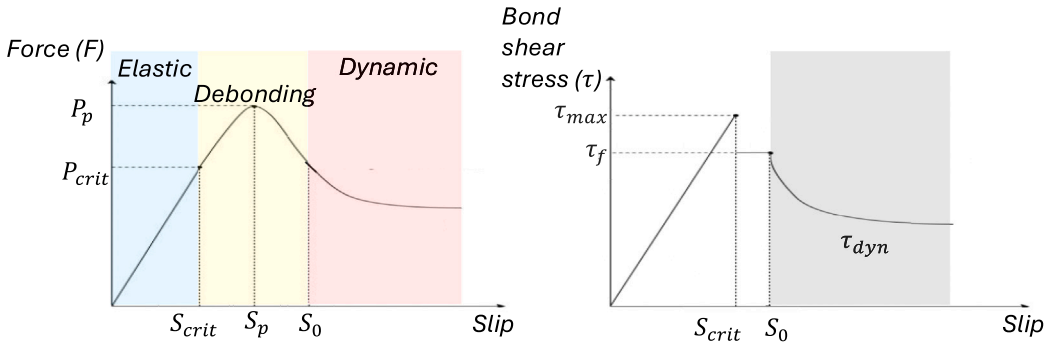


Fig. 3. Analytical fabric-matrix force-slip and bond shear stress-slip relationship in fabric pullout testing following Naaman's model [23,24].

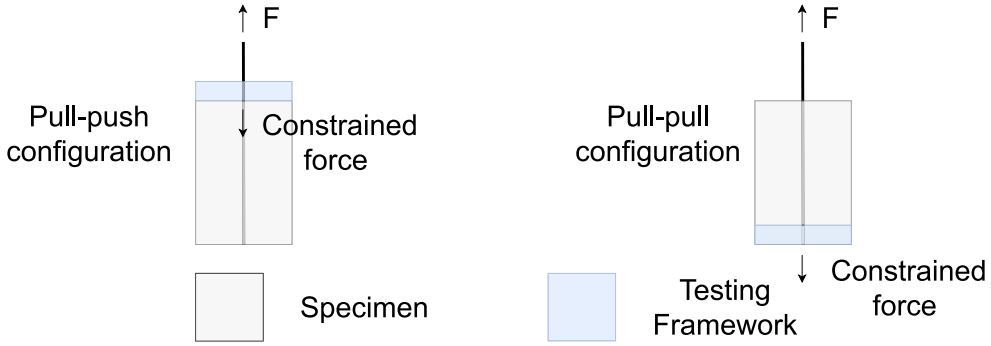


Fig. 4. Schematic representation of pull–push and pull–pull test setups.

force at the matrix support can influence debonding by compressing the matrix. Additionally, matrix support may damage brittle materials like POP. Therefore, a new test scheme is needed to ensure proper matrix support and accurate slip measurement.

Tensile properties of FP composite are critical, as the FP wad supports ceiling through this load. Direct tensile tests are widely used to characterise the tensile behaviour of FRCs; however, gripping brittle matrices like POP remains challenging. Several test setups have been developed to minimise matrix damage while preventing slippage [34,35]. The clevis-grip method, often applied to rectangular specimens with epoxy resin adhesion, is effective but can cause uneven stress distribution near the grips, leading to premature failure [35,36] (Fig. 5). Alternative geometries, such as waisted [37], bone-shaped [38,39], and dumbbell-shaped [40] specimens, reduce stress concentrations but are difficult to manufacture and still fail to produce predictable failure in the gauge region. A tailored specimen setup is needed to investigate the tensile properties of FP and how the composite behaves when cracks occur. Additionally, special attention must be given to the structure of wads, manually crafted by soaking twisted hessian in POP [4], which have not been extensively studied.

This paper characterises FP from the constituent to composite level, examining physical, chemical, and mechanical properties of POP and jute in historic FP, as well as modern counterparts representing them for analytical studies. Physical properties, including density, jute fibre/yarn diameters, and yarn's fibre volume ratio, were analysed using optical microscopy and Micro-X-ray computed tomography (μ-XCT). Chemical composition was determined via X-ray diffraction (XRD). Mechanical properties were assessed for jute yarn's tensile strength and POP's dynamic elastic modulus via Impulse Excitation Vibration (IEV). The static elastic modulus of modern POP was measured using incremental compression for comparison with Virtual Field Method (VFM) applied to DIC data. Compressive and tensile strengths of modern POP were evaluated through direct tensile, flexural, and Brazilian splitting tests. Fabric-matrix bonding were characterised by fabric pullout tests using a specialised clevis-grip pull–pull system, with slip measured by DIC, capturing force-slip data accurately. Fabric-matrix shear stress, including critical bond and frictional shear strength (τ_{max} and τ_f), were quantified using an adapted Naaman model and novel force-fitting method. FP's tensile properties were evaluated through direct tensile tests on dogbone specimens, designed to mimic wads while producing controllable failures. The paper is organised as follows: Section 2 covers specimen preparation and testing methods, Section 3 presents the adapted Naaman model and fitting methods, Section 4 discusses results, and Section 5 concludes the paper.

2. Materials and methods

2.1. Materials

Historic POP and hessian were sourced from the Grade-II listed ICE building. Representative modern ones were prepared using fine casting plaster and hessian from Industrial Plaster Ltd. [41,42], with a W/P of 0.7 for POP casting to replicate the historic counterpart [11]. The hessian had a mesh size of 5 mm × 10 mm, resembling the historic material. Jute yarn specimens were prepared following ASTM D3822M-14 [43], using pristine jute yarns.

2.2. Physical characterisation of constituent materials

Densities of historic and modern POP (ρ_{pop}) and jute (ρ_{fibre}) were measured following EN 13279-2:2014 [44] and ASTM D1577 [45], respectively.

Jute yarn/fibre diameters (D_{yarn} and D_{fibre}) were assessed using an optical microscope (Olympus BX51) by averaging measurements from twenty specimens, with three measurements taken per specimen (Fig. 6(a)). Fibre volume ratio of jute yarns (V_f), defined as the fibre volume of the yarn divided by the total volume of the yarn, was determined using μ-XCT, enabling non-destructive visualisation of the 3D microstructure of the FP specimen. Fig. 6(b) illustrates the test setup

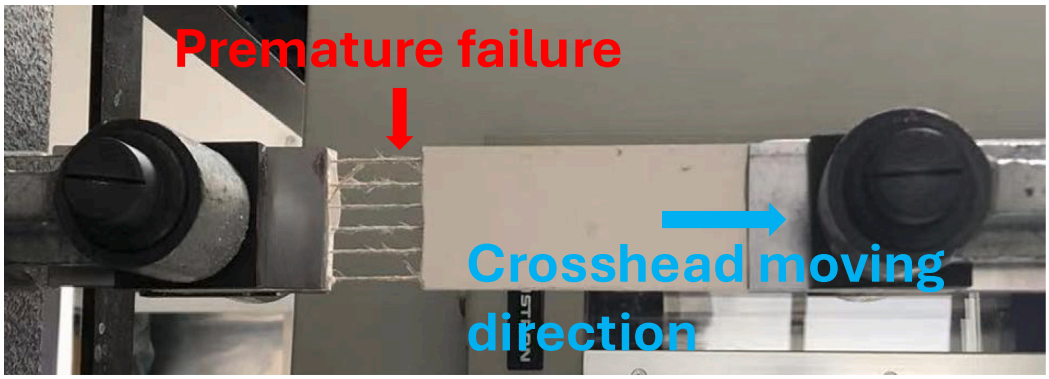


Fig. 5. Localised premature damage near the grips in direct tensile tests of a rectangular POP specimen with clevis grips.

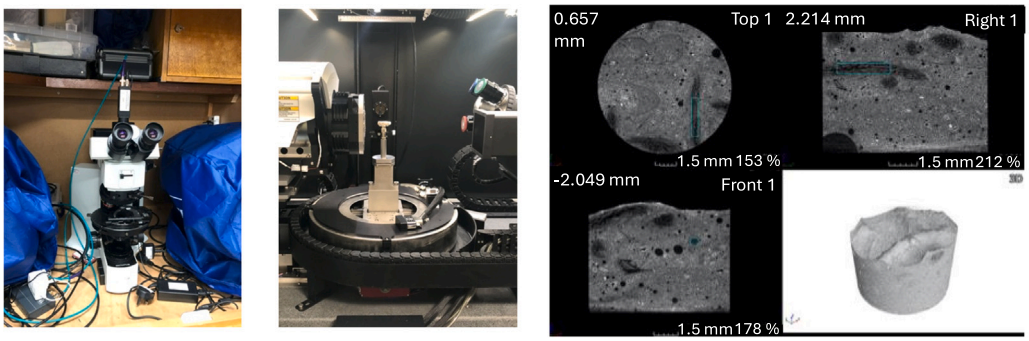


Fig. 6. Physical characterisation methods: (a) Optical microscopy measuring jute yarn/fibre diameter, (b) μ-XCT imaging of FP specimens, (c) μ-XCT reconstruction of FP specimens. (For interpretation of the references to colour in this figure legend, the reader is referred to the web version of this article.)

Table 1
μ -XCT imaging setup for historic and new FP specimens.

	H1	H2	M
Voltage (keV)	120	140	100
Current (mA)	145	149	140
Exposure time (s)	3	6	5
Voxel size (μm)	4.923700	7.556180	8.113920
ROI (mm)	10.08 × 9.88 × 9.95	7.74 × 7.59 × 7.63	8.31 × 8.15 × 8.19
Sub-ROI (mm)	0.55 × 2.13 × 2.57	0.58 × 0.81 × 1.65	0.58 × 0.83 × 7.46

for μ-XCT imaging (Xradia Versa 610). The X-ray attenuation of a material is governed by its attenuation coefficient, which quantifies photon transmission through a unit of material. Denser materials absorb more X-rays and thus appear as lighter grey levels in the reconstructed μ-XCT images. This allows the identification of materials with different densities based on their distinct greyscale values in the images. Two historic FP specimens (H1 and H2) and one modern FP specimen (M), each approximately 30 × 30 × 8 mm, were scanned. Table 1 provides details on the μ-XCT imaging setup, as well as the sizes of the region of interest (ROI) and sub-ROI for each specimen.

Fig. 6(c) presents the ROI from the reconstructed images of the historic FP specimen H2, illustrating material differentiation. A sub-ROI (marked with blue clipping boxes) was selected within the ROI, representing the volume of a single embedded jute yarn, comprising fibres and air. Image segmentation was conducted by thresholding using Avizo software to determine fibre volume ratios for both historic and modern jute yarns.

2.3. Chemical characterisation of constituent materials

Chemical characterisation of historic and modern POP and jute was performed using XRD. POP specimens were ground with a pestle and mortar, while jute specimens were dried at 70 °C for 48 h before being ground into a fine powder (Fig. 7). The powdered specimens were loaded into a standard holder (2.5 × 2.5 × 1 cm) and aligned in XRD chamber. Characterisation was conducted at room temperature using a Rigaku MiniFlex X-ray diffractometer in continuous scanning mode (Fig. 8). With a step size of 0.005° and a 2θ range of 2.0025°–89.9975°, a dataset of 17,600 points was generated. The XRD pattern exhibited peaks at specific angles, which were compared with previous studies [5] to identify characteristic peaks and phase compositions.

2.4. Mechanical characterisation of constituent materials

In select mechanical tests, stereo-DIC systems were used, each comprising two ME2P-2621-15U3M cameras, Kowa LM100FC24M lenses, and LED illumination, with a 0.2 mm speckle pattern applied. Image acquisition, calibration, and data processing were performed using MatchID software. Unless specified otherwise, images were captured at 2 Hz, and a subset size of 33 pixels and a step size of 10 pixels were applied. Before testing, stereo angles and image noise levels in both horizontal and vertical directions were measured for each stereo-DIC system.

Single jute yarn tensile testing followed ASTM D2256/D2256M [46] to assess the tensile strength (σ_{jute}) of historic and modern jute yarns.



Fig. 7. XRD specimens: (a) Historic POP, (b) Modern POP, (c) Historic and modern jute.

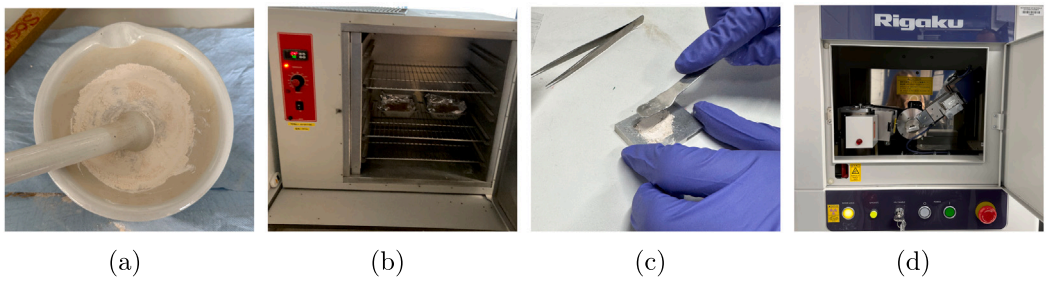


Fig. 8. XRD testing procedure: (a) Specimen grinding, (b) Dehydration (for jute only), (c) Specimen mounting, (d) Chemical characterisation.

Ten tests were conducted per yarn type. Each specimen was mounted on a precut cardboard frame, secured with Loctite Hysol 9466 epoxy resin, and tested at a 25 mm gauge length. An Instron 5582 with a 5 kN load cell was used at a crosshead speed of 300 mm/min. σ_{jute} was calculated using the cross-sectional area of the yarn containing only jute, excluding air, derived from the V_f obtained in prior characterisation. The test setup is shown in Fig. 9(a).

Three POP Prisms (40 × 40 × 160 mm) underwent the IEV test to determine the dynamic elastic modulus (E_{dyn}) following ASTM E1876-22 [47]. Specimens were excited using a metal bar, and signals recorded by a Polytec PDV-100 laser vibrometer provided flexural and torsional resonant frequencies for analysis. For historic POP, as intact prisms were unavailable, E_{dyn} was characterised using a thin plate (95 mm × 26.145 mm × 4.25 mm) extracted from the ICE building. The test setup is shown in Fig. 9(b).

The static elastic modulus of modern POP (E_{stat}) was measured following a method inspired by ASTM C469/C469M [48]. A 300/15 kN compression–flexure frame (Controls Group) with a 300 kN load cell was used. Three identical POP prisms (160 mm length, 40 × 40 mm contact area) were incrementally loaded from 10% to 13 kN in 5% steps at 50 N/s, with 120-s pauses for stereo-DIC measurements on the front and back surfaces. The stereo angles were 22.32° (front) and 16.76° (back), with image noise standard deviations of 0.32 μm (horizontal) and 0.36 μm (vertical) for the front, and 0.48 μm (horizontal) and 0.5 μm (vertical) for the back. The test setup is shown in Fig. 9(c). DIC measurements from a 60 mm central region of the specimen, where a uniform stress distribution was assumed, were analysed using the VFM to determine E_{stat} for each specimen on both surfaces.

Three identical POP prisms underwent flexural testing, followed by compression testing on the six halves, following EN 13279-2:2014 [44], to determine flexural (σ_{flex}) and compressive (σ_{comp}) strength. The 300/15 kN compression–flexure testing frame was used. Flexural and compression tests employed 15 kN and 300 kN load cells, with loading rates of 50 N/s and 300 N/s, respectively (Fig. 9(d)).

Three POP discs underwent Brazilian splitting tests to determine tensile strength (σ_{split}) following ISRM standards [49]. The discs were cast in 50 mm-diameter steel molds and trimmed to approximately 20 mm in height. Each specimen was positioned in a loading anvil with opposing steel jaws (54.74 mm diameter), with the upper jaw featuring a spherical opening for a 25 mm half-ball bearing. To minimise friction and ensure uniform force distribution, two Teflon sheets with lubricant oil were placed at the top and bottom. A 300/15 kN compression–flexure frame with a 300 kN load cell applied a loading rate of 80 N/s. The test setup is shown in Fig. 9(e).

Three dogbone POP specimens, fitted with a customised clevis-grip system, underwent direct tensile testing on the Instron 5582 universal testing machine with a 5 kN load cell and a 3 mm/min crosshead speed, to determine direct tensile strength (σ_{dir}). Specimen geometry and test setup are detailed in Section 2.6, as this configuration was primarily used for FP composite direct tensile testing.

2.5. Fabric-matrix bonding characterisation

Six specimens were prepared, each consisting of a POP matrix (180 mm × 50 mm × 10 mm) with a hessian layer embedded along its full length, extending beyond one end for loading. This ensured sufficient debonding for analysis. While some premature fibre failures occurred during pullout, they were negligible in the analysis. Specimens were secured using a clevis-grip system, with the bottom bonded to steel plates (100 mm × 50 mm × 1 mm) via epoxy resin, covering a 65 mm glued length. A steel board was pinned between the plates for gripping in a pull–pull setup. The extended hessian at the other end was placed between rubber pads, bonded with epoxy resin, to protect the yarns and enhance gripping. Specimen geometry and setup are shown in Figs. 10(a) and 10(b), respectively. A stereo-DIC system measured slip by tracking elongation between speckled markers at the upper clamp's bottom edge and the specimen's top edge on both sides using the MatchID Extensometer module (Fig. 10(c)). The two measurements were averaged for precision. The stereo angle was 15.67°, with image noise standard deviations of 0.48 μm (horizontal) and 0.43 μm (vertical).

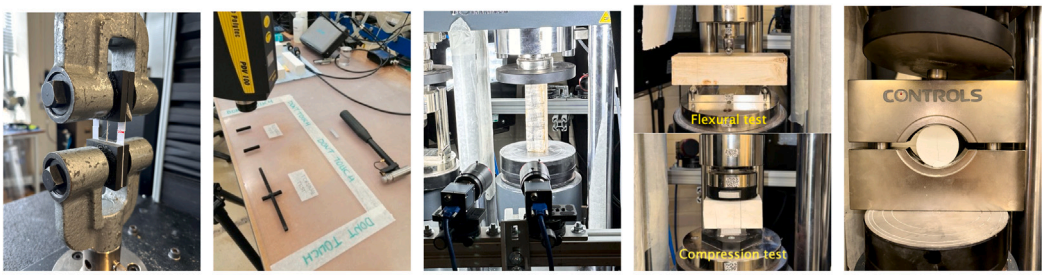


Fig. 9. Mechanical characterisation methods: (a) Single jute yarn tensile test, (b) IEV, (c) Static elastic modulus determination, (d) Flexural and compression tests, (e) Brazilian splitting test.

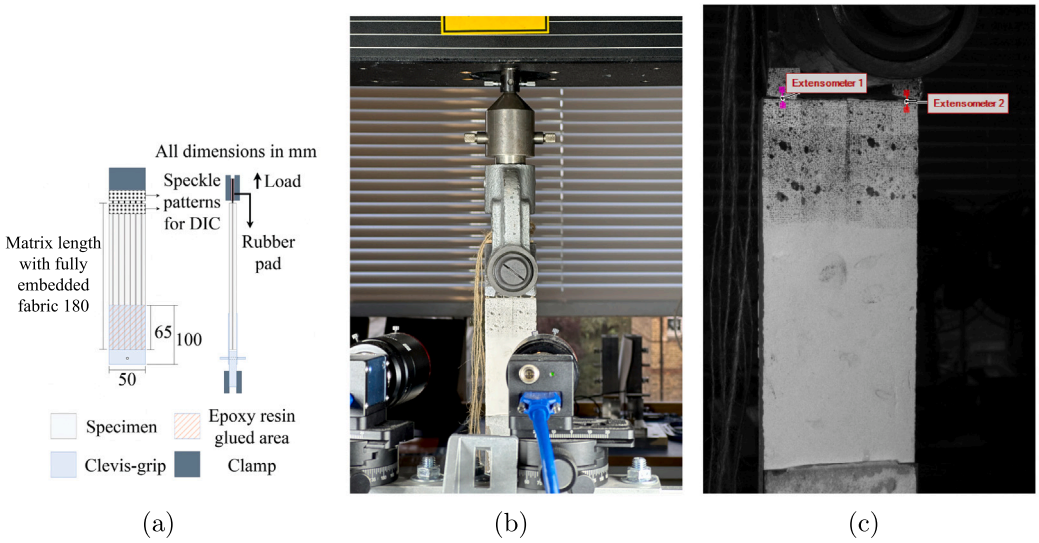


Fig. 10. Fabric pullout testing method: (a) Specimen geometry and supporting configuration, (b) Test setup, (c) Slip measurement.

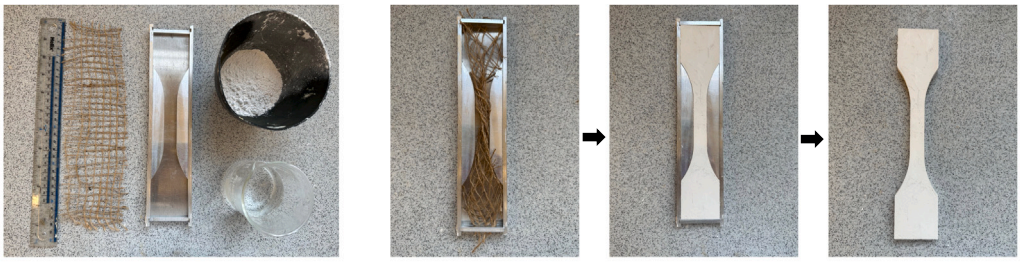


Fig. 11. Preparation of wad-like dogbone specimens.

2.6. FP composite tensile testing

A dogbone FP specimen was designed and handcrafted to represent the wad, with the preparation procedures shown in Fig. 11. A detailed description can be found in [50]. This specimen incorporates twisted hessians embedded in a POP matrix and features a customised geometry, as shown in Fig. 12(a). Stress concentrations were minimised through arched transitions between the gauge section and ends, while a clevis-grip system, applied at both ends with epoxy resin, ensured secure specimen gripping. Six specimens underwent direct tensile testing, along with three unreinforced POP specimens of the same geometry for comparison, as detailed in Section 2.4. The Instron 5582 universal testing machine, equipped with a 5 kN load cell and a 3 mm/min crosshead speed, was used. Displacement was measured via a stereo-DIC system, as in the fabric pullout test (Fig. 12(b)).

3. Adapted Naaman's analytical model for fabric-matrix bonding characterisation

3.1. Fundamental concepts

In Naaman's model [23,24], reinforcement is considered as a single fibre. However, in this study, each FP specimen for pullout testing is reinforced with a hessian layer containing six evenly spaced warp yarns. Naaman's model has been adapted to account for this difference.

Fig. 13(a) illustrates the global equilibrium of the specimen, where: L is the embedded length, u is the debonded length, x is the bonded length, P is the total force at the fabric's loaded end, F is the force in the fabric, and M is the force in the matrix. Since the warp yarns are evenly spaced within the matrix, M is assumed to be uniformly

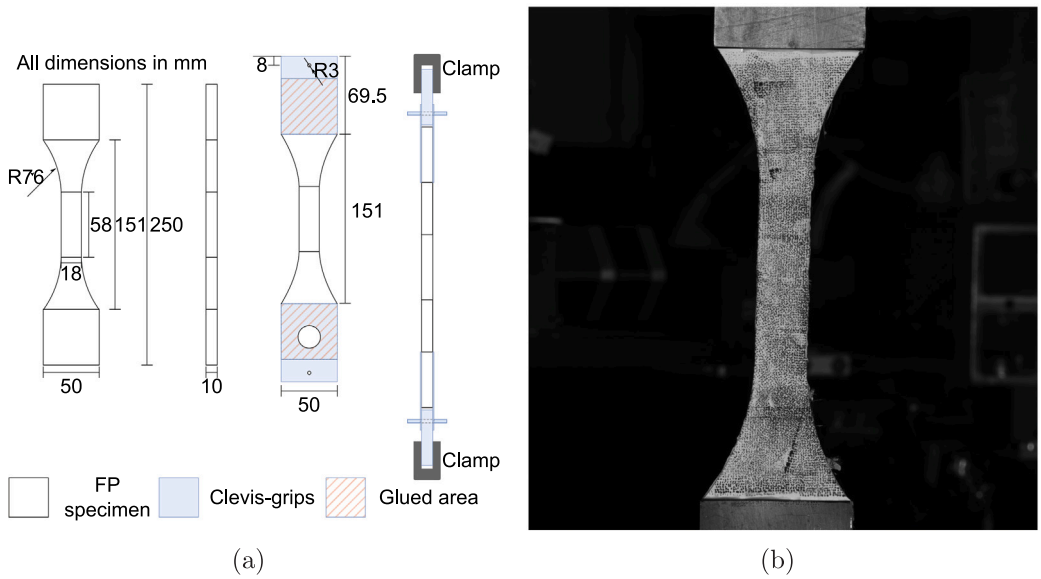


Fig. 12. FP composite tensile property characterisation: (a) specimen geometry and gripping system, and (b) Test setup.

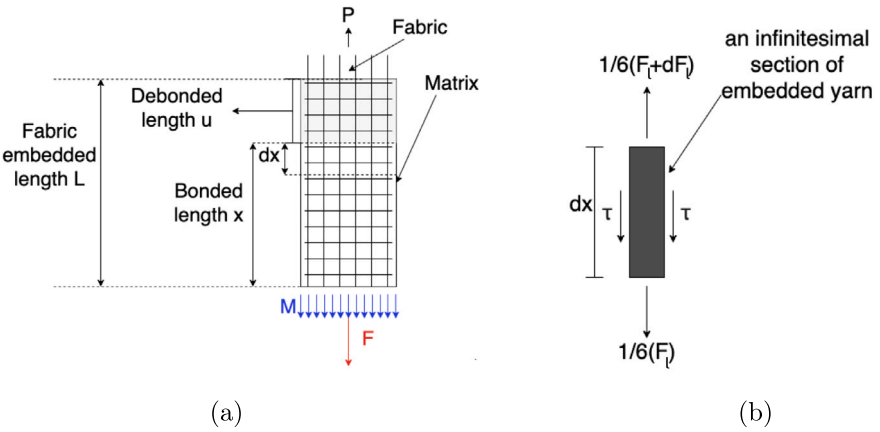


Fig. 13. Relevant variables for adapted Naaman's model: (a) Global equilibrium, (b) Local equilibrium for a differential element of a single warp jute yarn.

distributed. The global equilibrium covers the entire cross-sectional region of the specimen, where A_f and A_m denote the cross-sectional area, E_f and E_m denote the static elastic modulus, and ϵ_f and ϵ_m denote the strain of the yarn and the matrix, respectively. The following equations apply:

$$P = F + M, \tag{1}$$

$$F = nA_f E_f \epsilon_f, \tag{2}$$

$$M = A_m E_m \epsilon_m, \tag{3}$$

Fig. 13(b) shows the local equilibrium of a free-body diagram of a differential element, which is a single warp yarn of length dx, located at a distance x from the fabric-loaded end. The force in each warp yarn is $\frac{1}{n}F$, where $n = 6$, representing the number of warp yarns. The local equilibrium only considers a single warp yarn, where τ denotes the fabric-matrix shear stress, φ denotes the yarn perimeter, and κ denotes the bond shear modulus, the local force F_l on a differential element of a single warp yarn is given by:

$$dF_l = \tau\, dx\, \varphi, \tag{4}$$

$$\frac{d^2F_l}{dx^2} = \frac{d(\tau\varphi)}{dx} = \kappa\varphi\frac{dS}{dx} = \varphi\kappa(\epsilon_f - \epsilon_m), \tag{5}$$

The global force F is:

$$F = nF_l. \tag{6}$$

The slip S is:

$$S = \delta_f - \delta_m = \int_0^x (\epsilon_f - \epsilon_m)\, dx. \tag{7}$$

From Eqs. (5), (6), and (7), the following differential equation is derived:

$$\frac{d^2F}{ndx^2} - \lambda^2 F = -\frac{\lambda^2 P}{QA_m E_m}, \tag{8}$$

where:

$$Q = \left(\frac{1}{nA_f E_f} + \frac{1}{A_m E_m}\right), \tag{9}$$

$$\lambda = \sqrt{\kappa\varphi Q}. \tag{10}$$

Rearranging the differential equation (8) with boundary conditions $F(0) = 0$ and $F(L) = P$, and solving for A and B in the general solution (see the calculation in Appendix), $F(x)$ is:

$$F(x) = \frac{P\sinh\left(\sqrt{n}\lambda x\right)}{\sinh\left(\sqrt{n}\lambda L\right)}\left(1 - \frac{1}{QA_m E_m} + \frac{e^{-\sqrt{n}\lambda L}}{QA_m E_m}\right) - \frac{Pe^{-\sqrt{n}\lambda x}}{QA_m E_m} + \frac{P}{QA_m E_m}, \tag{11}$$

The corresponding shear stress τ is:

$$\tau = \frac{1}{\varphi}\frac{dF}{dx} = \frac{1}{\varphi}\left(\frac{P(1-\frac{1}{QA_mE_m}+\frac{e^{-\sqrt{n}\lambda L}}{QA_mE_m})\sqrt{n}\lambda\cosh\left(\sqrt{n}\lambda x\right)}{\sinh\left(\sqrt{n}\lambda L\right)} + \frac{P\sqrt{n}\lambda e^{-\sqrt{n}\lambda x}}{QA_mE_m}\right). \tag{12}$$

Stage I: Elastic stage

The maximum bond shear stress (i.e. bond shear strength) $\tau_{\max}$ at $x = L$ is:

$$\tau_{max} = \frac{P}{\varphi}\left(\frac{\left(1-\frac{1}{QA_mE_m}+\frac{e^{-\sqrt{n}\lambda L}}{QA_mE_m}\right)\sqrt{n}\lambda\cosh\left(\sqrt{n}\lambda L\right)}{\sinh\left(\sqrt{n}\lambda L\right)} + \frac{\sqrt{n}\lambda e^{-\sqrt{n}\lambda L}}{QA_mE_m}\right) \tag{13}$$

Using $\tau_{\max}$, the critical pressure P_{crit} is:

$$P_{crit} = \frac{\tau_{max}\varphi\cdot QA_mE_m\cdot\sinh\left(\sqrt{n}\lambda L\right)}{\sqrt{n}\lambda(\cosh\left(\sqrt{n}\lambda L\right)(QA_mE_m-1)+1)} \tag{14}$$

Integrating up to $x = L$, the elastic slip S_{ela} is:

$$S_{\text{ela}} = \frac{P_{\text{ela}}\left(\cosh\left(\sqrt{n}\lambda L\right)-1\right)}{\sqrt{n}\lambda\sinh\left(\sqrt{n}\lambda L\right)}\left(Q-\frac{2}{A_mE_m}\right) \tag{15}$$

The critical slip S_{crit} is:

$$S_{crit} = S_{\text{ela}}(P_{\text{ela}} = P_{crit}) \tag{16}$$

Stage II: Debonding stage

When debonding begins, the force P comprises two components: a non-uniform bond shear stress that increases along the bonded length and reaches its maximum value $\tau_{\max}$ at the debonding front located at $x = L - u$, and the frictional shear stress τ_f over the debonded length u. The force and slip are:

$$P_{\text{deb}} = \frac{\tau_{\max}\varphi\cdot QA_mE_m\cdot\sinh\left(\sqrt{n}\lambda(L-u)\right)}{\sqrt{n}\lambda\left(\cosh\left(\sqrt{n}\lambda(L-u)\right)(QA_mE_m-1)+1\right)} + n\tau_f\varphi u, \tag{17}$$

$$S_{\text{deb}} = -\frac{Pu}{nA_mE_m} - \frac{\tau_f\varphi uL}{A_mE_m} - \left(Q-\frac{2}{A_mE_m}\right) \times\left(\frac{n\tau_f\varphi u^2}{2} - \frac{(P-n\tau_f\varphi u)\left(1-\cosh(\sqrt{n}\lambda(L-u))+\sinh(\sqrt{n}\lambda(L-u))\right)}{\sqrt{n}\lambda\left(1+\cosh(\sqrt{n}\lambda(L-u))-\sinh(\sqrt{n}\lambda(L-u))\right)}\right). \tag{18}$$

The slip at full debonding is:

$$S_0 = S_{\text{deb}}(u = L) \tag{19}$$

Stage III: Dynamic stage

The slip S_{dyn} is the sum of the total rigid body movement of the yarn and its elongation:

$$S_{\text{dyn}} = \frac{-P_{dym}(L-\upsilon)}{A_mE_m} + n\left(\frac{Q\tau_f\varphi}{2}\right)(L-\upsilon)^2 + \upsilon \tag{20}$$

The force P_{dyn} is:

$$P_{\text{dyn}} = \left(1-\exp\left(\frac{-2\upsilon_f\mu x}{E_fr_f\left(\frac{1+\upsilon_m}{E_m}+\frac{1+\upsilon_f}{E_f}\right)}\right)\right)\delta E_f\pi\frac{r_f}{\upsilon_f} \tag{21}$$

where υ is the yarn's rigid body movement, x is the yarn's embedded length, υ_f and υ_m are the Poisson's ratios of the yarn and plaster, r_f is the yarn radius, μ (0.3) is the friction coefficient, and the yarn-plaster misfit δ is:

$$\delta = \delta_0\left(\frac{e^{-(S-S_0)\eta}-\xi e^{-(L)^\eta}}{1-\xi e^{-(L-S+S_0)^\eta}}\right) \tag{22}$$

with η is the decay rate for data fitting and ξ aligns the asymptotic values of the experimental and analytical data, where:

$$\delta_0 = \frac{n\tau_f\varphi L\upsilon_f}{E_f\pi r_f}\left(1-\exp\left(\frac{-2\upsilon_f\mu L}{E_fr_f\left(\frac{1+\upsilon_m}{E_m}+\frac{1+\upsilon_f}{E_f}\right)}\right)\right)^{-1} \tag{23}$$

The fabric-matrix shear stress at this stage is given by:

$$\tau_{\text{dym}} = \frac{P_{\text{dym}}}{n\varphi L} \tag{24}$$

3.2. Fitting methodologies

3.2.1. Traditional analytical fitting method

In Naaman's work, analytical force-slip data is fitted to the experimental data to characterise $\tau_{\max}$ and τ_f. From Eq. (15), $\frac{P_{\text{ela}}}{S_{\text{ela}}}$ can be derived to calculate λ using the following equation, where *Slope* is the initial slope measured from the experimental data:

$$\frac{P_{\text{ela}}}{S_{\text{ela}}} - Slope = 0 \tag{25}$$

From Eqs. (17) and (18), the following boundary conditions apply:

$$P_{\text{deb}}\Big|_{u=u_p} - P_p = 0 \tag{26}$$

$$S_{\text{deb}}\Big|_{u=u_p,P_{\text{deb}}=P_p} - S_p = 0 \tag{27}$$

$$\frac{dP_{\text{deb}}}{du}\Big|_{P_{\text{deb}}=P_p} = 0 \tag{28}$$

Solving Equations (26), (27), and (28) allows for the determination of the bond shear strength $\tau_{\max}$, the frictional shear strength τ_f, and the debonded length of the yarn at the peak force u_p.

3.2.2. Force-fitting method

To achieve a better fit, a novel force-fitting method was developed. This method iteratively optimises model parameters to minimise discrepancy between experimental and analytical force-slip data, involving following steps:

1. Provide initial guesses, including λ, $\tau_{\max}$, τ_f, *Slope*, and the elastic moduli E_f and E_m (optional).
2. Find the root of λ for Eq. (15) using the Nelder–Mead method.
3. Find P_{crit}, S_0, and S_{crit} using the initial guesses (or updated guesses if in iteration) and the corresponding λ.
4. Fit the analytical force-slip curve and compute the force-slip discrepancy between the analytical and experimental data for the debonding stage, then update the model parameters based on the initial guesses.

The reason for using error only in the debonding stage is that it effectively represents the goodness of the overall fit. This is because P_{crit} and S_{crit} define the transition from the elastic to the debonding stage, while S_0 marks the transition from the debonding to the dynamic stage. Additionally, prior trials have shown that the debonding stage is the most challenging to fit.

The final output includes the critical model parameters (P_{crit}, S_{crit}, and S_0), along with the bond shear strength $\tau_{\max}$, frictional shear strength τ_f, as well as the τ_{dyn}, quantifying the fabric-matrix shear stress. These parameters, derived from the optimal analytical fit, can

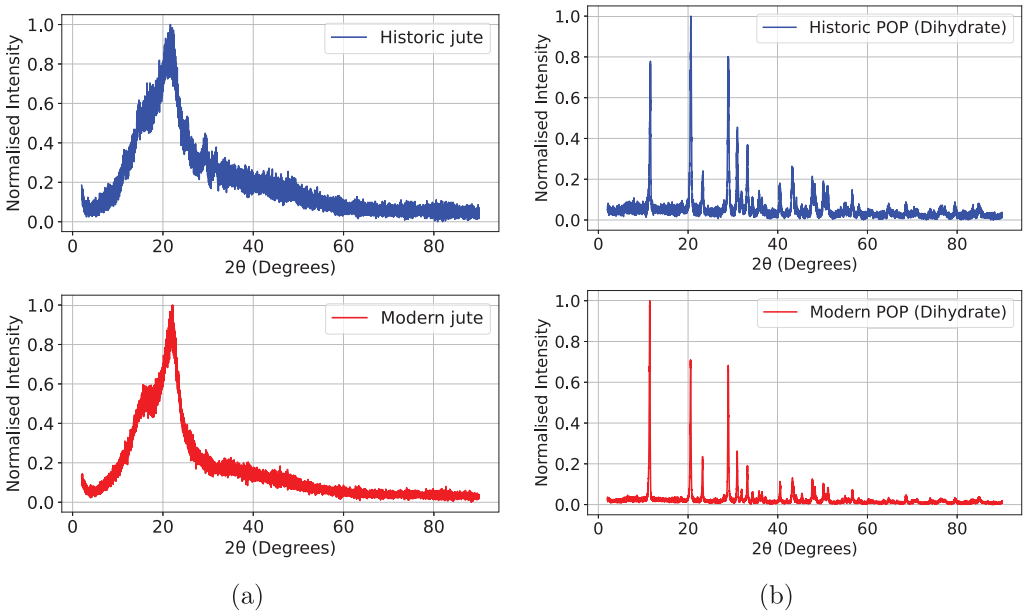


Fig. 14. XRD patterns: (a) Historic and modern jute, (b) Historic and modern POP.

accurately characterise the fabric-matrix bonding properties of FP. Optionally, optimised E_f and E_m can be predicted and compared to the existing elastic moduli.

4. Results and discussion

4.1. Chemical characterisation of constituent materials

The XRD patterns highlight differences in crystallinity and phase composition between the historic and modern materials, offering insights into the material's structural evolution over time. Fig. 14(a) shows characteristic cellulose peaks at approximately 15°, 16.5°, and 22.8° (2θ) for historic and modern jute, consistent with [51]. Fig. 14(b) displays peaks at around 11.5°, 20.5°, and 29.5° (2θ) for historic and modern POP, corresponding to $CaSO_4 \cdot 2H_2O$, in agreement with [5]. For both POP and jute, historic materials have broader peaks, indicating lower crystallinity and higher amorphous content, likely due to environmental degradation, while modern materials exhibit sharper peaks, suggesting higher crystallinity and better structural integrity. Despite these differences, the consistent alignment of peak locations shows that the intrinsic crystalline phases of historic materials remain intact. This correspondence confirms that modern materials are reliable proxies for their historic counterparts, with critical chemical and structural fidelity preserved.

4.2. Physical and mechanical properties

4.2.1. Hessian

The physical and mechanical characterisation results of the hessian are presented in Table 2.

Fig. 15(a) shows optical microscopy images for measuring D_{yarn} and D_{fibre} in historic and modern FP, using a 100 μm scale bar. Historic yarns, with a diameter of 0.72 mm, are similar to the modern ones (0.81 mm). However, historic fibres (45 μm) are significantly thinner than modern fibres (116 μm).

Fig. 15(b) shows the segmentation of reconstructed μ-XCT images, distinguishing air and fibres in the selected sub-ROI of jute yarn in historic and modern FP to determine V_f. μ-XCT images were denoised with a median filter and segmented via greyscale thresholding, classifying voxels as 'air' (red) or 'fibre'. The results show that V_f is slightly lower in historic jute yarns (58.90%) compared to modern jute yarns (68.47%).

Table 2
Physical and mechanical properties of historic and modern jute.

	Historic jute (CoV %)	Modern jute (CoV %)
D_{yarn} (mm)	0.72 (15)	0.81 (21.3)
D_{fibre} (μm)	45 (26.2)	116 (20.6)
V_f (%)	58.9 (0.54)	68.47 (0.55)
ρ_{fibre} (g/cm^3)	0.86 (3.85)	0.95 (3.14)
σ_{jute} (MPa)	35.05 (14.68)	123.93 (6.1)

Table 3
Physical and mechanical properties of historic and modern POP.

	Historic POP	Modern POP (CoV %)
ρ_{pop} (g/cm^3)	1.02	1.09 (0.78)
E_{dyn} (MPa)	4649.15	5482.33 (4.38)
E_{stat} (MPa)	–	5552.83 (0.97)
σ_{comp} (MPa)	–	8.23 (5.80)
σ_{dir} (MPa)	–	1.02 (7.7)
σ_{flex} (MPa)	–	3.86 (9.82)
σ_{split} (MPa)	–	2.44 (1.07)

ρ_{fibre} was derived from the yarn volume (calculated using D_{yarn} and specimen length), yarn weight, and V_f. It was 0.86 g/cm^3 for historic and 0.95 g/cm^3 for modern, indicating a minor difference between the two types.

σ_{jute} was 123.93 MPa for modern jute yarn, whereas historic jute yarn exhibited a significantly lower value of 35.05 MPa, likely due to environmental degradation, such as fungal attack.

4.2.2. POP

The physical and mechanical characterisation results of the POP are presented in Table 3.

As shown, ρ_{pop} in historic and modern FP was 1.02 g/cm^3 and 1.09 g/cm^3, respectively, showing a small difference.

E_{dyn} for historic and modern POP was 4649.15 MPa and 5482.33 MPa, respectively, indicating slight differences in stiffness. E_{stat} for modern POP, representing historic POP, was determined using VFM applied to DIC data from the central region on both the front and back surfaces of the specimen. The central region of the slender specimen

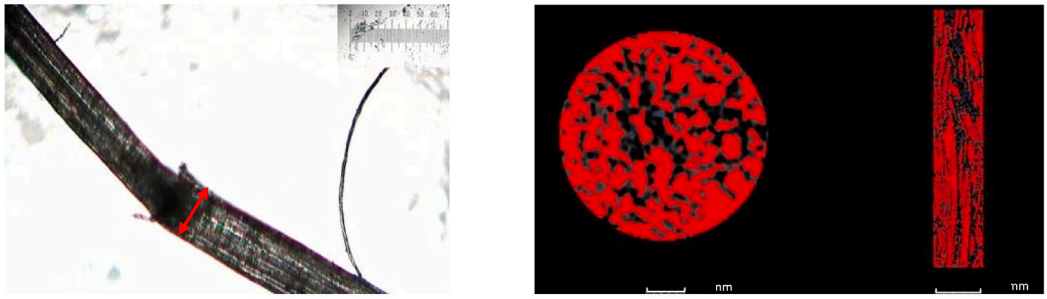


Fig. 15. Physical characterisation of jute: (a) Optical microscopy imaging for diameter measurement; (b) μ-XCT reconstruction showing air-fibre segmentation of a single jute yarn for measuring its fibre volume ratio.

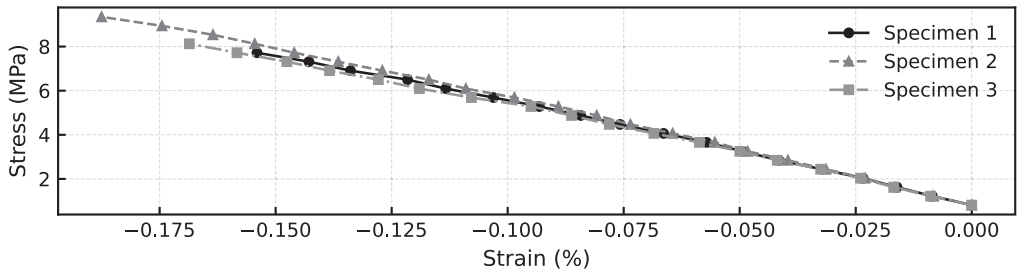


Fig. 16. Stress–strain relationship averaging front and back measurements of prisms in compression, used to determine E_{stat} of POP.

yields a uniform stress distribution, eliminating localised stress near the specimen's ends. Variations in E_{stat} between surfaces, due to slight misalignments during force application, were addressed by averaging measurements for a more reliable estimate. In contrast, some specimens showed nearly identical E_{stat} values for both surfaces, indicating optimal alignment. E_{stat} for modern POP was 5552.83 MPa, consistent with E_{dyn}. Stress–strain relationship averaging front and back measurements for all three specimens is shown in Fig. 16.

For further characterisation of modern POP, σ_{comp} was 8.23 MPa, within the established literature range. The tensile strength, assessed through direct tensile, flexural, and the Brazilian splitting testing, yielded values of 1.02 MPa (σ_{dir}), 3.86 MPa (σ_{flex}), and 2.44 MPa (σ_{split}), respectively. The results show that the direct tensile and flexural tests exhibit high variability, likely due to their sensitivity to defect locations, leading to premature failure. In contrast, the Brazilian splitting test exhibited lower variability, indicating a stable failure mechanism. This test, involving diametral compressive loading, creates a more uniform biaxial stress state in a large central region of the specimen, where the material's fracture is influenced more by the overall stress distribution than by individual defects, making it the most suitable method for characterising tensile properties of brittle materials like POP.

4.3. Fabric-matrix bonding properties between hessian and POP

The experimental force-slip response, averaged from six fabric pullout tests, is shown in Fig. 17(a), in black bold line. Using E_{stat} measured previously of representative modern POP (E_m = 5552.83 MPa) and the elastic modulus of jute yarns from prior research (E_f = 677 MPa, CoV = 5.82%) [22], the analytical fitting result is shown as a bold line, and the force-fitting as a dashed line. The force-fitting result with optimised elastic moduli (E_m = 5418.90 MPa and E_f = 764.14 MPa), minimising discrepancies between experimental and fitted data, is shown as a dotted line. The optimised E_m closely matches the existing E_m, while E_f shows a 10% increase compared to the prior value. Research

Table 4
Model parameters, and the bond shear strength τ_{max} and the frictional shear strength τ_f, derived from the optimal fit from force-fitting with optimised E_m and E_f, using the adapted Naaman's model.

S_{crit} (mm)	P_{crit} (N)	S_0 (mm)	τ_{max} (MPa)	τ_f (MPa)
0.37	116.73	2.49	1.83	0.09

suggests that this discrepancy may be due to various factors, including non-uniform fibre properties, which contribute to the structural heterogeneity of the yarn and cause premature failure, and test setup limitations, such as yarn misalignment [52], which can lead to a decrease in E_f measurement.

The results indicate that the previous snapback issue arose from an incorrect slip expression for the debonding stage, denoted as S_{deb}(old) [27], which differs from the adapted slip, S_{deb}. A comparison of these two slip behaviours, along with their difference, ΔS_{deb}, is shown in Fig. 18. As observed, S_{deb}(old) exceeds the S_0 for $0 < u < L$, before dropping to S_0 at $u = L$, causing the snapback. The shaded area represents ΔS_{deb}, which starts at 0 at $u = 0$, increases to a positive maximum, and then returns to 0 at $u = L$. Incorporating ΔS_{deb} by subtracting it from S_{deb}(old) results in S_{deb}, transforming the slip behaviour from parabolic to monotonic. This ensures that the maximum slip occurs at $u = L$, effectively resolving the snapback issue.

Compared to traditional analytical fitting, the force-fitting method provides a significantly better fit, with the optimised E_m and E_f yielding the most accurate results. This demonstrates that the adapted Naaman's model, using the force-fitting method with optimised E_m and E_f, is the most effective tool for modelling the realistic fabric-matrix debonding behaviour observed in fabric pullout tests. The fabric-matrix shear stress between the hessian and the POP, derived from this method, is presented in Fig. 17(b), with the model parameters (S_{crit}, P_{crit}, and S_0), the bond shear strength τ_{max}, and the frictional shear strength τ_f summarised in Table 4.

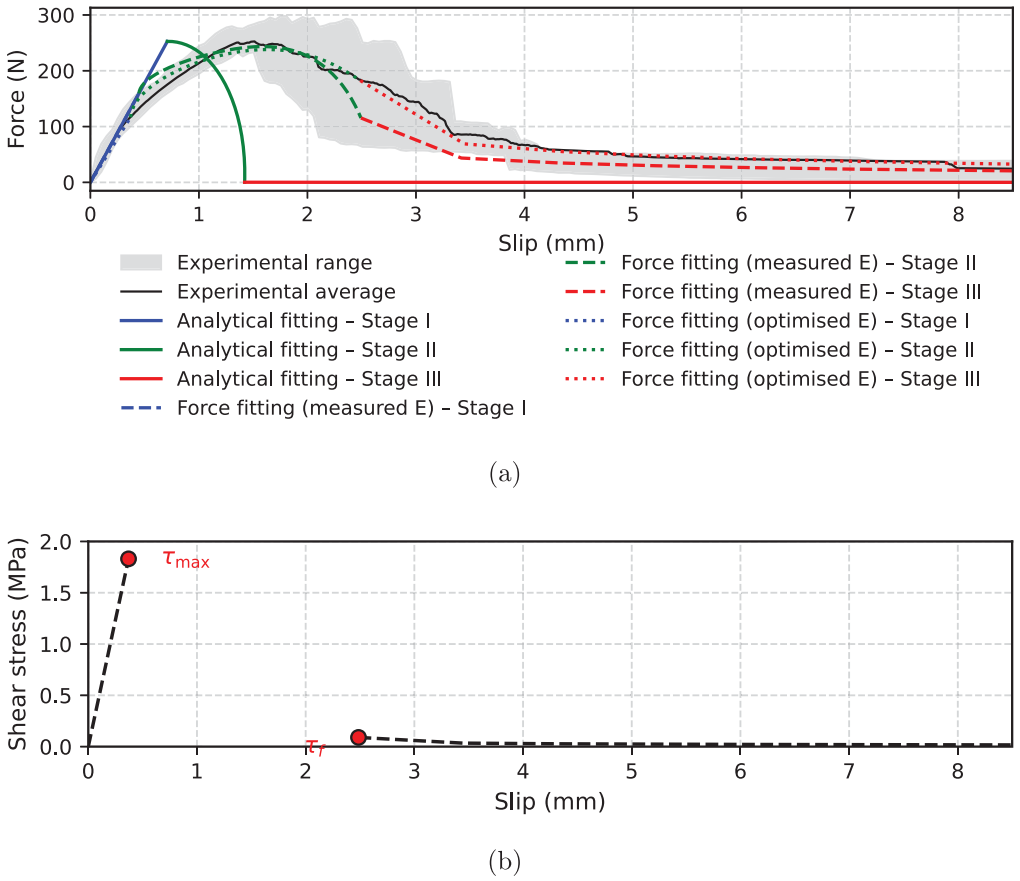


Fig. 17. Fabric pullout testing results analysed using the adapted Naaman model: (a) Experimental and analytical force-slip curves using different fitting methods; (b) Fabric-matrix shear stress-slip relationship for the optimal fit from force-fitting with optimised E_m and E_f, annotated with τ_{max} and τ_f.

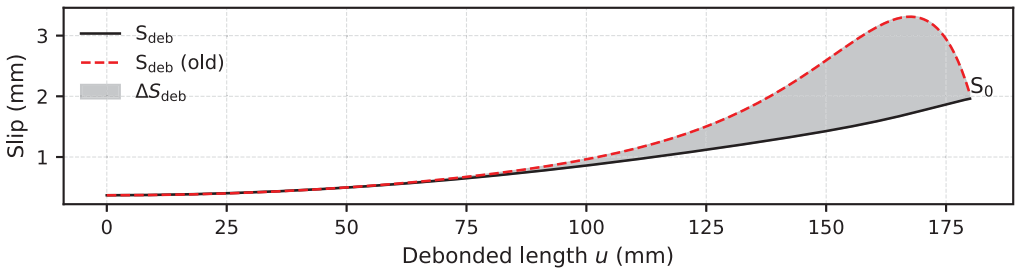


Fig. 18. Comparison of the old and adapted slip in the debonding stage and the residual ΔS_{deb} between them.

4.4. Wad-scale tensile behaviour of FP composite

The representative force–displacement response and the experimental range from FP wad-like dogbone tensile testing are shown in Fig. 19, alongside a reference example of unreinforced POP with the same geometry, which failed at the onset of the first matrix crack. This highlights the role of the hessian in crack bridging and enhancing ductility. The tensile response of FP is divided into three stages based on the failure types observed in the representative response presented, marked in grey, blue, and red, and described as follows.

- **Stage I**: Elastic deformation occurs as loading increases, ending at the first significant drop in the force–displacement relationship, marking the onset of the matrix crack. During this stage, the hessian remains intact, bridging the crack. Previous tests indicate that the fabric-matrix bond shear stress of FP (1.8305 MPa) exceeds the tensile strength of the POP (1.02 MPa), suggesting that matrix failure precedes debonding. No significant failure occurs until the first crack forms.
- **Stage II**: After the first matrix cracking, the hessian limits crack widening through enhanced mechanical interlocking and interfacial friction provided by the twisted yarns. The fabric-matrix bond, which has a higher shear strength than the tensile strength of POP, helps redistribute stresses, leading to multiple matrix cracking (typically 3–5) at different locations, each causing a sharp drop in the force–displacement response. During this stage, major failure types include matrix cracking and fabric-matrix debonding.
- **Stage III**: This stage begins after the final matrix cracking, marking the stabilisation of the crack pattern. As displacement continues to increase, progressive debonding and frictional sliding occur

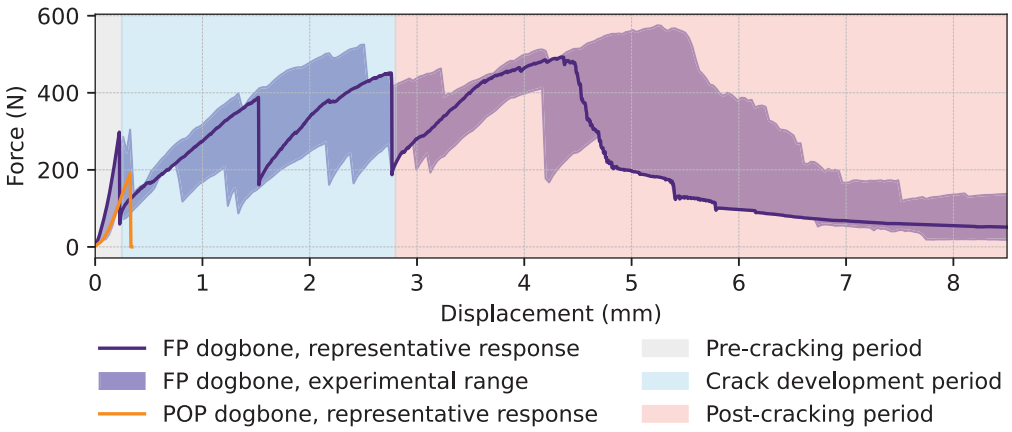


Fig. 19. Representative force–displacement relationship of direct tensile testing on FP and POP wad-like dogbone specimens. (For interpretation of the references to colour in this figure legend, the reader is referred to the web version of this article.)

at the fabric-matrix interface, leading to localised crack widening. Load resistance decreases as the interface gradually weakens, while the fabric continues to sustain force. Consequently, the force–displacement curve reaches a peak before gradually descending rather than showing a sharp drop. This process ultimately results in complete fabric–matrix debonding and fabric rupture, culminating in the specimen's collapse.

The testing process replicates the failure mechanism of the wad in real architectural structures, providing the first insight into FP at the wad scale, particularly concerning its critical tensile behaviour.

The elongation of the specimen's gauge length during the representative test, along with the elongation of each crack region and the onset timing of all cracks, measured using the MatchID Extensometer module in DIC, is shown in Fig. 20(a), while the corresponding crack visualisations are provided in Fig. 20(b). A plateau is observed following the formation of the first two cracks, during which elongation increases at a noticeably slower rate. This behaviour indicates that the twisted hessian remains engaged after cracking. When the second crack forms, the widening of the first crack slows significantly, while the second crack progressively widens before the third crack initiates. This suggests that the twisted hessian effectively bridges the cracks by (1) delaying their widening due to its higher fabric-matrix bond shear strength compared to the tensile strength of the matrix (POP) and (2) facilitating stress redistribution in well-bonded regions, thereby transferring stress from the first to the second crack region. This bridging mechanism promotes multiple cracking events, significantly enhancing the structural ductility of the wad.

The total elongation of all cracks corresponds to the overall gauge elongation in Fig. 20(a). Following the formation of the third crack, a sharp increase in elongation is observed, indicating that the system has reached its load-bearing capacity. The specimen bottom remains stationary, indicating that the cracking behaviour with respect to elongation aligns with the representative force–displacement data in Fig. 19.

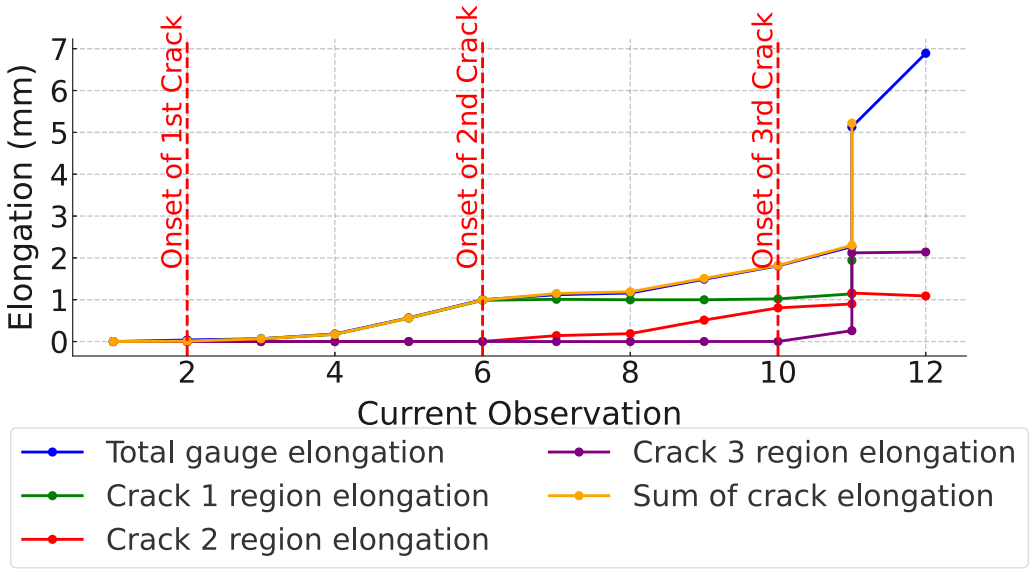
5. Conclusions

This study characterised FP from the constituent to the composite level, examining historic constituent materials and their modern proxies, as well as fabric-matrix bonding and FP composite tensile properties.

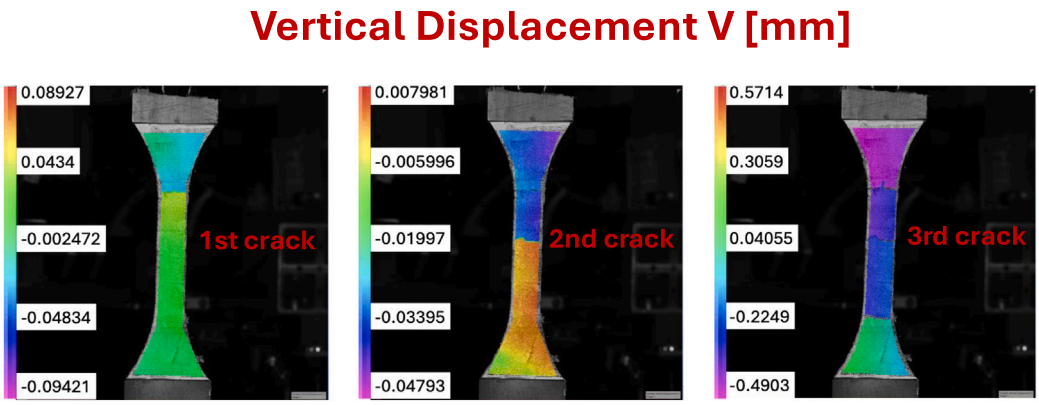
In this paper, modern constituent materials, POP with a specified W/P and hessian with a particular yarn spacing, are used as proxies for historic materials in analytical studies. Historic POP and jute are characterised for the first time using samples sourced from the Grade-II ICE building's FP ceiling. A comparison of the historic and modern constituent materials of FP, through physical, chemical, and mechanical characterisation, reveals that modern materials generally exhibit superior properties, such as higher density, crystallinity, tensile strength of the reinforcement, and stiffness of the matrix material, likely due to environmental degradation that compromises the structural integrity of the historic materials. However, modern constituent materials, owing to their similarities in overall behaviour and composition, have proven to be effective representations of the historic materials for the purposes of this study, providing a viable alternative for characterising historic FP in a controlled and reproducible manner. In this study, historic FP is thoroughly investigated from constituent to composite scale in various aspects using the representative modern materials for the first time.

The static elastic modulus, determined using VFM applied to DIC data from the central region of front and back surfaces of specimen, demonstrates results consistent with the dynamic elastic modulus, thus validating the testing methods. Focusing on the central region of a slender-shaped specimen effectively addresses inaccuracies caused by stress concentrations at the specimen's ends. Averaging measurements from the front and back surfaces helps mitigate errors introduced by misalignment during loading, which could otherwise lead to inaccurate readings. Using VFM to analyse DIC data offers significant advantages over traditional methods, as it directly accounts for the full-field displacement and strain, providing a more precise and spatially resolved measurement of the material's property. This advanced approach ensures the most accurate and consistent measurement of the static elasticity of brittle materials like POP. Compressive and tensile strengths from direct tensile, flexural, and Brazilian splitting tests are reported. A comparison is conducted for the first time on POP, with results from three tensile tests showing that the Brazilian splitting test yields the most reliable tensile strength measurements. This is due to the consistent stress distribution across the large central area of specimens, which makes it less sensitive to localised defects that affect direct tensile and flexural tests.

Fabric pullout tests using a novel clevis-grip pull–pull setup, coupled with slip measurement via DIC, enable precise determination of the experimental force-slip. Averaging slip readings from both sides of the specimen further eliminate errors caused by system movement and tilting. This test setup provides a reliable foundation for analytical fitting using the adapted Naaman's model for characterising fabric-matrix bonding properties in FP. The modified model accounts for the transition from single-fibre reinforcement to woven fabric for the first time. Furthermore, the newly proposed expression for S_{deb}, incorporating a term ΔS_{deb} derived from a careful equation derivation process, addresses the snapback issue observed in previous studies. Unlike traditional methods relying solely on mathematical models, the novel force-fitting method reduces the error between experimental and analytical



(a)



(b)

Fig. 20. Evolution of elongation. (a) Total gauge elongation, elongation at each crack region, their summation, and the onset timing of all cracks. (b) Vertical displacement (mm) for crack visualisations at different stages.

force-slip by iteratively updating model parameters. This approach, incorporating iteratively optimised E_m and E_f, enables the best-fitting with key parameters for describing analytical force-slip behaviour (P_{crit}, S_{crit}, and S_0), thereby providing the most accurate determination of fabric-matrix shear stress throughout the pullout process, with the bond and frictional shear strengths (τ_{max} and τ_f) effectively quantified. The optimised E_m and E_f demonstrate good consistency or explainable difference with the measured values, validating both the elastic modulus measurements and this force-fitting method. This novel methodology, encompassing testing, modelling, and fitting, offers a comprehensive framework for characterising reinforcement-matrix bonding properties in similar composites.

Direct tensile testing on an innovative dogbone specimen effectively characterises the tensile behaviour of FP at the wad scale. The role of hessian in enhancing ductility is initially demonstrated through comparisons with unreinforced POP specimens of the same geometry. Three distinct failure mechanisms are identified. The tensile behaviour aligns with the mechanical properties of POP and the fabric-matrix bonding properties characterised in this study, providing a quantitative explanation for why matrix cracking precedes fabric-matrix debonding. This paper, for the first time, highlights how hessian enhances the ductility of the wad by delaying crack widening in two ways: through crack-bridging and stress redistribution, as clearly demonstrated by DIC elongation measurements at various specimen locations during tensile loading. The results highlight how hessian enhances the structural stability and long-term performance of the historic FP wad.

CRediT authorship contribution statement

Jiaxu Zuo: Writing – review & editing, Writing – original draft, Visualization, Validation, Software, Resources, Methodology, Investigation, Formal analysis, Data curation, Conceptualization. **Sarah Mayfield:** Resources. **Kutsi Akcicek:** Writing – review & editing, Software. **Brian Sheil:** Supervision, Funding acquisition. **James Marrow:** Supervision, Software. **Sinan Acikgoz:** Writing – review & editing, Supervision, Software, Resources, Project administration, Methodology, Investigation, Funding acquisition, Formal analysis.

Funding

The authors would like to acknowledge the generous support of the ICE research and development enabling fund in the development and presentation of this research.

Declaration of competing interest

The authors declare the following financial interests/personal relationships which may be considered as potential competing interests: This research was financially supported by Institution of Civil Engineers (ICE). The authors declare that they have no other conflicts of interest.

Appendix. Equation derivation of adapted naaman's model

The differential equation for the local force F_l is:

$$\frac{d^2F}{ndx^2} - \lambda^2 F = -\frac{\lambda^2 P}{QA_mE_m}, \tag{A.1}$$

where:

$$Q = \left(\frac{1}{nA_fE_f} + \frac{1}{A_mE_m}\right), \tag{A.2}$$

$$\lambda = \sqrt{\kappa\varphi Q}. \tag{A.3}$$

Rearranging gives:

$$\frac{d^2F}{dx^2} - n\lambda^2 F = -n\lambda^2 \frac{P}{QA_mE_m}. \tag{A.4}$$

The homogeneous solution to the corresponding homogeneous equation $\frac{d^2F}{dx^2} - n\lambda^2 F = 0$ is:

$$F_h(x) = Ae^{\sqrt{n}\lambda x} + Be^{-\sqrt{n}\lambda x}. \tag{A.5}$$

The particular solution to the non-homogeneous equation is:

$$F_p(x) = \frac{P}{QA_mE_m}. \tag{A.6}$$

Thus, the general solution is:

$$F(x) = Ae^{\sqrt{n}\lambda x} + Be^{-\sqrt{n}\lambda x} + \frac{P}{QA_mE_m}. \tag{A.7}$$

Given the boundary conditions $F(0) = 0$ and $F(L) = P$, the final expression for $F(x)$ using the values of A and B is:

$$F(x) = \frac{P\sinh\left(\sqrt{n}\lambda x\right)}{\sinh\left(\sqrt{n}\lambda L\right)}\left(1 - \frac{1}{QA_mE_m} + \frac{e^{-\sqrt{n}\lambda L}}{QA_mE_m}\right) - \frac{Pe^{-\sqrt{n}\lambda x}}{QA_mE_m} + \frac{P}{QA_mE_m}, \tag{A.8}$$

where:

$$A = \frac{P\left[\left(1 - \frac{1}{QA_mE_m}\right) + \frac{e^{-\sqrt{n}\lambda L}}{QA_mE_m}\right]}{2\sinh(\sqrt{n}\lambda L)}, \tag{A.9}$$

and

$$B = P\left[-\frac{1}{QA_mE_m}\left(1 + \frac{e^{-\sqrt{n}\lambda L}}{2\sinh(\sqrt{n}\lambda L)}\right) - \frac{\left(1 - \frac{1}{QA_mE_m}\right)}{2\sinh(\sqrt{n}\lambda L)}\right]. \tag{A.10}$$

The corresponding shear stress τ is:

$$\tau = \frac{1}{\varphi}\frac{dF}{dx} = \frac{1}{\varphi}\left(\frac{P(1 - \frac{1}{QA_mE_m} + \frac{e^{-\sqrt{n}\lambda L}}{QA_mE_m})\sqrt{n}\lambda\cosh\left(\sqrt{n}\lambda x\right)}{\sinh\left(\sqrt{n}\lambda L\right)} + \frac{P\sqrt{n}\lambda e^{-\sqrt{n}\lambda x}}{QA_mE_m}\right). \tag{A.11}$$

Data availability

Data will be made available on request.

References

[1] E.M. Payne, The conservation of plaster casts in the nineteenth century, Stud. Conserv. 65 (1) (2020) 37–58, http://dx.doi.org/10.1080/00393630.2019.1610845.

[2] J. Cassar, The Materials Used in 19th and 20th Century Plasters: From Lime and Gypsum To Portland Cement, University of Malta Open Access Repository, 2001, Available: https://www.um.edu.mt/library/oar/handle/123456789/118286.

[3] B. Dams, S. Awang-Ngah, J. Stewart, R. Harrison, M.P. Ansell, M. Harney, R.J. Ball, Load bearing capacity and failure analysis of fibrous plaster wads, Studies in Conservation 70 (1) (2025) 67–87, http://dx.doi.org/10.1080/00393630.2024.2350278.

[4] Historic England, Historic fibrous plaster in the UK: Guidance on its care and management, 2019, Available: https://historicengland.org.uk/advice/technical-advice/buildings/inspection-and-maintenance-of-fibrous-plaster-ceilings/.

[5] S. Awang-Ngah, B. Dams, M.P. Ansell, J. Stewart, R. Hempstead, R.J. Ball, Structural performance of fibrous plaster. Part 1: Physical and mechanical properties of hessian and glass fibre reinforced gypsum composites, Constr. Build. Mater. 259 (2020) 120396, http://dx.doi.org/10.1016/j.conbuildmat.2020.120396.

[6] V. Risdonne, C. Hubbard, V.H. López Borges, C. Theodorakopoulos, Materials and techniques for the coating of nineteenth-century plaster casts: a review of historical sources, Stud. Conserv. 67 (4) (2022) 186–208, http://dx.doi.org/10.1080/00393630.2020.1864896.

[7] W.H. Gourdin, W.D. Kingery, The beginnings of pyrotechnology: Neolithic and Egyptian lime plaster, J. Field Archaeol. 2 (1–2) (1975) 133–150, http://dx.doi.org/10.1179/009346975791491277.

[8] M.T. Freire, A. Santos Silva, M.d.R. Veiga, J. de Brito, Studies in ancient gypsum-based plasters towards their repair: physical and mechanical properties, Constr. Build. Mater. 202 (2019) 319–331, http://dx.doi.org/10.1016/j.conbuildmat.2018.11.037.

[9] S.K. Dalui, M. Roychowdhury, K.K. Phani, Ultrasonic evaluation of gypsum plaster, J. Mater. Sci. 31 (5) (1996) 1261–1263, http://dx.doi.org/10.1007/BF00353105.

[10] P. Coquard, R. Boistelle, L. Amathieu, P. Barriac, Hardness, elasticity modulus and flexion strength of dry-set plaster, J. Mater. Sci. 29 (17) (1994) 4611–4617, http://dx.doi.org/10.1007/BF00376285.

[11] J. Zuo, S. Mayfield, A. Özdemir, J. Marrow, B. Sheil, S. Acikgoz, Preliminary experimental investigation on mechanical properties of historic fibrous plaster, in: Prelim. Exp. Invest. Mech. Prop. Hist. Fibr. Plaster, in: SAHC2023–13th Int. Conf. Struct. Anal. Hist. Constr., 2023, http://dx.doi.org/10.1007/978-3-031-39603-8_24.

[12] A. Majumder, F. Stochino, I. Farina, M. Valdes, F. Fraternali, E. Martinelli, Physical and mechanical characteristics of raw jute fibers, threads and diatons, Constr. Build. Mater. 326 (2022) 126903, http://dx.doi.org/10.1016/j.conbuildmat.2022.126903.

[13] W. Millar, G.P. Bankart, Plastering Plain and Decorative, fourth ed., Routledge/Donhead, London, ISBN: 978-1-873394-87-8, 2010.

[14] G. Vekinis, M.F. Ashby, P.W.R. Beaumont, Plaster of Paris as a model material for brittle porous solids, J. Mater. Sci. 28 (12) (1993) 3221–3227, http://dx.doi.org/10.1007/BF00354239.

[15] Q.L. Yu, H.J.H. Brouwers, Microstructure and mechanical properties of β-hemihydrate produced gypsum: An insight from its hydration process, Constr. Build. Mater. 25 (7) (2011) 3149–3157, http://dx.doi.org/10.1016/j.conbuildmat.2010.12.005.

[16] M.T. Freire, M.R. Veiga, A. Santos Silva, J. de Brito, Restoration of ancient gypsum-based plasters: Design of compatible materials, Cem. Concr. Compos. 120 (2021) 104014, http://dx.doi.org/10.1016/j.cemconcomp.2021.104014.

[17] A.S. Al-Ridha, A.A. Abbood, F.M. Hussein, L.S. Dheyab, E.L.N. Abdullah, E.H.Z. Ali, et al., Effect of chopped sisal fiber (CSF) on enhancing the compressive strength of local plaster of Paris (LPOP), Mater. Today: Proc. 47 (2021) 2575–2579, http://dx.doi.org/10.1016/j.matpr.2021.05.063.

[18] S.M. Chassib, S.K. Zemam, M.J. Madhi, New approach of concrete tensile strength test, Case Stud. Constr. Mater. 12 (2020) e00347, http://dx.doi.org/10.1016/j.cscm.2020.e00347.

[19] W.-C. Liao, P.-S. Chen, C.-W. Hung, S.K. Wagh, An innovative test method for tensile strength of concrete by applying the strut-and-tie methodology, Mater. (Basel) 13 (12) (2020) 2776, http://dx.doi.org/10.3390/ma13122776.

[20] L. Biolzi, S. Cattaneo, G. Rosati, Flexural/tensile strength ratio in rock-like materials, Rock Mech. Rock Eng. 34 (2001) 217–233, http://dx.doi.org/10.1007/s006030170010.

[21] M. Gatuu, A.S. Sanakanan, Effect of porosities on strength of plaster of Paris, 2018, http://hdl.handle.net/2080/2954.

[22] A.S. Ullah, S. Shahinur, H. Haniu, On the mechanical properties and uncertainties of jute yarns, Mater. 10 (5) (2017) 450, http://dx.doi.org/10.3390/ma10050450.

[23] A.E. Naaman, G.G. Namur, J.M. Alwan, H.S. Najm, Fiber pullout and bond slip. I: analytical study, J. Struct. Eng. 117 (9) (1991) 2769–2790, http://dx.doi.org/10.1061/(ASCE)0733-9445(1991)117:9(2769).

[24] A.E. Naaman, G.G. Namur, J.M. Alwan, H.S. Najm, Fiber pullout and bond slip. II: experimental validation, J. Struct. Eng. 117 (9) (1991) 2791–2800, http://dx.doi.org/10.1061/(ASCE)0733-9445(1991)117:9(2791).

[25] A. Dalalbashi, B. Ghiassi, D.V. Oliveira, Textile-to-mortar bond behavior: an analytical study, Constr. Build. Mater. 282 (2021) 122639, http://dx.doi.org/10.1016/j.conbuildmat.2021.122639.
[26] B. Ghiassi, D.V. Oliveira, V. Marques, E. Soares, H. Maljaee, Multi-level characterization of steel reinforced mortars for strengthening of masonry structures, Mater. Des. 110 (2016) 903–913, http://dx.doi.org/10.1016/j.matdes.2016.08.034.
[27] A. Dalalbashi, B. Ghiassi, D.V. Oliveira, A. Freitas, Effect of test setup on the fiber-to-mortar pull-out response in TRM composites: experimental and analytical modeling, Compos. Part B Eng. 143 (2018) 250–268, http://dx.doi.org/10.1016/j.compositesb.2018.02.010.
[28] A. Dalalbashi, B. Ghiassi, D.V. Oliveira, A. Freitas, Fiber-to-mortar bond behavior in TRM composites: effect of embedded length and fiber configuration, Compos. Part B Eng. 152 (2018) 43–57, http://dx.doi.org/10.1016/j.compositesb.2018.06.014.
[29] M. Baena, L. Torres, A. Turon, M. Llorens, C. Barris, Bond behaviour between recycled aggregate concrete and glass fibre reinforced polymer bars, Constr. Build. Mater. 106 (2016) 449–460, http://dx.doi.org/10.1016/j.conbuildmat.2015.12.145.
[30] J. Shannag, R. Brincker, W. Hansen, Pullout behavior of steel fibers from cement-based composites, Cem. Concr. Res. 27 (1997) 925–936, http://dx.doi.org/10.1016/S0008-8846(97)00061-6.
[31] S. Sueki, C. Soranakom, B. Mobasher, A. Peled, Pullout-slip response of fabrics embedded in a cement paste matrix, J. Mater. Civ. Eng. 19 (2007) 718–728, http://dx.doi.org/10.1061/(ASCE)0899-1561(2007)19:9(718).
[32] L. Huang, Y. Chi, L. Xu, P. Chen, A. Zhang, Local bond performance of rebar embedded in steel-polypropylene hybrid fiber reinforced concrete under monotonic and cyclic loading, Constr. Build. Mater. 103 (2016) 77–92, http://dx.doi.org/10.1016/j.conbuildmat.2015.11.040.
[33] Y. Li, J. Bielak, J. Hegger, R. Chudoba, An incremental inverse analysis procedure for identification of bond–slip laws in composites applied to textile reinforced concrete, Compos. Part B: Eng. 137 (2018) 111–122, http://dx.doi.org/10.1016/j.compositesb.2017.11.014.
[34] S. De Santis, F.G. Carozzi, G. de Felice, C. Poggi, Test methods for textile-reinforced mortar systems, Compos. Part B Eng. 127 (2017) 121–132, http://dx.doi.org/10.1016/j.compositesb.2017.03.016.
[35] V.D. Truong, D.J. Kim, A review paper on direct tensile behavior and test methods of textile-reinforced cementitious composites, Compos. Struct. 263 (2021) 113661, http://dx.doi.org/10.1016/j.compstruct.2021.113661.
[36] D. De Domenico, N. Maugeri, P. Longo, G. Ricciardi, G. Gullì, L. Calabrese, Clevis-grip tensile tests on basalt, carbon and steel FRCM systems realized with customized cement-based matrices, J. Compos. Sci. 6 (9) (2022) 275, http://dx.doi.org/10.3390/jcs6090275.
[37] J. Hegger, N. Will, O. Bruckermann, S. Voss, Load–bearing behaviour and simulation of textile-reinforced concrete, Mater. Struct. 39 (2006) 765–776, http://dx.doi.org/10.1617/s11527-005-9039-y.
[38] J. Orlowsky, M. Raupach, Modelling the loss in strength of AR-glass fibres in textile-reinforced concrete, Mater. Struct. 39 (6) (2006) 635–643, http://dx.doi.org/10.1617/s11527-006-9100-5.
[39] J. Orlowsky, M. Raupach, Durability model for AR-glass fibres in textile-reinforced concrete, Mater. Struct. 41 (2008) 1225–1233, http://dx.doi.org/10.1617/s11527-007-9321-2.
[40] T. D'Antino, C.C. Papanicolaou, Comparison between different tensile test set-ups for the mechanical characterization of inorganic-matrix composites, Constr. Build. Mater. 171 (2018) 140–151, http://dx.doi.org/10.1016/j.conbuildmat.2018.03.041.
[41] Industrial Plasters, Fine casting plaster, 2025, Available at: https://industrialplasters.com/products/fine-casting-plaster (Accessed June 2025).
[42] Industrial Plasters, Jute scrim, 2025, Available at: https://industrialplasters.com/products/jute-scrim (Accessed June 2025).
[43] ASTM D3822/D3822M-14, Standard Test Method for Tensile Properties of Single Textile Fibres, ASTM International, 2020.
[44] EN 13279-2, Gypsum Binders and Gypsum Plasters – Test Methods (Part 2), European Committee for Standardization, 2014.
[45] ASTM D1577-07(2018), Standard Test Method for Linear Density of Textile Fibers, ASTM International, 2018.
[46] ASTM D2256/D2256M–19, Standard Test Method for Tensile Properties of Yarns By the Single-Strand Method, ASTM International, 2019.
[47] ASTM E1876–22, Standard Test Method for Dynamic Young's Modulus, Shear Modulus, and Poisson's Ratio By Impulse Excitation of Vibration, ASTM International, 2022.
[48] ASTM C469/C469M–14, Standard Test Method for Static Modulus of Elasticity and Poisson's Ratio of Concrete in Compression, ASTM International, 2014.
[49] International Society for Rock Mechanics, Suggested methods for determining tensile strength of rock materials, Int. J. Rock Mech. Min. Sci. Geomech. Abstr. 15 (3) (1978) 99–103, http://dx.doi.org/10.1016/0148-9062(78)91677-7.
[50] J. Zuo, K. Akcicek, S. Nauriyal, B. Dams, S. Michalik, T. Zillhardt, M. Ansell, R. Ball, G. Burca, B. Sheil, J. Marrow, S. Acikgoz, Tensile failure mechanisms of historic fibrous plaster ceiling wads: experiments at the UK diamond light source, in: Proceedings of the SUBlime Conference 2024, 2024, http://dx.doi.org/10.1051/matecconf/202440304005.
[51] N. Terinte, R. Ibbett, K.C. Schuster, Overview on native cellulose and microcrystalline cellulose I structure studied by X-ray diffraction (WAXD): comparison between measurement techniques, Lenzing. Berichte 89 (1) (2011) 118–131, Available at: https://www.lenzing.com/fileadmin/content/PDF/02_Fasern/Innovation/Overview_on_native_cellulose_and_microcrystalline_cellulose_I_structure.pdf.
[52] D.U. Shah, R.K. Nag, M.J. Clifford, Why do we observe significant differences between measured and 'back-calculated' properties of natural fibres? Cellul. 23 (3) (2016) 1481–1490, http://dx.doi.org/10.1007/s10570-016-0926-x.

Statement of Authorship

Paper title	Constituent and composite level characterisation of fibrous plaster in decorative suspended ceilings
Authors	Jiaxu Zuo, Sarah Mayfield, Kutsi Akcicek, Brian Sheil, James Marrow, Sinan Acikgoz
Publication status	Published
Publication details	Zuo, Jiaxu, et al. "Constituent and composite level characterisation of fibrous plaster in decorative suspended ceilings." Construction and Building Materials 493 (2025): 143035.

Student Confirmation

Student name	Jiaxu Zuo
Contribution to the paper	First-author contribution: • Conceived research objectives • Designed and conducted experiments • Developed and implemented computational models • Prepared and presented the manuscript
Signature	
Date	23th September 2025

Supervisor Confirmation

By signing the Statement of Authorship, the supervisor is certifying that the candidate made a substantial contribution to the publication, and that the description above is accurate.

Supervisor name	Prof. Sinan Acikgoz
Supervisor comments	
Signature	
Date	23th September 2025

Chapter 4

Paper 2: A three-stage approach based on 1D-CNNs for AE source localisation on historic fibrous plaster ceilings

Check for updates

Original Article

Structural Health Monitoring
2025, Vol. 24(2) 1224–1240
© The Author(s) 2024

Article reuse guidelines:
sagepub.com/journals-permissions
DOI: 10.1177/14759217241245309
journals.sagepub.com/home/shm


A three-stage approach based on 1D-CNNs for AE source localisation on historic fibrous plaster ceilings

Jiaxu Zuo[1], Brian Sheil[2] and Sinan Acikgoz[1]

Abstract

Fibrous plaster (FP) ceilings were commonly used in historic buildings throughout the UK during the 19th and 20th centuries. These ceilings are typically supported by hanger elements called wads, which are made of woven jute fabric embedded in plaster of Paris (POP). Recent collapses of several FP ceilings have raised concerns on our ability to detect and localise damage in wads before they fail. To address this issue, we propose a novel acoustic emission (AE)-based system for non-invasive failure detection and localisation. In particular, we develop a three-stage approach that employs 1D convolutional neural networks (1D-CNNs) to analyse AE waveform data produced by pencil-lead break sources for 2D AE source localisation. The approach involves training and fine-tuning four 1D-CNN models with varying architectures, followed by an ensemble learning method to improve localisation accuracy. AE waveform data is recorded using several sensor cluster geometries, with four sensors arranged in a square cluster. Two AE sensor spacing configurations (50 mm and 30 mm) are investigated. The approach also considers the scenario when only three waveforms are available. Experimental results indicate that for input data containing four waveforms, more than 90% of the source location estimations have an error less than 20 mm regardless of the spacing. When only three waveforms are available, 88% of the source location estimations have an error less than 20 mm. The results show that the proposed approach accurately localises source without prior knowledge of wave propagation velocities in the structure. The results are benchmarked with the beamforming method. The proposed approach provides computational simplicity, improved positioning accuracy and fewer constraints related to sensor locations. This approach may facilitate non-invasive damage detection and localisation in the wads of historic FP ceilings by conducting AE measurements on the underside of ceilings. This approach can also be applied to other anisotropic plate-like structures.

Keywords

Acoustic emission, natural fabric-reinforced composite material, plate-like structure, acoustic source localisation, square-shaped sensor clusters, convolutional neural network, fine-tuning, ensemble learning

Introduction

Fibrous plaster (FP) is a natural fabric-reinforced composite material that comprises plaster of Paris (POP) as the matrix material and loosely woven jute fabric layers as the reinforcement material. This material has been widely used for suspended decorative ceilings in many historic buildings throughout the United Kingdom since the late 19th century.[1] Figure 1 presents the typical structure of a historic FP-suspended ceiling that consists of two critical structural components: the ceiling panel and the hangers ('wads'), both of which are made of FP. The ceiling panel is in the form of a laminated composite material, and the cross-section of a historic FP ceiling panel is shown in Figure 2. Large historic FP ceiling panels also feature timber elements that are embedded in the POP matrix. The ceiling panel is suspended from a timber/metal framework located in the ceiling void, which is the space between the structural floor and the ceiling panel, via wads.[2]

Due to limited knowledge of the mechanical properties of FP and the structural behaviour of FP-suspended ceilings, inspections are subjective and error-prone. The current guidance for FP ceiling inspections relies on

[1]Department of Engineering Science, University of Oxford, Oxford, UK
[2]Department of Engineering, University of Cambridge, Cambridge, UK

Corresponding author:
Jiaxu Zuo, Department of Engineering Science, University of Oxford, Parks Road, Oxford, OX1 3PJ, UK.
Email: jiaxu.zuo@eng.ox.ac.uk

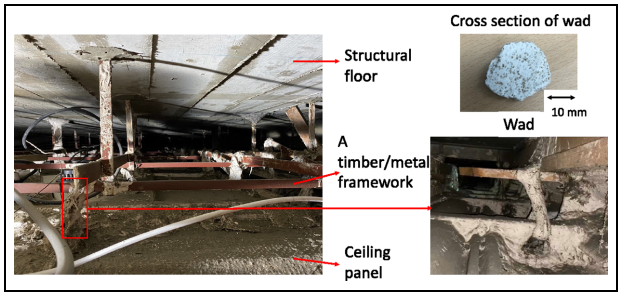


Figure 1. Typical structure of a historic FP-suspended ceiling.
FP, Fibrous plaster.

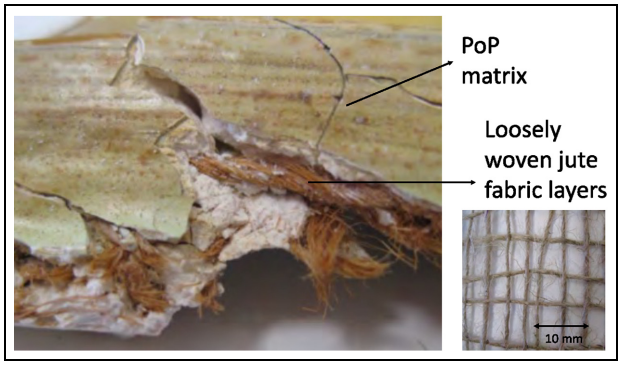


Figure 2. Cross-section of a historic FP ceiling panel.
FP, Fibrous plaster.

periodic visual and tactile assessments performed by experienced inspectors. This method necessitates the creation of access hatches on the ceiling, which can be costly.[3] Recent collapses of several historic FP ceilings in London highlighted the need for more accurate and objective monitoring approaches. Since FP ceiling collapses are often ascribed to failures in the wad elements which are inaccessible from the underside of the ceiling, the monitoring needs to be done remotely. Acoustic emission (AE) techniques have a proven track record in conducting remote damage localisation in anisotropic plate-like structures.[4,5] These techniques facilitate the identification of failure sources through non-destructive means, ensuring that the implementation process does not impose any detrimental effects on the integrity of the original building structures. This article examines a novel application of this approach to historic FP ceilings. The current paper does not differentiate between different failure types but focuses solely on localising the wad where a failure mechanism is generating AE events.

A generic block diagram illustrating an AE-based Structural Health Monitoring (SHM) system for damage source localisation in anisotropic plate-like structures is presented in Figure 3. AE signals produced by the rapid release of energy from microscopic failures can be acquired in situ. The recorded signals are used to estimate the location of the failure source using an array of sensors placed at the surface of the structure, with varying distances to the failure source, which can detect the respective AE waveform at different times.[6,7] The subsequent damage assessment and maintenance are also depicted, but are outside the scope this article and will not be explained in detail. With regards to localisation on homogeneous materials, the measured difference in the time-of-arrival (TOA) of AE signals can be converted directly into the distance between the sensor and the damage source due to the constant AE wave propagation velocity.[8] However, source localisation for historic FP ceiling panels remains a key challenge in practical applications. The TOA-based conventional methods are not suitable for the historic FP-suspended ceilings since the AE wave propagation is strongly influenced by anisotropy.[7] The direction- and location-dependent wave velocities are infeasible to measure due to the size and geometric complexity and variation of the composite structure.[9] Therefore, there is a need for a method that can be used for source localisation in historic FP ceiling panels that does not utilise the wave propagation properties of the structure.

Many methods have been proposed to improve the accuracy of the source localisation in anisotropic structures, as summarised in a recent review.[8] The time difference of arrival (TDOA) methods are popular in localising AE sources without pre-measuring wave velocities.[10,11] One specific technique in source localisation of plate-like structures is called the sensor cluster technique. This technique is mostly used by the beamforming method proposed by Kundu et al.[12] This method assumes that the velocities of the waves propagating from the source to the sensors are all the same due to the nature of the sensor cluster. Therefore, it does not require the wave propagation properties of anisotropic materials. The beamforming theory estimates wave incidence angles based on the geometry of sensor cluster placement. As shown in Figure 4, a classic L-shaped sensor cluster consisting of three receiving sensors (S1, S2 and S3) is placed on a plate-like structure. This is based on the understanding that three sensors represent the minimum number required for achieving two-dimensional AE event source localisation. The method assumes that the wave has a straight propagation path from the AE source to the sensor cluster. It can be assumed that the wave velocity of the straight path connecting the AE source to each sensor is approximately the same since the sensor spacing d is much smaller than the distance between the AE source and the nearest sensor D, resulting in similar signals with a slight time offset. The time offset can be used to determine the TDOA, which is the time it takes for the wavefront propagating from the source to reach sensors S2 and S3 after reaching S1. The results, denoted

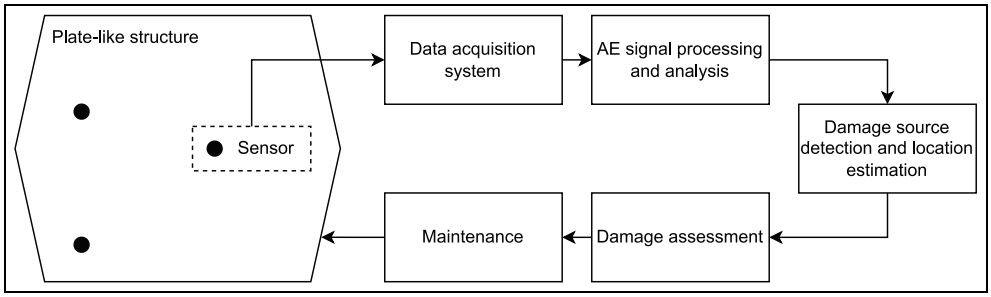


Figure 3. Block diagram of an AE-based SHM system for damage source localisation of plate-like structures.
AE, acoustic emission; SHM, Structural Health Monitoring.

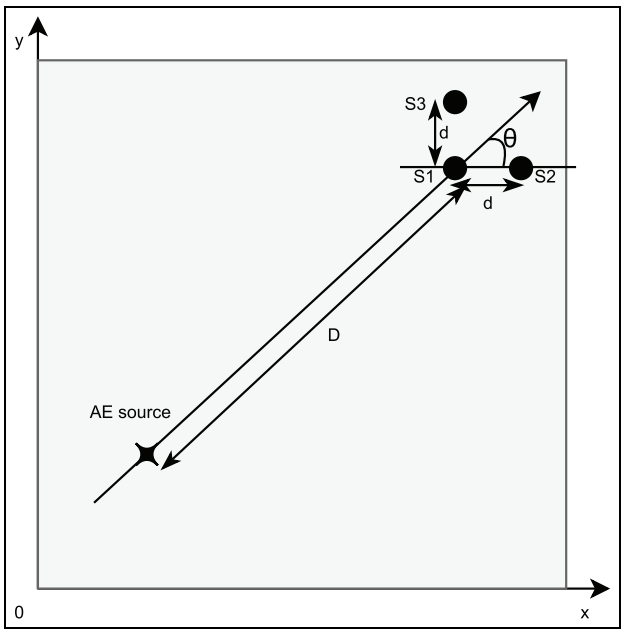


Figure 4. Basic L-shaped sensor cluster for TDOA-based beamforming technique.
AE, acoustic emission; TDOA, time difference of arrival.

as δt_{12} and δt_{13}, can be derived as $d\cos(\theta_1)/c(\theta)$ and $d\sin(\theta_1)/c(\theta)$, respectively, where $c(\theta)$ represents the wave velocity in the θ direction. The wave incidence angle θ can be obtained without requiring any information on the wave propagation velocity. This angle can be expressed as $\tan^{-1}(\delta t_{13}/\delta t_{12})$. In many studies, multiple sensor clusters are used to estimate AE source locations in anisotropic plate-like structures based on beamforming theory, owing to its computational simplicity and high accuracy.[13–19] However, the beamforming method has some disadvantages. The accuracy of the source localisation largely depends on the accuracy of the TDOA measured from the AE waveform recorded by the sensor cluster. This TDOA is used to estimate the wave incidence angle at a specific location on the plate-like structure.[20] This wave incidence angle may deviate notably from the actual wave incidence angle, leading to significant errors in the source location estimation.

Several approaches have been developed to enhance the accuracy of source localisation. Nakatani et al.[20] proposed a method for localising sources on anisotropic flat plates using two L-shaped sensor clusters. Only the initial part of the AE waveform signal is extracted to improve the accuracy of the TDOA measurement. This method has high accuracy in estimating source locations, and the direction error is limited to within $+10°$. However, the approach relies heavily on the accurate identification of first arrival waves, which is either done manually or by using arrival time detection algorithms such as the Akaike information criterion method.[21] Wavefront shape-based methods estimate source location using techniques such as time-delay estimation and direction-of-arrival estimation.[14,22,23] This method assumes that the AE wavefront propagates in a specific way, such as a spherical wave or a cylindrical wave. Sen et al.[14] used a wavefront shape-based approach by applying a square sensor cluster consisting of four L-shaped sensor clusters to improve the accuracy of source localisation. However, the signal processing required to estimate the direction of arrival can be computationally intensive, resulting in longer processing times and greater computing resource requirements. Furthermore, in practical environments, the wavefront may not obey the assumption that the AE wavefront propagates as a spherical or cylindrical wave, which leads to errors in the estimation of the source location. Neural network techniques have also been employed to improve the accuracy of source localisation using sensor clusters.[24–26] Fu et al.[27] applied the square-shaped sensor cluster for the source localisation on the plate-like anisotropic structure by establishing a neural network model. The model takes the measured TDOA as input data and the coordinates of damage sources as labels. The results report high accuracy. However, TDOA measurements based on the obtained group velocity distribution in composite materials are not suitable for

practical situations. The velocities can be measured experimentally for specific test objects but are generally not applicable to other structures. Any method that requires knowledge of the wave propagation properties in a plate-like anisotropic structure may, therefore, be of limited practical use.

The sensor cluster technique could be an appealing option for source localisation in historic FP-suspended ceilings. However, accurately and automatically extracting the information present in the AE waveform recorded by the sensor cluster can be challenging and requires novel methods. It has been reported that one-dimensional convolutional neural networks (1D-CNNs) can automatically extract features from AE waveform data and can be directly trained using such one-dimensional time-series signals.[28] Therefore, one possible approach to extract information from the AE waveform is to use 1D-CNNs.

This study presents a novel approach to AE source localisation, using 1D-CNNs to accurately estimate the locations of AE sources on historic FP ceiling panels. To achieve this, a square-shaped sensor cluster is used to record AE waveform data, and the 1D-CNN is used to estimate the source location directly using the AE waveform data without requiring any prior knowledge of wave propagation properties or TDOA measurements. A three-stage approach is proposed for achieving the objective. In stage I, a large amount of data is used to train four 1D-CNN models with different dropout layer implementations. In stage II, the trained models are fine-tuned using a smaller dataset from a new test object, in this case, a historic FP ceiling panel, to make the models adaptable to new test objects and able to perform AE source localisation using a limited amount of data and a short duration of fine-tuning. This historic FP ceiling panel is considered a new test object in practice, and the fine-tuning process is carried out for each new test object. In stage III, an ensemble learning approach is used to combine the localisation results provided by the fine-tuned models, which can significantly improve the localisation accuracy. 1D-CNN models take AE waveform data as input, and the corresponding AE source coordinates as labels. The results are benchmarked using the established TDOA-based beamforming method, which also uses sensor clusters.

The article is organised as follows: It commences with a brief introduction that presents an overview of the methodologies employed, including the data acquisition system and signal processing. This is followed by a detailed description of the designed CNN architectures and the different implementation details, along with an overview of the three-stage approach for establishing 1D-CNN models. The subsequent section describes the experimental setup utilised for AE waveform data collection, followed by the results obtained for AE source localisation in historic FP ceiling panels using the developed 1D-CNN-based method. Finally, a comprehensive assessment of the performance of the developed 1D-CNN method is presented.

Methodology

A block diagram illustrating the steps involved in developing the AE source localisation method, including data acquisition, signal processing and the implementation of a 1D-CNN architecture, is shown in Figure 5.

Data acquisition system and test configuration

The system is designed with four AE sensors denoted as S1, S2, S3, S4 arranged in a square configuration, mounted at the centre of a square-shaped monitoring area of a plate-like test object. Pencil-lead break sources are generated at pre-determined coordinates. Each sensor receives a single raw AE waveform generated by the pencil-lead break source. For a given pencil-lead break, each of the four sensors records a voltage waveform containing 4096 waveform data points at a data collection frequency of 2 million samples per second, as shown in Figure 6.

Three distinct configurations for testing are devised, as shown in Table 1. The sensor layout of configurations (a) and (b) are shown in Figure 7. Configuration (a) is the default configuration. Configuration (b) investigates the influence of sensor spacing on the accuracy of the proposed method. The selection of specific configurations involving the utilisation of a sensor cluster with 30 and 50 mm spacing of AE sensors is grounded in the prior work referenced within the paper,[12] which examined sensor spacings of 15, 30 and 50 mm. As shown in Figure 4, the study concluded that reducing the ratio of sensor cluster spacing d to the distance D between the acoustic source and the sensor cluster contributes to improved localisation accuracy. This enhancement can be attributed to a fundamental assumption of the localisation technique, where the lines connecting the acoustic source point to distinct sensors within the cluster exhibit a nearly parallel alignment, a condition met when d/D ratios are low. However, in this study, due to the sensor dimensions (with a diameter of 19 mm), it is impossible to achieve a sensor spacing of 15 mm. Consequently, the 30- and 50-mm configurations were selected. The input data for configuration (c) is generated by randomly dropping one waveform collected by one sensor for each pencil-lead break source using the dataset from the default configuration (a) using the same sensor layout. This configuration

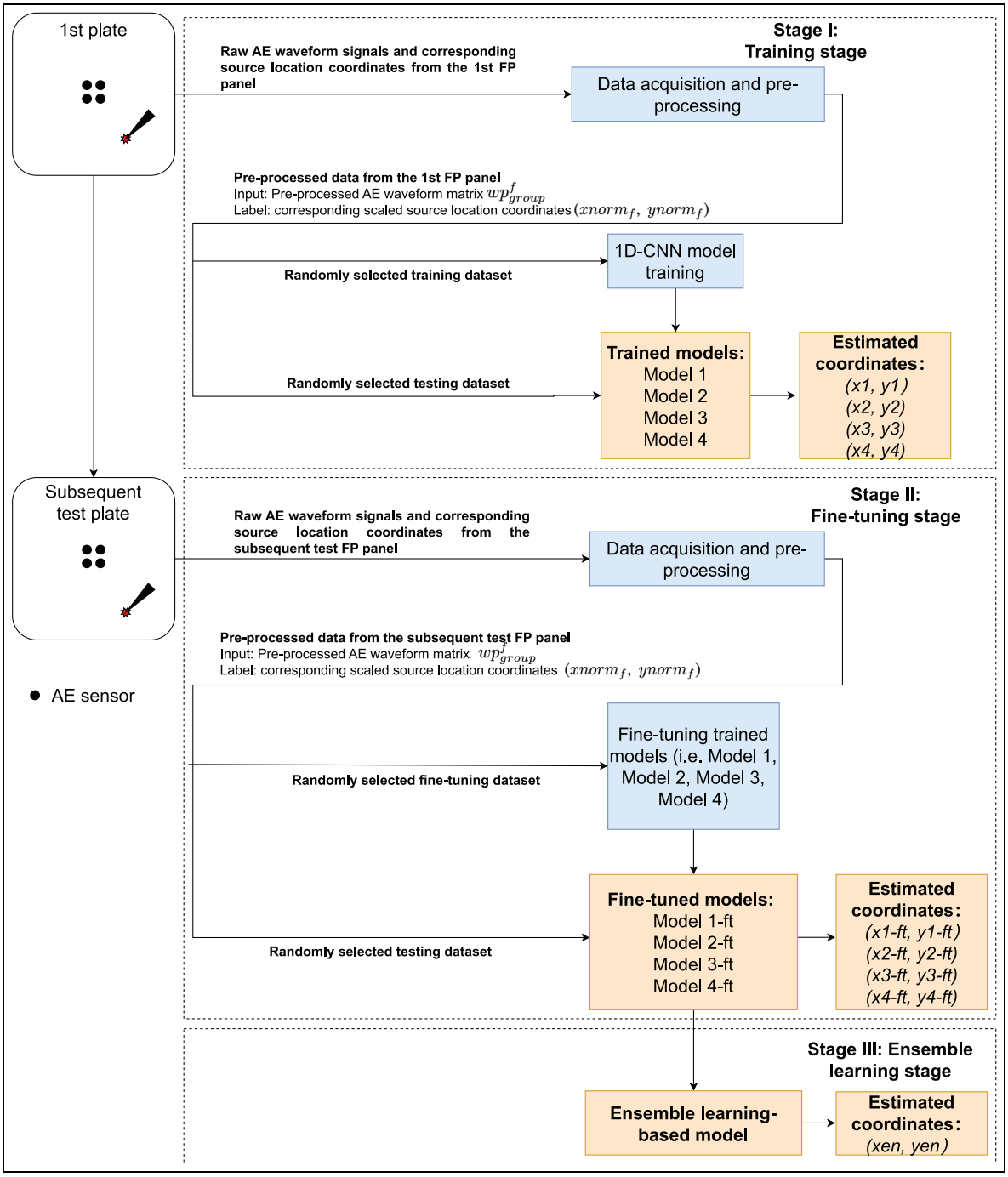


Figure 5. Block diagram of the steps involved in developing the AE source localisation method.
AE, acoustic emission.

considers the scenario when one waveform is not recorded, which can happen due to sensor malfunction.

AE signal processing

All raw AE waveform data generated by the same pencil-lead break source is synchronised and then organised into a 4×4096 matrix. Each matrix is normalised using L2 normalisation, also known as Euclidean normalisation. This ensures that the norm of the normalised vector or matrix is equal to 1, and the matrix is more comparable to other matrices with different scales or magnitudes.

Only the initial portion of each waveform up to the peak amplitude (PA) − is selected for learning (see Figure 8). This initial portion of the signal, during its

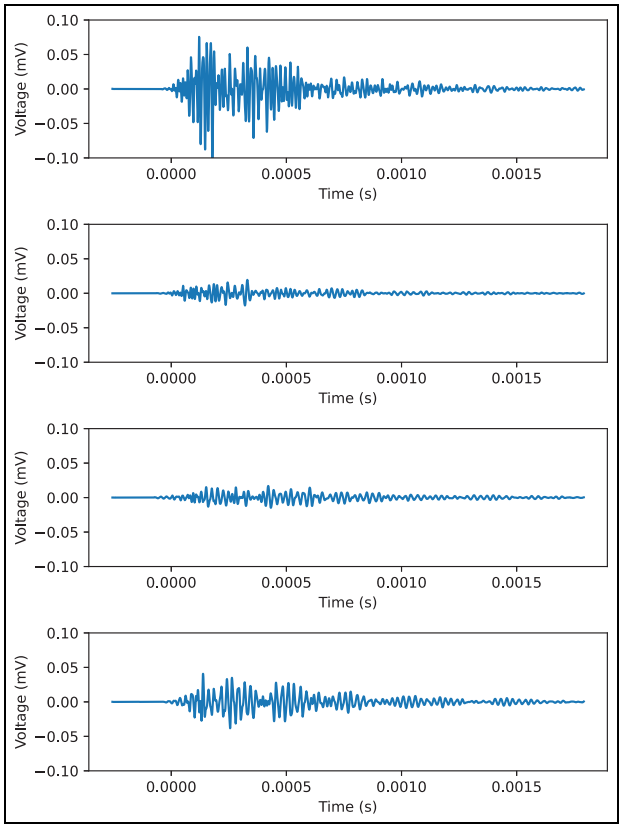


Figure 6. Raw single AE waveform signals generated by one pencil-lead break source recorded by sensors S1, S2, S3, S4 of the square-shaped sensor cluster of default configuration.
AE, acoustic emission.

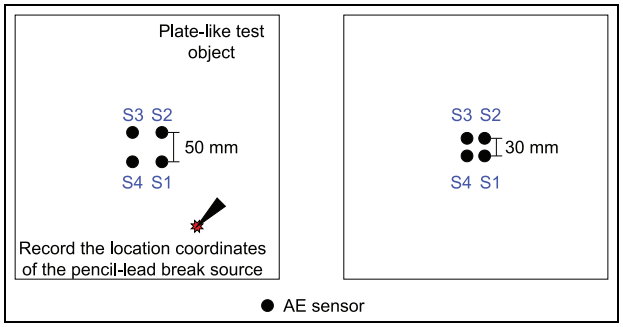


Figure 7. Square-shaped AE sensor clusters with 50 mm for configuration (a) (left) and 30 mm for configuration (b) (right) sensor spacing mounted on a plate-like test object.
AE, acoustic emission.

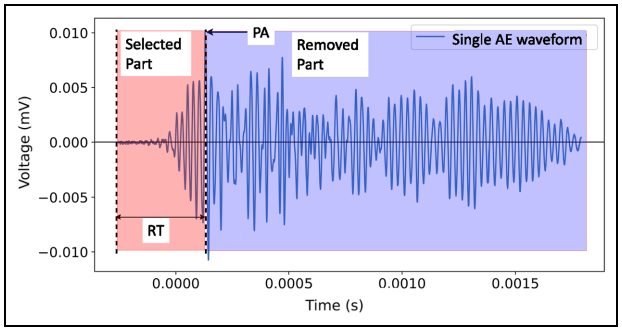


Figure 8. A typical AE waveform with a description of peak amplitude (PA) and rise time (RT).
AE, acoustic emission.

Table 1. Test configurations.

Configuration	Sensor spacing (mm)	Number of waveform signals
(a)	50	4
(b)	30	4
(c)	50	3

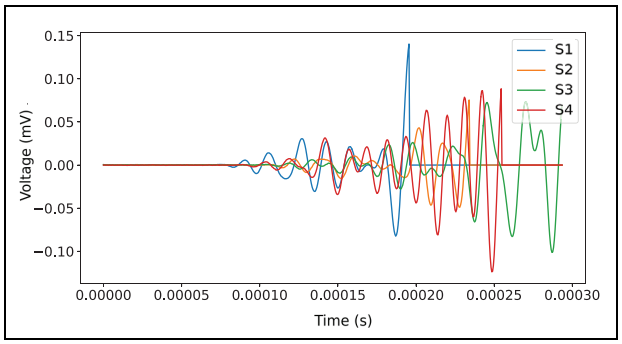


Figure 9. Pre-processed AE waveform signals generated by one pencil-lead break source recorded by sensor S1, S2, S3, S4 of the square-shaped sensor cluster of default configuration.
AE, acoustic emission.

rise time (RT)', − records the Lamb wave. Lamb wave is a type of ultrasonic guided wave that propagates through the plate-like structures and is not significantly affected by reflections from other sensors or the edge of the plate.[20] This truncation results in waveform lengths less than 4096. The waveforms are then zero-padded back to a length of 4096 to achieve consistency between input signals.

Figure 9 displays an example of a waveform matrix composed of four pre-processed AE waveform signals following a pencil-lead break event. The matrix featuring the pre-processed AE waveform signals is denoted as wp^{f}_{group}, where f is the AE source index. The coordinates of the corresponding pencil-lead break sources are scaled to a range between 0 and 1 and used as the output label for the 1D-CNN model learning. The normalised coordinate of the pencil-lead break source is denoted as $(x\text{norm}_f, y\text{norm}_f)$. wp^{f}_{group} and

$(x\text{norm}_f, y\text{norm}_f)$ are subsequently used as input and label for the subsequent 1D-CNN models, respectively.

CNN architecture and implementation details

CNN architecture. The CNN architecture used in this study is presented in Figure 10 with implementation details listed in Table 2. The model consists of four one-dimensional convolutional layers, each followed by a max pooling layer, and two fully connected layers. The convolutional layers have a kernel size of 5 and a stride of 1. The first, second, third and fourth convolutional layers (1DCONV1-1DCONV4) have output channel sizes of 32, 64, 128 and 256, respectively. Each max pooling layer (MP1 to MP4) has a kernel size of 2 and a stride of 2. The first fully connected layer (FC1) uses ReLU activation functions, while the second fully connected layer (FC2) uses Sigmoid activation functions since the target output values (i.e. normlised coordinates X and Y) are in the range of 0–1. The optimiser used is Adaptive Moment Estimation (ADAM), with an initial learning rate of 0.00075 and a cosine annealing scheduler, while the loss measure used is the Mean Squared Error (MSE).

Dropout layer implementation. Dropout is a regularisation technique to prevent over-fitting in neural networks. It randomly drops out − by setting the corresponding weights to 0 − neurons in the network during training with a probability of p. This exercise forces the network to learn more robust features and reduces its dependence on specific input features.

Different dropout layer implementations can introduce diversity in CNN models during ensemble learning. Ensemble learning involves aggregating predictions from different models. By combining predictions from 1D-CNN models with different dropout layer implementations, the overall predictive performance can be improved by reducing generalisation errors. It can also help to identify the strengths and weaknesses of each model and combine them in a way that maximises their benefits and minimises their drawbacks.

For the purpose of subsequent ensemble learning, four CNN models were trained using different dropout layer implementations, outlined in Table 3.

D-CNN models

To develop 1D-CNN models for AE source localisation that can be applied to various historic FP ceiling

Table 2. Designed CNN architecture.

Layer type	Input size	Output size	Filter height	Stride
1DCONV1	4 × 4096	32 × 4092	5	1
MP1	32 × 4092	32 × 2046	2	2
DCONV2	32 × 2046	64 × 2042	5	1
MP2	64 × 2042	64 × 1021	2	2
DCONV3	64 × 1021	128 × 1017	5	1
MP3	128 × 1017	128 × 508	2	2
DCONV4	128 × 508	256 × 504	5	1
MP4	256 × 504	256 × 252	2	2
FC1	256 × 252	1000	–	
FC2	1000	2	–	

CNN, convolutional neural networks.

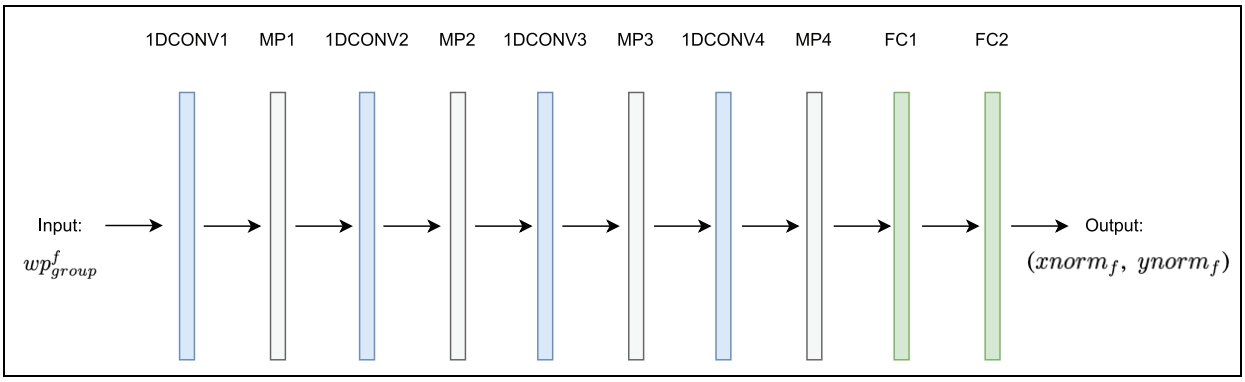


Figure 10. Adopted 1D CNN architecture.
1D CNN, 1D convolutional neural networks.

Table 3. Dropout layer implementations for different independent 1D-CNN models.

CNN model	Layer with the dropout layer applied	Dropout probability p
Model 1	FC2	0.3
Model 2	FC1	0.3
Model 3	FC1	0.5
Model 4	FC1	0.1

1D CNN, 1D convolutional neural networks.

panels, this study utilises two plate-like test objects, both of which are historic FP ceiling panels from the same site. The first FP panel is employed in stage I, where a large amount of data is recorded and used to train 1D-CNN models. The subsequent test FP panel is utilised in Stages II and III, where a small amount of data is collected to fine-tune the models trained in stage I and perform ensemble learning, respectively.

The use of two test objects allows for the assessment of the models' adaptability to new testing scenarios and the evaluation of the effectiveness of the proposed three-stage approach. The subsequent test object simulates a new area for monitoring, obtained from the same site as the first panel. The fine-tuned models and ensemble learning analysis are evaluated based on their ability to accurately localise AE sources on the subsequent test object, using a limited amount of data. This evaluation holds great practical significance for non-destructive testing applications.

For each site-specific application, stage I only needs to be conducted once on a randomly selected area of the monitored FP ceiling site. Stages II and III are required to be conducted for any new area of the site that needs monitoring, where a small dataset must be acquired for fine-tuning the model trained in the first stage.

Stage I: Training stage. During the training stage, the 1D-CNN models take wp^f group and $(xnormf, y_{normf})$ from the first FP panel as input and label, respectively. Four 1D-CNN models, Model 1, Model 2, Model 3, Model 4, with the mentioned architecture and dropout layer implementations, were trained independently. The estimated coordinates given by Model 1, Model 2, Model 3, Model 4 are denoted as *(x1, y1), (x2, y2), (x3, y3), (x4, y4)*, respectively. The estimation error is calculated by finding the difference between the recorded and the estimated coordinates, which can be denoted as Err_{pre}. The total number of epochs during training is 150. The batch size for training is 1.

Stage II: Fine-tuning. In the fine-tuning stage, the 1D-CNN models trained with weights from stage I are adopted for additional training with a small dataset containing wp^f group and $(x\mathrm{norm}_f, y_{\mathrm{norm}_f})$ from the subsequent test FP panel. The idea is to allow the trained models from the previous stage to learn task-specific features that are important for each new test object while still retaining the knowledge learned from the original dataset. The total number of epochs during training is 50, and the batch size is again 1. Using a smaller dataset and epoch number for fine-tuning the new object can help reduce the computational cost and time required for fine-tuning the model. However, it is important to ensure that the smaller dataset is representative of the new object and contains enough information for the model to learn meaningful features.

During this stage, the first two convolutional layers of the model are frozen, whereas the weights of other layers are updated to better capture the subsequent test panel data while training. The optimiser and loss functions remain unchanged. The estimated coordinates given by Model 1-ft, Model 2-ft, Model 3-ft, Model 4-ft are denoted as *(x1-ft, y1-ft), (x2-ft, y2-ft), (x3-ft, y3-ft), (x4-ft, y4-ft)*, respectively. The performance of the fine-tuned models from this stage is evaluated by calculating the difference between the recorded and estimated coordinates using a new dataset from the same test object for the fine-tuning, represented as $\mathrm{Err}_{\mathrm{ft}}$.

Stage III: ensemble learning. As a final refinement, estimations of the source location provided by the four distinct fine-tuned CNN models are subsequently combined. This approach seeks to harness the collective insights of these models for enhanced accuracy. Specifically, the two most proximate predictions of coordinates are averaged, leading to the computation of the final estimated coordinates, denoted as (*xen*, *yen*). To gauge the accuracy of the ensemble learning's final estimation, the disparity between the recorded coordinates and the estimated ones is computed, presenting itself as the quantified error $\mathrm{Err}_{\mathrm{el}}$.

Experiment

Test objects

Initially, AE data was collected from a POP (i.e. the matrix material of the FP) plate to train the aforementioned 1D-CNN models. This was done to ensure that the method could first be applied to simple homogeneous materials before moving on to complex anisotropic FP structures. 1D-CNN Model 1 and the default test configuration (a square-shaped sensor cluster with a sensor spacing distance of 50 mm) were employed. In this experiment, a total of 200 groups of data were collected from a POP plate-like test object, out of which 130 groups (65%) were used for training, 20 groups

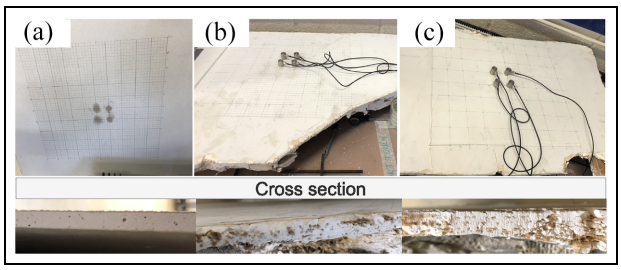


Figure 11. Plate-like test objects and cross sections of (a) POP plate, (b) the first historic FP panel, and (c) the subsequent test historic FP panel.
FP, Fibrous plaster; POP, plaster of Paris.

(10%) were used for validation during the training process for each epoch, and 50 (25%) groups were used for testing.

Two historic FP ceiling panels, sourced from the Great Stairs of the Institution of Civil Engineers (ICE) building (constructed in 1912), were then used for the data collection. These historical ceiling samples, originally intended for replacement in the ICE building, have been repurposed for controlled laboratory data collection. AE data produced by pencil-lead break sources, along with the corresponding source location coordinates, are collected to establish 1D-CNNs based on the three-stage approach. The dataset used for training stage from the first FP panel consisted of 252 groups of effective data. Out of these, 172 groups (68%) were randomly selected for training, 30 groups (12%) for validation and 50 groups ((20%)) for the test dataset. The validation data was used to monitor the model's improvement at each epoch, while the testing data was used to evaluate the performance of the models after they were trained. The dataset used for fine-tuning stage consisted of 149 groups of effective data collected from the subsequent test FP panel, of which 79 groups (53%) were randomly selected for training, 20 groups ((13%)) for validation, and 50 groups ((34%)) were used for testing. The same dataset is used for training, validation and testing for all four models, both during the training stage and the fine-tuning stage.

Figure 11 provides a visual representation of the test objects, including their cross-sectional views. The POP plate has a thickness of 10 mm, while the historic FP panels have a thickness ranging from 8 mm to 20 mm, excluding the timber laths. The timber laths are embedded inside with a thickness of around 40 mm. The historic FP panels are acquired through random selections from the onsite location. Their approximate dimensions are comprehensively detailed in Table 4.

Experimental setup

The experimental setup, as illustrated in Figure 12, consists of a Mistras system consisting of a 40 dB external amplifier, a four-channel PCI-2 AE data acquisition system, and four narrowband resonant AE sensors of model type R6a. The recorded signals are thresholded at 40 dB to eliminate noise. The 'AEwin' software is used to control the data acquisition process. A frequency band filter ranging from 35 to 100 kHz is used to filter the collected signal due to the low frequency of the AE signal generated by the plaster materials.

The square-shaped sensor cluster is mounted onto the surface of the test object, with a thin layer of grease applied in between to act as a coupling agent and improve the transfer of ultrasonic energy between the AE sensors and the surface of the test object. This allows for complete removal without causing lasting damage or alterations. For each test object, a flat 450 mm $\times$ 450 mm area was monitored. Since a threshold value of 40 dB is utilised, it means that if the AE signal released by an event exceeds this threshold value, the AE sensor can detect the event. If all four AE sensors in a sensor cluster detect the event, the AE cluster can localise the event source based on the received signal group. The attenuation curve indicates that the maximum detection distance for FP is approximately 1.5 m. Considering the geometry that the side length of a square is $\sqrt{2}/2$ times the length of the diagonal, a maximum detection area of approximately 2 m-by-2 m is achievable. Pencil-lead break sources were randomly distributed across the entire monitoring area to ensure full coverage. Within the framework of the 50 mm sensor spacing configuration, AE sensors labelled 1–4 are strategically positioned at the following coordinates: (200, 200), (200, 250), (250, 250), and (250, 200). Correspondingly, in the context of the 30 mm sensor spacing configuration, AE sensors, each

Table 4. Test object description.

Test object	Material	Source	Area dimensions (m)	Purpose
POP Plate	POP	–	1 $\times$ 1	Validation with a simple homogeneous material
First FP Panel	historic FP	ICE Building, 1912	1 $\times$ 1	Stage I: Training
Second FP Panel	historic FP	ICE Building, 1912	0.8 $\times$ 1.2	Stages II and III: Fine-tuning and Ensemble learning

FP, Fibrous plaster.

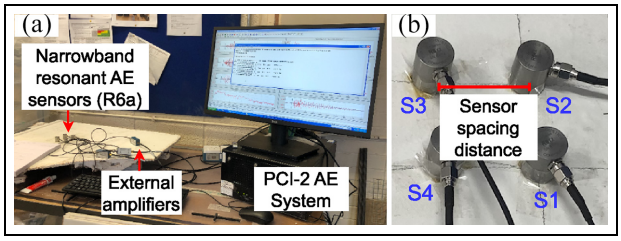


Figure 12. Experimental setup: (a) Measuring system and (b) square-shaped sensor cluster.

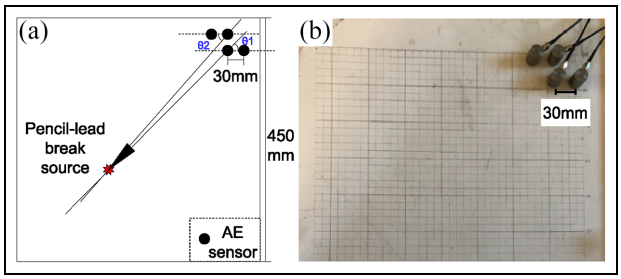


Figure 13. Z-shaped sensor cluster for TDOA-based beamforming method testing (a) schematic description, (b) experimental setup.
TDOA, time difference of arrival.

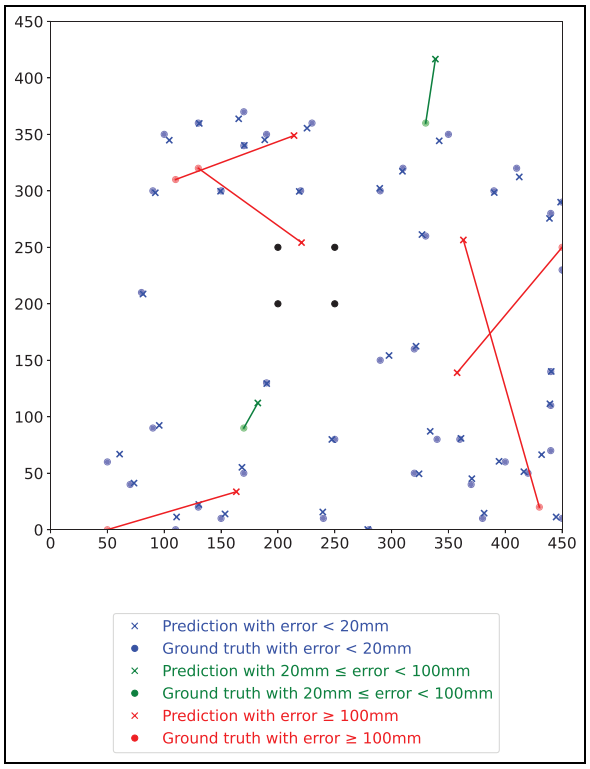


Figure 14. Exemplar AE source localisation results for the POP plate using 1D-CNN model Model 1, axis labels in units of mm.
1D-CNN, 1D convolutional neural networks; AE, acoustic emission; POP, plaster of Paris; TDOA, time difference of arrival.

designated as 1–4, are positioned at the coordinates (210, 210), (210, 240), (240, 240) and (240, 210), respectively. In the process of generating pencil-lead break sources, random x and y coordinates are selected within the range spanning from 0 to 450. However, meticulous measures are undertaken to ensure that these sources are deliberately placed outside the confines of the sensor cluster. All measurements are in millimetres.

To benchmark the 1D-CNNs predictions, the TDOA-based beamforming method is also tested on a historic FP panel (first FP panel) using a well-established Z-shaped cluster,[19] as shown in Figure 13. Two incidence angles, θ_1 and θ_2, were identified using the two L-shaped sensor clusters contained in the Z-shaped sensor cluster. It should be noted that the paper that proposed this method[19] used two Z-shaped sensor clusters positioned far apart for AE source localisation. However, in this study, a single Z-shaped sensor cluster was repeatedly used by placing it in two different locations to assess accuracy. Pencil-lead break sources were generated at the same positions for both scenarios. The initial part of the recorded signal was extracted manually, and the time shift was then determined using the cross-correlation method on the extracted waves as described in Nakatani et al.[20]

Accuracy of recorded source locations

Uncertainties. During the data collection process, the accuracy of the AE source location coordinates was affected by two factors. Firstly, a grid was manually drawn on the test object for assessing multiple AE sources, which may introduce an error of ±1 mm. Secondly, small variations in sensor positioning can occur (up to ±1 mm).

Accuracy thresholds for AE source localisation by 1D-CNNs. The 1D-CNNs used for AE source localisation have three accuracy thresholds: <20 mm for high accuracy, 20–100 mm for acceptable accuracy, and >100 mm for unacceptable accuracy. The 20 mm threshold was chosen as wads typically have diameters between 20 and 30 mm.

Results and discussion

Source localisation results on POP plate using 1D-CNN

The results of the AE source localisation are presented in Figure 14. The lines connect the predicted source location to the ground truth values, with different colours indicating the level of accuracy. Blue, green and red lines represent high, acceptable and unacceptable

Table 5. AE source location error distribution on the POP plate.

Error range (mm)	Percentage
<20	0.86
20–100	0.04
>100	0.1

AE, acoustic emission; POP, plaster of Paris.

accuracies, respectively. The percentage distribution of accuracy levels is summarised in Table 5. Out of the 50 test data groups, 96% had high to acceptable accuracy, indicating the good performance of the 1D-CNN method for simple homogeneous materials.

Source localisation for FP plate using 1D-CNN method: training stage

The results demonstrate the effectiveness of trained 1D-CNN models in AE source location estimation in FP plates. For the default configuration (i.e. four waveforms with a spacing of 50 mm), over 85% of the data had an error of estimation less than 20 mm, with only a few data points (<6%) predicted with an unacceptable error (>100 mm). The test results provided by all four trained 1D-CNN models at this stage are visualised in Figure 15. The corresponding error distributions are summarised in Table 6.

The subsequent test FP panel tests the source localisation performance of the trained 1D-CNN models on AE data from a different FP structure. The results showed that trained models used directly to estimate the source location can yield unacceptable accuracy, with only 20%–30% of the data having an error of estimation <20 mm, and most of the data estimated with large unacceptable errors exceeding 100 mm. For brevity, the results of this part are not shown. To overcome this issue, the approach of fine-tuning is applied to the trained models.

Source localisation for FP plate using 1D-CNN method: fine-tuning stage and ensemble learning stage

The AE source localisation results provided by the fine-tuned models for the default configuration on the subsequent test FP panel are shown in Figure 16, indicating a significant improvement in accuracy. The percentage of source location estimates with an error of less than 20mm has increased from 20%–30% to 60%–65%. However, despite the improvement, a considerable proportion of estimates (20%–30%) still have errors exceeding 100 mm, which is deemed unacceptable for real-world applications.

To improve the accuracy of source localisation, the ensemble learning method is used, and its effectiveness is demonstrated through the final results for AE source localisation for the default configuration, as shown in Figure 17. An example demonstrating the process of combining four predictions into one is visualised in Figure 18. Two closest predicted coordinates are averaged to obtain the final prediction. The results reveal that the ensemble learning-based estimation significantly outperformed the independent fine-tuned model estimations. Specifically, the proportion of estimates with small errors (less than 20mm) improved considerably with values of 94%. The percentage of estimates with unacceptable errors reduced substantially to only 2%. The corresponding error distributions are summarised in Table 7.

The study investigates two alternative ensemble learning methods: simple averaging and weighted averaging. The weights for the latter approach are determined based on the MSE of each fine-tuned model during its validation when the model converges during the fine-tuning training process. The results obtained indicate that, for simple averaging, there were 17 cases with errors falling within the 0–20 mm range (indicating high accuracy), 31 cases with errors between 20 and 100 mm (indicating acceptable accuracy), and 2 cases with errors exceeding 100 mm (indicating unacceptable

Table 6. Error distribution of AE source localisation results using trained 1D-CNN models from stage I using data from the first historic FP panel under different conditions.

Condition	Model 1	Model 2	Model 3	Model 4
4 waveforms, 50 mm sensor spacing	<20 mm: 0.88 20–100 mm: 0.08 >100 mm: 0.04	<20 mm: 0.88 20–100 mm: 0.06 >100 mm: 0.06	<20 mm: 0.88 20–100 mm: 0.06 >100 mm: 0.06	<20 mm: 0.88 20–100 mm: 0.08 >100 mm: 0.04
4 waveforms, 30 mm sensor spacing	<20 mm: 0.70 20–100 mm: 0.14 >100 mm: 0.16	<20 mm: 0.70 20–100 mm: 0.14 >100 mm: 0.16	<20 mm: 0.70 20–100 mm: 0.18 >100 mm: 0.12	<20 mm: 0.70 20–100 mm: 0.18 >100 mm: 0.12
3 waveforms, 50 mm sensor spacing	<20 mm: 0.62 20–100 mm: 0.2 >100 mm: 0.18	<20 mm: 0.6 20–100 mm: 0.16 >100 mm: 0.24	<20 mm: 0.56 20–100 mm: 0.26 >100 mm: 0.18	<20 mm: 0.6 20–100 mm: 0.18 >100 mm: 0.22

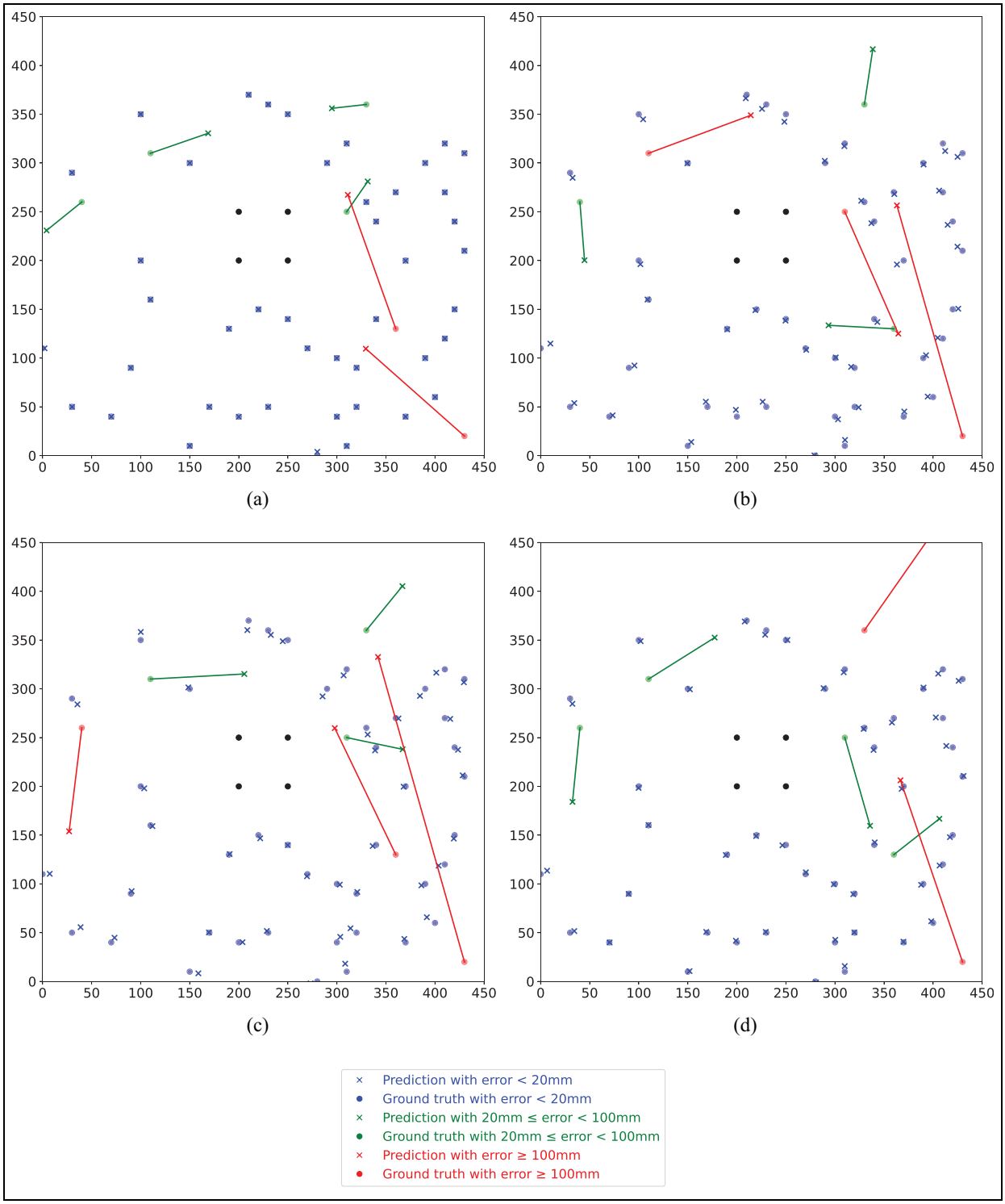


Figure 15. Source localisation results using the trained 1D-CNN models for the first historic FP panel (50 mm sensor spacing, 4 waveform signals): (a) model 1, (b) model 2, (c) model 3 and (d) model 4, axis labels in unit of mm.

accuracy). In the case of weighted averaging, there were 13 cases with errors within the 0–20 mm range (indicating high accuracy), 33 cases with errors between 20 and 100 mm (indicating acceptable accuracy), and 4 cases with errors exceeding 100 mm (indicating unacceptable accuracy). Comparing these accuracy metrics to the method described in the paper, it is evident that both simple and weighted averaging approaches exhibit

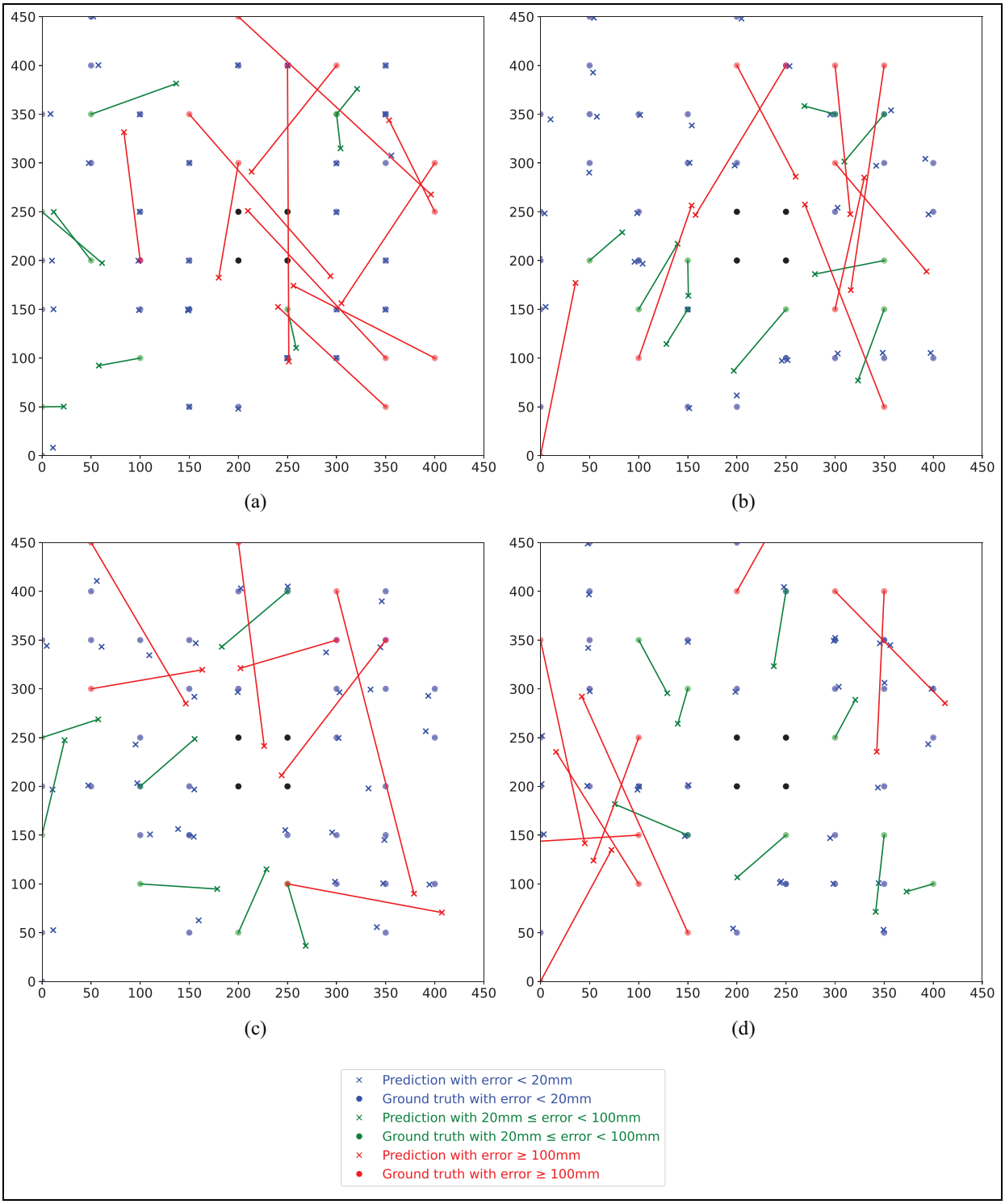


Figure 16. Source localisation results using the fine-tuned 1D-CNN models for the subsequent test historic FP panel (50 mm sensor spacing, 4 waveform signals): (a) model 1-ft, (b) model 2-ft, (c) model 3-ft and (d) model 4-ft, axis labels in unit of mm.
1D-CNN, 1D convolutional neural networks.

lower accuracy than the partial averaging approach developed in this study.

The computation time required by the proposed three-stage 1D-CNN method can be broken down as follows: The first training phase, which uses a dataset of 172 sets of data, requires around 8–9 h. The fine-tuning phase, which uses a smaller dataset of 79 sets for each new area, takes about 20 minutes. The

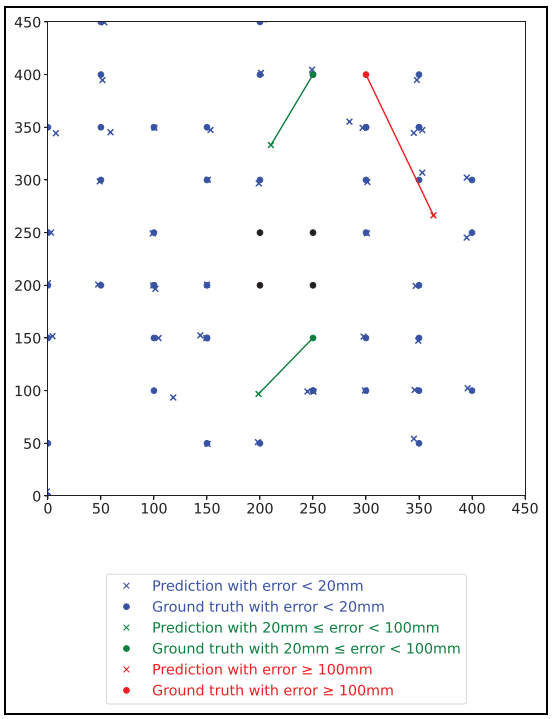


Figure 17. Source localisation results using the ensemble learning-based model for the subsequent test historic FP panel (50 mm sensor spacing, 4 waveform signals), axis labels in units of mm.
FP, Fibrous plaster.

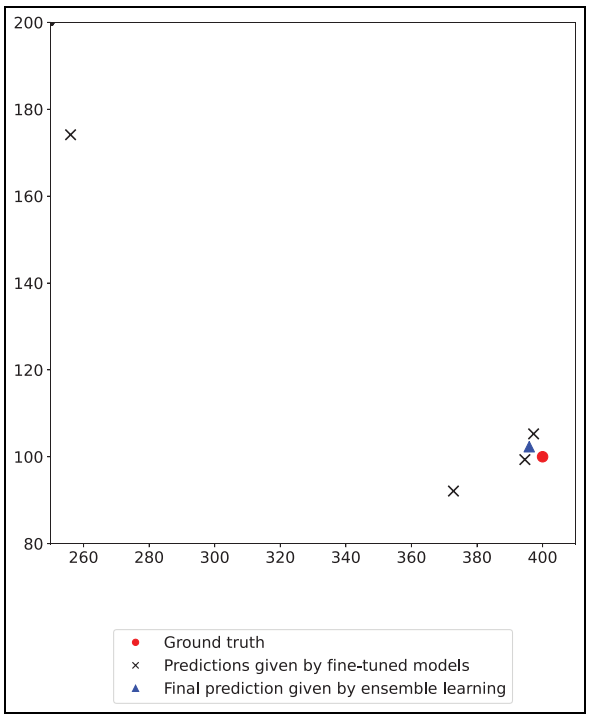


Figure 18. An example demonstrating the process of combining four predictions to one final prediction in stage III, axis labels in units of mm.

computer model utilised is a MacBook Pro equipped with a 2.3 GHz 8-Core Intel Core i9 processor (Intel Core i9-9880H, 9th Generation (Coffee Lake), 2.3 GHz base clock speed, up to 4.8 GHz Turbo Boost, 8 cores, 16 threads, 16 MB SmartCache, 45W TDP) and Intel UHD Graphics 630 1536 MB graphics (Intel UHD Graphics 630, 350 MHz base frequency, 1.20 GHz maximum dynamic frequency, 24 execution units, 4096 x 2304 @ 24Hz (HDMI 1.4), 5120 x 3200 @ 60Hz (DP), DirectX 12, OpenGL 4.5, 1536 MB shared memory).

These findings highlight the effectiveness of the ensemble learning approach in enhancing the accuracy of source localisation, especially in cases where individual fine-tuned models fail to provide accurate results. The low percentage of estimates with unacceptable errors indicates that the failure detection process will not be significant in practice. Overall, our study highlights the effectiveness of fine-tuning and ensemble learning in improving the accuracy of trained models in practical applications for the AE source localisation in historic FP ceilings.

Influence of sensor spacing and waveform number in 1D-CNN-based method

The AE source localisation results for configuration (b) (four sensors with 30 mm spacing) and configuration (c) (three sensors with 50 mm spacing) were also examined using the three-stage approach. The error distribution histogram of source localisation results using ensemble learning method for the subsequent test historic FP panel using the three configurations is shown in Figure 19. Tables 6 and 7 summarise the error distributions for the trained models during the training stage and the fine-tuning and ensemble learning stages.

The results indicate that configuration (b) had 90% of estimates with errors less than 20 mm and 6% of estimates with errors exceeding 100 mm, demonstrating that the sensor spacing had minimal effect on the AE source localisation performance provided by the proposed three-stage approach in configuration (b).

For configuration (c), the proposed three-stage approach was also found to be effective but with a slightly deteriorated accuracy, with 88% of estimates having small errors and only 4% of estimates having errors exceeding 100 mm. Although the high accuracy percentage of this configuration is 6% lower than the default configuration, the unacceptable error remains within acceptable limits. Thus, the results suggest that sufficient localisation can still be achieved with three sensors.

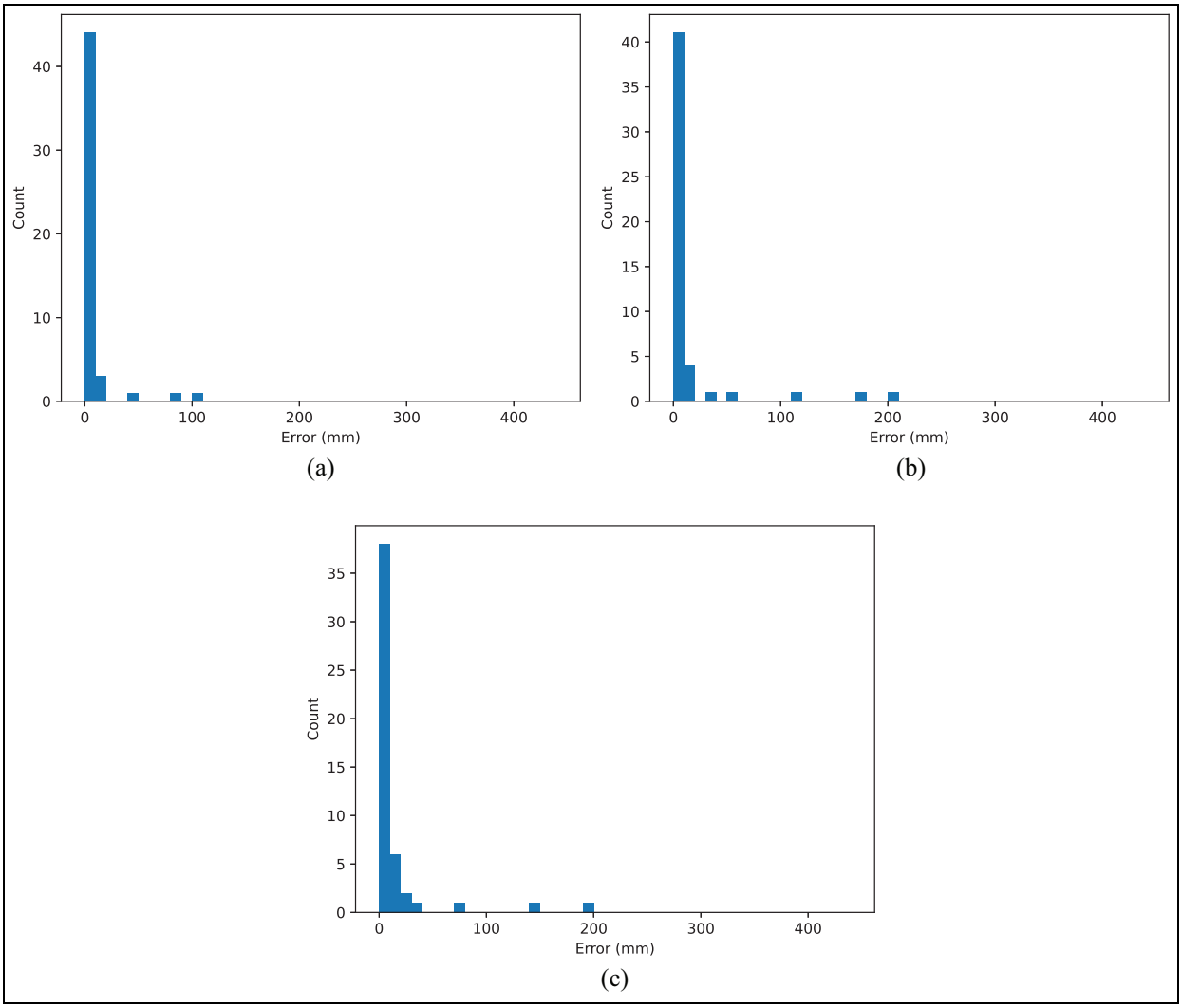


Figure 19. Error distribution histogram of source localisation results using ensemble learning method for the subsequent test historic FP panel using (a) configuration, (b) configuration and (c) configuration.
FP, Fibrous plaster.

Source localisation results by TDOA-based beamforming method using sensor cluster

The developed three-stage 1D-CNN method was evaluated by comparing its performance to that of the TDOA-based beamforming method. An example of the estimated incidence angles can be seen in Figure 20.

It can be observed that there is a significant deviation between the estimated incidence angles and the true incidence angles (connecting the source with the sensor cluster). The angle estimation error for the historical FP ceiling panel ranges from 20° to 40°. Even with two sensor clusters, it is not possible to achieve consistently high accuracy results. The blue area visualises the area where AE source may be predicted with the beamforming method. To experimentally compare measurement accuracy of the developed technique with the beamforming method, 20 pencil-lead breaks were produced at random positions within the (0, 450) range for both x and y coordinates. The coordinates were predicted using the sensor setup shown in Figure 20. The resulting average maximum distance between the actual and predicted coordinates within this area is 71 mm, with a standard deviation of 20.8 mm. This is primarily due to inaccurate identification of the TDOA which is complicated by uncertainties arising from the anisotropic structure of the test object and the attenuation of the received AE signal. In contrast, when utilising the proposed 1D-CNN-based method to predict the 50 pencil-lead break sources in the test dataset, the average error distance between the predictions and the ground truth is 4.07 mm, with a standard deviation of 2.84 mm.

Table 7. Error distribution of AE source localisation results using fine-tuned 1D-CNN models from stage II and ensemble learning method from stage III using data from the subsequent test historic FP panel under different conditions.

Condition	Model 1-ft	Model 2-ft	Model 3-ft	Model 4-ft	Ensemble learning-based model
4 waveforms, 50 mm sensor spacing	<20 mm: 0.62 20–100 mm: 0.16 >100 mm: 0.22	<20 mm: 0.64 20–100 mm: 0.18 >100 mm: 0.18	<20 mm: 0.72 20–100 mm: 0.14 >100 mm: 0.14	<20 mm: 0.66 20–100 mm: 0.16 >100 mm: 0.18	<20 mm: 0.94 20–100 mm: 0.04 >100 mm: 0.02
4 waveforms 30 mm sensor spacing	<20 mm: 0.64 20–100 mm: 0.16 >100 mm: 0.2	<20 mm: 0.7 20–100 mm: 0.08 >100 mm: 0.22	<20 mm: 0.64 20–100 mm: 0.08 >100 mm: 0.28	<20 mm: 0.62 20–100 mm: 0.1 >100 mm: 0.28	<20 mm: 0.90 20–100 mm: 0.04 >100 mm: 0.06
3 waveforms, 50 mm sensor spacing	<20 mm: 0.62 20–100 mm: 0.22 >100 mm: 0.16	<20 mm: 0.7 20–100 mm: 0.12 >100 mm: 0.18	<20 mm: 0.62 20–100 mm: 0.1 >100 mm: 0.28	<20 mm: 0.66 20–100 mm: 0.08 >100 mm: 0.26	<20 mm: 0.88 20–100 mm: 0.08 >100 mm: 0.04

1D-CNN, 1D convolutional neural networks; AE, acoustic emission; FP, Fibrous plaster.

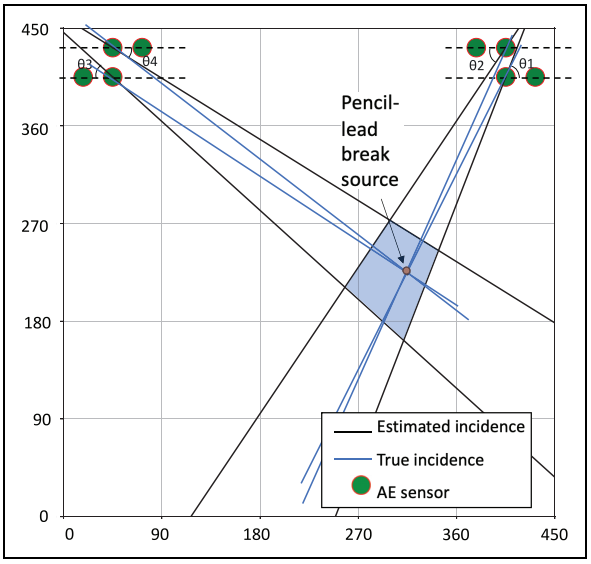


Figure 20. Source localisation results using the TDOA-based beamforming method with two Z-shaped sensor clusters with the estimated incidence angles, θ_1 and θ_2, θ_3 and θ_4, axis labels in units of mm.
TDOA, time difference of arrival.

This result highlights several limitations of this method in the damage source localisation for historic FP ceilings. Firstly, the accurate extraction of the first arrival wave is critical but relies on an empirical approach that can impact the localisation accuracy. Secondly, the method requires a minimum of six sensors to form two L-shaped clusters that are positioned far apart, increasing the hardware cost. In contrast, the method proposed in this manuscript, based on 1D-CNN, achieves accurate damage source localisation using only four sensors. This distinction highlights the efficient and cost-effective nature of the 1D-CNN-based method introduced in this paper.

Conclusion

The AE source localisation in anisotropic plate-like structures has long been recognised as a complex problem. This article addresses the limitations of the TDOA method using the beamforming technique, which is a commonly used approach for AE source localisation. To overcome these limitations, we propose a new technique. We applied this technique to historic FP ceiling panels, which are heterogenous and anisotropic. In our experimental setup, sensors are placed in a square-shaped cluster and collect signals produced by the pencil-lead breaking source. A three-stage approach was then adopted to process the data, where four 1D-CNN models with different dropout layer implementations were trained and validated to localise the pencil-break. These models were then fine-tuned to estimate the source location of a new FP panel. The ultimate estimation results from the combination of estimations provided by the four distinct fine-tuned models. The results of the experiments demonstrate that the 1D-CNN method developed in this study can provide highly accurate localisation, where up to 94% of location predictions are accurate to 20 mm. Adopting different sensor spacing or reducing the number of sensors from four to three sensors instead of four) does not significantly influence localisation accuracy.

Furthermore, the three-stage approach using 1D-CNN models shows superior accuracy and versatility in AE source localisation for historic FP panels, compared to the existing TDOA-based method using sensor clusters, with fast fine-tuning, automation and the ability to work with fewer sensors. Results suggest that the 1D-CNN model can be a promising method for detecting the failure source of historic FP ceilings. The localisation approach developed in this paper can also be applied to other anisotropic plate-like structures.

Declaration of conflicting interests

The author(s) declared no potential conflicts of interest with respect to the research, authorship, and/or publication of this article.

Funding

The author(s) disclosed receipt of the following financial support for the research, authorship, and/or publication of this article: The authors would like to acknowledge the generous support of the ICE research and development enabling fund in the development and presentation of this research.

ORCID iD

Jiaxu Zuo https://orcid.org/0000-0003-1289-6185

References

1. Ngah SA, Dams B, Ansell MP, et al. Structural performance of fibrous plaster. Part 1: physical and mechanical properties of hessian and glass fibre reinforced gypsum composites. *Constr Building Mater* 2020; 259: 120396.
2. Zuo J, Mayfield S, Ozdemir A, et al. Preliminary experimental investigation on mechanical properties of historic fibrous plaster. In: *Paper presented at SAHC2023: 13th International conference on structural analysis of historic constructions*, 2023.
3. Historic England. *Historic Fibrous Plaster in the UK: Guidance on its Care and Management*. Swindon. Historic England, 2019.
4. Gopinath VK and Ramadoss R. Review on structural health monitoring for restoration of heritage buildings. *Mat Today Proc* 2021; 43: 1534–1538.
5. Chandarana N, Sanchez DM, Soutis C, et al. Early damage detection in composites during fabrication and mechanical testing. *Materials* 2017; 10: 685.
6. Sause MG, Müller T, Horoschenkoff A, et al. Quantification of failure mechanisms in mode-I loading of fiber reinforced plastics utilizing acoustic emission analysis. *Compos Sci Technol* 2012; 72: 167–174.
7. Zhou J, Mathews VJ and Adams DO. Acoustic emission–based impact location estimation on composite structures. *Struct Health Monit* 2019; 18: 1652–1668.
8. Zhou W, Pan ZB, Wang J, et al. Review on acoustic emission source location, damage recognition and lifetime prediction of fiber-reinforced composites. *Journal of Materials Science*. 2023; 58(2): 5837–607.
9. Gangadharan R, Prasanna G, Bhat MR, et al. Acoustic emission source location in composite structure by Voronoi construction using geodesic curve evolution. *J Acoust Soc Am* 2009; 126: 2324–2330.
10. Romhany G, Czigany T and Karger-Kocsis J. Failure assessment and evaluation of damage development and crack growth in polymer composites via localisation of acoustic emission events: a review. *Polymer Rev* 2017; 57: 397–439.
11. Dong L, Zou W, Sun D, et al. Some developments and new insights for microseismic/acoustic emission source localisation. *Shock Vibr*. Epub ahead of print 22 July 2019. DOI: 10.1155/2019/9732606.
12. Kundu T, Nakatani H and Takeda N. Acoustic source localisation in anisotropic plates. *Ultrasonics* 2012; 52: 740–746.
13. Xiao D, He T, Pan Q, et al. A novel acoustic emission beamforming method with two uniform linear arrays on plate-like structures. *Ultrasonics* 2014; 54: 737–745.
14. Sen N, Gawronski M, Packo P, et al. Square-shaped sensor clusters for acoustic source localisation in anisotropic plates by wave front shape-based approach. *Mech Syst Signal Process* 2021; 153: 107489.
15. Park WH, Packo P and Kundu T. Acoustic source localisation in an anisotropic plate without knowing its material properties – a new approach. *Ultrasonics* 2017; 79: 9–17.
16. Aljets D, Chong A, Wilcox S, et al. Acoustic emission source location in plate-like structures using a closely arranged triangular sensor array. *J Acoust Emission* 2010; 28: 85–98.
17. Aljets D, Chong A, Wilcox S, et al. Acoustic emission source location on large plate-like structures using a local triangular sensor array. *Mech Syst Signal Proc* 2012; 30: 91–102.
18. Sen N and Kundu T. Acoustic source localisation in a highly anisotropic plate with unknown orientation of its axes of symmetry and material properties with numerical verification. *Ultrasonics*, 2020; 100: 105977.
19. Yin S, Cui Z and Kundu T. Acoustic source localisation in anisotropic plates with "Z" shaped sensor clusters. *Ultrasonics* 2018; 84: 34–37.
20. Nakatani H, Kundu T and Takeda N. Improving accuracy of acoustic source localisation in anisotropic plates. *Ultrasonics*, 2014; 54: 1776–1788.
21. De Simone ME, Ciampa F, Boccardi S, et al. Impact source localisation in aerospace composite structures. *Smart Mater Struct* 2017; 26: 125026.
22. Sen N and Kundu T. A new wave front shape-based approach for acoustic source localisation in an anisotropic plate without knowing its material properties. *Ultrasonics* 2018; 87, 20–32.
23. Sen N and Kundu T. Acoustic source localisation in a highly anisotropic plate with unknown orientation of its axes of symmetry and material properties with numerical verification. *Ultrasonics* 2020; 100: 105977.
24. Kalafat S and Sause MGR. Acoustic emission source localisation by artificial neural networks. *Struct Health Monit* 2015; 14: 633–647.
25. Sause MGR, Schmitt S, Hoeck B, et al. Acoustic emission based prediction of local stress exposure. *Compos Sci Technol* 2019; 173: 90–98.
26. Ding G, Xiu C, Wan Z, et al. Location of tensile damage source of carbon fiber braided composites based on two-step method. *Molecules* 2019; 24: 3524.
27. Fu T, Zhang Z, Liu Y, et al. Development of an artificial neural network for source localisation using a fiber optic acoustic emission sensor array. *Struct Health Monit* 2015; 14: 168–177.
28. Zhang X, Wang H, Hou B, et al. 1D-CNN-based damage identification method based on piezoelectric impedance using adjustable inductive shunt circuitry for data enrichment. *Struct Health Monit* 2022; 21: 1992–2009.

Statement of Authorship

Paper title	A three-stage approach based on 1D-CNNs for AE source localisation on historic fibrous plaster ceilings
Authors	Jiaxu Zuo, Brian Sheil, Sinan Acikgoz
Publication status	Published
Publication details	Zuo, Jiaxu, Brian Sheil, and Sinan Acikgoz. "A three-stage approach based on 1D-CNNs for AE source localisation on historic fibrous plaster ceilings." Structural Health Monitoring 24.2 (2024): 1224-1240.

Student Confirmation

Student name	Jiaxu Zuo
Contribution to the paper	First-author contribution: • Conceived research objectives • Designed and conducted experiments • Developed and implemented computational models • Prepared and presented the manuscript
Signature	
Date	23th September 2025

Supervisor Confirmation

By signing the Statement of Authorship, the supervisor is certifying that the candidate made a substantial contribution to the publication, and that the description above is accurate.

Supervisor name	Prof. Sinan Acikgoz
Supervisor comments	
Signature	
Date	23th September 2025

Chapter 5

Paper 3:Acoustic emission-based failure detection and event source localisation in a historical fibrous plaster ceiling

Cite this article
Zuo J, Mayfield S, Sheil B and Acikgoz S (2024)
Acoustic emission failure detection and localisation in historic fibrous plaster ceiling.
Proceedings of the Institution of Civil Engineers – Engineering History and Heritage
177(4): 147–159, https://doi.org/10.1680/jenhh.24.00004

Research Article
Paper 2400004
Received 27/04/2024; Accepted 10/09/2024
First published online 30/09/2024

Emerald Publishing Limited: All rights reserved

Engineering History and Heritage

Acoustic emission failure detection and localisation in historic fibrous plaster ceiling

Jiaxu Zuo MSc, BE
Department of Engineering Science, University of Oxford, UK
Sarah Mayfield MSc
National Trust, UK
Brian Sheil PhD, BE
Department of Engineering, University of Cambridge, UK
Sinan Acikgoz PhD, BSc
Department of Engineering Science, University of Oxford, UK

Fibrous plaster (FP) is a composite material that has been used for suspended decorative ceilings in historical buildings since the late nineteenth century. Such ceilings are susceptible to failures, particularly in hard-to-access structural hangers ('wads'). Due to a limited understanding of structural behaviour of FP ceilings, maintenance and reconstruction decisions are based on visual and tactile inspections. Such inspections are costly, intrusive and ultimately subjective. Non-destructive techniques are needed to detect and localise failures in FP ceilings. An acoustic emission (AE) system was recently developed to detect and localise damage sources in FP ceilings. The method processes data from AE sensor clusters with one-dimensional convolutional neural networks trained to account for wave propagation anisotropy. This paper presents a case study conducted at the Institution of Civil Engineers building in London (UK) to validate the method. The results confirm the ability of the method to localise failures under real site conditions in 450 mm by 450 mm monitoring areas. The method may enable non-intrusive detection of failures from the underside of ceilings during periodic inspections. The possibility of conducting pre-training in laboratories and covering large monitoring areas up to 1500 mm by 1500 mm is established and may facilitate practical applications in the future.

Keywords: acoustic emission/composite materials/fibrous plaster/historical buildings/machine learning/non-destructive testing/structural health monitoring

1. Introduction

Fibrous plaster (FP) is a fabric-reinforced composite material, composed of plaster of Paris (POP) as the matrix material and loosely woven jute fabrics (also known as 'scrims' or 'hessian') as the reinforcement material. Since the late nineteenth century, FP has been used for decorative suspended ceilings in historic UK buildings (Ngah *et al*., 2020). It provided a fast, cheap and light alternative to traditional plasterwork, becoming the preferred method for large spaces from the early twentieth century. Many post–World War I buildings with FP ceilings are now listed.

Figure 1 illustrates the structure of a typical FP suspended ceiling, comprising two critical components: the ceiling panel and the hanger. Both components are made of FP. The ceiling panel is a laminated composite that features a structural timber frame embedded in an FP panel. The ceiling panel is suspended from an overlying timber/metal framework located in the ceiling void above. Hangers, which are POP components reinforced by twisted scrim, are used to suspend the panel from the framework. The hanger elements are known as 'wads'.

Until recently, FP has been neglected in scientific research. Contemporary studies (Ngah *et al*., 2020; Zuo *et al*., 2023) have begun to address this knowledge gap by characterising the key physical and chemical characteristics of POP and jute fibres, such as gross density, real density, porosity, fibre volume ratio and material phases. Mechanical characteristics have also been examined, although it is difficult to obtain historical samples of requisite size for standard strength tests. Young's modulus of historical POP was determined using impact excitation of vibration tests; the results were then used to manufacture modern plaster mixes with similar Young's moduli, for further compressive and flexural strength testing. The tensile strength of jute fibres was determined by way of direct tension tests. Historical POP and jute fibres indicated reduced strength compared with virgin samples in the scientific literature, possibly due to degradation. The impact of environmental degradation processes driven by moisture and fungi on the mechanical characteristics of FP was examined by way of accelerated ageing and flexural tests (Maundrill *et al*., 2023).

FP ceiling collapses are frequently associated with structural failures in wads and wad interfaces (Dams *et al*., 2023). For instance, the collapse of an FP ceiling during a performance at the Apollo Theatre in London (UK) was attributed to structural degradation of wads (Historic England, 2019). Since wads are located in inaccessible ceiling voids, signs of damage are often hidden from sight. The inspection guidance for historical FP ceilings (Historic England, 2019) suggests periodic visual and tactile assessments by competent inspectors. Such inspections require temporary scaffolding to reach the underside of FP ceilings and invasive drilling of hatches in panels to access the wads. Despite the high associated costs, inspection of individual wads is often inconclusive;

Downloaded by [UNIVERSITY OF OXFORD] on [04/06/25]. Copyright © ICE Publishing, all rights reserved.

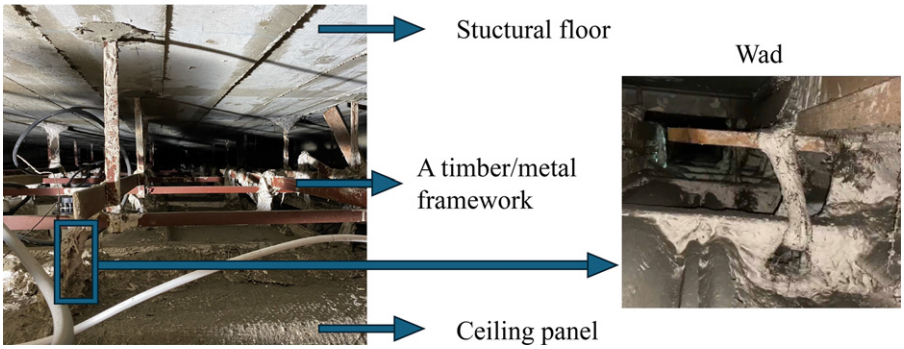


Figure 1. Structure of a typical historical FP ceiling

visual and tactile assessments alone are not sufficient to spot existing damage and judge the tensile integrity of a wad. Consequently, ceiling assessments lack a rational basis and often rely on the intuition and experience of the inspector.

The inspection guidance for historical FP ceilings (Historic England, 2019) suggests the use of point cloud data from periodic laser scanning surveys to support inspections. Commercial scanners offer single point measurement accuracy of 1 mm and above. This may not be sufficient for direct detection of hairline cracks (Laefer *et al*., 2014) for early warning of failures. Recently developed algorithms have shown promise in the localisation of geometric anomalies indicative of cracking (Jing *et al*., 2024) and sub-millimetre accuracy deformation and crack measurements from point clouds (Liu, 2024). These techniques still require further developments before they can be implemented on-site.

A non-destructive technique with a strong track record in failure detection is acoustic emission (AE) sensing. When a micro-crack forms, the strain energy stored in the material is released in the form of an elastic wave. These waves are detected by nearby sensors (e.g. ultrasound microphones) (Grosse *et al*., 2021). Laboratory tests have shown that continuous tracking of AE activity can provide reliable early indicators of collapse in laboratory samples (Nejati *et al*., 2020). However, it is not possible to continuously monitor wide expanses of large structures, such as FP ceilings, due to financial and logistical challenges. An alternative approach is to conduct monitoring periodically in different locations on the underside of the ceiling. This approach may help identify wads where failure events are ongoing.

The process of identifying the location of AE sources is known as localisation and requires multiple sensors. AE techniques have been previously used to localise damage sources in plate-like structures (Chandarana *et al*., 2017; Gopinath and Ramadoss, 2021). Damage sources are typically localised considering differences in the time of arrival (TOA) of AE signals at different sensors (Sause *et al*., 2012; Zhou *et al*., 2019). However, conventional TOA-based methods assume a constant AE wave propagation velocity, which is only suitable for homogeneous materials (Zhou *et al*., 2023). Due to anisotropy, wave velocities in historical FP ceilings are direction- and location-dependent (Gangadharan *et al*., 2009). Consequently, traditional TOA-based methods are infeasible for this application. Many methods have been proposed to enhance source localisation accuracy in anisotropic structures, as summarised in a recent review (Zhou *et al*., 2023). Time difference of arrival (TDOA) methods are popular for localising AE sources without pre-measuring wave velocities (Dong *et al*., 2019; Romhany *et al*., 2017). One notable technique commonly used by TDOA-based methods is the sensor cluster technique (Nakatani *et al*., 2014). This technique involves placing sensors close to each other in a cluster, eliminating the need for prior knowledge of the wave propagation properties of anisotropic materials. The sensor cluster technique could be a promising option for source localisation in historic FP suspended ceilings. However, improving accuracy remains a challenge, as TDOA-based methods rely on accurately and automatically extracting information from the AE waveform recorded by the sensor cluster. Novel methods are needed to address how anisotropy influences wave propagation from the data.

To address this challenge, an innovative approach for localising damage sources from the underside of historic FP ceilings was proposed by the authors in an earlier study (Zuo *et al*., 2024). This approach leverages AE techniques and one-dimensional convolutional neural networks (1D-CNNs) to accurately estimate damage source locations. A square-shaped sensor cluster records AE waveform data from historic FP ceilings, and the 1D-CNNs trained and fine-tuned using the data estimate the damage source location without needing prior knowledge of wave propagation, unlike traditional localisation techniques. The process involves three stages.

- *Stage I*: Train four 1D-CNN models with different dropout layer implementations using a large dataset from a historic FP ceiling panel.
- *Stage II*: Fine-tune the trained models with a smaller dataset from a new test object, in this case, a historic FP ceiling

Downloaded by [UNIVERSITY OF OXFORD] on [04/06/25]. Copyright © ICE Publishing, all rights reserved.

panel. This is considered a new test object in practice, and the fine-tuning process is carried out for each new test object.
- *Stage III*: Use an ensemble learning approach to combine the fine-tuned models' results, improving localisation accuracy.

The 1D-CNNs utilise AE waveform data as input and the corresponding AE source co-ordinates as labels. The localisation results were compared against the traditional TDOA-based beamforming method, which also employs sensor clusters (Nakatani *et al*., 2014), demonstrating improved performance under controlled laboratory conditions (Zuo *et al*., 2024).

While the method exhibits good performance in a laboratory setting, its ability to accurately predict damage source locations under field conditions remains uncertain. The primary objective of this study is to test the performance of the proposed AE-based damage source localisation method in a field application, specifically on a historic FP ceiling in the Institution of Civil Engineers (ICE) building. The hypothesis is that the proposed method can predict the location of artificial failure sources with high accuracy.

The article is structured as follows. First, previous research on AE localisation techniques are discussed, with a focus on the authors' previously proposed three-stage approach. Following this, the three stages for implementing this method under controlled laboratory conditions are outlined, and the performance results are briefly demonstrated. Subsequently, the article details the field set-up used for the AE waveform data collection, followed by the presentation of results obtained from the ICE's historic FP ceilings. The performance results of lab-trained models and field-trained models are compared. Finally, the article concludes with a comprehensive assessment of the field performance of the proposed method.

2. Proposed three-stage approach based on 1D-CNNs for AE source localisation

The method has been comprehensively detailed in previous research (Zuo *et al*., 2024). This work summarises the sensor layout configurations and describes the process of training and fine-tuning 1D-CNNs using AE signals obtained from historic FP ceiling panels under controlled laboratory conditions.

2.1 Sensor layout and data acquisition

A sensor cluster formed of four AE sensors, arranged in a square configuration with 50 mm spacing at the centre of a 500 mm by 500 mm plate, is used for data acquisition according to previous work (Zuo *et al*., 2024). The monitoring area was 450 mm by 450 mm. For convenience, the same size of monitoring area is assumed in the current study. The size of the monitoring area primarily depends on the sensors and the ceiling materials, which determine the attenuation rate of signals.

AE signals for 1D-CNN model training and fine-tuning are generated by producing pencil-lead breaking events (also known as Hsu-Nielsen source) at predetermined co-ordinates within the monitoring area. For each pencil-lead breaking event, each sensor in the cluster records a raw AE waveform consisting of 4096 data points at a sampling frequency of 2 million samples per second. This results in the collection of four waveform signals per event from the four sensors included in the sensor cluster. This artificial waveform data are pre-processed and utilised as the input data, and the corresponding normalised co-ordinates of the failure location serve as the label data, denoting the ground truth failure location used for training and fine-tuning the 1D-CNN models.

2.2 1D-CNNs implementations

In previous research, a three-stage approach involving the implementation of 1D-CNNs for developing the AE source localisation method was demonstrated (Zuo *et al*., 2024).

In Stage I, four distinct 1D-CNNs with predefined architectures are initially trained on a substantial pencil-lead breaking event dataset (featuring more than 250 events, randomly distributed over the monitoring area) generated from an arbitrarily selected area of the monitored ceiling. Models trained this way are called fundamental models, since they form the basis of all other models. If similar materials are available, fundamental models can be trained in the laboratory using the same techniques.

In Stage II, the four fundamental models from Stage I undergo fine-tuning for each specific 450 mm by 450 mm area of the monitored FP ceiling, employing small AE signal datasets (featuring less than 100 events) from the corresponding area. This fine-tuning process customises the fundamental models and generates area-specific models.

In Stage III, predictions from the four fine-tuned area-specific 1D-CNN models for a given area are combined through an ensemble learning process, entailing the averaging of the two nearest predictions. In a previous study (Zuo *et al*., 2024), it was observed that this deliberate combination of model outputs significantly enhances the predictive performance of the method.

Regarding model architecture, each 1D-CNN model comprises four one-dimensional convolutional layers, each followed by a max-pooling layer, and two fully connected layers. To prevent overfitting during ensemble learning, dropout layers are implemented. Each 1D-CNN architecture incorporates a unique dropout layer implementation, with varying dropout probabilities, to introduce diversity in the ensemble learning process. Interested readers are referred to the previous study (Zuo *et al*., 2024) for further details on model architecture.

2.3 Accuracy thresholds and experimental results

The localisation of AE sources using 1D-CNNs is categorised according to three accuracy thresholds: less than 20 mm error denotes high accuracy, 20–100 mm for acceptable accuracy, and

Downloaded by [UNIVERSITY OF OXFORD] on [04/06/25]. Copyright © ICE Publishing, all rights reserved.

greater than 100 mm for unacceptable accuracy. Wads tend to have a radius around 50 mm and the acceptable accuracies ensure that failures are localised within the footprint of the wad. It was observed that the system can achieve high accuracy more than 90% of time under controlled laboratory conditions (Zuo *et al*., 2024). An in situ localisation experiment is discussed next to investigate the performance of the method under realistic conditions.

3. Field application

3.1 Field environment and experimental set-up

One Great George Street is a Grade-II listed Edwardian building, constructed as the headquarters of the ICE between 1910 and 1913. Inspection and replacement works on its FP ceilings have been ongoing since 2022 and involve temporary scaffolding for visual and tactile inspections, as shown in Figure 2.

The field application was conducted in the library of the ICE building between 27 and 30 June 2023. During this time, a scaffold was in place to access the underside of the library central room FP ceiling, as shown in Figure 3. Hatches were drilled, as depicted in Figure 4, to allow access to the topside of the ceiling panel and the wads, for inspections and, where necessary, repair works. Visual inspections of the ceiling topside indicated an irregular and insufficient distribution of hangers that were failing. ICE archival evidence told of contractual disputes, as well as non-trade industrial action when the library was fitted. This may explain the incomplete metalwork, which was subcontracted through the plasterers, as well as the apparently rushed fitting of this ceiling compared with other examples built in 1912 in the same building.

The experimental set-up is illustrated in Figure 5. The equipment for AE signal collection consists of a Mistras Micro-SHM system and four narrow-band resonant R6a sensors, each equipped with a 40 dB external amplifier. Recorded AE signals are thresholded at 40 dB to eliminate noise. The software AEwin is employed to manage the data acquisition and pre-processing processes. To capture the low-frequency AE signals generated by the plaster materials, a frequency band filter of 35–100 kHz is applied. The sensor cluster is mounted onto the underside surface of the FP ceiling using tapes, with a thin layer of grease applied in between to act as a coupling agent and improve the transfer of ultrasonic energy between the AE sensors and the surface of the test object. This allows for complete removal without causing lasting damage or alterations.



Figure 2. Temporary scaffolding for FP ceiling inspection in the Telford Theatre of the ICE building



Figure 3. A scaffold to access the underside of the FP ceiling of the ICE library



Figure 4. A hatch drilled into the ICE library FP ceiling panel

3.2 1D-CNN model field training and fine-tuning for *A1* and *A2*

The fundamental models are initially field trained using a substantial AE signal dataset from a 450 mm by 450 mm area on the library ceiling, namely *A1*. The AE sensors are securely mounted on the underside of the FP ceiling within *A1*. Four 1D-CNN

Downloaded by [UNIVERSITY OF OXFORD] on [04/06/25]. Copyright © ICE Publishing, all rights reserved.

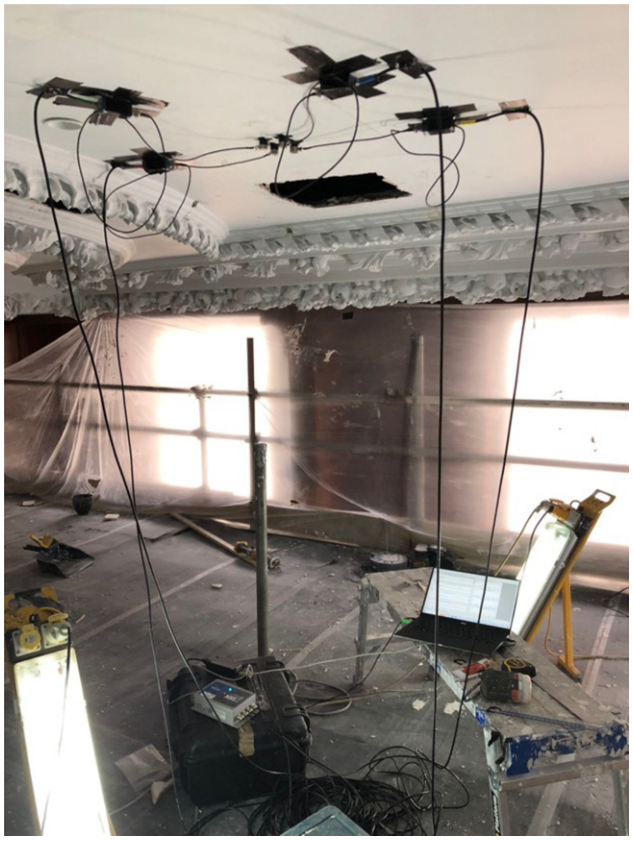


Figure 5. AE system set-up

architectures are then trained to generate the fundamental models. Another 450 mm by 450 mm area on the ceiling is then randomly selected, namely *A2*. A small AE signal dataset is collected from *A2* by placing the same sensor cluster in the centre of *A2*, which fine-tunes the fundamental models. The fine-tuned models are subsequently employed to predict locations of different types of damage sources within *A2* resulting from various types of events occurring on the wads above the ceiling panels based on the AE signals they produce.

The locations of *A1* and *A2* on the library ceiling are shown in Figures 6 and 7. *A1*, as illustrated in Figure 8, is superimposed with a fine grid. A substantial dataset containing 230 pencil-lead breaking events is collected first and serves as the training dataset to develop the fundamental models. For *A2*, as shown in Figure 9, a coarser grid is drawn, and a smaller dataset comprising 80 pencil-lead breaking events is gathered for fine-tuning. The AE sensors are mounted on the underside of the ceiling for both *A1* and *A2* at co-ordinates (200, 200), (200, 250), (250, 250) and (250, 200) (units in millimetres, see the corner origins in Figures 8 and 9). All pencil-lead breaking events for 1D-CNN model training and fine-tuning are induced on the underside of *A1* and *A2* of the ceiling panel. This ensures that training data can be gathered non-invasively, without opening hatches. The wads above monitoring area *A2* are shown in Figure 10.

3.3 Artificial damage source events in *A2* for model validation

Different types of artificial events are produced on either the underside or the topside of *A2* for the established 1D-CNNs method to predict the locations, validating the method's performance.

Pencil-lead breaks on the underside of the ceiling are produced. Established 1D-CNNs are utilised to predict their locations, following the evaluation procedure outlined in previous research under laboratory conditions (Zuo *et al*., 2024). This is to test the influence of the environmental noise and the complex structure on the performance of the method.

To assess performance for topside event localisation, two types of damage events – pencil-lead breaks and impact strikes – are examined. The reason for using two distinct event types is to investigate if different waveform characteristics produced by different event types influence the localisation performance. Also, since wad strikes more closely resemble real failures, they provide an opportunity to test localisation more rigorously. Both event types are artificially triggered on the spread ends of the two bulked wads (wad 1 and wad 2) (radius approximately 50 mm) on the topside of the ceiling panels, accessed through the hatch. The bulked ends

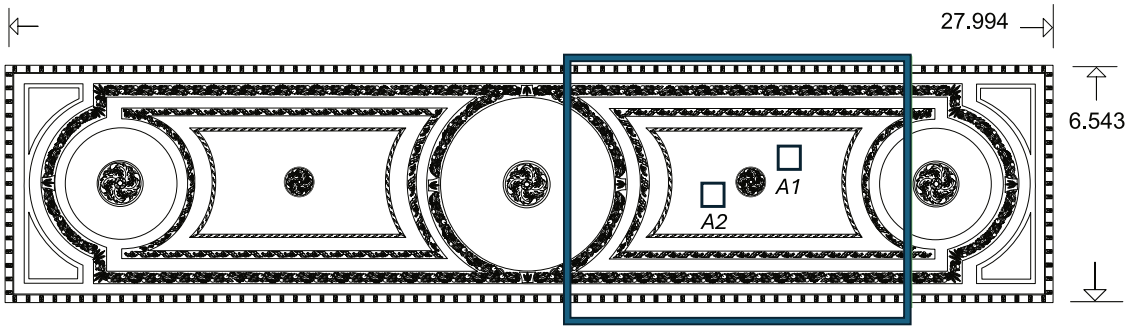


Figure 6. Location of monitoring areas A1 and A2 highlighted on a drawing of the library central room FP ceiling

Downloaded by [UNIVERSITY OF OXFORD] on [04/06/25]. Copyright © ICE Publishing, all rights reserved.

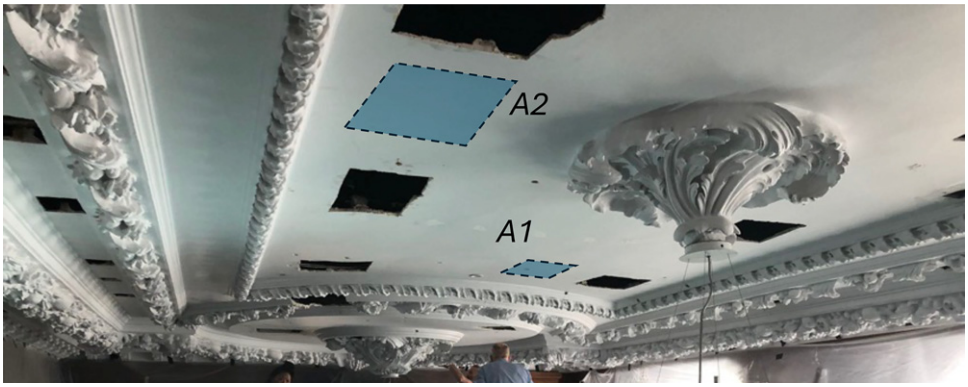


Figure 7. Location of monitoring areas A1 and A2 highlighted on a photograph of the library central room FP ceiling

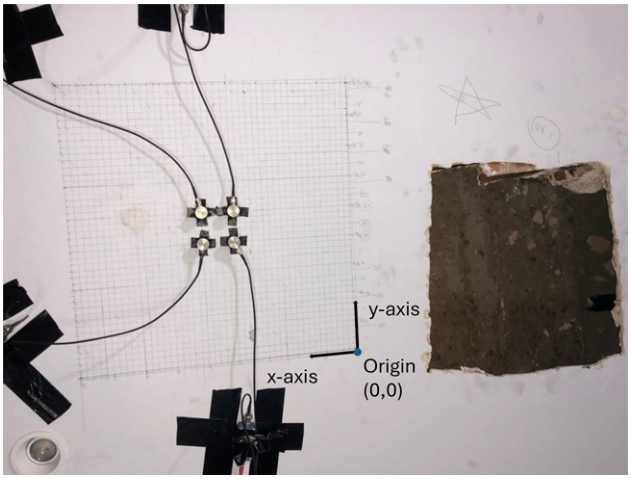


Figure 8. Monitoring area A1

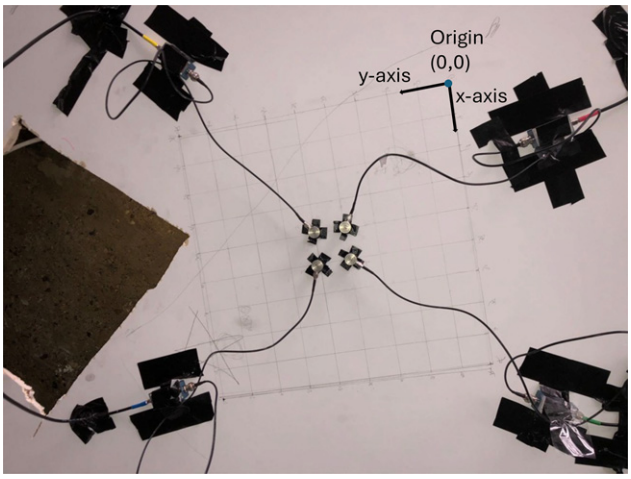


Figure 9. Monitoring area A2



Figure 10. Wads above monitoring area A2

of these two wads within *A2* are mapped in Figure 11. For pencil-lead breaks on wads, a 3 mm pencil-lead break is executed at a specific point on the bulked ends of the wad. For strikes, a steel bar is used to tap the same point. The projections of the events within the footprint of *A2* are recorded. To ensure repeatability while applying pencil-lead breaks and strikes at wad elements, small stickers were used to mark the nominal event locations. Twenty groups of AE signal data are collected for each case.

4. Results

After the 1D-CNNs were trained on AE data from *A1* and fine-tuned using AE data from *A2*, three tests were conducted in this fieldwork. First, pencil-lead breaks were produced on the underside of *A2*, and the locations were predicted, by following the same test routine outlined in previous work (Zuo *et al*., 2024). Second, two different artificial events – pencil-lead breaks and impact strikes – were induced on the two wad ends (wad 1 and wad 2) located on the topside of *A2*. A 2D Gaussian distribution

Downloaded by [UNIVERSITY OF OXFORD] on [04/06/25]. Copyright © ICE Publishing, all rights reserved.

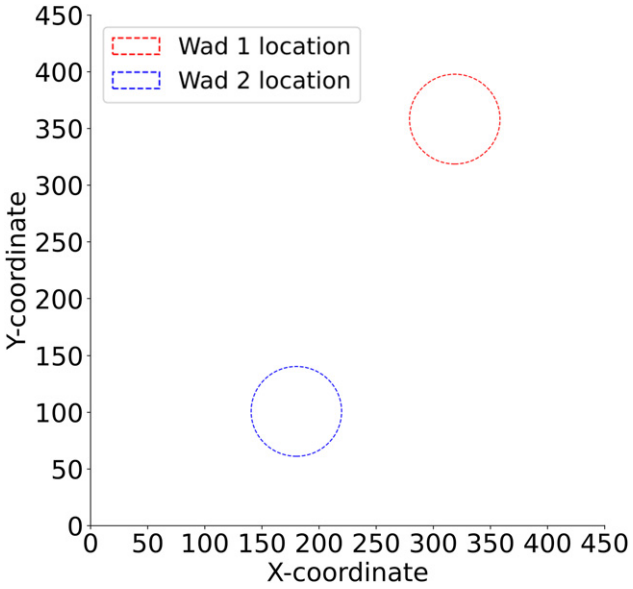


Figure 11. Wad 1 and wad 2 locations

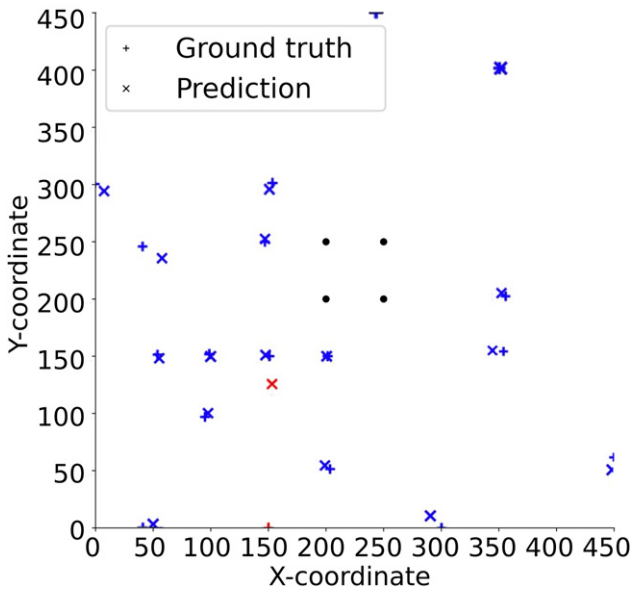


Figure 12. Predicted co-ordinates of the pencil-lead breaking events on the underside of the FP ceiling within A2 using fine-tuned field-trained fundamental models. Blue, green and red markers indicate high accuracy, acceptable and unacceptable predictions, respectively. Black circular markers refer to AE sensor cluster

was generated for each case. Third, the fundamental trained models, previously trained with laboratory data from a historic FP ceiling panel (Zuo *et al*., 2024) rather than field data from *A1*, were used for *A2* data fine-tuning. These two established 1D-CNNs – the lab-trained model and the field-trained model – were compared regarding their performance.

4.1 Pencil-lead breaking event localisation on the underside of the FP ceiling within *A2*

The predicted co-ordinates of the pencil-lead breaking events on the underside of the ceiling within *A2* are presented in Figure 12, alongside the ground truth co-ordinates. Blue markers indicate high prediction accuracy and constitute 17 out of 18 events (94%).

4.2 Damage source localisation for pencil-lead breaking and strikes on wads in *A2*

The fine-tuned models are applied to localise artificial failure events at the wads above *A2*. The projected co-ordinates of these events on wad 1 and wad 2 are (320, 360) and (180, 100), respectively (units in mm). The predictions for pencil-lead breaking events on wad 1 and wad 2 are displayed in Figures 13(a) and 13(b), respectively. The results show that 12 (60%) and 13 (65%) out of 20 events are predicted with acceptable accuracy for wad 1 and wad 2, respectively. The localisation results for strikes on wad 1 and wad 2 are presented in Figures 14(a) and 14(b), respectively. The results indicate that 18 (90%) and 13 (65%) out of 20 events are predicted with acceptable accuracy, respectively. It is important to note that despite their potentially different waveforms, wad strike localisation accuracies are comparable to pencil-lead break accuracies. Prediction accuracy distributions are summarised in Table 1.

In comparison to the prediction results in Figure 12 for the pencil-lead breaking events on the underside of the FP ceiling within *A2*, wad pencil-lead break and the strike predictions in Figures 13(a) and 13(b) exhibit reduced accuracy. This is partially attributed to the more complex wave propagation paths from the event source at the wad to the sensor surface, resulting in increased scatter. However, while evaluating results, it should also be considered that non-local events may be generated during pencil breaking and strikes. This could partially explain the reduced prediction accuracy.

To evaluate the statistical reliability of predictions, the 20 predicted co-ordinates are used to calculate the mean prediction and a covariance matrix. A 2D Gaussian distribution based on the calculated parameters is created. The calculated covariance matrix is then used to compute the eigenvalues and eigenvectors. The standard deviations along the major and minor axes are subsequently calculated. The 1-Sigma ellipse plots (marked in red) are shown in Figures 15(a) and 15(b) for the localisation predictions of the pencil-lead breaking events on wad 1 and wad 2, respectively. For strikes on wad 1 and wad 2, the scatter plots are shown in Figures 16(a) and 16(b), respectively. The calculated means, standard deviations along the major and minor axes for each case are presented in Table 2.

For wad 1, the distances between the calculated mean of the predicted co-ordinates and the actual co-ordinates are 17.15 mm and 16.79 mm, respectively, for the pencil-lead breaks and the strikes.

Downloaded by [UNIVERSITY OF OXFORD] on [04/06/25]. Copyright © ICE Publishing, all rights reserved.

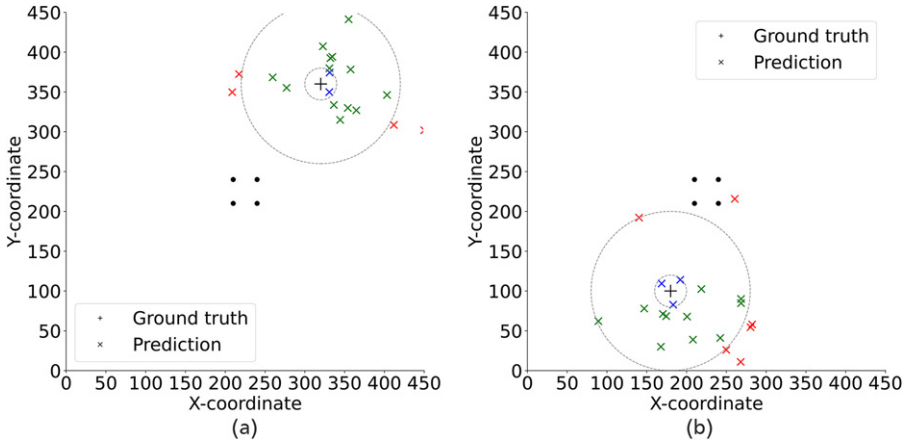


Figure 13. Predicted event source locations for pencil-lead breaks within A2 on (a) wad 1 and (b) wad 2 using fine-tuned field-trained fundamental models. Blue, green and red markers indicate high accuracy, acceptable and unacceptable predictions, respectively. Dashed line grey circles highlight 20 mm and 100 mm boundaries. Black circular markers refer to AE sensor cluster

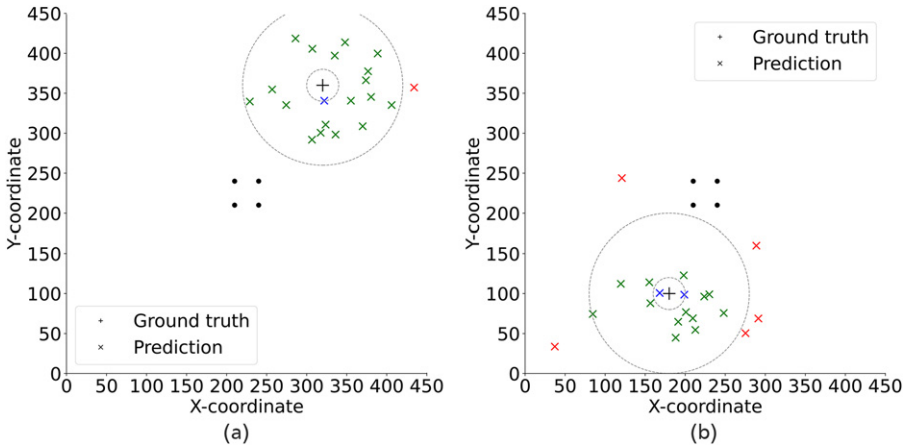


Figure 14. Predicted event source locations for strikes within A2 on (a) wad 1 and (b) wad 2 using fine-tuned field-trained fundamental models. Blue, green and red markers indicate high accuracy, acceptable and unacceptable predictions, respectively. Dashed line grey circles highlight 20 mm and 100 mm boundaries. Black circular markers refer to AE sensor cluster

Table 1. Prediction accuracy distributions of the wads within A2

Event type	Wad index	High accuracy	Acceptable accuracy	Unacceptable accuracy
Pencil-lead break	1	3	12	5
	2	3	11	6
Strike	1	1	18	1
	2	2	13	5

For wad 2, the distances are 23.84 mm and 10.10 mm, respectively. As presented in Table 2, in each case, both the largest and smallest standard deviations fall within the range of acceptable accuracy, indicating consistent and well-contained prediction variations.

4.3 Comparison: field-trained versus lab-trained fundamental models

Instead of the field-trained fundamental models (i.e. the fundamental models trained by AE signals collected from the field), lab-trained fundamental models (i.e. fundamental models trained by AE signals generated on a laboratory sample (Zuo *et al.*, 2024)) may be employed to minimise the time required for conducting site measurements. In this study, lab-training was possible, since similar ICE FP ceilings (obtained from the decommissioned stairway ceiling) were salvaged during repair works and investigated in a previous study (Zuo *et al.*, 2024). The lab-trained fundamental models are fine-tuned using the fine-tuning dataset from *A2* and then applied to localise the pencil-lead breaking events and strikes above the ceiling within *A2*. The prediction results for

Downloaded by [UNIVERSITY OF OXFORD] on [04/06/25]. Copyright © ICE Publishing, all rights reserved.

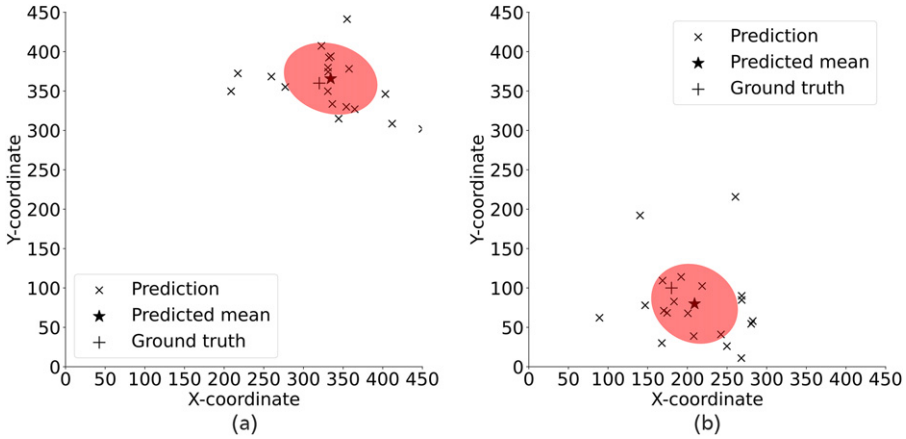


Figure 15. 2D Gaussian distribution for predicted co-ordinates of pencil-lead breaks within A2 on (a) wad 1 and (b) wad 2. Red shadowed areas indicate 1-Sigma ellipse plots based on the 2D Gaussian distribution

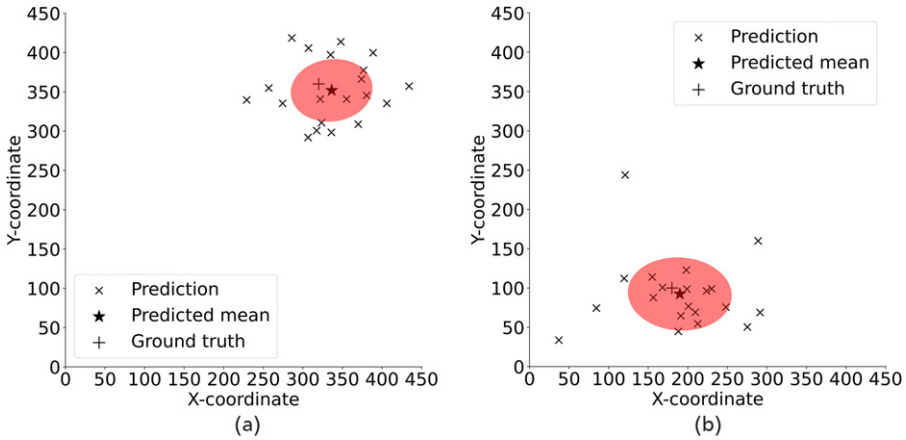


Figure 16. 2D Gaussian distribution for predicted co-ordinates of strikes within A2 on (a) wad 1 and (b) wad 2, using fine-tuned field-trained fundamental models. Red shadowed areas indicate 1-Sigma ellipse plots based on the 2D Gaussian distribution

Table 2. 2D Gaussian distribution information for the localisation predictions of wad 1 and wad 2 of A2 using fine-tuned field-trained fundamental models

Event type	Wad index	Mean	Largest SD	Smallest SD
Pencil-lead break	1	(334.32, 365.72)	58.92	45.61
	2	(209.07, 79.94)	54.58	50.69
Strike	1	(336.37, 351.88)	51.53	39.76
	2	(189.94, 92.41)	65.54	46.51

SD, standard deviation

pencil-lead break events on wad 1 and wad 2 are displayed in Figures 17(a) and 17(b), respectively. For strikes on wad 1 and wad 2, the results are presented in Figures 18(a) and 18(b), respectively. The prediction accuracy distribution is detailed in Table 3. Comparing these results to the results in Table 1, a noticeable increase in predictions outside the acceptable range is observed. This is likely due to increased dissimilarity of *A2* to the lab sample obtained from the ICE stairway than to *A1*.

The predictions are utilised to generate 2D Gaussian distributions. The calculated 1-Sigma ellipse plots (marked in red) for the pencil-lead breaks on wad 1 and wad 2 are shown in Figures 19(a) and 19(b), respectively. For strikes, the plots are depicted in Figures 20(a) and 20(b), respectively. The calculated means and standard deviations along the major and minor axes for each case can be found in Table 4. For wad 1, the distances between the calculated mean of the predicted co-ordinates and the actual co-ordinates are 39.56 mm and 5.33 mm, respectively, for the pencil-lead breaks and the strikes. For wad 2, the distances are 32.07 mm and 39.42 mm, respectively. These results indicate significantly larger errors, and the largest and smallest

Downloaded by [UNIVERSITY OF OXFORD] on [04/06/25]. Copyright © ICE Publishing, all rights reserved.

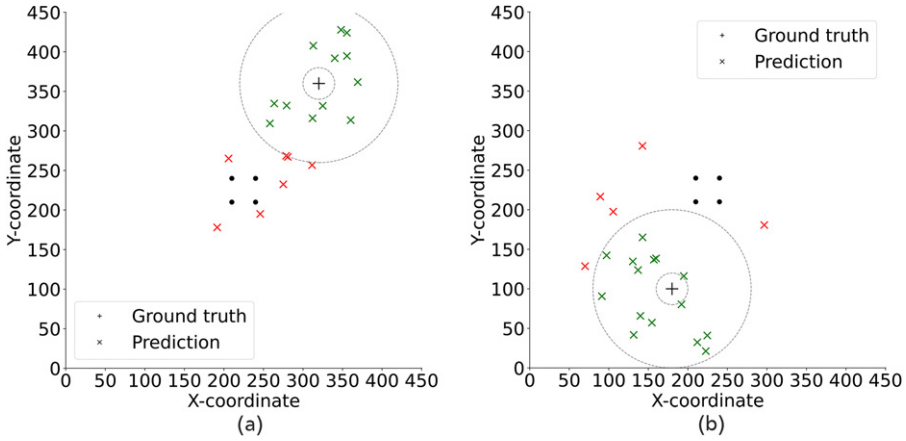


Figure 17. Predicted event source locations for pencil-lead breaks within A2 on (a) wad 1 and (b) wad 2, using fine-tuned lab-trained fundamental models. Blue, green and red markers indicate high accuracy, acceptable and unacceptable predictions, respectively. Dashed line grey circles highlight 20 mm and 100 mm boundaries. Black circular markers refer to AE sensor cluster

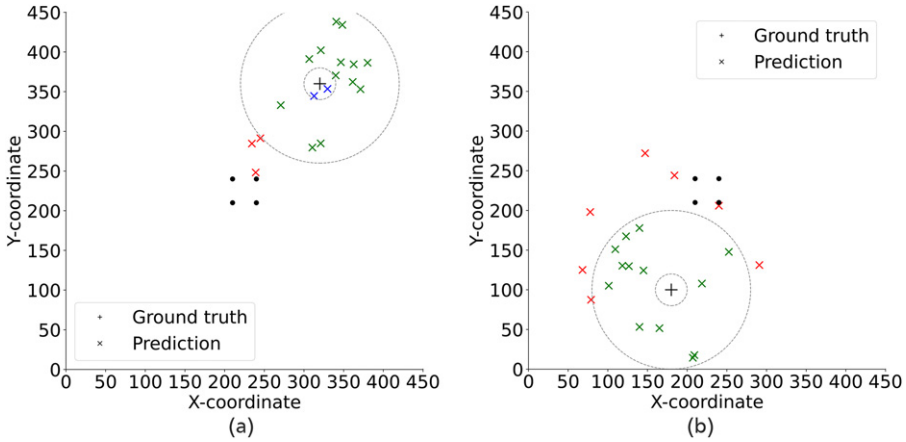


Figure 18. Predicted event source locations for strikes within A2 on (a) wad 1 and (b) wad 2, using fine-tuned lab-trained fundamental models. Blue, green and red markers indicate high accuracy, acceptable and unacceptable predictions, respectively. Dashed line grey circles highlight 20 mm and 100 mm boundaries. Black circular markers refer to AE sensor cluster

Table 3. Prediction accuracy distributions of the wads within A2 using fine-tuned lab-trained fundamental models

Event type	Wad index	High accuracy	Acceptable accuracy	Unacceptable accuracy
Pencil-lead break	1	0	12	8
	2	0	13	7
Strike	1	2	13	5
	2	0	13	7

deviations display notable disparities, resulting in prediction areas with non-uniform shapes. However, despite these drawbacks, the results may still be considered practically sufficient, considering that standard deviations remain within the diameter of the bulked area of the wad.

4.4 Discussion

This study evaluated the effectiveness of an AE-based method for localising event sources in a real historic FP ceiling. Pencil-lead breaks on the underside of the FP ceiling within *A2* were successfully localised with a high accuracy rate of 94%, demonstrating the method's real-world applicability and robustness against environmental noise.

When applying the established 1D-CNNs to localise artificial failure events on wad 1 and wad 2 above *A2*, the location prediction

Downloaded by [UNIVERSITY OF OXFORD] on [04/06/25]. Copyright © ICE Publishing, all rights reserved.

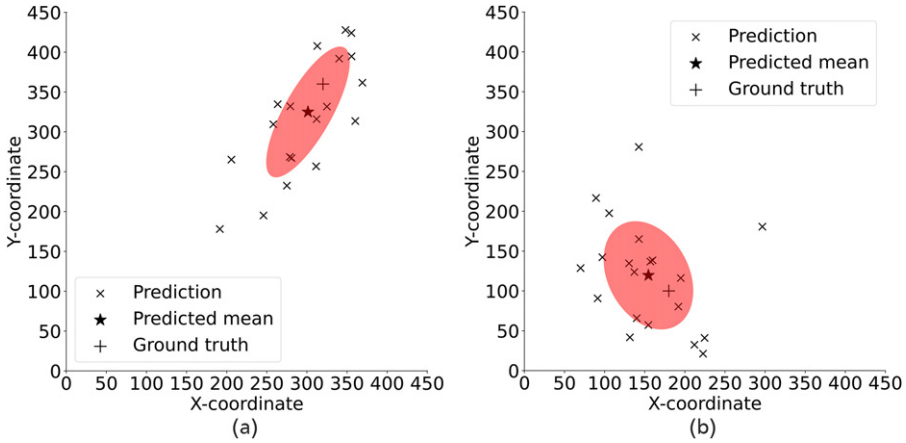


Figure 19. 2D Gaussian distribution for predicted co-ordinates of pencil-lead breaks above A2 on (a) wad 1 and (b) wad 2, using fine-tuned lab-trained fundamental models. Red shadowed areas indicate 1-Sigma ellipse plots based on the 2D Gaussian distribution

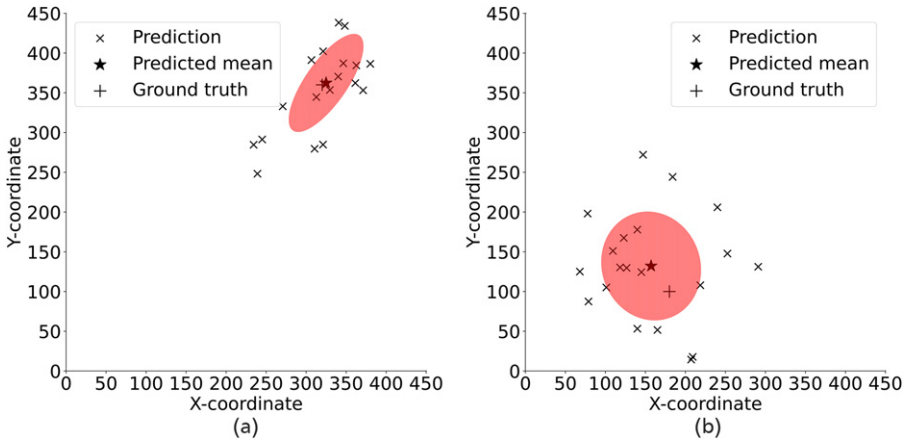


Figure 20. 2D Gaussian distribution for predicted co-ordinates of strikes above A2 on (a) wad 1 and (b) wad 2, using fine-tuned lab-trained fundamental models. Red shadowed areas indicate 1-Sigma ellipse plots based on the 2D Gaussian distribution

Table 4. 2D Gaussian distribution information for the localisation predictions of wad 1 and wad 2 of A2, using fine-tuned lab-trained fundamental models

Event type	Wad index	Mean	Largest SD	Smallest SD
Pencil-lead break	1	(301.32, 324.95)	81.98	52.00
	2	(154.59, 119.61)	67.81	55.76
Strike	1	(324.94, 362.39)	61.66	46.65
	2	(157.13, 132.11)	68.42	62.34

SD, standard deviation

accuracy reduced. Approximately 60%–65% of events were predicted accurately for both pencil-lead breaks and impact strikes. This lower accuracy is attributed to the more complex wave propagation paths and non-local events. However, statistical analyses demonstrated that the algorithm could deliver consistent event localisation by evaluating the Gaussian distribution of subsequent event location predictions. The standard deviation of event locations fell within the footprint of the wad, indicating sufficiently accurate performance. These results demonstrate the method's applicability in predicting inaccessible topside failures in wads, using measurements from the underside of the ceiling.

A comparison between field-trained and lab-trained fundamental models further revealed differences. Lab-trained models, which are less time-consuming due to being fundamentally trained on similar ICE FP ceiling samples, exhibited increased prediction errors in *A2* due to the significant differences caused by environmental and material variability between the lab-trained samples and the field samples. The use of 2D Gaussian distributions illustrated larger errors and non-uniform prediction shapes for lab-

Downloaded by [UNIVERSITY OF OXFORD] on [04/06/25]. Copyright © ICE Publishing, all rights reserved.

trained models. However, the predictions were still acceptable. This highlights a potential trade-off between time efficiency and localisation accuracy depending on real-world conditions.

4.5 Extended monitoring area using AE-based localisation method for historic FP ceilings

The proposed event source localisation method was originally developed using historical FP ceiling samples, which had a square area of approximately 500 mm by 500 mm (Zuo *et al*., 2024). However, a larger area can be monitored for localisation using the same AE kit. This would reduce the number of monitoring areas in ceilings and facilitate field applications.

In the current configuration of the proposed method, if an AE signal released by an event exceeds the 40 dB threshold, the AE sensor can detect the event. If all four AE sensors in a sensor cluster detect the event, the AE cluster can localise the event source based on the received signal group. If D represents the longest distance where the waveform has an amplitude higher than 40 dB, the system can be applied to a square area with a side length of $\sqrt{2}D$ (the sensor spacing within the sensor cluster is relatively small compared with D and therefore negligible). The attenuation curve is generated based on AE signals released by pencil-lead breaking events induced on the FP material surface at various distances (ranging from 100 mm to 1500 mm with a spacing of 100 mm) from the attached AE sensor. Due to the attenuation, the amplitude of the signal decays as the distance increases. The data were collected from a historical sample from the ICE building in the laboratory, along the longest axis of the sample, with a total length of 1.5 m. Since similar materials are used, the data can be considered representative and applicable to the FP ceiling in the ICE building, as well as to other FP ceilings with similar materials and structures. Figure 21 illustrates the attenuation curve of the FP for the applied AE sensor, with D equal to 1500 mm. This implies that the method, utilising the applied AE kit, may be effectively employed in a 1500 mm by 1500 mm square area of FP. To achieve a larger coverage area, it is possible to simply train and fine-tune the method using FP ceilings with corresponding areas as described in Section 2.1.

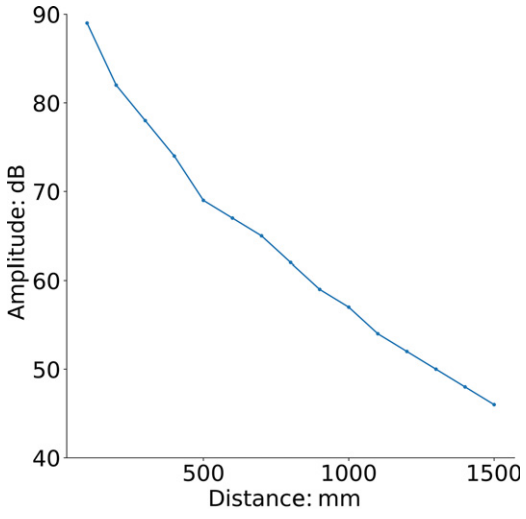


Figure 21. Attenuation curve of the FP for the applied AE sensor

5. Conclusion

This paper comprehensively evaluates the field application of a recently developed AE-based method for detecting and localising failures in historic FP ceilings. Experiments were carried out on an FP ceiling undergoing repairs in the library of the Grade-II listed ICE building in London (UK).

The localisation method requires the measurement of the AE signals released by failure events using a sensor cluster to establish 1D-CNNs for event source localisation. The proposed AE-based localisation method, which performed well under laboratory controlled conditions, proved effective in field for localising damage sources for both underside and topside of the historic FP ceiling within 450 mm by 450 mm areas. The results show that the method achieved high prediction accuracy through a combination of field-trained fundamental models and area-specific fine-tuning, regardless of the environmental disturbances in the field. The method also demonstrated robustness in accurately localising both pencil-lead breaks and strikes, indicating precise location accuracy despite varying waveform characteristics. The lab-trained model exhibits a slightly lower but still acceptable localisation accuracy compared with the field-trained model. However, the advantage of time-saving should be duly considered in practical applications.

The system's non-intrusive and non-destructive nature was highlighted by demonstrating that accurate localisation predictions are possible only with access to the underside of the ceiling; training data can simply be created by conducting pencil-lead break tests from the underside. Other factors, such as pre-training the 1D-CNN algorithms in the laboratory or increasing the size of the measurement area to 1500 mm by 1500 mm, were also explored and deemed feasible to improve the practicability of the technique.

The AE-based damage detection and localisation method addresses a crucial industrial requirement. Current inspection tests rely on visual and tactile assessments, which are inherently destructive and subjective. The proposed approach facilitates non-invasive and objective evaluation of ongoing cracking and its precise location in historic FP ceilings. The proposed AE-based method can accurately localise failures in specific areas identified by engineers as potentially compromised, complementing the broader coverage provided by techniques such as laser scanning, which may be useful for identifying large geometric distortions. The AE method can be applied on a periodic basis to provide inspectors and building owners useful data that can complement traditional inspections.

In the future, AE methods can be further developed to monitor structural health by categorising failure mechanisms such as matrix cracking, matrix–fabric debonding and fabric breakage based

Downloaded by [UNIVERSITY OF OXFORD] on [04/06/25]. Copyright © ICE Publishing, all rights reserved.

on AE signals. These events may offer new insight into the state of damage; for example, identification of fibre debonding events may indicate a more advanced failure state, contrasting with early stages dominated by cracking in the stiffer plaster matrix. These advancements could enable proactive maintenance and timely intervention, ultimately enhancing the longevity and safety of structures and will be the focus of the authors' further work.

Declaration of conflicting interests

The author(s) declare no potential conflicts of interest with respect to the research, authorship, and/or publication of this article.

Funding

The authors would like to acknowledge the generous support of the ICE Research and Development Enabling Fund in the development and presentation of this research.

REFERENCES

Chandarana N, Sanchez DM, Soutis C and Gresil M (2017) Early damage detection in composites during fabrication and mechanical testing. *Materials* **10(7)**: 685.

Dams B, Kumar N, Kurchania R *et al.* (2023) Interfacial bond strength and failure modes of traditional and modern repair materials for historic fibrous plaster. *Materials and Structures* **56(8)**: 149.

Dong L, Zou W, Sun D *et al.* (2019) Some developments and new insights for microseismic/acoustic emission source localisation. *Shock and Vibration* **2019(1)**.

Gangadharan R, Prasanna G, Bhat MR, Murthy CRL and Gopalakrishnan S (2009) Acoustic emission source location in composite structure by Voronoi construction using geodesic curve evolution. *The Journal of the Acoustical Society of America* **126(5)**: 2324–2330.

Grosse CU, Ohtsu M, Aggelis DG and Shiotani T (2021) *Acoustic Emission Testing: Basics for Research-Applications in Engineering*. Springer Nature, London.

Gopinath VK and Ramadoss R (2021) Review on structural health monitoring for restoration of heritage buildings. *Materials Today: Proceedings* **43**: 1534–1538.

Historic England (2019) *Historic Fibrous Plaster in the UK: Guidance on Its Care and Management*.

Jing Y, Sheil B and Acikgoz S (2024) *Geometric Detection of Cracks in Masonry Arch Bridge Point Clouds Using Fast Point Feature Histograms and Patchcore*. Under review.

Laefer DF, Truong-Hong L, Carr H and Singh M (2014) Crack detection limits in unit based masonry with terrestrial laser scanning. *NDT & E International* **62**: 66–76.

Liu Y (2024) Displacement and Damage Monitoring for Masonry Buildings Subjected to Ground Movements Induced by Underground Constructions, DPhil thesis, University of Oxford.

Maundrill ZC, Dams B, Ansell M *et al.* (2023) Moisture and fungal degradation in fibrous plaster. *Construction and Building Materials* **369**: 130604.

Nakatani H, Kundu T and Takeda N (2014) Improving accuracy of acoustic source localisation in anisotropic plates. *Ultrasonics* **54(7)**: 1776–1788.

Nejati HR, Nazerigivi A, Imani M and Karrech A (2020) Monitoring of fracture propagation in brittle materials using acoustic emission techniques-a review. *Comput. Concr* **25**: 15–27.

Ngah SA, Dams B, Ansell MP *et al.* (2020) Structural performance of fibrous plaster. Part 1: physical and mechanical properties of hessian and glass fibre reinforced gypsum composites. *Construction and Building Materials* **259**: 120396.

Romhany G, Czigany T and Karger-Kocsis J (2017) Failure assessment and evaluation of damage development and crack growth in polymer composites via localisation of acoustic emission events: a review. *Polymer Reviews* **57(3)**: 397–439.

Sause MG, Müller T, Horoschenkoff A and Horn S (2012) Quantification of failure mechanisms in mode-I loading of fiber reinforced plastics utilising acoustic emission analysis. *Composites Science and Technology* **72(2)**: 167–174.

Zhou J, Mathews VJ and Adams DO (2019) Acoustic emission–based impact location estimation on composite structures. *Structural Health Monitoring* **18(5–6)**: 1652–1668.

Zhou W, Pan ZB, Wang J *et al.* (2023) Review on acoustic emission source location, damage recognition and lifetime prediction of fiber-reinforced composites. *Journal of Materials Science* **58(2)**: 583–607.

Zuo J, Mayfield S, Ozdemir A *et al.* (2023) Preliminary experimental investigation on mechanical properties of historic fibrous plaster, In *Paper presented at SAHC2023: 13th International Conference on Structural Analysis of Historic Constructions*.

Zuo J, Sheil B and Acikgoz S (2024) A three-stage approach based on 1D-CNNs for AE source localisation on historic fibrous plaster ceilings. *Structural Health Monitoring* 14759217241245309.

How can you contribute?

To discuss this paper, please email up to 500 words to the editor at support@emerald.com. Your contribution will be forwarded to the author(s) for a reply and, if considered appropriate by the editorial board, it will be published as discussion in a future issue of the journal.

Proceedings journals rely entirely on contributions from the civil engineering profession (and allied disciplines). Information about how to submit your paper online is available at www.icevirtuallibrary.com/page/authors, where you will also find detailed author guidelines.

Downloaded by [UNIVERSITY OF OXFORD] on [04/06/25]. Copyright © ICE Publishing, all rights reserved.

Statement of Authorship

Paper title	Acoustic emission-based failure detection and event source localisation in a historical fibrous plaster ceiling
Authors	Jiaxu Zuo, Sarah Mayfield, Brian Sheil, Sinan Acikgoz
Publication status	Published
Publication details	Zuo, Jiaxu, et al. "Acoustic emission failure detection and localisation in historic fibrous plaster ceiling." Proceedings of the Institution of Civil Engineers-Engineering History and Heritage 177.4 (2024): 147-159.

Student Confirmation

Student name	Jiaxu Zuo
Contribution to the paper	First-author contribution: • Conceived research objectives • Designed and conducted experiments • Developed and implemented computational models • Prepared and presented the manuscript
Signature	
Date	23th September 2025

Supervisor Confirmation

By signing the Statement of Authorship, the supervisor is certifying that the candidate made a substantial contribution to the publication, and that the description above is accurate.

Supervisor name	Prof. Sinan Acikgoz
Supervisor comments	
Signature	
Date	23th September 2025

Chapter 6

Paper 4:Acoustic emission and in-situ synchrotron X-ray computed tomography for the investigation of tensile failures in fibrous plaster

Composites Part B 319 (2026) 113659

Contents lists available at ScienceDirect

Composites Part B

journal homepage: www.elsevier.com/locate/composites

Acoustic emission and in-situ synchrotron X-ray computed tomography for the investigation of tensile failures in fibrous plaster

Jiaxu Zuo [a,*], Sarah Mayfield [b], Thomas Zillhardt [c], Stefan Michalik [c], Genoveva Burca [c,d,e], James Marrow [f], Sinan Acikgoz [a]

[a] Department of Engineering Science, University of Oxford, Parks Road, Oxford, OX1 3PJ, United Kingdom
[b] National Trust, United Kingdom
[c] Diamond Light Source Ltd, Harwell Science and Innovation Campus, Oxford, OX11 0DE, United Kingdom
[d] ISIS Pulsed Neutron and Muon Source, Harwell Science and Innovation Campus, Didcot, OX11 0QX, United Kingdom
[e] Faculty of Science and Engineering, The University of Manchester, Oxford Road, Manchester, M13 9PL, United Kingdom
[f] Department of Materials, University of Oxford, Parks Road, Oxford, OX1 3PJ, United Kingdom

ARTICLE INFO

Keywords:
Fibrous plaster (FP)
Acoustic emission (AE)
Unsupervised clustering
RA–AF method
Failure mechanism classification
Digital image correlation (DIC)
Direct tensile testing
Synchrotron X-ray computed tomography (sCT)
Digital volume correlation (DVC)
Crack analysis
Kabsch algorithm

ABSTRACT

Fibrous plaster (FP) is a fabric-reinforced composite (FRC) comprising plaster of Paris (POP) and woven jute fabric ('hessian'), historically used in decorative ceilings across the UK since the late 19th century. Despite its architectural significance, FP remains under-researched, limiting the development of reliable structural assessment methods. Recent ceiling failures have been linked to the tensile failure of the supporting component known as the 'wad'. Acoustic emission (AE) provides a non-destructive means of remotely sensing and locating such failures from the underside of ceilings, yet its potential for extracting detailed information on FP wad failure processes remains unexplored. This study comprises two parts. First, an AE-based failure classification model was developed using unsupervised spherical k-means clustering to distinguish matrix cracking and fabric–matrix debonding based on the RA-AF method. Second, the first in-situ direct tensile tests on FP wad-analogue specimens conducted under synchrotron X-ray imaging were conducted at the I12 beamline of Diamond Light Source (DLS), UK, integrating AE monitoring with digital image correlation (DIC) and synchrotron X-ray computed tomography (sCT). This multi-modal dataset enabled examination of the AE model and internal failure analysis through digital volume correlation (DVC), while complementary crack analysis and the Kabsch algorithm provided new insight into the failure mechanisms of FP wads and revealed the reinforcement-bridging role of the hessian during progressive fracture. By linking remote AE monitoring with multi-scale observations, this study advances understanding of FP failure processes, offering a pathway for assessing historic ceilings and informing the design of more resilient FP components.

1. Introduction

Fibrous plaster (FP) is a fabric-reinforced composite (FRC) comprising plaster of Paris (POP) as the matrix and woven jute fabric (hessian) as the reinforcement. It has been widely used in decorative suspended ceilings in the UK since the late 19th century [1]. Column-like FP components, known as 'wads', are formed by twisted hessian embedded in POP and connect ceiling panels to a supporting framework located beneath the structural floor (Fig. 1). Wads are prone to tensile failure due to their irregular geometry, the brittleness of POP [1], its sensitivity to humidity [2], and the degradability of hessian [1]. Recent tests have confirmed their structural limitations [3], and such failures have been linked to ceiling collapses in London [2]. Current inspection methods, conducted via visual or tactile checks through ceiling hatches [2,4], are subjective and the enabling works for these inspections can be destructive. Despite the difficulties associated with conducting these inspections, current approaches are unable to detect early-stage internal micro-failures in the wad elements. An objective and non-intrusive method is therefore urgently needed to assess wad integrity and predict performance.

FP exhibits tensile behaviour consistent with the Aveston–Cooper–Kelly (ACK) theory [5]. This behaviour can be characterised with the following stages: (i) pre-cracking, where the matrix and reinforcement are fully bonded and deform elastically, with the matrix carrying most of the load; (ii) crack development, where matrix cracking induces load transfer (the redistribution of axial force from the cracked matrix to the reinforcement via interfacial shear), leading to debonding and enabling

* Corresponding author.
E-mail address: jiaxu.zuo@eng.ox.ac.uk (J. Zuo).

https://doi.org/10.1016/j.compositesb.2026.113659
Received 11 December 2025; Received in revised form 5 March 2026; Accepted 29 March 2026
Available online 30 March 2026
1359-8368/© 2026 The Authors. Published by Elsevier Ltd. This is an open access article under the CC BY license (http://creativecommons.org/licenses/by/4.0/).

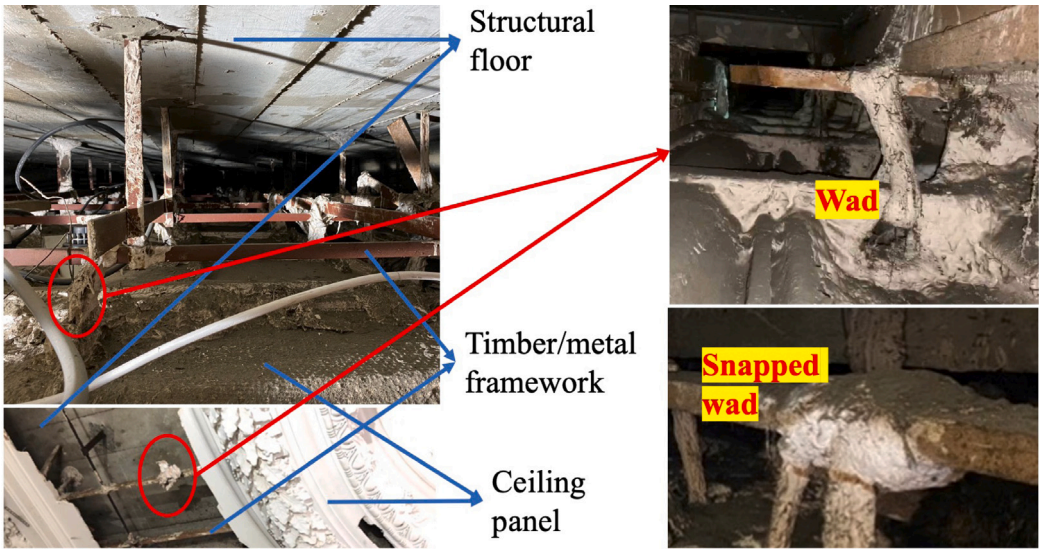


Fig. 1. Typical structure of historic FP ceilings (photos by authors).

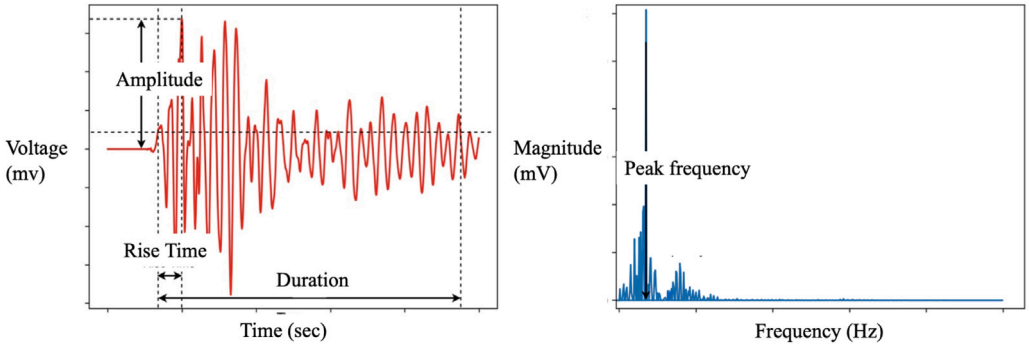


Fig. 2. AE waveform with key parameters in the time and frequency domains.

reinforcement-mediated crack bridging; and (iii) post-cracking, where tensile resistance is sustained by the reinforcement–matrix interface and the reinforcement until ultimate failure. Tests on dog-bone FP wad-analogue specimens confirmed this type of response [6]. The force–displacement curves highlight the multiple instances of recovery of load carrying capacity after matrix crack development, due to the crack bridging provided by twisted hessian. The maximum load capacity is reached only after the final stage of crack development. Consequently, FP specimens demonstrate notable displacement capacity (in the order of several millimetres) at ultimate failure.

[6] have highlighted the two essential failure mechanisms in FP under tension as matrix cracking and debonding. Matrix cracking precedes debonding due to the stiff matrix and flexible reinforcement materials. As cracks develop, the stiffness of the matrix degrades and the load is transferred to the fibres. Since the tensile strength of fibres are higher than the interfacial debonding strength, debonding failures dominate the behaviour of fibres. Tracking the evolution of these failure mechanisms can be useful for objective assessment of structural condition and performance prediction.

Acoustic emission (AE) is a non-destructive technique that detects transient elastic waves generated by the rapid release of strain energy during micro-failures such as cracking and debonding [7]. Each micro-failure produces an AE waveform whose features, termed AE parameters, reflect the underlying mechanism. Parameter-based analysis, which extracts and evaluates these AE parameters, is widely applied for failure classification [8–11]. Typical AE parameters in the time and frequency domains are illustrated in Fig. 2 and are described in Table 1 [12].

Table 1
Descriptions of key AE parameters [12].

AE parameter	Description
Threshold	Voltage level used to filter low-amplitude noise.
Counts	Number of ascending threshold crossings within a waveform.
Amplitude (AMP)	Peak amplitude of a waveform.
Duration (DUR)	Time from first to last threshold crossing.
Rise time (RT)	Time from first crossing to AMP.
Average frequency (AF)	Counts divided by DUR.
Rise angle (RA)	RT divided by AMP.
Peak frequency (PF)	Frequency with maximum spectral magnitude.
Energy (ENE)	Total signal energy of a waveform, calculated as the area under the rectified voltage–time waveform over DUR.

In FRCs, failures are generally classified as tensile or shear modes, each producing distinct AE waveforms. Tensile failures, associated with matrix cracking, generate denser, P-wave-dominated signals, whereas shear failures, such as fabric–matrix debonding, yield sparser, S-wave-dominated signals [13]. The differences between these signals can be captured via AE parameter relationships [14,15], as outlined in the JCMS guidelines [16]. Tensile-type signals exhibit higher AF and PF, lower RA, and shorter DUR and RT [13–15,17,18], while shear-type signals show the opposite trends. The lower velocity and higher attenuation of S-waves [15,19] explain their longer RT, lower ENE,

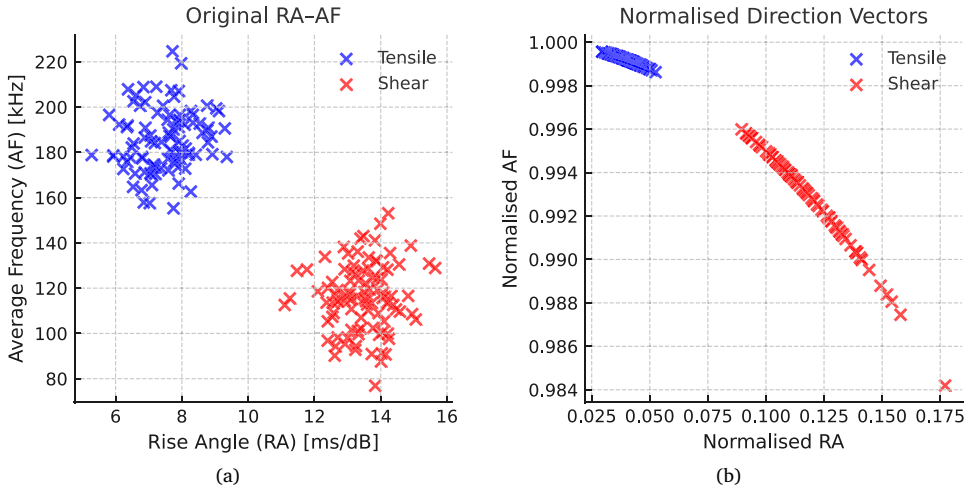


Fig. 3. RA–AF distributions for tensile–shear failure mode classification: (a) original features, (b) normalised vectors.

and reduced detectability, whereas P-wave-dominated tensile events typically have higher ENE due to reduced dissipation and greater radiation efficiency [20]. These contrasts underpin the use of RA-AF space for tensile–shear classification [14,15].

Fig. 3(a) shows a representative RA-AF distribution, with tensile events clustering in the upper-left quadrant (high AF, low RA) and shear events in the lower-right quadrant (low AF, high RA). While these modes can be qualitatively separated, no standard criterion defines the boundary, and empirical RA-AF ratios used in practice vary across materials [21]. As an alternative, machine learning (ML) techniques have been applied to RA-AF classification, offering data-driven failure mode identification [8,22–24]. Das et al. [8] combined Gaussian Mixture Model (GMM) pre-labelling with Support Vector Machines (SVM) for supervised classification. Ju et al. [23] used K-means and GMM clustering, with SVM and k-Nearest Neighbours (k-NN) enhancing accuracy. Chen et al. [24] proposed a four-step GMM framework for failure mode classification in corroded concrete, achieving more objective results than threshold-based methods. Collectively, these studies highlight the value of unsupervised clustering for unlabelled AE data, given the absence of ground truth. However, methods such as K-means [23,25,26] and GMM [8,23,24] assume round-shaped or Gaussian data distributions, which may not capture the nature of AE waveforms and can introduce bias [8]. To address this, Yue et al. [27] proposed a direction-based clustering method that normalises RA and AF into unit-length vectors, $\vec{AR} = \begin{bmatrix} AF & RA \end{bmatrix}$, eliminating scale effects and retaining only directional information. A Self-Organising Map (SOM)-inspired competitive learning algorithm was then applied for two-class classification. SOMs are unsupervised neural networks that project high-dimensional data onto a lower-dimensional grid while preserving topological relationships, making them effective for clustering. Fig. 3(b) shows tensile and shear events in normalised RA-AF space, where each point is a unit-length feature vector defined by its direction.

Imaging data provides an opportunity to comparatively evaluate the failure modes recognised by AE. In particular, DIC offers real-time, high-resolution surface displacement measurements by tracking surface speckle patterns [28]. In a previous study, some of the authors applied Digital Image Correlation to investigate matrix cracking in dog-bone FP specimens [6]. Although the use of surface speckle patterns allows measurements with small uncertainty, DIC cannot capture subsurface behaviour. This limitation can be addressed by combining synchrotron X-ray computed tomography (sCT) with DVC, which computes three-dimensional displacement and strain fields using the existing phase contrasts in volumetric datasets [29]. DVC enables identification of internal failure modes including fabric–matrix debonding and fibre fracture [28,30–35]. Both DIC and DVC measure strain components, which allows distinguishing between tensile and shear failures [28]. Local DVC measurements can capture discontinuities but are prone to high measurement uncertainty. In contrast, global DVC enforces continuity through finite element meshes, improving robustness but risking smearing displacement discontinuities introduced by cracks. Combined use of DIC and DVC may allow high resolution surface data to validate volumetric results. In addition, the simultaneous use of local and global DVC techniques to respectively measure cracks and strains could offer a robust strategy for describing different modes of deformations in the FP samples.

This study presents an AE-based failure classification model employing unsupervised spherical k-means clustering on a large RA-AF dataset derived from AE waveforms recorded during direct tensile tests on wad-analogue dog-bone FP specimens. The model distinguishes matrix cracking from fabric–matrix debonding and is examined through first of its kind in-situ experiments at the I12-JEEP beamline, Diamond Light Source (UK) [36], which integrates AE monitoring, stereo-DIC, and sCT. The novel combination of various Digital Image Correlation (DIC) and Digital Volume Correlation (DVC) techniques provide a complementary framework for comprehensively deformations in the sample. Clustering results are compared temporally and spatially with DIC and DVC observations, while FP failure mechanisms and the bridging role of hessian within the POP matrix are further investigated through crack analysis and rigid-body rotation using the Kabsch algorithm based on DIC and DVC analyses. The paper first outlines the clustering methodology, followed by the in-situ synchrotron experiment, data processing and analysis. By cross examining the AE results with imaging data, the paper aims to improve our understanding of tensile mechanisms and provide a non-destructive and objective approach to sense wad failures from the underside of ceilings. Together, these findings aim to establish a practical monitoring pathway and provide insights to guide the reconstruction of more resilient wad elements in heritage FP ceilings.

2. AE-based failure mechanism classification model

2.1. Data acquisition

Dog-bone specimens, adapted from Zuo et al. [6], were prepared for AE data collection during direct tensile tests. Each specimen was cast in a custom steel mould, with the central fabric arranged to reflect the winding configuration observed in traditional wads (Fig. 4). A POP paste with a water-to-plaster ratio of 0.7, representative of historic FP [37], was prepared according to EN13279-2:2014 [38].

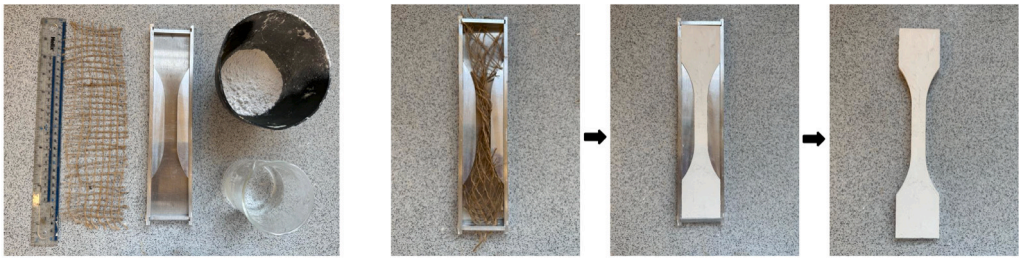


Fig. 4. Preparation procedure for dog-bone FP wad-analogue specimens.

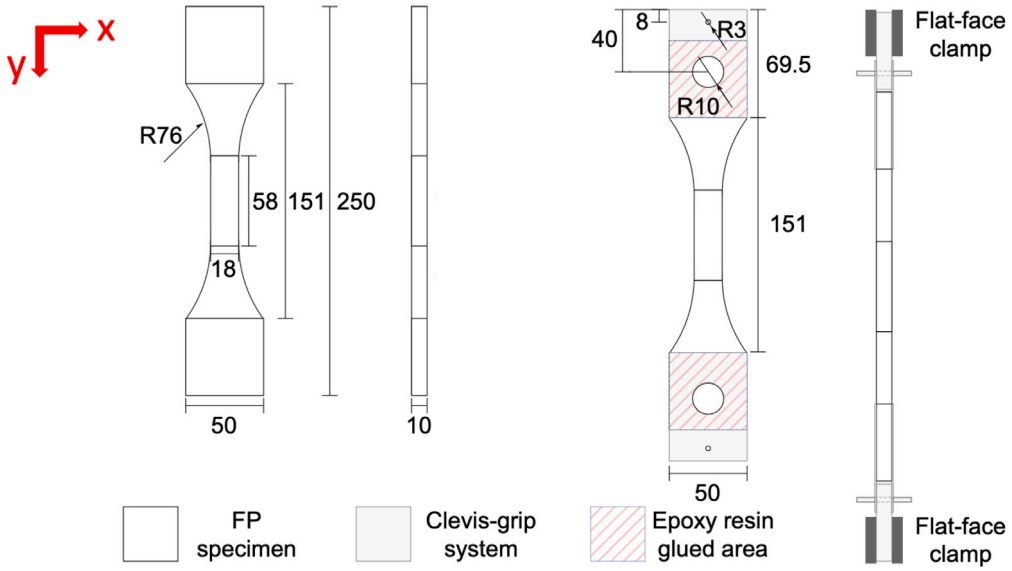


Fig. 5. Specimen geometry and clevis-grip system (dimensions in mm).

A 250 mm × 100 mm hessian sheet with eight warp yarns was embedded, twisted at the centre to replicate wad reinforcement, and spread at the ends. The specimens are not intended to replicate the exact geometry of historic wads; instead, a wound jute fabric was concentrated in the gauge section to form a column-shaped reinforcement zone, reproducing the key functional characteristics of wads while allowing controlled testing. POP and hessian were supplied by Industrial Plaster Ltd. [39,40]. Fig. 5 shows the specimen geometry and clevis-grip system, comprising a central rectangular gauge section (58 mm × 18 mm × 10 mm), arched transitions, and widened ends with 10 mm-radius holes for AE sensor attachment. Steel plates were bonded with Loctite Hysol 9466 epoxy and pinned through the holes to form the clevis grips, minimising slippage and premature failure while ensuring stable mechanical response and AE acquisition. Six dog-bone FP specimens were tested on an Instron 5582 with a 5 kN load cell under displacement control at 3 mm/min. The force–displacement responses were consistent across specimens (Fig. 6), in agreement with previous findings [6].

The AE system comprised a Mistras micro-SHM controller and four R6a sensors (S_1–S_4) connected to 40 dB amplifiers. Signals were acquired in AEwin [41] with a 40 dB threshold and band-pass filtered between 35–100 kHz to capture the low-frequency response events in FP. Sensors S_1 and S_2 were mounted on the front and S_3 and S_4 on the back of each specimen using tape within the clevis-grip holes (Fig. 7), with RS PRO grease ensuring acoustic coupling. System verification followed ASTM E976-15 [42] using Hsu–Nielsen (e.g. pencil lead breaking) sources applied at predefined positions. AE signals were sampled at 2 MSPS with 4096 points per event. Each AE event was localised using the Time of Arrival (TOA) method, based on arrival-time differences between sensor pairs, yielding a one-dimensional coordinate. The average wave speed in FP was measured as 2.53×10^6 mm/s using Hsu–Nielsen sources. Sensors S_1 and S_3 were placed at $y = 0$ mm (top) and S_2 and S_4 at $y = 210$ mm (bottom), forming front (S_1, S_2) and back (S_3, S_4) pairs. The localisation range was set to 0–210 mm, with only events within this window retained to exclude external noise and rig artefacts. For events detected by both front and back pairs, the waveform with the highest ENE across all four channels was retained; otherwise, the higher-ENE waveform from the active pair was used for parameter extraction.

2.2. RA-AF clustering analysis

With all four AE sensors active, 181,359 waveforms were recorded from six repeated tests. To maximise the dataset for clustering-based failure classification, one-dimensional localisation and related filtering were omitted. After discarding invalid records, 174,606 waveforms remained. For each waveform i ($i = 0, \ldots, 174,605$), features were computed as $RA_i = RT_i/AMP_i$ and $AF_i = counts_i/DUR_i$, forming the 1×2 vector $\vec{AR}_i = [AF_i \quad RA_i]$. Five random subsets of 1000 vectors were used for evaluation ($D_{\text{test}}^{(i)}$, $i = 1, \ldots, 5$), and the remaining 169,606 formed the training set D_{train}. All vectors were normalised to unit Euclidean norm, and the normalised $\vec{AR}_i^{\text{norm}} \in D_{\text{train}}$ were used to train unsupervised models that classify AE waveforms from FP direct tensile tests into two clusters: matrix cracking (MC) and fabric–matrix debonding (DB). These two clusters correspond to the dominant failure mechanisms observed prior to the final peak of the force–displacement curves in Fig. 6. Only the AE signals within this loading regime were analysed, and therefore the identified clusters represent the dominant mechanisms active before ultimate peak load. Other mechanisms, such as fibre fracture, were not evidently observed within

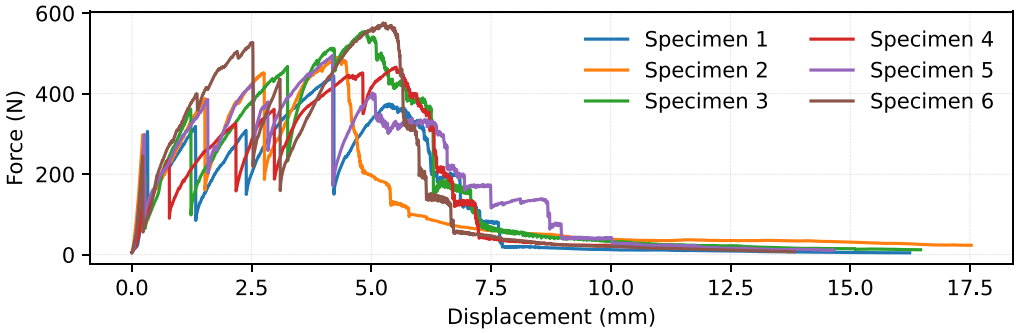


Fig. 6. Force–displacement responses from direct tensile tests on dog-bone wad-analogue FP specimens.

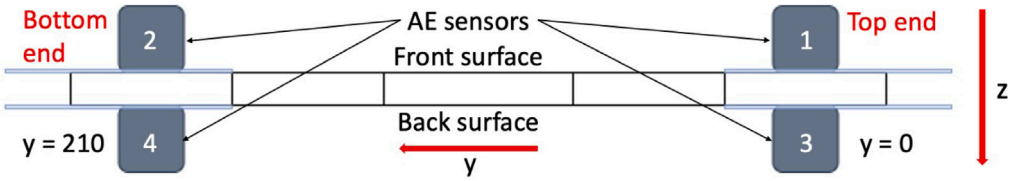


Fig. 7. AE sensors (S_1–S_4) placed within the clevis-grip system of the FP specimen.

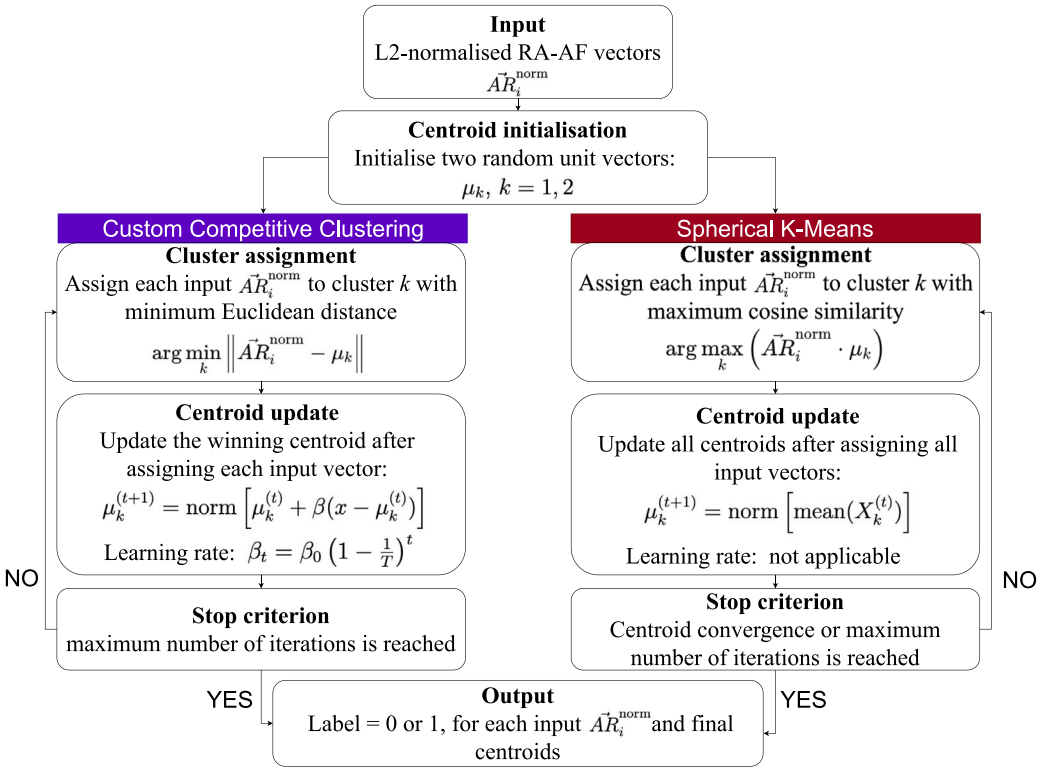


Fig. 8. Workflows of two direction-based clustering algorithms: custom competitive clustering and spherical k-means, applied for tensile–shear classification.

the present dataset. Two direction-based algorithms were evaluated: a SOM-inspired competitive method proposed by Yue et al. [27] and spherical k-means [43] (workflows in Fig. 8). Conventional k-means minimises squared Euclidean distance, which is magnitude-sensitive, whereas spherical k-means maximises cosine similarity, making assignments direction-dependent [44] and better suited to the RA-AF analysis. The comparison was restricted to the two direction-based algorithms, which induce separating hyperplanes through the origin and therefore align with the direction-dominated RA-AF geometry. As will be shown next, despite differing objectives, both approaches yielded similar classifications, indicating robustness.

Fig. 9 shows the distribution of RA-AF vectors for a representative subset $D_{\text{test}}^{(i)}$. Events cluster near the origin (low AF, RA), mainly in the upper-left and lower-right quadrants, with density decreasing as AF or RA increase, forming a sparse pattern. Clustering results on this subset using the trained SOM-inspired competitive method and spherical k-means are compared in Fig. 10. These clusters are used to pre-label the subset. Then SVM classifiers are trained to separate MC (tensile) and DB (shear) events. The resulting hyperplanes had mean angles of 32.51° (CoV 17.53%) and 32.69° (CoV 16.92%) for the two methods across all test subsets, showing consistent orientation. The clustered MC and DB distributions conform to the RA-AF theory [14,15] and agree with Yue

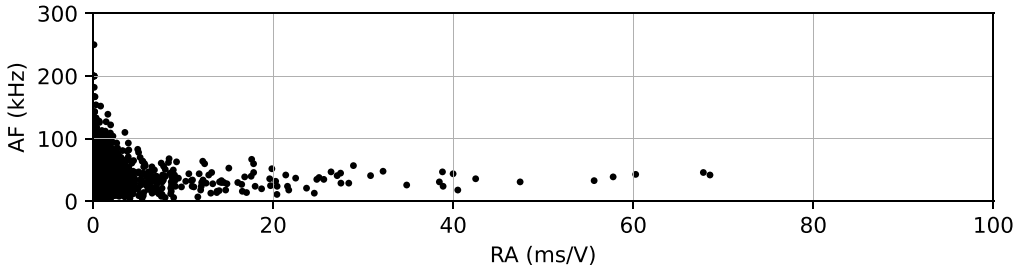


Fig. 9. Distribution of original RA-AF feature vectors, $\vec{AR}_i = [AF_i \quad RA_i]$.

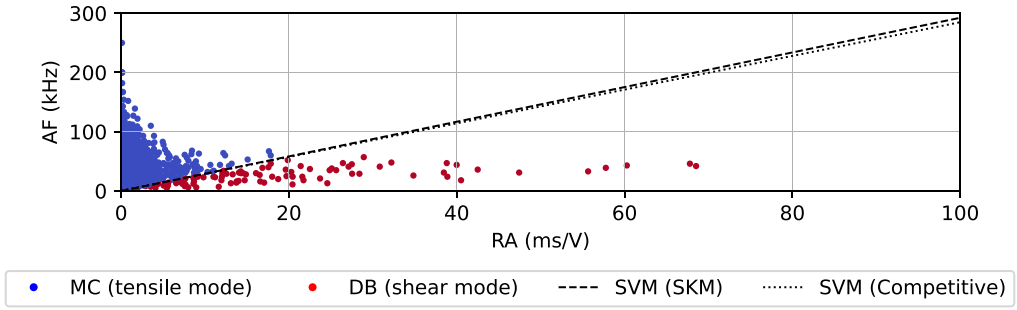


Fig. 10. Clustering results in RA-AF space using the SOM-inspired competitive clustering and spherical k-means models, along with their corresponding SVM hyperplanes.

et al. [27]. Clustering quality was evaluated over a limited range of cluster numbers (k = 2–4) using the cosine silhouette score [45] and cosine Davies–Bouldin Index (cDBI) [46], averaged over all test subsets. Both models performed well, with highest silhouette scores > 0.9 and lowest cDBI < 0.2.

Although results were similar, the SOM-inspired method was slower sample-wise updates and less automated owing to fixed-iteration termination. Spherical k-means, using batch updates and convergence-based termination, was faster and more robust, and was therefore adopted for subsequent analyses.

3. Beamline in-situ experiment

3.1. Experimental setup

To build confidence in the AE-based classification with imaging data, in-situ direct tensile tests were performed on dog-bone FP specimens at the I12-JEEP beamline, Diamond Light Source (UK), integrating AE, DIC, and sCT. The setup in the beamline coordinate system is shown in Fig. 11(a). Uniaxial loading was applied using a 10 kN servo-hydraulic Instron rig on a motorised table [47], controlled via an 8800MT controller and Console software. Flat-faced clamps (25 mm × 25 mm) secured the clevis-grip system. The table allowed translation along the x, y, and z axes, and restricted rotation along y from −70.9° to 60.5°. The X-ray beam is aligned with the z-axis, and the detector placed downstream. sCT scans were acquired at 7.9 μm × 7.9 μm, to be able to clearly resolve jute yarns (which have characteristic diameters of 0.64–1.14 mm [37]) in the tomography data.

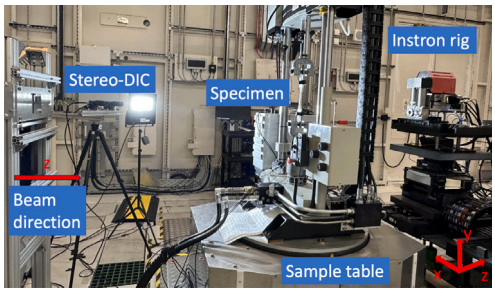
To cover the 120 mm gauge length, the specimen was scanned in 12 overlapping sub-volumes (Z_1–Z_{12}) along the y-axis (Fig. 11(b)). Each sub-volume had a Field of View (FoV) of 2560 × 1450 pixel (20.22 × 11.46 mm^2) in the XY-plane, with a vertical overlap of 1.7 mm for stitching. Acquisition time per sub-volume was around 5 min.

Fig. 11(c) shows the AE sensor setup, with sensors fixed in the clevis grips using tape. The stereo-DIC system (Fig. 11(d)) used two ME2P-2621-15U3M cameras with Kowa LM100FC24M 100 mm lenses and LED illumination. Acquisition, calibration, and processing were performed in MatchID [48]. The stereo angle was 15.85°, with noise standard deviations of 6.54 μm (horizontal) and 4.49 μm (vertical), based on 33-pixel subset and 10-pixel step sizes. Images were recorded at 2 Hz. AE and DIC sensors were connected to the controllers located outside the experimental hutch via long cables. This allowed remote actuation of the measurement system when the beam is on.

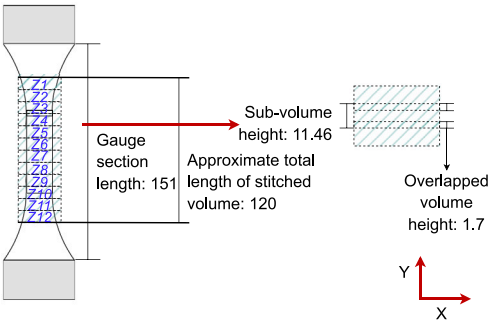
3.2. Data acquisition

Two tests were performed at I12. Only the second test will be discussed in this paper, since the first test indicated uncharacteristic premature failure. The first specimen failed prematurely due to setup-induced eccentric loading caused by slight grip misalignment, which generated unintended bending and localised stress concentrations near the grip region. This resulted in failure outside the intended central gauge section, indicating that the response was influenced by experimental artefacts rather than intrinsic material behaviour. After correcting the alignment conditions, the second specimen was tested under improved loading symmetry and is therefore considered to provide the only valid dataset for the present analysis, with performance consistent with previous tests. The effective sample size is thus one, which represents a limitation; accordingly, the findings should be interpreted as a detailed mechanistic investigation under controlled conditions rather than as statistically generalisable results.

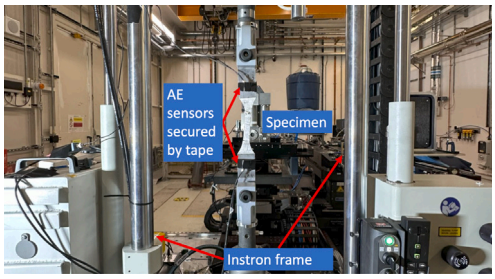
The Instron, operated in displacement control, was paused at predefined loads for sCT acquisition, each pause denoted as an observation point. Seventeen points O_i ($i = 1, \ldots, 17$) were defined: O_1 and O_2 without load, O_3 at 25 N pre-tension, and O_4-O_{17} covering the remainder of the test. Fig. 12 shows the load–displacement response with all observations annotated. The corresponding load and displacement values are provided in Appendix. At each observation point, sCT data were acquired while the Instron was held at the same displacement. Once the data acquisition was completed, the loading resumed. During loading, AE and DIC were recorded, with extra DIC images taken at each pause. This ensured sCT captured static states, AE monitored real-time damage, and DIC provided continuous high-resolution full-field displacement.



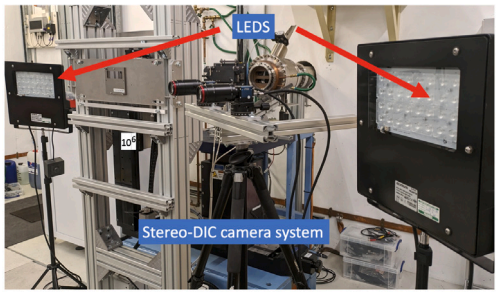
(a) In-situ experimental setup within the beamline coordinate system.



(b) Overlapping sub-volumes (Z_1-Z_{12}) for sCT measurement (in mm).



(c) Dog-bone FP specimen mounted with AE sensors for real-time monitoring.



(d) DIC system for full-field surface displacement measurement.

Fig. 11. in-situ experimental setup integrates AE, stereo-DIC, and sCT monitoring.

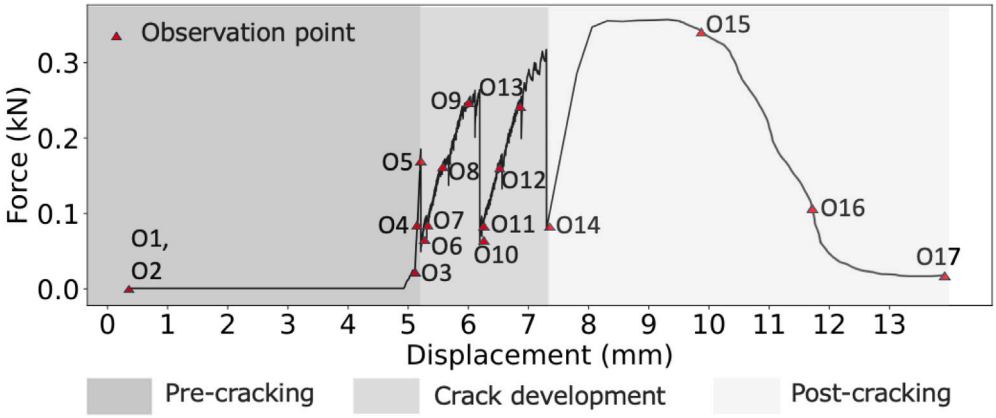


Fig. 12. Load–displacement response of the wad-analogue FP specimens from in-situ direct tensile testing, with observation points O_1–O_{17} annotated.

3.3. Data preprocessing

For each valid event, the AE waveform and one-dimensional source coordinate y ($0 \leq y \leq 210$ mm) were recorded. RA-AF arrays were formed from extracted AE parameters and normalised to unit vectors. The trained spherical k-means model (Section 2.2) classified events as MC or DB. Additional AE parameters (counts, AMP, DUR, RT, PF, ENE) were also extracted.

While the specimen was stationary at each observation point, 30 frames per camera were averaged to reduce noise before DIC analysis. Full-field displacements were then obtained using a 33-pixel subset and 10-pixel step size.

The sCT data preprocessing involved:

- Faulty flat- or dark-field images were replaced with the nearest valid image to ensure reconstruction accuracy.
- The optimal centre of rotation was determined for each sub-volume.
- Trial reconstructions on random slices identified the best method and iteration number; the Simultaneous Iterative Reconstruction Technique (SIRT) with 145 iterations was selected, and full sub-volume reconstructions were then performed on the Diamond Light Source computer.
- In ImageJ, each sub-volume was cropped to $2560 \times 1450 \times 1811$ voxels ($X \times Y \times Z$) to remove air and other unwanted content, then slices were normalised and converted from 32-bit to 8-bit for further analysis.

The reconstructed sub-volumes were then used for feature-based stitching and for local and global DVC analyses in Avizo. Since the stitching was not precise enough, all DVC analyses were conducted within individual sub-volumes.

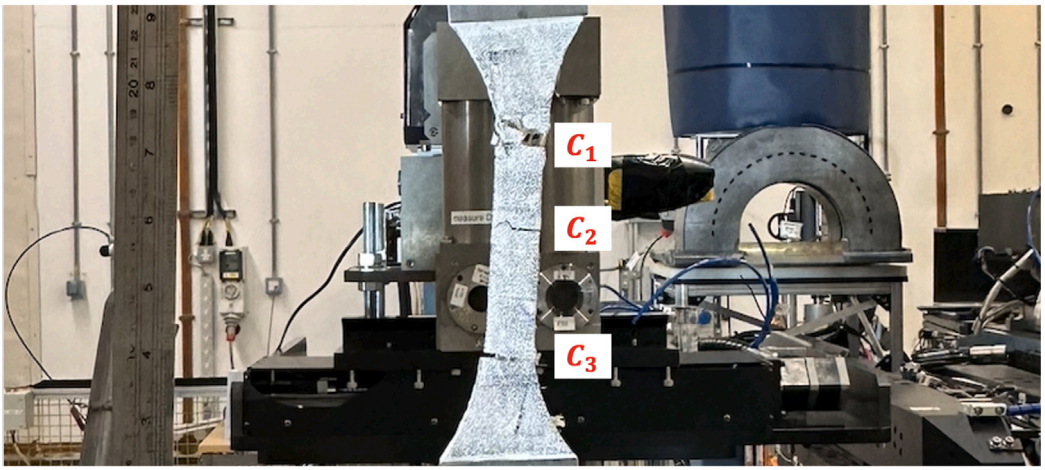


Fig. 13. Final crack pattern of the FP specimen after the in-situ test.

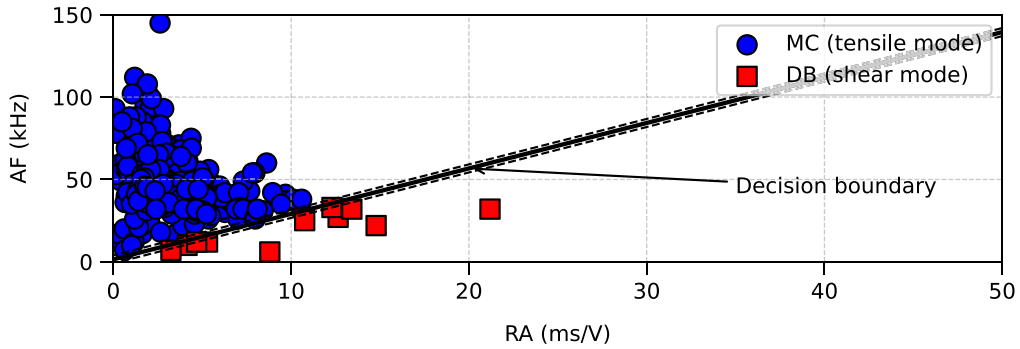


Fig. 14. RA-AF clustering of MC and DB events during the in-situ test.

4. Results and discussion

Based on the load–displacement response, the intervals before O_5, between O_5 and O_{14}, and after O_{14} correspond to pre-cracking, crack development, and post-cracking, consistent with ACK theory and reported FP behaviour [6]. Points O_6, O_{10}, and O_{14} were recorded immediately after the initiation of major transverse cracks C_1, C_2, and C_3, each preceded by a sharp load drop. These cracks formed sequentially, and the final crack pattern is shown in Fig. 13, with ultimate failure occurring at C_1, where the first major crack had formed.

4.1. AE-based failure mechanism classification

No AE events were detected before O_5, confirming elastic behaviour and the absence of major cracks. Between O_5 and O_{14}, major cracks formed sequentially with progressive widening, during which valid AE events were recorded. After O_{14}, crack widening reduced AE-based localisation reliability. As critical cracking occurred between O_5 and O_{14} and valid events persisted to O_{15}, events from O_5-O_{15} were used for failure mechanism classification. A total of 450 valid AE waveforms were classified as MC (n = 401) or DB (n = 49). Fig. 14 shows their RA-AF distribution from the trained spherical k-means model. The two clusters are linearly separable by an SVM boundary: MC events cluster in the upper-left quadrant (high AF, low RA), while DB events occupy the opposite region (low AF, high RA), reflecting tensile and shear characteristics. Appendix figures show DUR, RT, PF, and ENE distributions for both clusters, following the expected trends discussed in Chapter 1.

Fig. 15 shows the spatio-temporal evolution of MC and DB events between O_5 and O_{15}. All events localised within the gauge region, with none near the clevis grips, confirming setup validity and absence of premature failure. Their spatial distribution relates closely to the location of cracks C_1, C_2, and C_3, as described below:

1. From C_1 initiation to just before C_2 (O_5–O_9): Between O_5 and O_6, C_1 initiated with only MC events and no change in the MC/DB ratio. From O_7 to O_9, DB events appeared in small but increasing numbers, raising the DB proportion to 1.39% and indicating onset of interfacial shear linked to crack widening, while the matrix still carried most of the load.
2. From C_2 initiation to just before C_3 (O_9–O_{13}): C_2 initiated between O_9 and O_{10}, marked by localised MC events, a rebound in MC proportion, and reduced DB. No AE occurred between O_{10} and O_{11}, indicating a stable phase. From O_{11} to O_{13}, DB rose sharply to 20% as C_2 widened, with events concentrated at its site. This reflects intensified debonding, with shear resistance aiding crack bridging and load transfer as the matrix degraded. The absence of AE near C_1 suggests its widening had ceased, restrained by yarn interlocking and stress redistribution to C_2.
3. From C_3 initiation to the end of crack development (O_{13}–O_{15}): Between O_{13} and O_{14}, C_3 initiated with MC events at its site. DB persisted at C_2 but fell to 16.67%, mirroring the temporary drop after C_2 formed and suggesting brief subsidence of interfacial activity. Unlike C_1 during C_2 formation, C_2 did not fully lock, indicating further loss of FP integrity. From O_{14} to O_{15}, MC and DB events concentrated between C_1 and C_2, with DB still high at 9.52%. This localisation shows deformation had shifted back to this region, consistent with ultimate failure at C_1. Extensive cracking and degradation likely impaired AE detection and localisation, explaining the absence of events near C_3 and reduced DB during O_{14}–O_{15}.

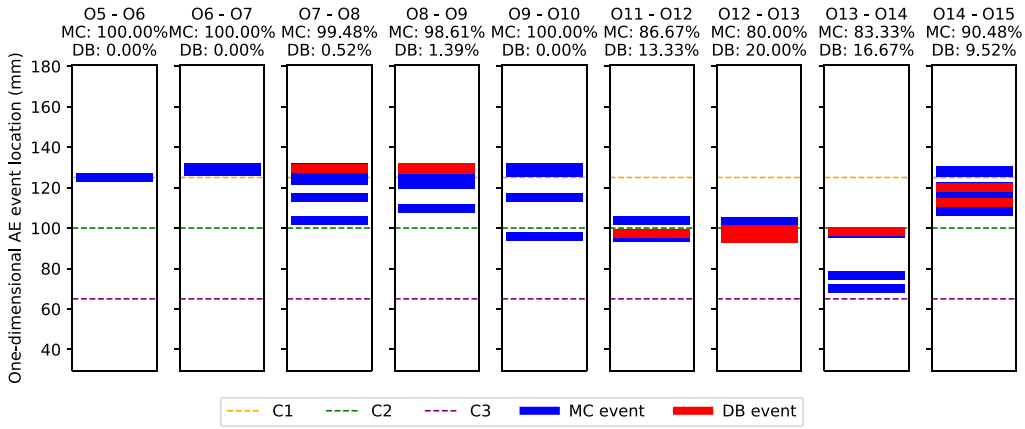


Fig. 15. Spatio-temporal evolution of classified MC and DB events between O_5 and O_{15}. Dashed horizontal lines in different colours indicate experimentally observed crack locations (C1–C3), while coloured bars show the spatial distribution of AE events classified as matrix cracking (MC, blue) and fabric–matrix debonding (DB, red). (For interpretation of the references to colour in this figure legend, the reader is referred to the web version of this article.)

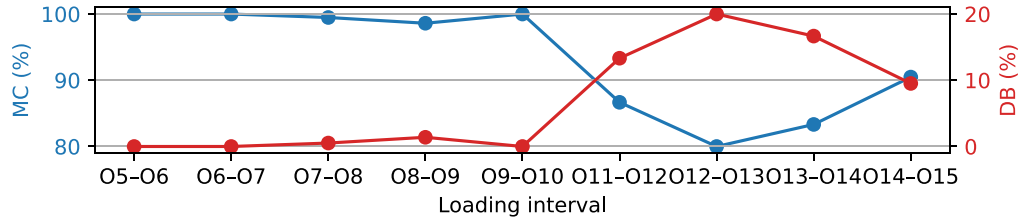


Fig. 16. MC and DB proportions between O_5 and O_{15}.

Fig. 16 shows MC and DB proportions, illustrating the progression of matrix cracking and interfacial debonding. Early in the test, MC dominated and DB was minimal, indicating the matrix bore most of the load. As loading progressed, DB increased, marking load transfer to the fabric as the matrix degraded. The DB trend closely followed the load–displacement response between O_5 and O_{14}, reflecting progressive crack widening and interfacial engagement. This progression in AE data indicates degradation of structural integrity in the FP wad system.

It is also worth noting that each major crack showed a distinct AE signature: MC dominated during initiation, while DB increased during widening. This sequence highlights yarn bridging in resisting crack opening and fabric–matrix bonding in shear resistance. Stress redistribution is evident as AE subsides at a stabilised crack and reappears at a new site.

4.2. 2D/3D crack analysis

According to AE data, MC and DB clusters were closely linked with the evolution of active cracks, with MC associated with initiation and DB with widening. Validation is achieved by further evaluating crack widening using DIC and local DVC. For the former, the Crack Analysis Module in MatchID is used, where major crack openings are computed as the average displacement jump $\delta(V, \text{avg})$ across the crack from one-sided images pertaining to observation points O_3–O_{15}, with O_3 serving as reference.

For local DVC calculations, the full sCT volume at each observation point was reconstructed by stitching sub-volumes Z_1–Z_{12}. Fig. 17 shows representative stitched and cropped volumes. O_3 is the pre-tensioned state, O_6, O_{10}, and O_{14} follow major crack initiation, and O_{15} is the final observation. These volumes clearly show cracks C_1–C_3 and a continuous hessian network (no major absences) in an irregular, winding, wad-analogue pattern. A representative XZ-plane slice representing cross-section of the specimen is also shown, with materials and air voids distinguished by phase contrast (shown with a greyscale).

For computational efficiency, the volume was resampled from 7.91 μm to 15.82 μm per voxel, sufficient to capture crack widening. Two VOIs centred on C_1 and C_2 were selected for local DVC (Fig. 17), with their dimensions and locations given in Table 2; C_3 was excluded due to large rigid body movements that shifted the scanned region and compromised accuracy. Radial autocorrelation estimated the microstructural correlation length at $\approx$ 64 voxels. A subset size of 3000 μm was thus adopted, within the recommended 192–256 voxel range (3037.44–4049.92 μm) for reliable computation [49]. Local DVC was chosen over global DVC for direct displacement discontinuity measurement across cracks. For both cracks, pre-cracking states served as references, followed by selected deformed states listed in Table 2. Crack width was calculated as the difference between the uppermost and lowermost averaged vertical displacements, $\delta(U_y, \text{avg})$, excluding poorly correlated regions. The temporal evolution of C_1 and C_2 in the XY and YZ planes is presented in Appendix.

Fig. 18 shows the temporal evolution of major crack widths from DIC and local DVC. In general, each crack widened rapidly after initiation, then plateaued before the next one formed. Crack opening evolution correlated with failure mechanisms: widening began with MC events (O_5-O_6 for C_1, O_9-O_{10} for C_2), while high-rate widening aligned with DB events (O_7-O_9 for C_1, O_{11}-O_{14} for C_2).

Although absolute crack widths from DVC differed slightly from DIC, overall trends were consistent. These discrepancies arose from differing reference states and from the surface sensitivity of DIC versus the volumetric insight of sCT-based DVC. Overall, DIC and local DVC showed strong agreement, supporting interpretation of crack initiation and progression and indicating effectively 2D behaviour of the sample.

4.3. Characterisation of matrix cracking and interfacial debonding failure mechanisms

To characterise FP failure mechanisms in further detail, global DVC was applied to the unbinned sCT data (voxel size 7.91 μm) to resolve fine microstructural features. A structured tetrahedral mesh (with

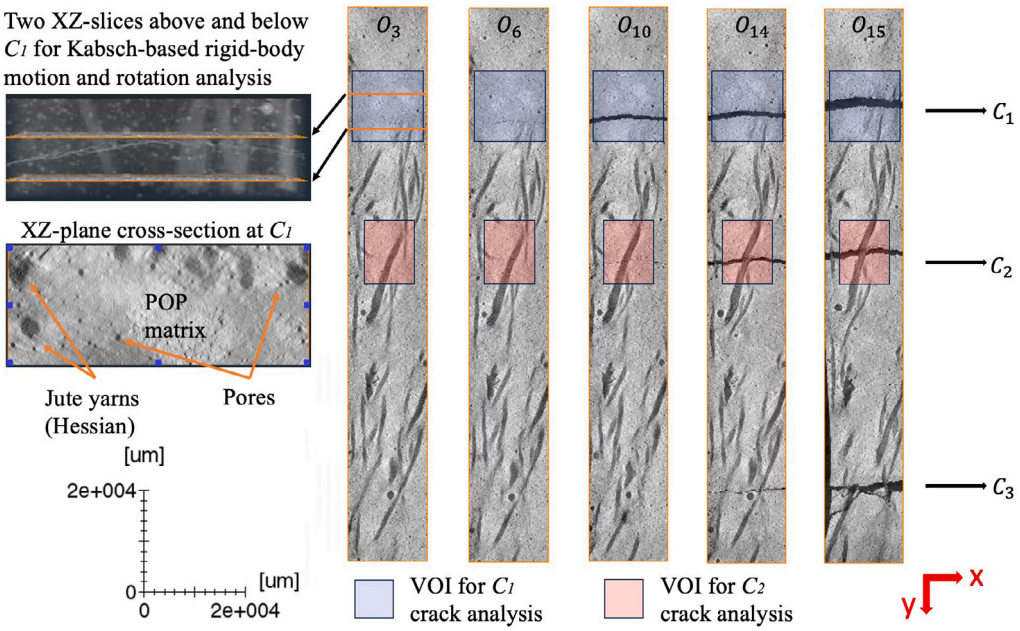


Fig. 17. Representative stitched volume of the FP specimen in XY view; VOIs for C_1 and C_2 crack analysis; two XZ slices above and below C_1 for rigid-body motion and rotation computing via the Kabsch algorithm.

Table 2
VOIs for crack analysis of C_1 and C_2 using resampled volumes with a voxel size of 15.82 μm based on local DVC.

	Dimensions (X × Y × Z, voxels)	Location	Reference state	Selected deformed state
C_1	1000 × 1000 × 400	Spanning Z_3, Z_4	O_5	O_5–O_{11}
C_2	701 × 906 × 351	Centred at Z_6	O_9	O_9–O_{14}

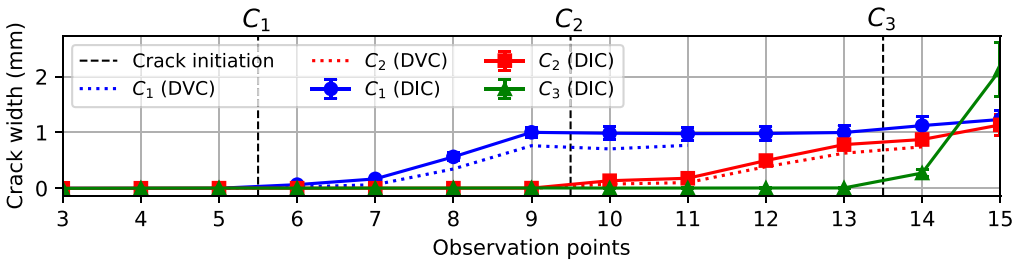


Fig. 18. 2D and 3D crack opening evolution from DIC and local DVC analyses.

700 μm sides) with incremental updating at each deformed step was used. A VOI spanning O_5-O_{13}, located between C_1 and C_2 but excluding the cracks using a narrow buffer of 1–2 voxels around the segmented crack surfaces to minimise correlation artefacts from discontinuities, captures pre-crack shear strain localisation immediately adjacent to the crack while ensuring physically meaningful strain fields, measured 1800 × 3000 × 377 voxels (≈ 14.24 × 23.73 × 2.98 mm^3). The reference VOI (Fig. 19) shows its location, geometry, and hessian distribution. It comprised three vertically stacked sub-VOIs (Z_4, Z_5, Z_6) aligned in the XZ plane. To avoid misalignment, global DVC was performed independently on each sub-VOI, and displacement and strain fields were stitched using half-overlapped regions without further processing.

The maximum shear strain field,

$$\gamma_{\max} = \frac{\varepsilon_1 - \varepsilon_3}{2},$$

where ε_1 and ε_3 are the maximum and minimum principal strains, was extracted. Key observations are as follows:

- After C_1 initiation, before C_2 initiation (O_5–O_9): As shown in Fig. 20, from O_5 to O_7, $\gamma_{\max}$ remained low, indicating negligible debonding, consistent with AE showing no DB events. From O_7 to O_9, $\gamma_{\max}$ rose sharply and extended downward along the interface, marking a propagating debonding front resisting crack widening, in agreement with DB events from C_1.
- After C_2 initiation (O_9–O_{13}): Between O_9 and O_{10}, MC events occurred at C_2 (outside the VOI and not visualised). As shown in Fig. 21, from O_9 to O_{11}, $\gamma_{\max}$ in the upper VOI (near C_1) stabilised without downward propagation, indicating halted debonding and crack widening, consistent with the absence of DB events from C_1. In the lower VOI (near C_2), $\gamma_{\max}$ also remained stable with no AE activity. From O_{11} to O_{13}, $\gamma_{\max}$ in the lower VOI rose sharply and spread upward, consistent with progressive DB events from C_2.

While the DB proportion generally correlates with the evolution of $\gamma_{\max}$ from global DVC, their spatial distribution does not fully align. AE-detected DB events remain concentrated near the crack front, with no

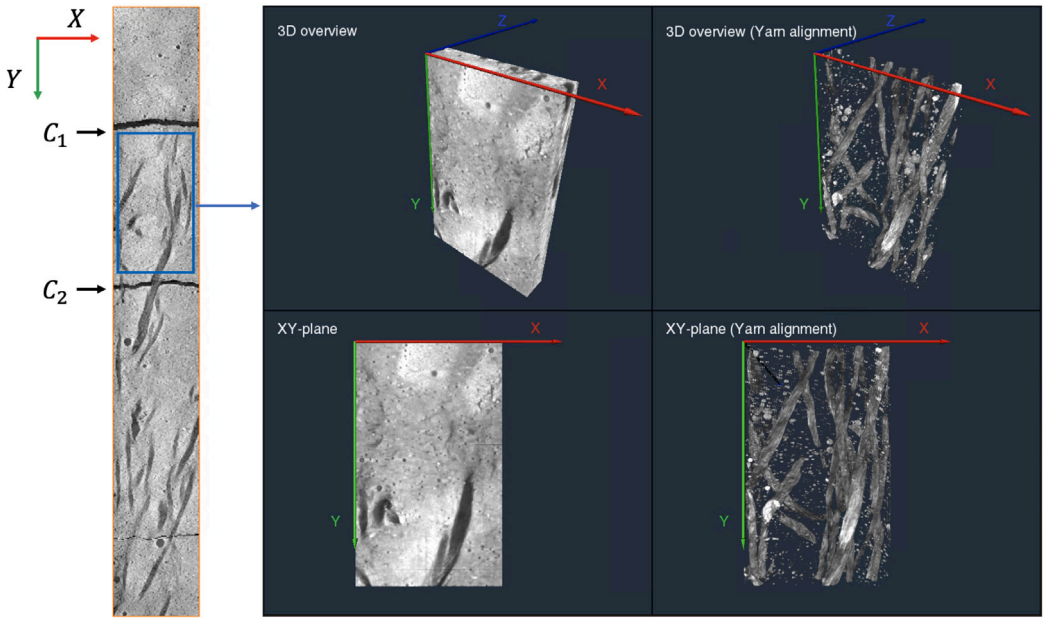


Fig. 19. Reference-state VOI for failure mechanism characterisation via global DVC.

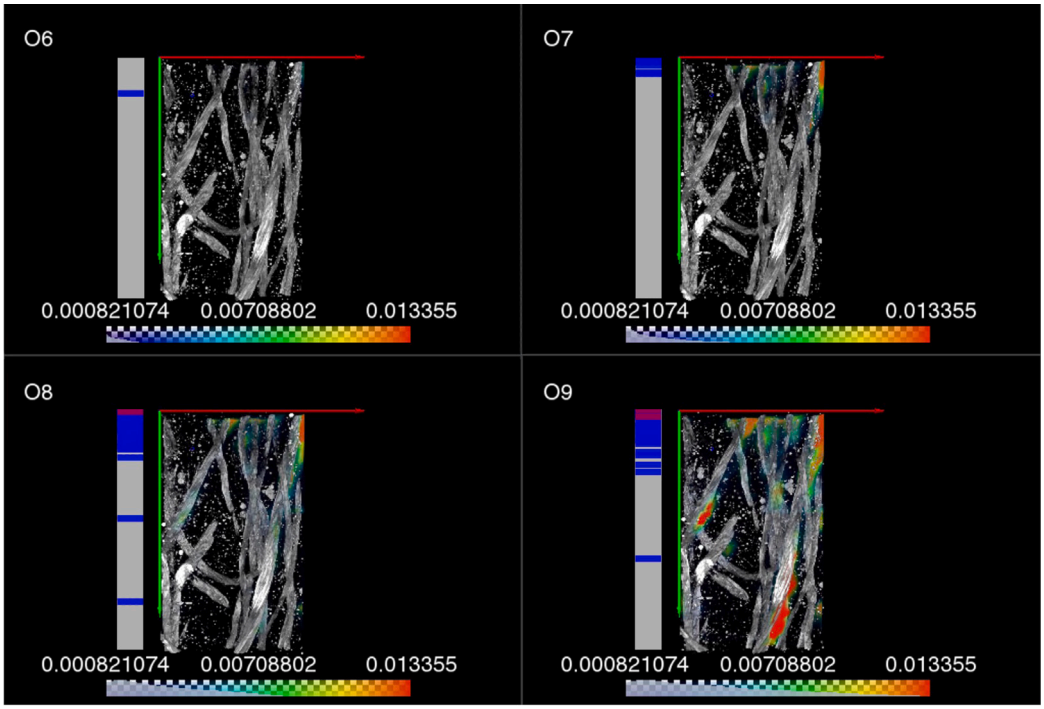


Fig. 20. Maximum shear strain (γ_{max}) between C_1 and C_2, along with AE events classified as either MC (blue) or DB (red) (O_5–O_9). (For interpretation of the references to colour in this figure legend, the reader is referred to the web version of this article.)

clear evidence of propagation along the yarn–matrix interface. Fig. 22 shows γ_{max} in the XZ plane from the top (near the C_1 crack front) downward, together with the specimen cross-section at the corresponding y-location. Owing to the twisted yarn architecture, interfacial stresses vary both along and around each yarn; debonding therefore initiates at local hotspots, progresses non-uniformly in a staggered manner, and remains concentrated near the crack front. From an AE perspective, γ_{max} is typically highest at the crack front, producing greater strain–energy release and stronger, more detectable signals, thus keeping DB events consistently localised there.

In contrast, MC events remain the predominant failure mechanism and propagate more clearly in line with γ_{max}, particularly between O_7

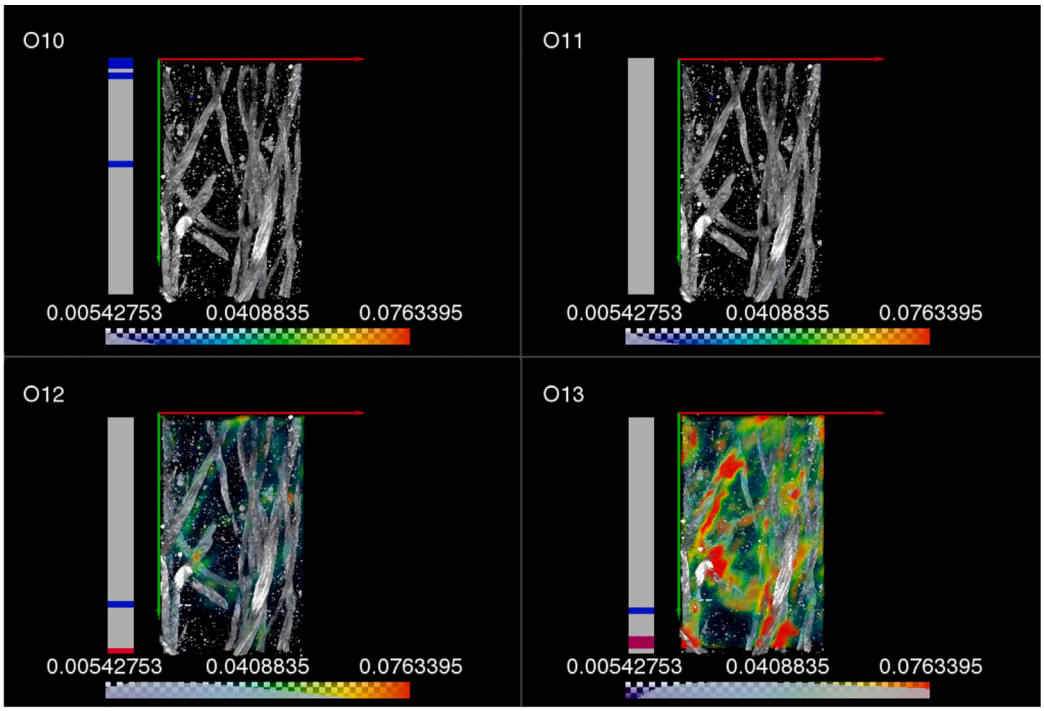


Fig. 21. Maximum shear strain (γ_{max}) between C_1 and C_2, along with AE events classified as either MC (blue) or DB (red) (O_9–O_{13}). (For interpretation of the references to colour in this figure legend, the reader is referred to the web version of this article.)

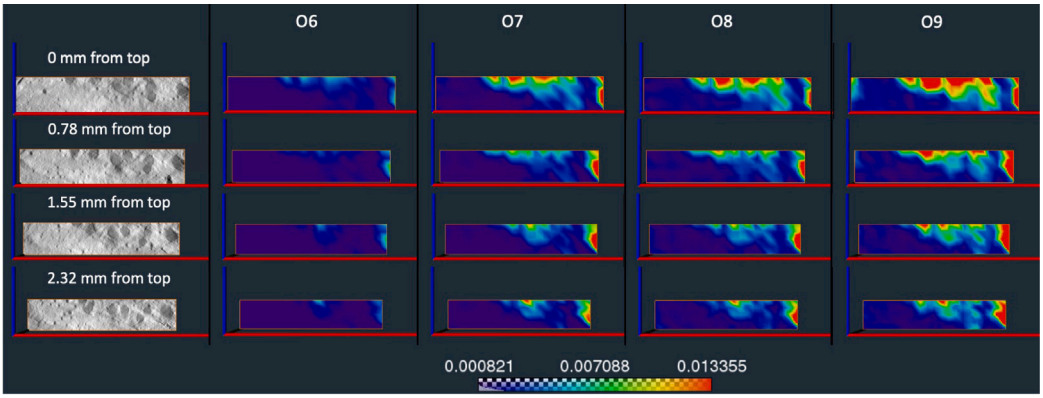


Fig. 22. Maximum shear strain (γ_{max}) in XZ plane from top (near C_1) downward, with corresponding specimen cross-sections.

and O_9. sCT revealed that near the crack front, major cracks induced interfacial activity that fragmented the matrix into small regions or triggered secondary branches adjacent to the main crack (Fig. 23), showing that interface stresses promote micro-cracking. As the debonding front advanced, jute fibres penetrating the matrix also acted as stress risers, initiating localised cracks along the interface even without visible sCT damage.

The predominance of MC and limited detection of extended DB also reflect AE properties. DB events, dominated by lower-energy, slower S-waves, attenuate more strongly, making extended debonding less detectable. In contrast, MC events generate higher-energy, faster P-waves, which attenuate less and can be detected over greater distances. Moreover, the reduction in AE-detected events after O_{10} is likely due to crack widening, as AE waveforms require a solid medium to propagate, and progressive separation within the fractured matrix limits this.

4.4. Hessian-bridging characterisation

The Kabsch algorithm was applied to quantify rigid-body translation and rotation across crack C_1, characterising hessian bridging in FP. Local DVC results from both sides of C_1 were analysed using O_5 as the reference and O_6-O_{10} as deformed states. The analysis used the original sCT dataset (voxel size 7.91 μm) with a 700 μm subset. Local DVC, rather than global DVC, was chosen to capture true displacement without enforcing artificial continuity. Two XZ-plane slices above and below C_1 (Fig. 17) were extracted to calculate relative displacement field across C_1. The Kabsch algorithm yielded the rotation matrix and translation vector for each deformed state. Relative displacement fields U_x, U_y, and U_z were obtained as differences between the above- and below-crack slices, clarifying the rigid-body motion of the FP matrix (Fig. 24). Validation comes from U_y, which rose sharply between O_7 and O_9, consistent with the crack width evolution of C_1 (Fig. 18).

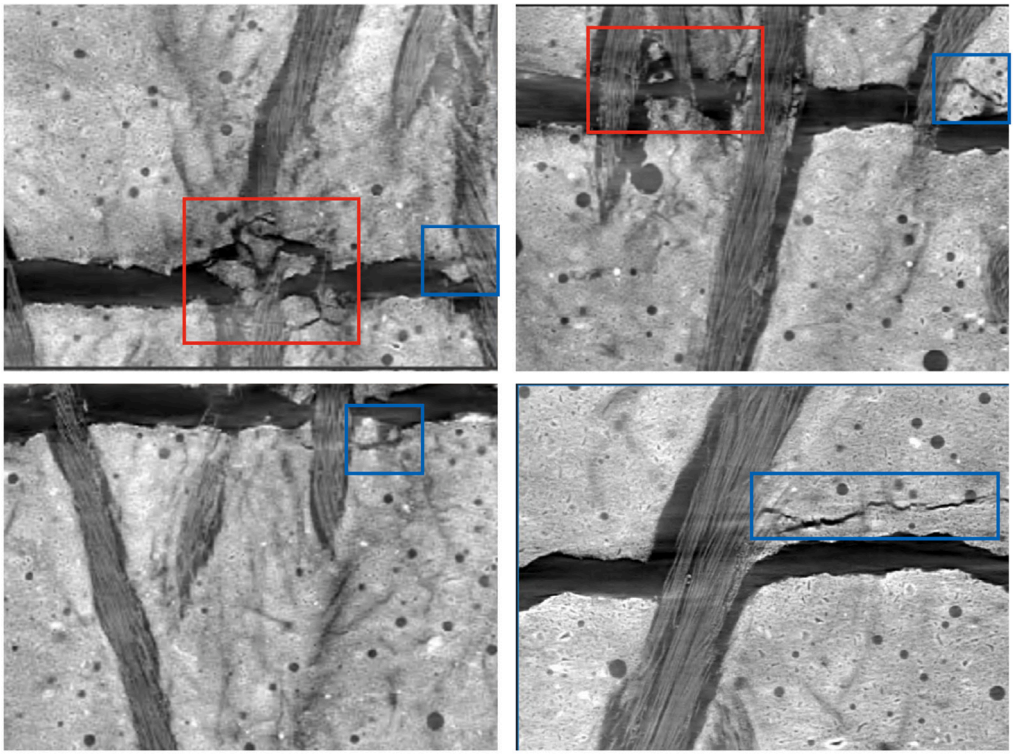


Fig. 23. Small matrix crumbles (marked in red) and secondary branching cracks (marked in blue) at the fabric–matrix interface near the major crack site. (For interpretation of the references to colour in this figure legend, the reader is referred to the web version of this article.)

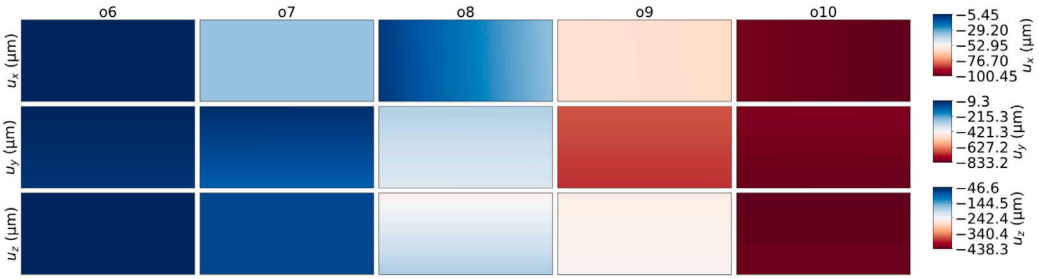


Fig. 24. Relative displacement field across the crack C_1 from O_6 to O_{11}, calculated from Kabsch algorithm using local DVC results.

A cross-section of the specimen in the XZ-plane near C_1 is shown in Fig. 17, highlighting the yarn distribution. Yarns are unevenly distributed, with higher concentrations in the top-right and left regions. This non-uniformity is reflected in U_y: in O_7 and O_8, crack opening is smaller in the upper part, indicating a bridging effect of yarns resisting widening. U_x and U_z show that the above-crack slice shifts toward $-Z$ and $-X$ relative to the below-crack slice, corresponding to leftward and forward motion. To quantify relative rotation, normals of the above- and below-crack slices were extracted for each deformed state. From these, the relative azimuth (difference in orientation of their XZ-plane projections) and relative tilt (difference in inclination to the vertical y-axis) of the top slice with respect to the bottom were computed, as summarised in Table 3.

From O_5–O_7, the slice normals remain essentially aligned, with azimuthal differences below 0.05° and tilt differences below 0.03°, confirming that the crack faces are nearly parallel and open with negligible torsional motion. From O_7–O_9, a distinct counter-clockwise twist develops: the top slice rotates by 2.35° relative to the bottom in the XZ-plane at O_8, before reducing slightly to 1.8° at O_9. The associated tilt differences remain small ($\lesssim 0.26°$), marking the onset of torsional mismatch that then stabilises as the crack continues to open, likely associated with non-uniform yarn bridging. At O_{10}, the twist direction reverses, with the top slice rotated clockwise by 1.7°

Table 3
Relative azimuth and tilt of the above-crack slice normal with respect to the below-crack slice normal for each deformed step.

Step	O_6	O_7	O_8	O_9	O_{10}
Δ Azimuth (°)	+0.049	+0.026	+2.354	+1.817	−1.668
Δ Tilt (°)	0.024	0.027	0.255	0.144	0.096

relative to the bottom, while the tilt difference remains very small (0.10°). This reversal indicates a reconfiguration of the crack faces, potentially linked to slip or re-engagement of bridging yarns. The crack faces exhibit negligible relative rotation during the early steps (O_5–O_7), a modest counter-clockwise twist that develops and stabilises in steps (O_7–O_9), and a slight clockwise reversal at O_{10}. Throughout, tilt differences remain consistently small (< 0.3°), confirming that the crack opening is predominantly characterised by direct face separation, with minor torsional adjustments due to the hessian-bridging mechanism.

In historic FP ceilings, wads function as localised load-transfer elements, transmitting the load of ceiling panels to the supporting structure. Damage typically develops through progressive matrix cracking and interfacial degradation rather than sudden failure. The direct tensile configuration adopted in this study represents a simplified stress state that isolates these governing mechanisms. Although the in-service stress state of wads is more complex, the observed sequence of matrix cracking followed by fabric–matrix debonding is consistent with damage processes reported in historic FP ceilings. The present results should therefore be interpreted as providing mechanistic insight into wad-level damage evolution, which can inform condition assessment strategies for in-service FP ceilings.

5. Conclusion

This study developed an AE-based failure mechanism characterisation model to distinguish two typical failure mechanisms in FP wad-analogue specimens under tensile loading: matrix cracking (MC) and fabric–matrix debonding (DB). Unsupervised clustering approaches were applied to categorise unlabelled AE waveform data generated by micro-failures. Direction-based clustering based on tensile–shear mode classification with RA-AF theory was used, owing to its reduced sensitivity to scale and distribution biases. Spherical k-means was selected for its computational efficiency and robustness. The method provides an objective way to extract AE signal features, reveal the underlying nature of damage, and link these features to the corresponding failure mechanisms. By connecting the deformation behaviour of FP to the progression of these mechanisms, the model establishes a basis for assessing the structural health of FP wads.

An in-situ tensile test at Beamline I12 of the Diamond Light Source was then conducted, integrating AE, DIC, and sCT monitoring. Local and global DVC were applied to the sCT data to capture deformation. The spatio-temporal distributions of AE-classified MC and DB events were compared with crack widths from 2D DIC and 3D local DVC, which showed consistent evolution, confirming the reliability of AE-based classification. High-resolution surface monitoring by DIC validated and complemented the internal monitoring provided by DVC, improving accuracy and demonstrating the novelty of combining the two techniques. Global DVC results further provided maximum shear strain fields across the loading sequence, revealing the spatio-temporal progression of fabric–matrix interfacial activity, which correlated with the temporal distribution of AE-detected DB events. Despite some limitations, the proportion of DB events proved to be a useful indicator of progressive loss of integrity, particularly in the early stages of degradation. These results also provide a deeper understanding of the damage behaviour of FP wads.

The hessian-bridging mechanism in FP was characterised through rigid-body translation and rotation analyses using the Kabsch algorithm on regions above and below the crack. Relative displacement fields across the crack were calculated for each deformed step, quantifying in-plane and out-of-plane mismatches between the crack faces. Relative rotation was described by relative azimuth and tilt angles, with tilt and torsion correlating with crack width evolution from 2D/3D analysis. These results showed that the fractured matrix separated and moved according to non-uniform yarns, providing direct evidence of the bridging effect and reflecting a staggered pattern of interfacial activity. This non-uniform debonding, together with the associated shear resistance, contributes to the extended service life of FP.

Overall, by integrating remote AE monitoring with multi-scale experimental observations, this study establishes a framework for assessing the condition of historic ceilings and provides new insights into FP failure processes. Rather than proposing a complete in-situ monitoring solution, the present study focuses on providing mechanistic insight into wad-level damage processes that complement existing field applications of AE monitoring. The practical feasibility of AE-based condition assessment for historic FP ceilings has been demonstrated in previous work through successful damage localisation using an underside-mounted multi-sensor array [50]. The deeper understanding of wad behaviour under damage also offers guidance for the design of more resilient FP components.

Table A.4
Load and displacement values recorded at observation points O_1–O_{17}.

	Load (kN)	Displacement (mm)		Load (kN)	Displacement (mm)
O_{1-2}	0.000	0.000	O_{10}	0.070	6.190
O_3	0.025	5.112	O_{11}	0.093	6.225
O_4	0.095	5.155	O_{12}	0.167	6.560
O_5	0.175	5.200	O_{13}	0.240	6.880
O_6	0.063	5.210	O_{14}	0.088	7.300
O_7	0.094	5.308	O_{15}	0.320	10.075
O_8	0.168	5.672	O_{16}	0.112	11.725
O_9	0.245	6.110	O_{17}	0.025	14.025

CRediT authorship contribution statement

Jiaxu Zuo: Writing – original draft, Visualization, Validation, Software, Methodology, Investigation, Formal analysis, Data curation, Conceptualization. **Sarah Mayfield:** Resources. **Thomas Zillhardt:** Validation, Software, Resources. **Stefan Michalik:** Validation, Software, Resources. **Genoveva Burca:** Supervision, Resources. **James Marrow:** Writing – review & editing, Supervision. **Sinan Acikgoz:** Writing – review & editing, Supervision, Funding acquisition.

Funding and acknowledgement

The authors would like to acknowledge the generous support of the ICE research and development enabling fund in the development and presentation of this research.

This work was carried out with the support of Diamond Light Source, United Kingdom, instrument I12 (proposal MG34540).

Declaration of competing interest

The authors declare that they have no known competing financial interests or personal relationships that could have appeared to influence the work reported in this paper.

Appendix

See Figs. A.25 and A.26 and Table A.4.

Data availability

Data will be made available on request.

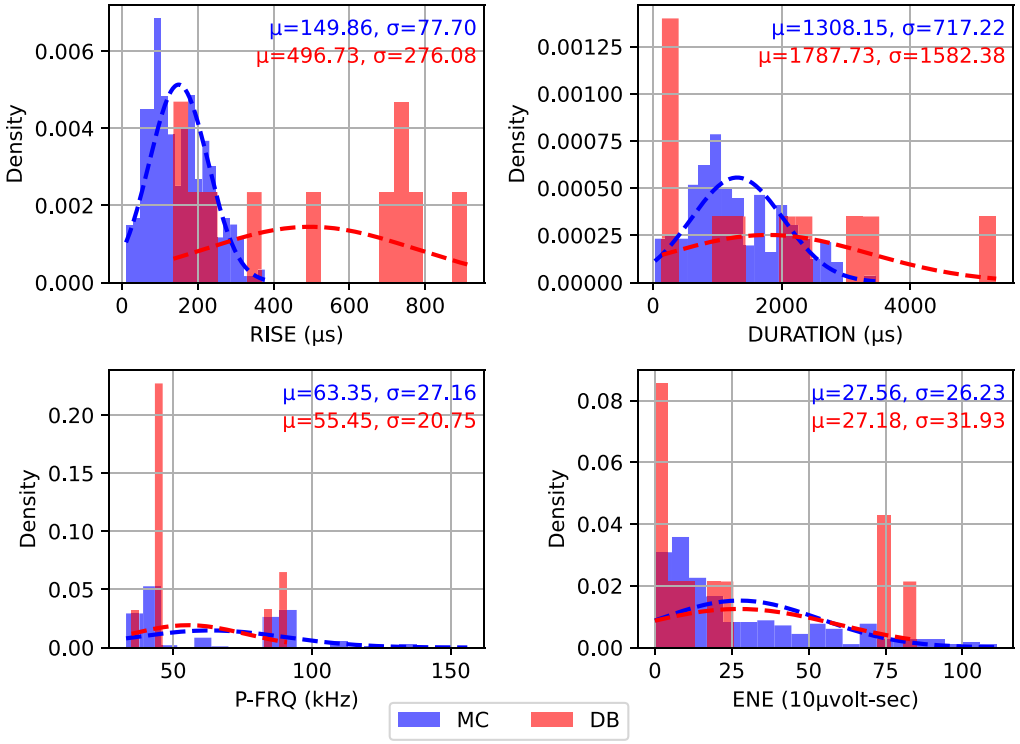
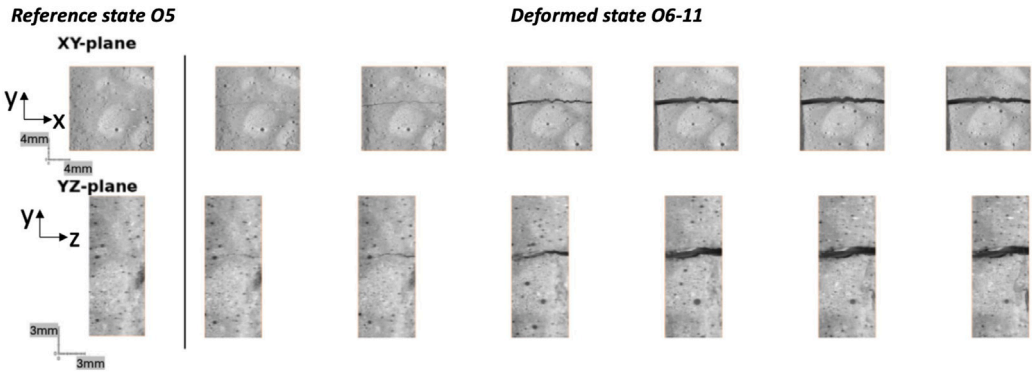
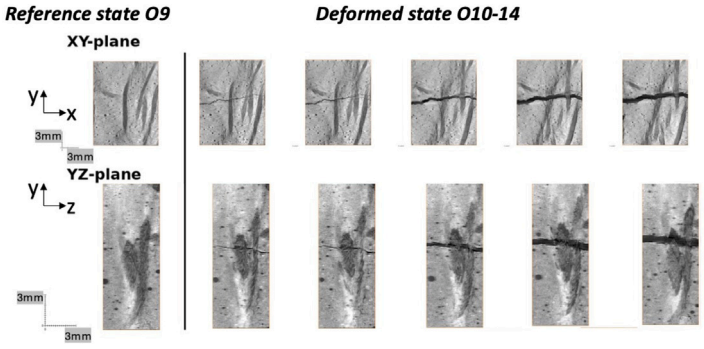


Fig. A.25. Distributions of key AE parameters for each cluster during the in-situ test.



(a) C_1



(b) C_2

Fig. A.26. Temporal crack evolution in the XY and YZ planes for: (a) C_1; (b) C_2.

References

[1] Awang-Ngah S, Dams B, Ansell MP, Stewart J, Hempstead R, Ball RJ. Structural performance of fibrous plaster. Part 1: Physical and mechanical properties of hessian and glass fibre reinforced gypsum composites. Constr Build Mater 2020;259:120396. http://dx.doi.org/10.1016/j.conbuildmat.2020.120396.

[2] Historic England. Historic fibrous plaster in the uk: guidance on its care and management. 2019, Available: https://historicengland.org.uk/advice/technical-advice/buildings/inspection-and-maintenance-of-fibrous-plaster-ceilings/.

[3] Dams B, Awang-Ngah S, Stewart J, Harrison R, Ansell MP, Harney M, Ball RJ. Load bearing capacity and failure analysis of fibrous plaster wads. Studies in Conservation, Studies in Conservation, 2025;70(1):67–87.http://dx.doi.org/10.1080/00393630.2024.2350278,

[4] ABTT. Advice to theatre owners and managers regarding suspended fibrous plaster ceilings: Survey, certification, record keeping, etc.. 2015, ABTT Guidance Note 20, Available at: https://www.abtt.org.uk/wp-content/uploads/woocommerce_uploads/2019/09/abtt-guidance-note-20-19may2015.pdf.

[5] Aveston J. The properties of fiber composites. In: Conference proceedings, national physical laboratory. IPC Science and Technology Press; 1971.

[6] Zuo J, Mayfield S, Sheil BB, Marrow J, Acikgoz S. Constituent and composite level characterisation of fibrous plaster in decorative suspended ceilings. SSRN Electron J 2025. http://dx.doi.org/10.2139/ssrn.5250456, Available at: https://ssrn.com/abstract=5250456 or.

[7] Chandarana N, Sanchez D Martinez, Soutis C, Gresil M. Early damage detection in composites during fabrication and mechanical testing. Materials 2017;10(7):685. http://dx.doi.org/10.3390/ma10070685.

[8] Das AK, Suthar D, Leung CKY. Machine learning-based crack mode classification from unlabeled acoustic emission waveform features. Cem Concr Res 2019;121:42–57. http://dx.doi.org/10.1016/j.cemconres.2019.04.007.

[9] Li L, Lomov SV, Yan X, Carvelli V. Cluster analysis of acoustic emission signals for 2D and 3D woven glass/epoxy composites. Compos Struct 2014;116:286–99. http://dx.doi.org/10.1016/j.compstruct.2014.05.005.

[10] Nasiri A, Bao J, Mccleeary D, Louis SYM, Huang X, Hu J. Online damage monitoring of SiC_f-SiC_m composite materials using acoustic emission and deep learning. IEEE Access 2019;7:140534–41. http://dx.doi.org/10.1109/ACCESS.2019.2943986.

[11] Grosse CU, Ohtsu M, Aggelis DG, Shiotani T. Acoustic emission testing: basics for research-applications in engineering. Springer Nature; 2021, http://dx.doi.org/10.1007/978-3-030-58307-2.

[12] Physical Acoustics. PCI-2 based AE system: User's manual. NJ: Princeton Junction; 2005, Available at: https://material.karlov.mff.cuni.cz/people/mathis/Navody/PCI2.pdf.

[13] Zhang F, Yang Y, Fennis SAAM, Hendriks MAN. Developing a new acoustic emission source classification criterion for concrete structures based on signal parameters. Constr Build Mater 2021;300:126163. http://dx.doi.org/10.1016/j.conbuildmat.2021.126163.

[14] Ohno K, Ohtsu M. Crack classification in concrete based on acoustic emission. Constr Build Mater 2010;24:2339–46. http://dx.doi.org/10.1016/j.conbuildmat.2010.05.004.

[15] Aggelis DG. Classification of cracking mode in concrete by acoustic emission parameters. Mech Res Commun 2011;38:153–7. http://dx.doi.org/10.1016/j.mechrescom.2011.03.007.

[16] Federation of Construction Materials Industries, Japan. Monitoring method for active cracks in concrete by acoustic emission (JCMS-III B5706). 2003.

[17] Dong L, Zhang Y, Ma J. Micro-crack mechanism in the fracture evolution of saturated granite and enlightenment to the precursors of instability. Sensors 2020;20(16):4595. http://dx.doi.org/10.3390/s20164595.

[18] Ou J, Wang E, Wang X, Wang B, Zhu G. Acoustic emission characteristics and damage evolution of different rocks under uniaxial compression conditions. Sci Rep 2024;14:4179. http://dx.doi.org/10.1038/s41598-024-10642-4.

[19] Bormann P, Engdahl B, Kind R. Seismic wave propagation and earth models. In: Bormann P, editor. New manual of seismological observatory practice 2. NMSOP2, GFZ German Research Centre for Geosciences; 2012.

[20] Li X, da Costa D Dias, Si G, Jiang S, Bournival G, Shen L. Radiation efficiency and acoustic efficiency in rock cracking: a new understanding from low and high frequency waveforms. Int J Rock Mech Min Sci 2025;170:106129. http://dx.doi.org/10.1016/j.ijrmms.2025.106129.

[21] Yue JG, Kunnath SK, Xiao Y. Uniaxial concrete tension damage evolution using acoustic emission monitoring. Constr Build Mater 2020;232:117281. http://dx.doi.org/10.1016/j.conbuildmat.2019.117281.

[22] Farhidzadeh A, Mpalaskas AC, Matikas TE, Farhidzadeh H, Aggelis DG. Fracture mode identification in cementitious materials using supervised pattern recognition of acoustic emission features. Cem Concr Res 2013;50:1–9. http://dx.doi.org/10.1016/j.cemconres.2013.02.005.

[23] Ju S, Li D, Jia J. Machine-learning-based methods for crack classification using acoustic emission technique. Mech Syst Signal Process 2022;170:109098. http://dx.doi.org/10.1016/j.ymssp.2022.109098.

[24] Chen C, Liu W, Yuan X, Fei L, Ou J. Acoustic emission analysis of crack type identification of corroded concrete columns under eccentric loading: A comparative analysis of RA-AF method and Gaussian mixture model. In: Case studies in construction materials, vol. 19, 2023, p. e02000. http://dx.doi.org/10.1016/j.cscm.2023.e02000.

[25] Gutkin R, Green CJ, Vangrattanachai S, Pinho ST, Robinson P, Curtis PT. On acoustic emission for failure investigation in CFRP: Pattern recognition and peak frequency analyses. Mech Syst Signal Process 2011;25(4):1393–407. http://dx.doi.org/10.1016/j.ymssp.2010.11.007.

[26] McCrory JP, Al-Jumaili SK, Crivelli D, Pearson MR, Eaton MJ, Featherston CA, Guagliano M, Holford KM, Pullin R. Damage classification in carbon fibre composites using acoustic emission: A comparison of three techniques. Compos Part B: Eng 2015;68:424–30. http://dx.doi.org/10.1016/j.compositesb.2014.08.016.

[27] Yue JG, Wang YN, Beskos DE. Uniaxial tension damage mechanics of steel fiber reinforced concrete using acoustic emission and machine learning crack mode classification. Cem Concr Compos 2021;119:104205. http://dx.doi.org/10.1016/j.cemconcomp.2021.104205.

[28] Mehdikhani M, Breite C, Swolfs Y, Soete J, Wevers M, Lomov SV, Gorbatikh L. Digital volume correlation for meso/micro in-situ damage analysis in carbon fiber reinforced composites. Compos Sci Technol 2021;213:108944. http://dx.doi.org/10.1016/j.compscitech.2021.108944.

[29] Maire E, Withers PJ. Quantitative X-ray tomography. Int Mater Rev 2014;59(1):1–43. http://dx.doi.org/10.1179/1743280413Y.0000000023.

[30] Holmes J, Sommacal S, Stachurski Z, Das R, Compston P. Digital image and volume correlation with X-ray micro-computed tomography for deformation and damage characterisation of woven fibre-reinforced composites. Compos Struct 2022;279:114775. http://dx.doi.org/10.1016/j.compstruct.2021.114775.

[31] Wu J, Wang H, Gao Y, Sun L. Research on damage evolution mechanisms under compressive and tensile tests of plain weave SiC_f/SiC composites using in-situ X-ray CT. Sci Eng Compos Mater 2024;31(1):20220233. http://dx.doi.org/10.1515/secm-2022-0233.

[32] Garcea SC, Sinclair I, Spearing SM, Withers PJ. Mapping fibre failure *in-situ* in carbon fibre reinforced polymers by fast synchrotron X-ray computed tomography. Compos Sci Technol 2017;152:192–203. http://dx.doi.org/10.1016/j.compscitech.2017.04.034.

[33] Wang P, Wen J, Lei H, Xu B, Liu Y, Yang L, et al. Morphology characterization and *in-situ* three-dimensional strain field monitoring of short carbon fiber-reinforced polymer composites under tension. Compos Struct 2021;262:113634. http://dx.doi.org/10.1016/j.compstruct.2021.113634.

[34] Schöberl E, Breite C, Melnikov A, Swolfs Y, Mavrogordato MN, Sinclair I, et al. Fibre-direction strain measurement in a composite ply under quasi-static tensile loading using digital volume correlation and *in-situ* synchrotron radiation computed tomography. Compos Part A: Appl Sci Manuf 2020;137:105935. http://dx.doi.org/10.1016/j.compositesa.2020.105935.

[35] Lee S, Jo E, Ji W. Digital volume correlation technique for characterizing subsurface deformation behavior of a laminated composite. Compos Part B: Eng 2020;194:108052. http://dx.doi.org/10.1016/j.compositesb.2020.108052.

[36] Drakopoulos M, Connolley T, et al. I12: the joint engineering, environment and processing (JEEP) beamline at diamond light source. J Synchrotron Radiat 2015;22(4):828–38. http://dx.doi.org/10.1107/S1600577515003513.

[37] Zuo J, Mayfield S, Özdemir A, Marrow J, Sheil B, Acikgoz S. Preliminary experimental investigation on mechanical properties of historic fibrous plaster. In: Prelim. exp. invest. mech. prop. hist. fibr. plaster. sAHC2023-13th int. conf. struct. anal. hist. constr., 2023, http://dx.doi.org/10.1007/978-3-031-39603-8_24.

[38] EN 13279-2. Gypsum binders and gypsum plasters - test methods (Part 2). European Committee for Standardization; 2014.

[39] Industrial Plasters. Fine Casting Plaster, Available at: https://industrialplasters.com/products/fine-casting-plaster.

[40] Industrial Plasters. Jute Scrim, Available at: https://industrialplasters.com/products/jute-scrim.

[41] Physical Acoustics. AEwin™: Real-time data acquisition and replay software. Phys Acoust 2025. Available: https://www.physicalacoustics.com/by-product/aewin/.

[42] ASTM International. Standard guide for determining the reproducibility of acoustic emission sensor response. In: ASTM E976-15. 2015, http://dx.doi.org/10.1520/E0976-15.

[43] Hornik K, Feinerer I, Kober M, Buchta C. Spherical K-means clustering. J Stat Softw 2012;50(10):1–22. http://dx.doi.org/10.18637/jss.v050.i10.

[44] Dhillon IS, Modha DS. Concept decompositions for large sparse text data using clustering. Mach Learn 2001;42:143–75. http://dx.doi.org/10.1023/A:1007612920971.

[45] Gülcü A, Çalışkan S. Clustering electricity market participants via FRM models. Intell Decis Technol 2020;14(4):453–67. http://dx.doi.org/10.3233/IDT-200092.

[46] Krasnov F, Sen A. The number of topics optimization: Clustering approach. Procedia Comput Sci 2019;169:510–7. http://dx.doi.org/10.3390/make1010025.

[47] Diamond Light Source. Introduction to I12 JEEP. 2024, [Accessed 8 May 2024], Available at: https://www.diamond.ac.uk/Instruments/Imaging-and-Microscopy/I12.html.

[48] MatchID. Compose the software stack that best fits your needs. 2025, [Accessed 17 June 2025], Available at: https://www.matchid.eu/en/solutions-overview/software.

[49] Thermo Fisher Scientific. Tutorial: Generate a DVC mesh of complex shapes. In: Xtra library - thermo fisher scientific. 2024, Available at: https://www.thermofisher.com/software-em-3d-vis/xtra-library/xtras/tutorial-generate-a-dvc-mesh-of-complex-shapes.

[50] Zuo J, Mayfield S, Sheil B, Acikgoz S. Acoustic emission failure detection and localisation in historic fibrous plaster ceiling. Proc Inst Civ Eng – Eng Hist Herit 2024;177(4):147–59. http://dx.doi.org/10.1680/jenhh.24.00004.

Statement of Authorship

Paper title	Acoustic emission and in-situ synchrotron X-ray computed tomography for the investigation of tensile failures in fibrous plaster
Authors	Jiaxu Zuo, Thomas Zillhardt, Stefan Michalik, Genoveva Burca, James Marrow, and Sinan Acikgoz
Publication status	Submitted
Publication details	Zuo, Jiaxu, et al. "Acoustic emission and in-situ synchrotron X-ray computed tomography for the investigation of tensile failures in fibrous plaster. " Composites Part B: Engineering (2025).

Student Confirmation

Student name	Jiaxu Zuo
Contribution to the paper	First-author contribution: • Conceived research objectives • Designed and conducted experiments • Developed and implemented computational models • Prepared and presented the manuscript
Signature	
Date	23th September 2025

Supervisor Confirmation

By signing the Statement of Authorship, the supervisor is certifying that the candidate made a substantial contribution to the publication, and that the description above is accurate.

Supervisor name	Prof. Sinan Acikgoz
Supervisor comments	
Signature	
Date	23th September 2025

Chapter 7

Conclusions and future work

7.1 Conclusions

The present work delivers a multi-scale characterisation of FP, spanning constituent, composite, and structural (wad) levels, and develops AE-based objective, non-destructive monitoring approaches for historic FP ceiling inspection. It quantifies key material properties through innovative experimental and analytical frameworks that integrate advanced techniques, and establishes explicit linkages between micro-scale damage processes and macro-scale structural response. In doing so, it provides a rigorous scientific representation of FP's material properties and deformation mechanisms while simultaneously advancing deployable AE-based monitoring strategies for heritage protection. The following summary highlights the key findings and contributions in relation to the two main research objectives: (i) material characterisation of FP, and (ii) development of AE-based SHM approaches.

(i) **Material characterisation of FP:**

- Generated new quantitative data on FP constituents (physical, chemical, and mechanical), including dynamic and static elasticity derived from VFM methods using novel test setups, tensile strength of POP determined through flexural, Brazilian, and direct tensile tests, and jute yarn properties characterised by micro X-ray techniques. These results clarified the constitutive roles of the constituents within the composite system.
- Developed a novel clevis-grip pullout test with DIC-based slip measurement, together with a newly adapted analytical model based on Naaman's formulation, to overcome existing fitting challenges and accurately quantify the bonding properties between POP and jute yarns.

- Designed complementary wad-like FP specimens for direct tensile testing to characterise the structural behaviour of FP ceiling-supporting components, revealing the multi-stage failure processes of FP. The critical mechanisms of matrix cracking and fabric-matrix debonding were identified, with their characteristics and evolution patterns quantified. For the first time, a novel in-situ experiment at the DLS I12 JEEP beamline, integrating AE, DIC, and DVC analyses, captured surface and subsurface deformation mechanisms. This demonstrated staggered debonding and fabric bridging that enhanced the durability of FP wads, providing a mechanistic basis for reconstructing resilient heritage elements in future conservation practice.

(i) **Development of AE-based SHM approaches:**

- Developed an AE-based source localisation model to detect and locate micro-failures within wads from the ceiling underside, without requiring access above the ceiling panels. A large dataset was acquired from historic FP panel samples retrieved from the ICE building, ensuring data reliability. An innovative sensor clustering technique was employed for placement, and a novel 1D-CNN trained on this dataset and tested in the laboratory significantly outperformed traditional localisation techniques. It achieved up to 94% accuracy within 20 mm error over a 2 $\times$ 2 m coverage area, while remaining robust to sensor reductions and varied layouts. Field trials on a Grade-II listed library ceiling at the ICE building validated the method under real conditions, demonstrating reliable localisation from underside-only access, scalability to larger ceiling areas, and resilience to environmental noise.
- Developed an AE-based classification model to distinguish matrix cracking from fabric-matrix debonding in FP wads. This was motivated by experimental observations of multi-stage failure behaviour in wad-like dogbone specimens under direct tensile loading, which showed that the progression of these two mechanisms reflects the health condition and stages of damage development. Categorisation of AE events into specific mechanisms therefore provides an effective means of condition assessment, and this functionality can be integrated with the localisation algorithm. Unsupervised direction-based spherical k-means clustering was applied to achieve robust classification based on RA-AF feature analysis of AE signals. The spatio-temporal distribution of clustered AE events was cross-validated

against DIC and DVC during in-situ sCT experiments, showing strong agreement and confirming that macro-scale failure stages were consistent with progressive micro-debonding. The integration of in-situ sCT testing and multi-technique verification represents a novel and powerful confirmation of AE-based monitoring, while also advancing mechanistic understanding of FP behaviour.

Collectively, these contributions establish both the scientific basis and the practical tools for the inspection and conservation of historic FP ceilings. By deriving quantitative constitutive and composite properties through advanced experimental and analytical characterisation, and by developing an AE-based SHM system grounded in a mechanistic representation of FP material response and failure evolution, this work not only fills a critical gap in the literature by providing a rigorous scientific framework for understanding FP's material properties and structural behaviour, but also offers compelling evidence of a deployable monitoring system. The combined AE-based localisation and classification functions were shown to provide a non-destructive and objective alternative to current visual and tactile inspection practices, enabling early-stage, wad-level warning of damage and delivering reliable detection of hidden deterioration in heritage ceilings. Together, these advances create a pathway to improved inspection, proactive maintenance, and the reconstruction of more resilient FP systems.

7.2 Future work

Although this thesis has established a strong foundation for the characterisation of FP and for deployable AE-based SHM approaches validated in both laboratory and field settings, further research could be done to advance fracture- and crystal-scale material characterisation, enhance durability prediction, and facilitate integration into conservation practice. The following section summarises the background and preliminary work (if any) related to each of these aspects, identifies current limitations and motivations, and outlines potential pathways for future investigation.

7.2.1 Fracture toughness characterisation of POP (extended to FP)

As a brittle material, fracture analysis is critical to understanding the crack behaviour in historic POP, since crack formation represents its most critical failure

mechanism. Prior work reported a fracture toughness for POP (W/P = 0.625) of 0.14 ± 0.015 MPa m$^{1/2}$ [18], and a range of Mode I fracture test methods, including three-point bending, wedge-splitting, chevron bending, and cracked chevron-notched Brazilian disc, have been applied [130–135]. While DIC enables real-time tracking of crack growth and the detection of subtle crack-tip advances [136], many conventional test setups are prone to unstable crack propagation, which hinders reliable stress-intensity evaluation. Accurate crack-growth identification, together with a specimen geometry and test configuration that promote stable crack propagation, are therefore essential for the estimation of stress-intensity factors (SIFs) via Williams-series or J-integral approaches.

Two fracture modes are of interest: Mode I, characterised by tensile crack opening, which gives the Mode I SIF (K_I); and Mode II, characterised by in-plane shear sliding along the crack, which gives the Mode II SIF (K_{II}). Building on recent work that introduced a keyhole geometry to initiate controllable crack paths [137], two types of 100 mm-diameter POP discs were manufactured with central keyholes oriented at 0° and 30° to favour Mode I (K_I) and Mode II (K_{II}) loading, respectively. Tests were performed on an Instron 5582 (50 kN) under displacement control at 0.5 μm s^{-1} up to 2 kN, followed by 0.1 μm s^{-1} to promote slow, trackable crack growth. The specimen was supported on a spherical bearing plate, with two lubricated PTFE (Teflon) sheets ensuring even load distribution. Double-sided DIC monitoring was employed to capture potential asymmetry in crack-tip propagation due to specimen thickness. DIC at 1 Hz (front/back stereo angles 17.44°/14.03°) yielded image-noise standard deviations of approximately 0.33/0.37 μm (horizontal/vertical) at the front and 0.31/0.36 μm at the back.

Crack paths were traced from the keyhole to the specimen edge. Current analyses used the MatchID Williams-series module, with parameters selected based on prior experience: crack-tip positions were identified using a 0.015 mm crack-opening-displacement (COD) threshold, and near-tip displacements within a 4 mm-thick, 4 mm-radius, 60° sector were fitted to linear-elastic fracture-mechanics (LEFM) fields. Crack growth under Modes I and II is visualised through horizontal displacement fields (Figure 7.1). However, the results remain problematic.

The principal limitation at present lies in the accurate detection of crack tips, which hinders the reliable evaluation of SIFs. In this study [138], a new fracture characterisation method for quasi-brittle material, such as plaster. The phase-field method can simultate the fracture process, and the crack paths can be approximately identified through a binary mesh representation by applying morphological operations

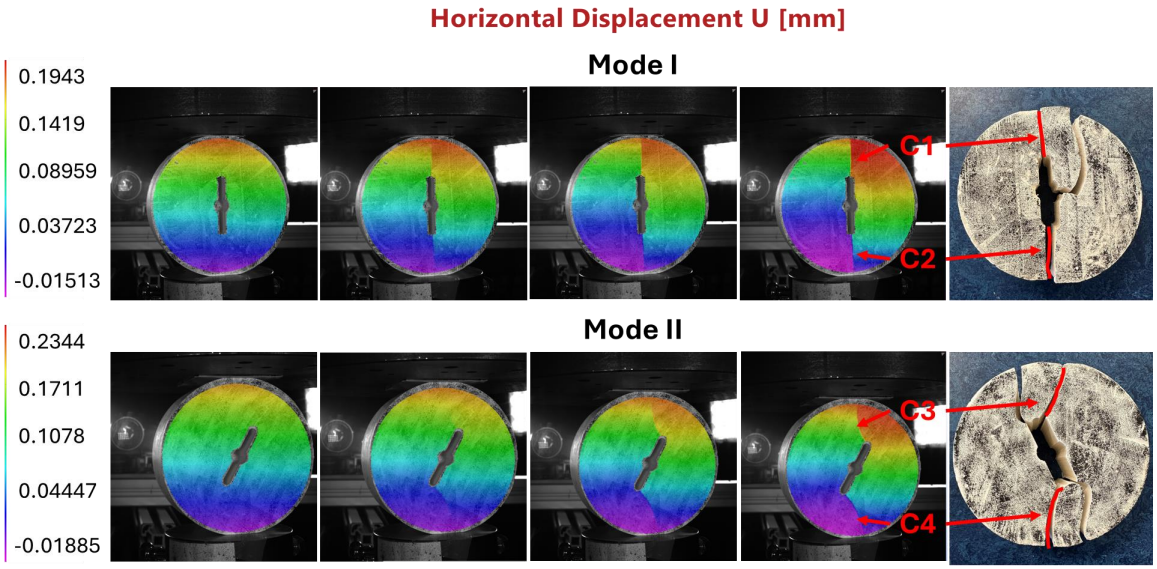


Figure 7.1: Crack initiation and propagation under Mode I and II loading.

on the phase field variable. Using a defined crack threshold (0.5), the model phase results can be binarised in to cracked (1) and non-cracked (0) zones. The binarised model mesh can be projected to a structured rectangular grid and the crack can be skeletonised using a medial-axis transform. Crack branches can be identified based on the connected components. Building on this, future work can employ the phase-field framework to establish stable crack-growth paths that enable direct interpretation of elastic displacement fields around crack tips via Williams' series expansion, thereby permitting robust extraction of fracture parameters.

This strategy offers a controlled framework for fracture-toughness testing of POP and FP, delivering reproducible Mode I/II toughness values and associated SIFs derived directly from full-field displacement measurements. The novelty lies in coupling stable crack-initiation geometries, obtained from phase-field simulation, with Williams-series-based fracture parameter identification, thereby advancing beyond conventional methodologies. The framework also can enable the role of fabric-matrix interfacial mechanisms in FP under Mode I/II loading to be investigated and quantified for the first time. These outputs can provide essential input parameters for the material characterisation of historic FP, which can enhance predictive capacity for ceiling-scale failure detection and monitoring, and informing conservation strategies.

7.2.2 Synchrotron X-ray diffraction strain mapping during in-situ tensile testing

A valuable extension of the FP characterisation is synchrotron XRD strain mapping to study how its matrix, POP, behaves under tensile loading. While DIC and DVC capture high-resolution surface and volumetric deformations, respectively, XRD provides information at an even smaller scale, revealing lattice-level changes within the crystal structure of POP. This is important because the first signs of damage, such as microcracking or stress redistribution, originate at the scale of the crystals. By measuring strain within the crystal lattice, XRD shows how internal stresses accumulate, how they are shared between phases, and where failure is likely to start. The outputs are strain and stress maps that directly illustrate how the crystalline phase of POP responds to loading.

XRD data have already been collected during in-situ tensile tests on wad-like FP specimens at the I12-JEEP beamline, DLS. A high-resolution diffraction grid (1 mm $\times$ 1 mm slits in an array of 61 $\times$ 11 points across the central gauge section, with short exposure times per point) was employed using a Pilatus3 detector, enabling the creation of detailed maps that capture how strain develops inside the POP as load increases. In principle, X-rays are diffracted by the crystal lattice of a material, and the angle or energy of the diffracted X-rays is directly related to the distance between atomic planes (lattice spacing). Strain changes the lattice spacing, so by measuring these changes across a specimen, the local strain distribution can be determined [139]. By systematically recording diffraction patterns at different points across the material, a spatial map of strain variation is generated [140]. Early XRD analysis confirmed that POP is mainly composed of β-dihydrate, and future work will examine how this phase accommodates and transfers load. These maps can then be converted into stress fields, helping to identify stress concentrations, load transfer mechanisms, and the nucleation of cracks.

Synchrotron XRD strain mapping can generate crystallographic strain and stress fields in FP during mechanical loading. These outputs, when combined with AE, DIC, and DVC, can provide a unique multiscale dataset linking lattice-level behaviour with microscopic cracking and debonding mechanisms. The novelty lies in applying high-resolution in-situ XRD mapping to historic FP for the first time, enabling direct observation of how β-dihydrate phases carry and redistribute stress. This approach can help identify stress concentrations and the initiation of cracks in POP, particularly at fabric-matrix interfaces, which is essential for predicting and preventing structural

failure. It can also advance the interpretation of AE signals and refine associated SHM approaches. In addition, the method can provide insights into how variations in reinforcement distribution affect strain development, offering a pathway to optimise wad design. The resulting insights can strengthen the characterisation of FP and establish an improved scientific basis for the conservation of historic FP ceilings.

7.2.3 Durability characterisation via accelerated ageing

An additional material property directly relevant to the behaviour of historic FP is hygrothermal durability. To investigate this, an adaptive accelerated ageing programme can be undertaken on constituent POP specimens and wad-like FP specimens using environmental chambers.

The IEC 60068–2–30 standard (cyclic damp heat) can be applied to simulate realistic hygrothermal cycling [141]. Test severities can be defined by combinations of temperature, relative humidity (RH), and total exposure duration within the ranges prescribed by the standard. Specimens can be conditioned for specified periods prior to mechanical testing.

The plan is to make specimens subjected to several cycles, using an environmental test chamber. For POP specimens, mechanical properties will be measured both before and after exposure to quantify degradation, including dynamic elastic modulus (via impulse excitation), flexural tensile strength, and compressive strength. For FP wad-like specimens, direct tensile testing will be performed. During all mechanical tests, DIC can be employed to capture the full-field displacement. The resulting property changes will be used to evaluate the impact of accelerated ageing on POP and FP durability.

This accelerated ageing programme can deliver quantitative measures of strength degradation in POP and FP under controlled hygrothermal cycling. The outputs will include mechanical property loss curves, displacement and strain maps from DIC, and comparative performance trends between constituent POP and reinforced FP specimens. The novelty lies in applying a cyclic damp-heat protocol, derived from an international environmental standard, to FP for the first time and combining it with DIC-based full-field measurement. Importantly, this framework links laboratory ageing conditions with realistic deterioration mechanisms. The results will provide long-term FP performance, and thereby contribute essential evidence to conservation practice by enabling assessment of service life, prioritisation of at-risk ceilings, and the design of preventive interventions.

7.2.4 Large-scale deployment of integrated AE-based SHM system into heritage practice

A critical next step is the large-scale deployment of AE-based SHM systems across historic FP ceilings. While laboratory and pilot field studies have demonstrated the potential of AE localisation and classification methods individually, their combined application within an integrated system must be validated under diverse real-world conditions. Field implementation should encompass ceilings of varying construction types, ages, and conservation states, as well as sites exposed to fluctuating environmental conditions and active use. Such studies will provide the basis for establishing the reliability, sensitivity, and practicality of AE monitoring in heritage contexts.

Equally important is close collaboration with conservation professionals to ensure that monitoring systems are compatible with established heritage practices. The ultimate aim is to translate AE-based SHM into practical inspection guidelines that can be adopted by heritage organisations. Integrating AE-based SHM into routine conservation practice has the potential to provide early warnings of deterioration, enhance risk assessment, and safeguard the integrity of historic FP ceilings.In summary, large-scale deployment of AE-based SHM offers a novel and transformative pathway to move beyond traditional inspection, enabling proactive, evidence-based conservation of historic FP ceilings.

Bibliography

[1] Historic England. Historic fibrous plaster in the uk: guidance on its care and management. `https://historicengland.org.uk/advice/technical-advice/buildings/inspection-and-maintenance-of-fibrous-plaster-ceilings/`, 2019.

[2] E. M. Payne. The conservation of plaster casts in the nineteenth century. *Studies in Conservation*, 65(1):37–58, 2020.

[3] W. Millar and G. P. Bankart. *Plastering Plain and Decorative*. Routledge/Donhead, London, 4th edition, 2010.

[4] ABTT. Advice to theatre owners and managers regarding suspended fibrous plaster ceilings: survey, certification, record keeping etc., May 2015.

[5] Cathedral Communications Limited. Maintaining large fibrous plaster ceilings, 2019.

[6] Shamsiah Awang Ngah, Barrie Dams, Martin P. Ansell, John Stewart, Russell Hempstead, and Richard J. Ball. Structural performance of fibrous plaster. part 1: Physical and mechanical properties of hessian and glass fibre reinforced gypsum composites. *Construction and Building Materials*, 259, 2020.

[7] The Gazette. Another gig postponed as blackpool's empress ballroom repair gets underway, 2017.

[8] The Telegraph. Savoy ceiling collapses during auction for princess anne's former school, 2019.

[9] V. Risdonne, C. Hubbard, V. H. López Borges, and C. Theodorakopoulos. Materials and techniques for the coating of nineteenth-century plaster casts: A review of historical sources. *Studies in Conservation*, 67(4):186–208, 2022.

[10] Taiwo Martins Esan. Review of gypsum reinforced composites as building materials. *Discover Civil Engineering*, 1(1):1–25, 2024.

[11] J. Cassar. The materials used in 19th and 20th century plasters: from lime and gypsum to portland cement. University of Malta Open Access Repository, 2001.

[12] M. T. Freire, A. Santos Silva, M. d. R. Veiga, and J. de Brito. Studies in ancient gypsum-based plasters towards their repair: physical and mechanical properties. *Constr. Build. Mater.*, 202:319–331, 2019.

[13] P. Coquard, R. Boistelle, L. Amathieu, and P. Barriac. Hardness, elasticity modulus and flexion strength of dry-set plaster. *J. Mater. Sci.*, 29(17):4611–4617, 1994.

[14] Jonathan Mitchell, B. K. Tanner, A. R. Kennedy, and K. G. Sharp. Observing microstructural evolution during plaster hydration. *Diffusion Fundamentals*, 10:22.1–22.3, 2009.

[15] M. Singh and B. Middendorf. Calcium sulphate hemihydrate hydration leading to gypsum crystallization. *Progress in Crystal Growth and Characterization of Materials*, 53(1):57–77, 2007.

[16] W. H. Gourdin and W. D. Kingery. The beginnings of pyrotechnology: Neolithic and egyptian lime plaster. *J. Field Archaeol.*, 2(1–2):133–150, 1975.

[17] S. K. Dalui, M. Roychowdhury, and K. K. Phani. Ultrasonic evaluation of gypsum plaster. *J. Mater. Sci.*, 31(5):1261–1263, 1996.

[18] G. Vekinis, M. F. Ashby, and P. W. R. Beaumont. Plaster of paris as a model material for brittle porous solids. *Journal of Materials Science*, 28(12):3221–3227, 1993.

[19] Q. L. Yu and H. J. H. Brouwers. Microstructure and mechanical properties of β-hemihydrate produced gypsum: An insight from its hydration process. *Construction and Building Materials*, 25(7):3149–3157, 2011.

[20] M. T. Freire, A. Santos Silva, A. Candeias, J. Mirão, R. Veiga, and E. Ferreira. Restoration of ancient gypsum-based plasters: Design of compatible materials. *Cement and Concrete Composites*, 120:104014, 2021.

[21] A. S. Al-Ridha, A. A. Abbood, F. M. Hussein, L. S. Dheyab, E. L. N. Abdullah, E. H. Z. Ali, et al. Effect of chopped sisal fiber (csf) on enhancing the compressive strength of local plaster of paris (lpop). *Materials Today: Proceedings*, 47:2575–2579, 2021.

[22] S. M. Kabir, H. Wang, K. T. Lau, and F. Cardona. Chemical treatments on plant-based natural fibre reinforced polymer composites: An overview. *Composites Part B: Engineering*, 43(7):2883–2892, 2013.

[23] A. Majumder, F. Stochino, I. Farina, M. Valdes, F. Fraternali, and E. Martinelli. Physical and mechanical characteristics of raw jute fibers, threads and diatons. *Construction and Building Materials*, 326:126903, 2022.

[24] A. S. Ullah, S. Shahinur, and H. Haniu. On the mechanical properties and uncertainties of jute yarns. *Materials*, 10(5):450, 2017.

[25] Mohammad Salman Haque and M. A. Islam. Microbial degradation of the waste jute fiber and sawdust fiber-based epoxy composites in drainage system. *Heliyon*, 10(20):e39397, 2024.

[26] Jianqiang Wei and Christian Meyer. Degradation rate of natural fiber in cement composites exposed to various accelerated aging environment conditions. *Corrosion Science*, 88:118–132, 2014.

[27] Richard Ireland. Report on the apollo theatre ceiling collapse. Technical report, Association of British Theatre Technicians (ABTT), 2014.

[28] M. A. Ali and F. J. Grimer. Mechanical properties of glass fibre-reinforced gypsum. *Journal of Materials Science*, 4(5):389–395, 1969.

[29] ASTM International. *Standard Test Method for Dynamic Young's Modulus, Shear Modulus, and Poisson's Ratio by Impulse Excitation of Vibration*. ASTM International, West Conshohocken, PA, 2022.

[30] J. D. Lord and R. Morrell. *Elastic Modulus Measurement, A National Measurement Good Practice Guide*. DTI, National Physical Laboratory, Teddington, UK, 2006.

[31] British Standards Institution. BS EN 13279-2:2004 Gypsum binders and gypsum plasters — Test methods. *British Standards*, 2004.

[32] ASTM International. ASTM C472-99: Standard Test Methods for Physical Testing of Gypsum, Gypsum Plasters and Gypsum Concrete. *ASTM Standards*, 1999.

[33] S. M. Chassib, S. K. Zemam, and M. J. Madhi. New approach of concrete tensile strength test. *Case Studies in Construction Materials*, 12:e00347, 2020.

[34] International Society for Rock Mechanics. Suggested method for determining the Brazilian tensile strength of rock. *International Journal of Rock Mechanics and Mining Sciences & Geomechanics Abstracts*, 18(6):85–90, 1981. ISRM Suggested Methods.

[35] W.-C. Liao, P.-S. Chen, C.-W. Hung, and S. K. Wagh. An innovative test method for tensile strength of concrete by applying the strut-and-tie methodology. *Materials (Basel)*, 13(12):2776, 2020.

[36] Yousef Navidtehrani, María Covadonga Betegón, Robert W. Zimmerman, and Emilio Martínez-Pañeda. Griffith-based analysis of crack initiation location in a brazilian test. *International Journal of Rock Mechanics and Mining Sciences*, 159:105227, 2022.

[37] Aditya Kumar, Yangyuanchen Liu, John E. Dolbow, and Oscar Lopez-Pamies. The strength of the brazilian fracture test. *Journal of the Mechanics and Physics of Solids*, 182:105473, 2024.

[38] Víctor J. García, Carmen O. Márquez, Alonso R. Zúñiga-Suárez, Berenice C. Zúñiga-Torres, and Luis J. Villalta-Granda. Brazilian test of concrete specimens subjected to different loading geometries: Review and new insights. *International Journal of Concrete Structures and Materials*, 11(2):343–363, 2017.

[39] José Rafael Capua Proveti and Gérard Michot. The brazilian test: a tool for measuring the toughness of a material and its brittle to ductile transition. *International Journal of Fracture*, 139(3):455–460, 2006.

[40] M. Gatuu and A. S. Sanakanan. Effect of porosities on strength of plaster of paris. Available at: `http://hdl.handle.net/2080/2954`, 2018.

[41] ASTM International. ASTM D3822/D3822M-14: Standard Test Method for Tensile Properties of Single Textile Fibers. *ASTM Standards*, 2020.

[42] ASTM International. ASTM D1577-07(2018): Standard Test Method for Linear Density of Textile Fibers. *ASTM Standards*, 2018.

[43] L. A. Donaldson. Analysis of fibres using microscopy. In S. J. Eichhorn, J. W. S. Hearle, M. Jaffe, and T. Kikutani, editors, *Handbook of Textile Fibre Structure: Fundamentals and Manufactured Polymer Fibres*, volume 1 of *Woodhead Publishing Series in Textiles*, pages 121–153. Woodhead Publishing, 2009.

[44] Yulin Deng, Zuhua Zhang, Caijun Shi, Zemei Wu, and Chaohui Zhang. Steel fiber–matrix interfacial bond in ultra-high performance concrete: A review. *Engineering*, 8:34–48, 2022. Under a Creative Commons license.

[45] R.J. Gray. Experimental techniques for measuring fibre/matrix interfacial bond shear strength. In *Proceedings of the International Conference on Testing, Evaluation and Quality Control of Composites (TEQC83)*, pages 3–11, 1983.

[46] Bahman Ghiassi, Daniel V. Oliveira, Vera Marques, Edgar Soares, and Hamid Maljaee. Multi-level characterization of steel reinforced mortars for strengthening of masonry structures. *Materials and Design*, 110:903–913, 2016.

[47] A. Dalalbashi, B. Ghiassi, D. V. Oliveira, and A. Freitas. Effect of test setup on the fiber-to-mortar pull-out response in trm composites: Experimental and analytical modeling. *Composites Part B: Engineering*, 143:250–268, 2018.

[48] A. E. Naaman, G. G. Namur, J. M. Alwan, and H. S. Najm. Fiber pullout and bond slip. i: Analytical study. *Journal of Structural Engineering*, 117(9):2769–2790, 1991.

[49] A. E. Naaman, G. G. Namur, J. M. Alwan, and H. S. Najm. Fiber pullout and bond slip. ii: Experimental validation. *Journal of Structural Engineering*, 117(9):2791–2800, 1991.

[50] J. Shannag, R. Brincker, and W. Hansen. Pullout behavior of steel fibers from cement-based composites. *Cement and Concrete Research*, 27:925–936, 1997.

[51] S. Sueki, C. Soranakom, B. Mobasher, and A. Peled. Pullout-slip response of fabrics embedded in a cement paste matrix. *Journal of Materials in Civil Engineering*, 19(9):718–728, 2007.

[52] A. Dalalbashi, B. Ghiassi, D. V. Oliveira, and A. Freitas. Fiber-to-mortar bond behavior in trm composites: Effect of embedded length and fiber configuration. *Composites Part B: Engineering*, 152:43–57, 2018.

[53] A. Dalalbashi, B. Ghiassi, and D. V. Oliveira. Textile-to-mortar bond behavior: An analytical study. *Construction and Building Materials*, 282:122639, 2021.

[54] J. Aveston. The properties of fiber composites. In *Conference Proceedings, National Physical Laboratory*. IPC Science and Technology Press, 1971.

[55] Pierre Dalmay, Agnès Smith, Thierry Chotard, P. Sahay-Turner, Vincent Gloaguen, and Pierre Krausz. Properties of cellulosic fibre reinforced plaster: Influence of hemp or flax fibres on the properties of set gypsum. *Journal of Materials Science*, 45(3):793–803, 2010.

[56] Fabio Iucolano, Domenico Caputo, Flavio Leboffe, and Barbara Liguori. Mechanical behavior of plaster reinforced with abaca fibers. *Construction and Building Materials*, 99:184–191, 2015.

[57] Tara Sen and H. N. Jagannatha Reddy. Strengthening of rc beams in flexure using natural jute fibre textile reinforced composite system and its comparative study with cfrp and gfrp strengthening systems. *International Journal of Sustainable Built Environment*, 2(1):41–55, 2013.

[58] Tara Sen and H. N. Jagannatha Reddy. Flexural strengthening of rc beams using natural sisal and artificial carbon and glass fabric reinforced composite system. *Sustainable Cities and Society*, 10:195–206, 2014.

[59] Niki Trochoutsou, Matteo Di Benedetti, Kypros Pilakoutas, and Maurizio Guadagnini. Mechanical characterisation of flax and jute textile-reinforced mortars. *Construction and Building Materials*, 271:121564, 2021.

[60] J. Hartig, Frank Jesse, K. Schicktanz, and Ulrich Häußler-Combe. Influence of experimental setups on the apparent uniaxial tensile load-bearing capacity of textile reinforced concrete specimens. *Materials and Structures*, 45(3):433–446, 2012.

[61] Stefano De Santis, Francesca Giulia Carozzi, Gianmarco de Felice, and Carlo Poggi. Test methods for textile reinforced mortar systems. *Composites Part B: Engineering*, 127:121–132, 2017.

[62] Ayman Shamseldein, Fareed Elgabbas, and Hany Elshafie. Tensile behavior of basalt textile-reinforced mortar (btrm). *Ain Shams Engineering Journal*, 13(1):101488, 2022.

[63] Van Doan Truong and Dong Joo Kim. A review paper on direct tensile behavior and test methods of textile reinforced cementitious composites. *Composite Structures*, 263:113661, 2021.

[64] J. Hegger, N. Will, O. Bruckermann, and S. Voss. Load–bearing behaviour and simulation of textile-reinforced concrete. *Materials and Structures*, 39:765–776, 2006.

[65] J. Orlowsky and M. Raupach. Modelling the loss in strength of ar-glass fibres in textile-reinforced concrete. *Materials and Structures*, 39(6):635–643, 2006.

[66] J. Orlowsky and M. Raupach. Durability model for ar-glass fibres in textile-reinforced concrete. *Materials and Structures*, 41:1225–1233, 2008.

[67] T. D'Antino and C. C. Papanicolaou. Comparison between different tensile test set-ups for the mechanical characterization of inorganic-matrix composites. *Construction and Building Materials*, 171:140–151, 2018.

[68] C. R. Farrar and K. Worden. An introduction to structural health monitoring. In A. Deraemaeker and K. Worden, editors, *New Trends in Vibration Based Structural Health Monitoring*, volume 520 of *CISM Courses and Lectures*, pages 1–17. Springer, Vienna, 2010.

[69] Herbert Wiggenhauser, Rosemarie Helmerich, Alexander Taffe, Martin Krause, Thomas Kind, Wai-Lok Lai, Horst Scheel, Gerd Wilsch, and Ernst Niederleithinger. Nondestructive testing in civil engineering. In *Nondestructive Testing*, chapter 6. Wiley-VCH, 2011.

[70] Christian U. Grosse, Masayasu Ohtsu, Dimitrios G. Aggelis, and Tomoki Shiotani. *Acoustic Emission Testing: Basics for Research-Applications in Engineering*. Springer Nature, 2021.

[71] Qing-Hua Han, Guang Yang, and Jie Xu. Experimental study on the relationship between acoustic emission energy and fracture energy of crumb rubber concrete. *Structural Control and Health Monitoring*, 26(5):e2240, 2018.

[72] N. Chandarana, D. Martinez Sanchez, C. Soutis, and M. Gresil. Early damage detection in composites during fabrication and mechanical testing. *Materials*, 10(7):685, 2017.

[73] A. K. Das, D. Suthar, and C. K. Y. Leung. Machine learning-based crack mode classification from unlabeled acoustic emission waveform features. *Cement and Concrete Research*, 121:42–57, 2019.

[74] L. Li, S. V. Lomov, X. Yan, and V. Carvelli. Cluster analysis of acoustic emission signals for 2d and 3d woven glass/epoxy composites. *Composite Structures*, 116:286–299, 2014.

[75] A. Nasiri, J. Bao, D. Mccleeary, S. Y. M. Louis, X. Huang, and J. Hu. Online damage monitoring of sic_f-sic_m composite materials using acoustic emission and deep learning. *IEEE Access*, 7:140534–140541, 2019.

[76] Vinoth Kanna Gopinath and Ravi Ramadoss. Review on structural health monitoring for restoration of heritage buildings. *Materials Today: Proceedings*, 43:1534–1538, 2021.

[77] W. Zhou, Z. B. Pan, J. Wang, S. Qiao, L. H. Ma, J. Liu, X. Y. Ren, and Y. Z. Liang. Review on acoustic emission source location, damage recognition and lifetime prediction of fiber-reinforced composites. *Journal of Materials Science*, pages 1–25, 2023.

[78] M. E. De Simone, F. Ciampa, S. Boccardi, and M. Meo. Impact source localisation in aerospace composite structures. *Smart Materials and Structures*, 26(12):125026, 2017.

[79] Nelson N. Hsu and F. R. Breckenridge. Characterization and calibration of acoustic emission sensors. In *Proceedings of the 6th International Acoustic Emission Symposium*, pages 17–31. Japanese Society for Non-Destructive Inspection, 1981.

[80] J. Zhou, V. J. Mathews, and D. O. Adams. Acoustic emission–based impact location estimation on composite structures. *Structural Health Monitoring*, 18(5–6):1652–1668, 2019.

[81] R. Gangadharan, G. Prasanna, M. R. Bhat, C. R. L. Murthy, and S. Gopalakrishnan. Acoustic emission source location in composite structure by voronoi construction using geodesic curve evolution. *The Journal of the Acoustical Society of America*, 126(5):2324–2330, 2009.

[82] Tribikram Kundu, Hayato Nakatani, and Nobuo Takeda. Acoustic source localization in anisotropic plates. *Ultrasonics*, 52(6):740–746, 2012.

[83] D. Xiao, T. He, Q. Pan, X. Liu, J. Wang, and Y. Shan. A novel acoustic emission beamforming method with two uniform linear arrays on plate-like structures. *Ultrasonics*, 54(2):737–745, 2014.

[84] N. Sen, M. Gawronski, P. Packo, T. Uhl, and T. Kundu. Square-shaped sensor clusters for acoustic source localisation in anisotropic plates by wave front shape-based approach. *Mechanical Systems and Signal Processing*, 153:107489, 2021.

[85] W. H. Park, P. Packo, and T. Kundu. Acoustic source localisation in an anisotropic plate without knowing its material properties: a new approach. *Ultrasonics*, 79:9–17, 2017.

[86] D. Aljets, A. Chong, S. Wilcox, and K. Holford. Acoustic emission source location on large plate-like structures using a local triangular sensor array. *Mechanical Systems and Signal Processing*, 30:91–102, 2012.

[87] N. Sen and T. Kundu. Acoustic source localisation in a highly anisotropic plate with unknown orientation of its axes of symmetry and material properties with numerical verification. *Ultrasonics*, 100:105977, 2020.

[88] S. Yin, Z. Cui, and T. Kundu. Acoustic source localisation in anisotropic plates with "z" shaped sensor clusters. *Ultrasonics*, 84:34–37, 2018.

[89] H. Nakatani, T. Kundu, and N. Takeda. Improving accuracy of acoustic source localisation in anisotropic plates. *Ultrasonics*, 54(7):1776–1788, 2014.

[90] N. Sen and T. Kundu. Acoustic source localisation in a highly anisotropic plate with unknown orientation of its axes of symmetry and material properties with numerical verification. *Ultrasonics*, 100:105977, 2020.

[91] T. Fu, Z. Zhang, Y. Liu, and J. Leng. Development of an artificial neural network for source localisation using a fiber optic acoustic emission sensor array. *Structural Health Monitoring*, 14(2):168–177, 2015.

[92] S. Kalafat and M. G. R. Sause. Acoustic emission source localisation by artificial neural networks. *Structural Health Monitoring*, 14(6):633–647, 2015.

[93] M. G. R. Sause, S. Schmitt, B. Hoeck, and A. Monden. Acoustic emission based prediction of local stress exposure. *Composites Science and Technology*, 173:90–98, 2019.

[94] G. Ding, C. Xiu, Z. Wan, J. Li, X. Pei, and Z. Zheng. Location of tensile damage source of carbon fiber braided composites based on two-step method. *Molecules*, 24(19):3524, 2019.

[95] X. Zhang, H. Wang, B. Hou, J. Xu, and R. Yan. 1d-cnn-based damage identification method based on piezoelectric impedance using adjustable inductive shunt circuitry for data enrichment. *Structural Health Monitoring*, 21(5):1992–2009, 2022.

[96] K. Ohno and M. Ohtsu. Crack classification in concrete based on acoustic emission. *Construction and Building Materials*, 24:2339–2346, 2010.

[97] D. G. Aggelis. Classification of cracking mode in concrete by acoustic emission parameters. *Mechanics Research Communications*, 38:153–157, 2011.

[98] F. Zhang, Y. Yang, S. A. A. M. Fennis, and M. A. N. Hendriks. Developing a new acoustic emission source classification criterion for concrete structures based on signal parameters. *Construction and Building Materials*, 300:126163, 2021.

[99] Federation of Construction Materials Industries, Japan. Monitoring method for active cracks in concrete by acoustic emission (jcms-iii b5706), 2003. Tokyo, Japan.

[100] J. G. Yue, S. K. Kunnath, and Y. Xiao. Uniaxial concrete tension damage evolution using acoustic emission monitoring. *Construction and Building Materials*, 232:117281, 2020.

[101] Satish Chander and P. Vijaya. Unsupervised learning methods for data clustering. In Bidyadhar Subudhi and B. K. Panigrahi, editors, *Artificial Intelligence in Data Mining: Theories and Applications*, pages 41–64. Academic Press, 2021.

[102] S. Ju, D. Li, and J. Jia. Machine-learning-based methods for crack classification using acoustic emission technique. *Mechanical Systems and Signal Processing*, 170:109098, 2022.

[103] C. Chen, W. Liu, X. Yuan, L. Fei, and J. Ou. Acoustic emission analysis of crack type identification of corroded concrete columns under eccentric loading: A comparative analysis of ra-af method and gaussian mixture model. *Case Studies in Construction Materials*, 19:e02000, 2023.

[104] R. Gutkin, C. J. Green, S. Vangrattanachai, S. T. Pinho, P. Robinson, and P. T. Curtis. On acoustic emission for failure investigation in cfrp: Pattern recognition and peak frequency analyses. *Mechanical Systems and Signal Processing*, 25(4):1393–1407, 2011.

[105] Michael A. Sutton, Scott R. McNeill, Joel D. Helm, and Y. J. Chao. Advances in two-dimensional and three-dimensional computer vision. In Pramod K. Rastogi, editor, *Photomechanics*, volume 77 of *Topics in Applied Physics*, pages 323–372. Springer, Berlin, Heidelberg, 2000.

[106] Hubert Schreier, Jean-José Orteu, and Michael A. Sutton. *Image Correlation for Shape, Motion and Deformation Measurements*. Springer, New York, NY, 1 edition, 2009.

[107] François Hild and Stéphane Roux. Comparison of local and global approaches to digital image correlation. *Experimental Mechanics*, 52(9):1503–1519, November 2012.

[108] Peter Jannotti. The utility of 3d digital image correlation for characterizing high-rate deformation. In Jennifer Kimberley, L. Lamberson, and S. Mates, editors, *Dynamic Behavior of Materials, Volume 1*, Conference Proceedings of the Society for Experimental Mechanics Series. Springer, Cham, 2019.

[109] Bing Pan, Kemao Qian, Huimin Xie, and Anand Asundi. Two-dimensional digital image correlation for in-plane displacement and strain measurement: a review. *Measurement Science and Technology*, 20(6):062001, 2009.

[110] L. Salvo, P. Cloetens, E. Maire, S. Zabler, J.J. Blandin, J.Y. Buffière, W. Ludwig, E. Boller, D. Bellet, and C. Josserond. X-ray micro-tomography an attractive characterisation technique in materials science. *Nuclear Instruments and Methods in Physics Research Section B: Beam Interactions with Materials and Atoms*, 200:273–286, 2003.

[111] J.-Y. Buffière, E. Maire, P. Cloetens, G. Lormand, and R. Fougères. Characterization of internal damage in a mmc_p using x-ray synchrotron phase contrast microtomography. *Acta Materialia*, 47(5):1613–1625, 1999.

[112] E. Maire and P. J. Withers. Quantitative x-ray tomography. *International Materials Reviews*, 59(1):1–43, 2014.

[113] Bing Pan and Bo Wang. Some recent advances in digital volume correlation. *Optics and Lasers in Engineering*, 135:106189, 2020.

[114] J.Y. Buffière, E. Maire, J. Adrien, and et al. In situ experiments with x ray tomography: an attractive tool for experimental mechanics. *Experimental Mechanics*, 50:289–305, 2010.

[115] Brian P. Flannery and W.G. Roberge. Observational strategies for three-dimensional synchrotron microtomography. *Journal of Applied Physics*, 61(12):5860–5868, 1987.

[116] W. Graeff, K. Engelke, S. Ebashi, M. Koch, and E. Rubenstein. Handbook of synchrotron radiation. In *Handbook of Synchrotron Radiation, Volume 4*, page 407. North-Holland Publishing Company, 1991.

[117] G.T. Herman. Image reconstruction from projections. *Real-Time Imaging*, 1(1):3–18, 1995.

[118] Diamond Light Source. Introduction to i12 jeep, 2024.

[119] Stuart R. Stock. *MicroComputed Tomography*. CRC Press, Boca Raton, FL, second edition, 2019.

[120] Jun-bo Xie, Chong Liu, Li Chen, et al. Mechanical modeling of textile composites using fiber-reinforced voxel models. *Journal of the Textile Institute*, 111(11):1678–1689, 2020.

[121] Z. Yousaf, P.J. Withers, and P. Potluri. Compaction, nesting and image based permeability analysis of multi-layer dry preforms by computed tomography (ct). *Composite Structures*, 263:113676, 2021.

[122] K. Naresh, K.A. Khan, R. Umer, and W.J. Cantwell. The use of x-ray computed tomography for design and process modeling of aerospace composites: A review. *Materials & Design*, 190:108553, 2020.

[123] R. Böhm, J. Stiller, T. Behnisch, M. Zscheyge, R. Protz, S. Radloff, M. Gude, and W. Hufenbach. A quantitative comparison of the capabilities of in situ computed tomography and conventional computed tomography for damage analysis of composites. *Composites Science and Technology*, 110:62–68, 2015.

[124] Qingliang Zeng, Lijuan Sun, Jingran Ge, Wenwang Wu, Jun Liang, and Daining Fang. Damage characterization and numerical simulation of shear experiment of plain woven glass-fiber reinforced composites based on 3d geometric reconstruction. *Composite Structures*, 233:111746, 2020.

[125] S.C. Garcea, Y. Wang, and P.J. Withers. X-ray computed tomography of polymer composites. *Composites Science and Technology*, 156:305–319, 2018.

[126] Yuan Chai, Ying Wang, Zeshan Yousaf, Malte Storm, Nghia T. Vo, Kaz Wanelik, Timothy L. Burnett, Prasad Potluri, and Philip J. Withers. Following the effect of braid architecture on performance and damage of carbon fibre/epoxy composite tubes during torsional straining. *Composites Science and Technology*, 200:108451, 2020.

[127] A. Buljac, C. Jailin, A. Mendoza, and et al. Digital volume correlation: Review of progress and challenges. *Experimental Mechanics*, 58:661–708, 2018.

[128] John Holmes, Silvano Sommacal, Zbigniew Stachurski, Raj Das, and Paul Compston. Digital image and volume correlation with x-ray micro-computed tomography for deformation and damage characterisation of woven fibre-reinforced composites. *Composite Structures*, 279:114775, 2022.

[129] M. Mehdikhani, C. Breite, Y. Swolfs, J. Soete, M. Wevers, S. V. Lomov, and L. Gorbatikh. Digital volume correlation for meso/micro in-situ damage analysis in carbon fiber reinforced composites. *Composites Science and Technology*, 213:108944, 2021.

[130] Jian-ping Zuo, He-ping Xie, Feng Dai, and Yang Ju. Three-point bending test investigation of the fracture behavior of siltstone after thermal treatment. *International Journal of Rock Mechanics and Mining Sciences*, 70:133–143, 2014.

[131] S. Xu and H. W. Reinhardt. A simplified method for determining double-k fracture parameters for three-point bending tests. *International Journal of Fracture*, 104(2):181–209, 2000.

[132] E. Brühwiler and F. H. Wittmann. The wedge splitting test, a new method of performing stable fracture mechanics tests. *Engineering Fracture Mechanics*, 35(1–3):117–125, 1990.

[133] H. M. Abdalla and B. L. Karihaloo. Determination of size-independent specific fracture energy of concrete from three-point bend and wedge splitting tests. *Magazine of Concrete Research*, 55(2):133–141, 2003.

[134] Mingdong Wei, Feng Dai, Nuwen Xu, Tao Zhao, and Yi Liu. An experimental and theoretical assessment of semi-circular bend specimens with chevron and straight-through notches for mode i fracture toughness testing of rocks. *International Journal of Rock Mechanics and Mining Sciences*, 99:28–38, 2017.

[135] M. R. M. Aliha and M. R. Ayatollahi. Rock fracture toughness study using cracked chevron notched brazilian disc specimen under pure modes i and ii loading – a statistical approach. *Theoretical and Applied Fracture Mechanics*, 69:17–25, 2014.

[136] G. Gao, W. Yao, K. Xia, and Z. Li. Investigation of the rate dependence of fracture propagation in rocks using digital image correlation (dic) method. *Engineering Fracture Mechanics*, 138:146–155, 2015.

[137] H. Chen, J. Shen, D. Scotson, X. Jin, H. Wu, and T. J. Marrow. Fracture toughness evaluation of a nuclear graphite with non-linear elastic properties by 3d imaging and inverse finite element analysis. *Engineering Fracture Mechanics*, 293:109719, 2023.

[138] Sinan Acikgoz, Emilio Martínez Pañeda, and François Hild. Fracture characterisation of masonry materials using flattened and notched disc samples. In *Proceedings of the Structural Analysis of Historical Constructions*. SAHC, Geneva, May 2025.

[139] J. S. Park, A. Chuang, J. Okasinski, et al. A new residual strain mapping program using energy dispersive X-Ray diffraction at the Advanced Photon Source. *Experimental Mechanics*, 62:1363–1379, 2022.

[140] Bruce Duncan. Developments in testing adhesive joints. In *Advances in Structural Adhesive Bonding*, Woodhead Publishing in Materials, pages 389–436. Woodhead Publishing, 2010.

[141] Iec 60068-2-30: Environmental testing—part 2-30: Tests—test db: Damp heat, cyclic (12 h + 12 h cycle), 2010.